

A GAS-SURFACE INTERACTION MODEL  
FOR THE NUMERICAL STUDY OF ROCKET  
NOZZLE FLOWS OVER PYROLYZING  
ABLATIVE MATERIALS

by

Alessandro Turchi





Dipartimento di Ingegneria Meccanica e Aerospaziale  
Dottorato in Tecnologia Aeronautica e Spaziale – XXV ciclo

# A gas-surface interaction model for the numerical study of rocket nozzle flows over pyrolyzing ablative materials

by

Alessandro Turchi

Thesis Advisor: Prof. Francesco Nasuti

April 2013



---

## **Abstract**

**A gas–surface interaction model for the numerical study of rocket  
nozzle flows over pyrolyzing ablative materials**

Alessandro Turchi

Ablative materials provide a widespread, reliable, and relatively low-cost way to manage the extremely high heat fluxes that are normally encountered in a wide variety of aerospace applications. Typically, both non-pyrolyzing carbon-based and pyrolyzing carbon- and silica-based materials are used with this intent in rocket nozzles. Unfortunately, during the rocket firing these materials undergo a consumption that modifies the nozzle internal contour increasing the nozzle throat area and causing a drop down of the chamber pressure that, ultimately, results in an overall rocket performance reduction. For this reason, it is important to advance the fundamental understanding of the nozzle erosion processes and to develop useful scientific tools in this subject area. To this aim, a comprehensive

model that would allow the study of the behavior of different ablative materials in rocket nozzle environment accounting for surface ablation, pyrolysis gas injection and resin decomposition has been developed, tested and validated. The model relies on surface mass and energy balances and deals with the gas–surface interaction erosive phenomena, accurately solving the gas side, using a CFD approach. Two different ablation models have been implemented to simulate both the erosion of carbon– and silica–based materials. The steady–state ablation approximation is used in order to estimate the solid conductive heat flux, as well as the pyrolysis gas mass flow rate, in a closed way and without requiring the accurate resolution of the material heating by means of a thermal response code. Firstly, the talk will address a thorough description of the theoretical/numerical model. Then, several simulations, from sub–scale to full–scale nozzles, will be presented and the results will be compared with the experimental results.



---

## Acknowledgments

I would like to gratefully and sincerely thank Dr. Daniele Bianchi for his invaluable support. Our daily discussions have been the starting point every single argument dealt with in this work. His willingness to give his time so generously made the planning and the development of this research possible.

I express all my gratitude to Prof. Francesco Nasuti for suggesting the following work and serving as my advisor over these three years. I also wish to thank Prof. Renato Paciorri and Prof. Mauro Valorani for their precious advises in the reviewing phase of this work.

My gratitude to Prof. Vigor Yang and his research group for hosting me during my visiting period at the Georgia Institute of Technology. It has been an amazing and scientifically stimulating experience. I would like to express my great appreciation to Dr. Alexandre Martin who invited me to share part of this work in a lecture of the “William Maxwell Reed Seminar Series” at the University of Kentucky.

Thanks also to my roommates and friends at the University of Rome for their

“on the fly” assistance.

Thanks to Avio Group S.p.A. for the financial support to this work and for supplying part of the needed experimental data.

Finally, I would like to thank my family for their encouragement to continue my education over the years and, from the depth of my heart, thanks to Chiara for her comprehensive “worldwide” support.



---

# **Contents**

<b>1</b>	<b>Introduction</b>	<b>1</b>
<b>I</b>	<b>Modeling and validation</b>	<b>17</b>
<b>2</b>	<b>Theoretical background</b>	<b>19</b>
2.1	Hot-gas modeling . . . . .	21
2.1.1	Gas-phase governing equation . . . . .	21
2.1.2	Perfect gas mixture . . . . .	23
2.1.3	Transport properties . . . . .	28
2.1.4	Turbulence modeling . . . . .	32
2.2	Solid phase modeling . . . . .	34
2.2.1	Solid-phase conservation equations . . . . .	34
2.2.2	Steady-state ablation approximation . . . . .	38

2.3	Surface phenomena modeling for ablative materials . . . . .	40
2.3.1	Surface mass balance . . . . .	40
2.3.2	Surface energy balance . . . . .	46
<b>3</b>	<b>Numerical method</b>	<b>51</b>
3.1	Governing equations . . . . .	51
3.2	Non-dimensional form of governing equations . . . . .	53
3.3	The $\lambda$ -scheme . . . . .	55
3.4	Solving technique . . . . .	62
3.4.1	Equations in the computational plane . . . . .	63
3.4.2	Time-marching finite difference method . . . . .	69
3.5	Boundary conditions . . . . .	73
3.5.1	Inflow and outflow conditions . . . . .	74
3.5.2	Wall conditions . . . . .	78
3.5.3	Error accumulation on the boundaries . . . . .	84
<b>4</b>	<b>Ablation model for non-pyrolyzing carbon-based materials</b>	<b>87</b>
4.1	Surface balances . . . . .	89
4.2	Thermochemical ablation model . . . . .	90
4.3	Numerical procedure . . . . .	92
4.4	Bates motor test . . . . .	93
4.4.1	Input data . . . . .	93
4.4.2	Results and discussion . . . . .	95
<b>5</b>	<b>Ablation model for pyrolyzing carbon-based materials</b>	<b>99</b>
5.1	Resin pyrolyzation modeling . . . . .	99
5.2	Surface balances . . . . .	103
5.3	Numerical procedure . . . . .	106
5.4	RSRM subscale nozzle test . . . . .	107

---

5.4.1	Input data . . . . .	107
5.4.2	Results and Discussion . . . . .	109
<b>6</b>	<b>Ablation model for pyrolyzing silica-based materials</b>	<b>119</b>
6.1	Surface balances . . . . .	120
6.2	Ablation model . . . . .	123
6.3	Numerical procedure . . . . .	124
6.4	Arc-plasma silica-phenolic nozzle test . . . . .	126
6.4.1	Input data . . . . .	131
6.4.2	Results and discussion . . . . .	134
<b>II</b>	<b>Application Results</b>	<b>137</b>
<b>7</b>	<b>Zefiro 9 and Zefiro 23 nozzle erosion analysis</b>	<b>139</b>
7.1	Input data . . . . .	140
7.2	Simulation results . . . . .	142
<b>8</b>	<b>Ablation in oxygen/methane thruster environment</b>	<b>159</b>
8.1	Input Data . . . . .	160
8.2	Simulation results . . . . .	161
<b>9</b>	<b>Coupled flow/material transient analysis</b>	<b>179</b>
9.1	Surface balances . . . . .	181
9.2	Heat conduction in the solid phase . . . . .	181
9.2.1	Finite-difference method for the in-depth solution . . . . .	182
9.2.2	Simplified analysis of TPS transient behavior . . . . .	186
9.3	Coupling Technique . . . . .	190
9.4	Analysis of Coupled Solutions . . . . .	192
9.4.1	Input data . . . . .	192

9.4.2 Simulation results . . . . .	193
<b>10 Conclusions</b>	<b>209</b>
<b>References</b>	<b>217</b>
<b>Appendices</b>	<b>231</b>
<b>Appendix A Derivation of the flow-field governing equations</b>	<b>231</b>
<b>Appendix B Diffusive terms in the computational plan</b>	<b>237</b>
<b>Appendix C Two-Dimensional axisymmetric problems</b>	<b>241</b>
<b>Appendix D Discretization of the in-depth energy balance</b>	<b>245</b>



---

## List of Symbols

$\mathcal{D}_{ij}$  = binary diffusion coefficient,  $\text{m}^2/\text{s}$

$\mathcal{D}_{im}$  = effective diffusion coefficient,  $\text{m}^2/\text{s}$

$\mathcal{E}$  = total specific energy,  $\text{J}/\text{kg}$

$\mathcal{M}$  = molecular mass,  $\text{kg}/\text{mol}$

$\mathcal{R}$  = universal gas constant,  $\text{J}/(\text{mol K})$

$\dot{w}_i$  = species source term,  $\text{kg}/(\text{m}^3 \text{ s})$

$\dot{m}$  = mass flow rate,  $\text{kg}/(\text{m}^2 \text{ s})$

$\dot{m}_{blow}$  = blowing mass flow rate,  $\text{kg}/(\text{m}^2 \text{ s})$

$\dot{m}_f$  = fail mass rate,  $\text{kg}/(\text{m}^2 \text{ s})$

$\dot{q}_{rad_{in}}$  = radiative heat flux towards the wall,  $\text{W}/\text{m}^2$

$\dot{q}_{rad_{out}}$  = radiative heat flux from the wall, W/m<sup>2</sup>

$\dot{s}$  = erosion rate, mm/s

$\mathbb{I}$  = identity matrix

$\mathbf{S}$  = stress tensor, Pa

$\mathbf{u_i}$  = diffusion velocity, m/s

$\mathbf{v}$  = flow velocity, m/s

$\dot{\mathbf{q}}$  = heat flux, W/m<sup>2</sup>

$\mathbf{j}$  = diffusive mass flux, kg/(m<sup>2</sup> s)

$\mu$  = dynamic viscosity, Pa s

$\nu$  = kinematic viscosity, m<sup>2</sup>/s

$\phi$  = interaction coefficient

$A$  = area, m<sup>2</sup>

$a$  = Speed of sound, m/s

$c_p$  = heat capacity at constant pressure, J/(kg K)

$c_v$  = heat capacity at constant volume, J/(kg K)

$e$  = internal specific energy, J/kg

$g$  = Gibbs free energy, J/K

$h$  = enthalpy, J/kg

$k$  = thermal conductivity, W/(m K)

$K_b$  = Boltzmann constant (1.380658), J/(mol K)

$Le$  = Lewis number

$N_A$  = Avogadro number (6.0221367)

$N_c$  = total number of species

$N_r$  = total number of reactions

$p$  = pressure, Pa

$Pr$  = Prandtl number

$R$  = specific gas constant, J/(kg K)

$s$  = entropy, J/K

$Sc$  = Schmidt number

$T$  = temperature, K

$t$  = time, s

$V$  = volume, m<sup>3</sup>

$X$  = molar fraction

$y_i$  = mass fraction

### Greek

$\gamma$  = heat capacity ratio

$\hat{\omega}_i$  = species source term for reaction different than ablation, kg/(m<sup>2</sup> s)

$\Lambda$  = generalized characteristic slope

$\Phi$  = porosity

$\rho$  = density, kg/m<sup>3</sup>

$\tilde{\omega}_i$  = species source term for sublimation, kg/(m<sup>2</sup> s)

$\varphi$  = mass flow rate ratio

$\omega_i$  = species source term for thermochemical erosion, kg/(m<sup>2</sup> s)

### Subscripts

$c$  = charred material

$f$  = fail

$g$  = pyrolysis gas

$h$  = solid-solid homogeneous in-depth reaction gaseous products

$in$  = in-depth condition

$s$  = solid phase

$s$  = virgin material

$w$  = wall condition

Chapter

**1**

---

# Introduction

Ablative materials provide a widespread, reliable, and relatively low-cost way to manage the extremely high heat fluxes that are normally encountered in a wide variety of aerospace applications. Modern re-entry vehicles [1] as well as last generation launchers [2] provide some recent examples of the use of this kind of thermal protection system (TPS), whose main peculiarity is to withstand harsh thermal and chemical conditions. In this context, the material behavior and its consumption represent a major issue when working with ablative TPS. Erosion, material weakening and thermal properties modification can, in fact, have a strong impact on the overall performance of the vehicle/nozzle and severe damages can occur to the underlying structure in case of TPS failure.

Focusing on the propulsive application of TPS materials, their main employment is that of passive cooling systems in rocket nozzles (Fig. 1.1). Normally, nozzle design requirements and constraints are imposed specifically by contract, are specified by propulsion or vehicle system analysis, or are left to the discretion



**Figure 1.1** – Comparison of silica-phenolic nozzles before and after firing.

of nozzle designer [3]. Requirements from system analysis are, in part, based on estimated nozzle weight, performance and envelope. An iterative process is therefore involved, and nozzle design parameters can be expected to change during a design process. During the nozzle design the designer is required to manage and optimize a large amount of variables [3]:

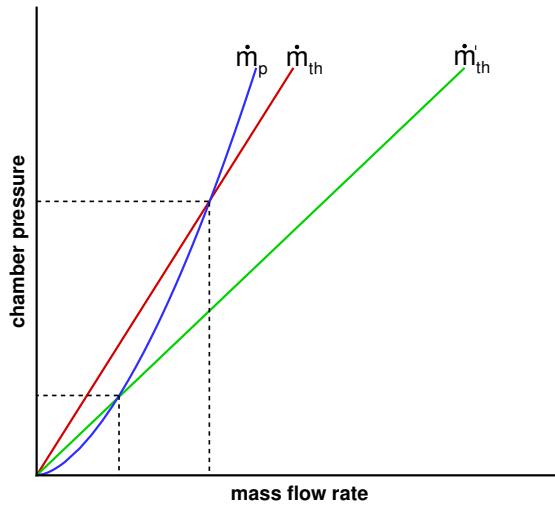
- Design pressure
- Predicted pressure-time trace
- Propellant properties
- Throat size
- Acceptable throat-size change
- Expansion ratio
- Weight, reliability, and cost
- Etc...

Among these variables, two that are strongly connected: the good understanding of the pressure–time trace and the capability of estimating the throat size variation during firing. In fact, they lead together to a good prediction of the overall motor performance. Therefore, to facilitate the development of high-pressure

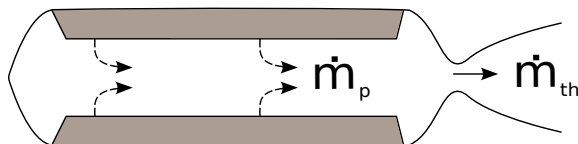
rockets, it is important to advance the fundamental understanding of the nozzle erosion processes and to develop useful simulation tools in this subject area.

In ablative rocket motor nozzles, the material consumption depends on numerous factors including the propellant composition, engine operating conditions, duration of firing, nozzle geometry, material properties, transport of reacting species, homogeneous reactions in the gas phase, and heterogeneous reactions at the nozzle surface. Specification of ablative material composition and thickness for adequate thermal protection requires taking into account the interactions between the ablative material and its operating environment. Furthermore, attention has to be paid to the fact that, in rocket nozzles, the occurrence of material erosion reduces the nozzle area ratio, and consequently decreases the overall engine performance (Fig. 1.2). For these reasons, a deep understanding of the erosion phenomena may help to optimize nozzle design and improve rocket performance. Generally, to determine the ablative material thickness needed to protect the structural components of the nozzle, and to quantify the nozzle erosion rate, firing tests on full-scale motors are conducted. Multiple firing tests, however, are demanding both in time and expense. Therefore, an efficient and more economical approach is to couple the full-scale experiments with the numerical modeling studies.

In ablative nozzles, two principal components can be identified. The thermal liner, whose surface is exposed to the exhaust-product flow, forms the nozzle aerodynamic contour. The insulator is the material placed behind the liner to serve as a thermal barrier to protect the structural component from excessive temperature rises. Often, a single material thickness serves as both liner and insulator (and sometimes as structure also) [3]. A throat insert is a special erosion-resistant liner usually placed in the throat region of a nozzle to limit the nozzle erosion. In practice, the throat insert and other liners, selected for their



(a) Chamber pressure variation with throat mass flow rate ( $\dot{m}_{th}$  is before erosion and  $\dot{m}'_{th}$  is after erosion).



(b) Schematic of solid rocket motor mass flows.

**Figure 1.2** – Qualitative example of performance reduction because of the nozzle erosion.

erosion resistance, are usually designed first during the nozzle design process. Thereafter, a candidate insulator is chosen looking for materials with low thermal diffusivity in order to minimize the heat penetration. The materials suitable for liners are, in general, considerably more expensive and heavy than those suitable for insulators; so liner use is generally minimized [3].

Ablative materials for rocket nozzle application liners can be distinguished into two main categories: pyrolyzing and non-pyrolyzing.<sup>1</sup> A pyrolyzing (charring)

---

<sup>1</sup>The term “ablative materials” is normally referred to the pyrolyzing materials in the

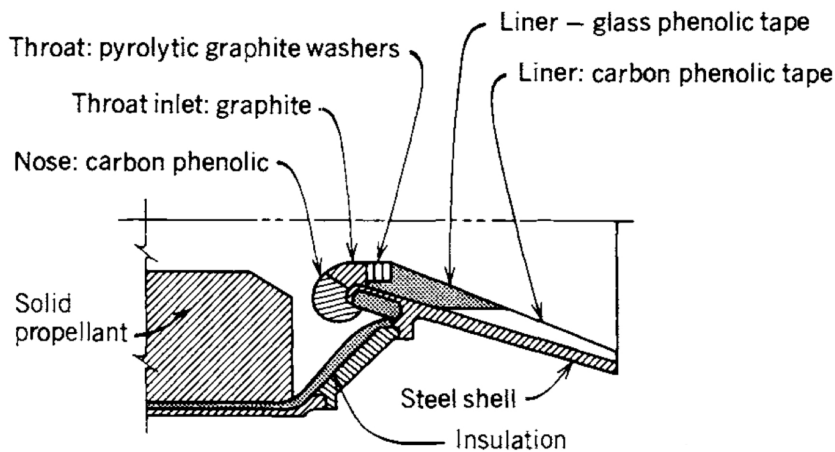


**Figure 1.3** – Typical nozzle assembled with different materials. [4]

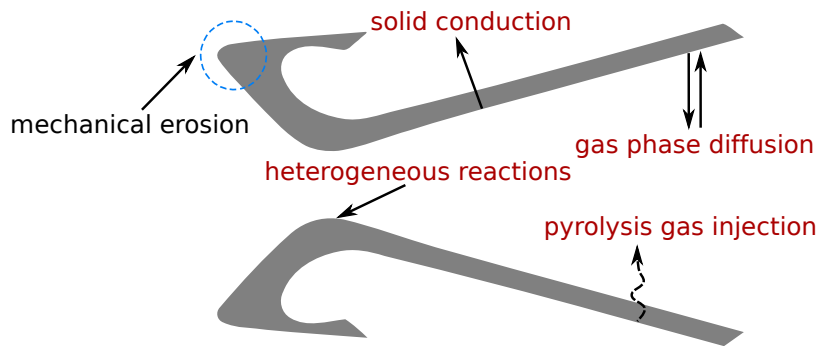
material is made of a resin matrix and a reinforcing material (carbon, silica, etc...). When heated, the resin experiences a series of chemical reactions releasing gaseous products and leaving a porous layer of char or residue that can recede due to different phenomena. Differently, in a non-pyrolyzing material the mass loss occurs only at surface (surface melt/sublimation, thermochemical erosion, mechanical erosion).

Various kinds of composite materials with high thermal strength and ablation resistance are used to protect different parts of rocket nozzles (Fig. 1.3). Normally, non-pyrolyzing carbon-based composite materials such as graphite and carbon-carbon are used for the throat lining, and charring composite materials such as silica- and carbon-phenolics are used for the converging and diverging section of the nozzle and for the insulation of the throat part [3]. During firing, the inner wall surface of the nozzle recedes due to the thermochemical and mechanical ablation under the action of both gas and particles.<sup>2</sup> In the meantime, pyroly-

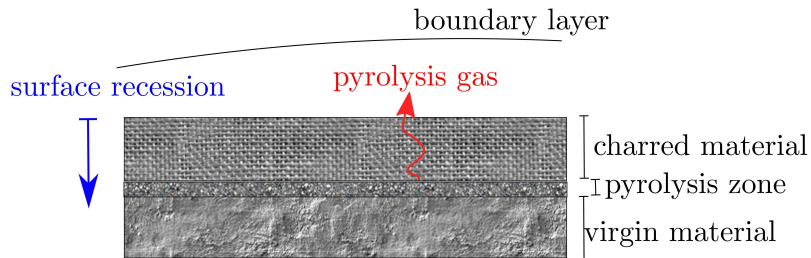
---

literature. However, for the sake of straightforwardness, the term "ablative" will be used in the text to indicate both the pyrolyzing and the non-pyrolyzing materials.

<sup>2</sup>The term "ablation" will be used indistinctly in the text to indicate the consumption of both pyrolyzing and non-pyrolyzing materials.



(a) Phenomena involved in nozzle erosion.



(b) Ablating material sketch.

**Figure 1.4 – Erosion in rocket nozzles.**

sis processes occur inside the charring composite material moving continuously the interfaces between the virgin material layer and the pyrolysis layer, and the pyrolysis layer and the char layer (Fig. 1.4).

Concerning carbon-based materials, efforts have been made in the past in understanding of the fundamental phenomenon that causes the nozzle material consumption. When a pyrolyzing material is considered (e.g carbon-phenolic), the internal decomposition of the resin generates a pyrolysis gas that reaches the material surface and flows into the external gas, driven by the pressure rise inside the porous char. The products of the decomposition are a mixture of gases and a residual solid carbon. Hence, the charred material is composed essentially by carbon and the surface ablation mechanism is exactly the same as

for a non-pyrolyzing carbon-based material. Early investigations have indicated that the solid carbon removal mainly depends on the endothermic heterogeneous reactions that occur between the oxidizing species present in combustion stream, such as  $H_2O$ ,  $CO_2$  and  $OH$ , and the heated nozzle material [5, 6, 7]. When the oxidizing species inside the combustion gases diffuse across the boundary layer towards the surface a concentration boundary layer is formed. The nozzle recession rate can be influenced by both chemical kinetics of the heterogeneous reactions at the surface and diffusion of the oxidizing species across the boundary layer. These mechanisms can be affected, in turn, by the flow and by the thermal and chemical characteristics of the TPS material. Moreover, since solid propellants normally contain a certain amount of aluminum particles, the influence of this particulate on the nozzle throat erosion has been the subject of many investigations. The presence of aluminum particles in the combustion gases has been found to be such to restrain the thermochemical erosion by their oxidation to  $Al_2O_3$  which reduce the presence of oxidizing species in the mixture [8]. On the contrary, the contribution of the mechanical erosion, obviously enhanced by increasing the aluminum content in the solid propellant, can be considered negligible in the throat region and in the divergent part of the nozzle being the particle trajectories almost parallel to the wall (particularly true for conical nozzle) [4, 8]. In case of silica-based materials, although the same resin decomposition process occurs, a more complex set of sub-surface phenomena take place. As the pyrolysis proceeds, the decomposition zone recedes and penetrates inside the material [9]. The products of the pyrolysis are, again, a mixture of gases and a residual solid carbon. However, the latter, together with the silica reinforcement fibers, forms a complex charred layer whose chemical elemental composition is essentially given by silicon, oxygen and carbon. If the heat flux is sufficiently high, the silica fibers within the char may melt forming a liquid film on the char surface. The

pyrolysis gases then percolate through the char and then bubble through the molten layer. Moreover, complex post-pyrolytic homogeneous chemical reactions between the carbon and the silica, in solid state, take place in the char and, near the surface of the molten layer, heterogeneous (liquid-solid) carbon-silica reactions may occur. Surface ablation occurs essentially because of the shear stresses acting on the liquid layer of melted silica that covers the solid char. Differently, when the surface heat flux is not sufficiently high to cause the silica fiber melting, the oxidation of the solid carbon in the char is the only surface mass removal. However, this mass loss does not really influence the structural integrity of the fiber matrix and, from a practical point of view, no surface recession occurs [10, 11]. Since the ablation process of a silica-based material is totally different with respect to the carbon-based ones, no direct effect of the propellant aluminum content can be found when silica-based liners are used.<sup>3</sup>

Whatever the TPS material is used, to faithfully reproduce every phenomenon involved in such a complex environment, a strong coupling between transient CFD simulations with accurate ablative boundary condition (specific for the analyzed material) and transient calculations of the material response is needed. However, this kind of approach is computationally demanding, sometimes even unfeasible, because of the largely different time scales of the physical phenomena. Therefore, different levels of simplification are used to obtain accurate and useful solutions for the specific problem to be analyzed. The common approaches to study the ablation of a TPS material are substantially of two different types. The first approach, which is focused on the material side, requires limited computational resources and has the merit to provide quick results. It is based on the accurate transient computation of the conduction inside the material by enforcing a raw boundary condition (i.e. transfer coefficient approach) at the gas–solid interface

---

<sup>3</sup>The gas temperature enhancement, that can favor the silica melting, can be considered an indirect effect of the propellant aluminum content on the silica-phenolic erosion.

[12]. Basically, the flow side is solved in a simplified manner and surface conditions (i.e. temperature or thermal convective heat flux) are obtained by means of semi-empirical relations and then imposed at the material-gas interface. The second approach, focused on the gas-side physics, treats the erosion using accurate “ablative” boundary conditions for the CFD simulation of the complex flow field. In this approach, if coupling with a solid conduction solver is not available, the conduction inside the solid material is treated in a simplified manner.

## **Literature review on nozzle recession computational models**

The nozzle erosion phenomenon for carbon-based materials has been the subject of many investigations and several ablation models have been developed over the years. In preliminary studies, back to the early 1960s, researchers focused their attention on the behavior of pure graphite in solid rocket nozzle environment. Delaney et al. [13] showed that graphite erosion is limited by both the diffusion and the surface chemical reactions. They also pointed out that pressure is probably the most important single variable involved in erosion. However, they stated that the relative importance of one of these two mechanisms with respect to the other is not strongly dependent on pressure as both the reaction rate and the mass-transfer rate increase almost linearly with pressure. McDonald et al. [14], in a similar work, concluded that, since at that time the reaction-rate constant data for different grades of graphite were unavailable, the erosion could be more accurately predicted by assuming chemical equilibrium at the surface. They also stated that this diffusion-limited approach could be safely used for predicting the erosion of graphite where transient effects were not significant.

A much more detailed and comprehensive model has been later developed by

Kuo and Keswani [15, 16] to study the thermochemical erosion of carbon-carbon nozzles accounting for both diffusion and chemical kinetics effects. Their model included the effects of propellant composition, chamber pressure, surface roughness of the nozzle, and the density of the carbon-carbon composite on recession behavior. The model considered finite heterogeneous reaction rates and thus determined whether the nozzle recession process was either diffusion or chemical kinetics controlled. The model also accounted for the transient nature of the recession process and predicted the variation in recession rate during motor firing.

The Kuo and Keswani model was updated by Acharya and Kuo [17]. Even if the underlying assumptions of combining an inviscid one-dimensional flow in the core region with a viscous axisymmetric flow near the nozzle wall was kept identical to the original model, they performed a broad analysis on the effect of pressure and propellant composition (metallized and non-metallized propellant were analyzed) on the erosion rate for a graphite nozzle. They analyzed the erosion behavior up to very high pressure (55 MPa) using different kinetic schemes for the graphite oxidation. The erosion rate was found to increase almost linearly with respect to pressure due to a higher rate of energy transfer, while the rate of increase depends on the choice of chemical kinetic scheme and propellant composition. In a more recent work [18], the effect of the reaction kinetic scheme on the erosion rate has been investigated. The obtained results have been compared against experimental data, and the predictions using the MOS [19, 20] scheme has shown the best agreement with the experimental data. Using the same numerical framework, a systematic analysis on various parameters that affect the nozzle thermochemical erosion (i.e. oxidizing species concentrations, flame temperature, operating pressure and thermal properties of graphite) has been carried out in Ref. [21]. Based upon this research, they have concluded that

flame temperature can affect the thermochemical erosion rate the most, followed by chamber pressure and major oxidizing species concentrations.

Despite these results, that widely extend the comprehension on the erosion behavior, the underlaying approximations still limited the analysis of the involved phenomena. For instance, the use of two different flow models for the core and the next-to-wall regions implied that the species conservation equations were not solved and the erosion rate was calculated empirically as the harmonic mean of the kinetics- and diffusion-limited rates (where the former was obtained based on the species concentrations in the core flow). Therefore, during the last years, more comprehensive studies based on full Navier-Stokes approaches have been carried out independently by different researchers. Thakre and Yang [22, 23] developed a comprehensive numerical/theoretical framework that takes into account detailed thermo-fluid dynamics for a multicomponent reacting flow, heterogeneous reactions at the nozzle surface (MOS model), and condensed-phase energy transport. They analyzed the erosion behavior in case of both metallized and non-metallized propellants and validated their model against experimental results. From their analysis they determined that the water vapor is the most detrimental oxidizing species in dictating the nozzle erosion and confirmed the linear dependency with pressure of the erosion rate. Moreover, they found that the erosion rate is dictated by heterogeneous chemical kinetics for non-metallized propellants for which the surface temperatures are sufficiently low and by a diffusion-controlled process for metallized propellants, for which the surface temperatures are higher. Recently, in [24], they implemented a modification in the turbulence model to account for surface roughness and include the contribution from the radiative heat transfer in their ablative boundary condition. Interesting results came out from this preliminary analysis; the surface roughness was found to enhance the erosion rate, whereas the effect of the net radiative heat transfer has been found

to slightly decrease the erosion rate when non-metallized propellant are considered. Almost contemporaneously, Bianchi et al. [25, 26] developed an ablative boundary condition based on heterogeneous chemical equilibrium. Comparison of the obtained results against experimental data for various propellant composition, both metallized and non-metallized, showed very good results despite the rather strong approximation of heterogeneous equilibrium at the surface. In particular, for the metallized propellant, which experiences higher adiabatic combustion temperature, the heterogeneous equilibrium assumption was found to be more than reasonable; the erosion rate is in the diffusion limited regime and the oxidizing species are totally consumed at the surface as estimated by the equilibrium calculation. Again, simulations at different chamber pressures confirmed the almost linear erosion rate dependency upon pressure. Subsequently [27], the MOS reaction mechanism has been implemented in the code and a comparative analysis of the two ablation models, the surface equilibrium approach and the finite rate model, was carried out. Results showed that the erosion rate is diffusion limited for metallized propellants and the finite-rate model results confirmed those obtained using the surface equilibrium approximation. For less aluminized propellant (lower surface temperatures due to both higher erosion rate and lower chamber temperature with respect to aluminized propellants) the equilibrium model slightly overpredicted the experimental recession and the finite-rate model excellently agreed with the experimental data predicting a kinetic limited erosion rate. More recently, Bianchi and Nasuti [28] applied the finite-rate ablation model to perform an analysis on two full-scale solid rocket motor nozzles belonging to the second and third stage of the Vega launcher. First, a single steady-state simulation at the mean chamber pressure was performed. Then, the obtained erosion rate was used to evolve the nozzle geometry up to the firing test time in order to capture the final nozzle profile. Subsequently, a more complex shape

change procedure was established and a series of steady-state CFD simulations were performed choosing several pressure point along the pressure-time trace. CFD simulations were started with the initial unablated shape, and the surface erosion rate is computed; after that, the shape evolution model was run for a portion of the burning time (up to the time of the next selected pressure on the pressure-time trace). Then, a new CFD grid was generated using the receded shape, and a new CFD solution using this grid and the selected chamber pressure was computed. Subsequently, the erosion rate distribution was updated, and the procedure is repeated until the total burning time was reached. The single-step procedure gave results in very good agreement with the final experimental profile for both the nozzles; however, the shape change effect resulted necessary especially if long burning time, high erosion rate and small nozzle dimension are considered. The results obtained with the shape change are, in fact, in excellent agreement with the experimental data. Substantially, the study confirmed that a steady-state CFD simulation approach can be a reliable mean to support nozzle design and optimization. In contrast with the large number of studies on the simulation of the erosion behavior of non-pyrolyzing carbon-based materials, the CFD approach has not been yet applied to predict nozzle erosion in case of pyrolyzing material. Chen and Milos [29] applied a similar approach to simulate the erosion behavior of a pyrolyzing TPS heat shield during Earth reentry from a planetary mission. However, there is a lack of specific CFD analyses on pyrolyzing carbon-based materials in rocket nozzle environment, despite their widespread use.

The lack of specific studies is even more evident when considering the silica-based pyrolyzing material. No specific works have been done to simulate the behavior of this material in rocket nozzle environment using a CFD approach. In the past, some works [30, 31, 32, 33, 34] focused on the characterization

of the internal phenomena involved in the material decomposition or in the homogeneous solid-solid reactions. Other works [9, 35, 36] formulated theories to simulate surface ablation or developed material thermal response code to account for silica-phenolic ablation but, perhaps because of the more complicated involved phenomena, no comprehensive model using approaches similar to those that have been described for carbon-based materials have been developed.

In this scenario, a comprehensive model, capable of accounting for surface ablation, resin decomposition and pyrolysis gas injection for different kinds of pyrolyzing and non-pyrolyzing materials in rocket nozzle environment, has not been appeared yet in the literature.

## Research aims and work outline

The main objective of the present thesis is to fill the gap mentioned in the previous section and, in particular, to develop an accurate theoretical/mathematical model to describe the complex fluid-surface interactions over carbon- and silica-based charring ablative materials and to numerically integrate it within a Navier-Stokes flow solver. Beside this main objective, a thorough investigation over some fundamental aspects of the ablating material modeling is also addressed. In the following, a brief description of the structure of the work is presented.

- **Part I** deals with the model description and validation and is organized as follows:
  - ✓ **Chapter II** is dedicated to the description of the gas-surface interaction physics over a generic ablative material and its modeling. Moreover, the gas-phase governing equations are presented together with the thermodynamic and transport model.

- ✓ **Chapter III** describes the numerical implementation the Navier-Stokes solver.
  - ✓ **Chapter IV** illustrates the ablative boundary condition and its validation in case of carbon-based non-pyrolyzing ablative materials.
  - ✓ **Chapter V** presents the pyrolysis gas modeling and describes the developed boundary condition for pyrolyzing carbon-based pyrolyzing ablative materials. Moreover the model validations against experimental results are presented.
  - ✓ **Chapter VI** describes the developed boundary condition for pyrolyzing silica-based pyrolyzing ablative materials and its validation against experimental results.
- **Part II** presents the results of the model in practical applications and illustrates a study of a peculiar aspect of the ablation phenomenon:
    - ✓ **Chapter VII** shows the results of the simulations performed to reproduce the nozzle erosion of two different stages of the Vega launcher.
    - ✓ **Chapter VIII** presents the application of the developed model for the study of the ablative material behavior in oxygen/methane thruster environment.
    - ✓ **Chapter IX** deals with the development and the application of a loose coupling technique between the CFD solver and a transient heating calculator.

## **Part I**

### **Modeling and validation**

---

## Theoretical background

A detailed analysis of the performance of TPS materials should consider the complex interaction of the different phenomena that occurs over an ablating surface. Numerous mechanisms, among which thermochemical erosion, mechanical erosion, and internal decomposition, cause the surface and subsurface TPS material consumption. To correctly analyze the phenomena involved when the TPS material is exposed to sever thermal and chemical condition, it is worthwhile to identify two different sides of the problem: the flow-field side and the material side. The peculiarity of high temperature flow over an ablating material is that these two “separate” worlds are continuously interacting with each other through the material surface. Taking into account this logical division, this Chapter presents the theoretical background necessary to formulate a comprehensive model of the gas/surface interaction over pyrolyzing ablative materials in rocket nozzle environment.

The internal flow in a propulsive rocket nozzle is characterized by:

- severe environmental conditions (very high temperature and pressure in the combustion chamber);
- strong variation of flow state variables caused by the flow expansion;
- formation of strong gradients due to the wall;

therefore its analysis requires to account for such aspects as:

- variation of thermodynamic properties of the gas with temperature and mixture composition;
- importance of transport mechanisms;
- variation of transport properties of the gas with temperature and mixture composition.

Consequently, the hypothesis of ideal gas cannot be made [37].

To explain the theoretical formulation adopted in the present work, a description of the gas-phase governing equations, the adopted physical variable and the thermodynamic and transport properties is given first.

After that, the description of the solid-side phenomena and porous solid governing equations is presented. A general pyrolyzing ablative material, characterized by internal physical mechanisms (decomposition, homogeneous solid-solid reaction) is considered. The in-depth energy behavior of TPS material is analyzed and a useful form of this balance is formulated. Finally, the link between solid and gas, the gas/surface interface, is analyzed. Since this interface is characterized by a series of local phenomena, and is also sensitive to the phenomena taking place in both the gas and the solid side, to describe its behavior, the mass and energy balances over a generic ablating wall are presented.

## 2.1 Hot-gas modeling

### 2.1.1 Gas-phase governing equation

By applying Newton's law of motion to a fluid element, the element motion can be described by a vector governing equation, momentum balance equation, known as Navier-Stokes equation. This equation is normally complemented by the mass and energy conservation equations. In fluid dynamics it is common referring to this set of equations as the Navier-Stokes equations. The complete derivation of these equations is given in Appendix A for a mixture (ideal) gases reacting at finite rates, and only a brief description of the formulations suitable for the purpose of the present work is given here.

#### Quasi-linear form of the reactive Navier-Stokes equations

The Navier-Stokes equation can be casted in the so called quasi-linear form that, when dealing with chemical reacting mixture, reads [37]:

$$\left\{ \begin{array}{l} \rho \frac{Dy_i}{Dt} + \nabla \cdot (\rho y_i \mathbf{u}_i) = \dot{w}_i \quad i = 1, \dots, N_c - 1 \\ \frac{D\rho}{Dt} + \rho \nabla \cdot \mathbf{v} = 0 \\ \rho \frac{D\mathbf{v}}{Dt} - \nabla \cdot \mathbf{S} = 0 \\ \rho \frac{D\mathcal{E}}{Dt} = \nabla \cdot (\mathbf{S} \cdot \mathbf{v}) - \nabla \cdot \dot{\mathbf{q}} \end{array} \right. \quad (2.1)$$

where the equations, from top to bottom are: the species continuity equation, the mixture continuity equation, the momentum balance (vectorial equation) and the energy conservation equation. In this formulation, the operator  $D/Dt$

represents the substantial derivative, defined as:

$$\frac{D}{Dt} := \frac{\partial}{\partial t} + \mathbf{v} \cdot \nabla$$

It should be noted that only  $N_c - 1$  species continuity equations are needed to close the problem since the  $N^{th}$  is provided by the definition of mixture density:

$$\rho = \sum_{i=1}^{N_c} \rho_i y_i = \sum_{i=1}^{N_c} \rho_i \quad (2.2)$$

Equations (2.1) are particularly appealing to be used in a certain class of numerical methods despite the fact that they lack in a direct physical interpretation with respect to the conservative form of the Navier-Stokes equations.

### Reactive Euler equations

The Euler equations for a mixture of (ideal) gases can be obtained from the reactive Navier-Stokes equations (Eq. (2.1)) by neglecting the viscous terms due to viscosity, thermal conductivity, and mass diffusion. The quasi-linear form of the reactive Euler equations, obtained directly from Eqs.(2.1) reads:

$$\left\{ \begin{array}{l} \rho \frac{Dy_i}{Dt} = \dot{w}_i \quad i = 1, \dots, N_c - 1 \\ \frac{D\rho}{Dt} + \rho \nabla \cdot \mathbf{v} = 0 \\ \rho \frac{D\mathbf{v}}{Dt} + \nabla \cdot (p\mathbb{I}) = 0 \\ \rho \frac{D\mathcal{E}}{Dt} + \nabla \cdot (p\mathbb{I} \cdot \mathbf{v}) = 0 \end{array} \right. \quad (2.3)$$

Because of their hyperbolic nature, advantages can be taken when developing numerical methods for this set of equations. Moreover, since the viscous effects are important only in a limited part of the flowfield (near walls, shock waves, contact discontinuities, etc...), methods used to solve the Euler equations can be extended to the Navier-Stokes equations by decoupling the convective operator from the diffusive operator.

### 2.1.2 Perfect gas mixture

The gas mixture is considered to be thermally perfect. The thermodynamic model allows the definition of the caloric and thermal equation of state, giving part of fluid property relations needed to close the system of Eqs. (2.1).

#### Caloric equation of state

The caloric equation of state is an equation which gives the energy as a function of two independent state variables. The caloric equation of state of a system can be written either in terms of internal energy or enthalpy.

For a thermally perfect gas, the heat capacity at constant volume is a function of the temperature only, and its definition comes directly from the first law of thermodynamics when heat is added at constant volume. For the single species,  $i$ , this definition reads:

$$c_{v_i} = \left( \frac{de_i}{dT} \right)_{v=const} \quad (2.4)$$

by integrating Eq. (2.4) one can obtain the internal energy per unit mass of a single gaseous species in a mixture of thermally perfect gases

$$e_i = \int_{T_{ref}}^T c_{v_i}(T) dT + (\Delta h_f)_i^{T_{ref}} \quad (2.5)$$

where  $(\Delta h_f)_i^{T_{ref}}$  is the heat of formation of the  $i^{th}$  species at the temperature  $T = T_{ref}$ . Using Eq. (2.2), the internal specific energy of the mixture can be written as:

$$e = \sum_{i=1}^{N_c} \frac{\rho_i}{\rho} e_i = \sum_{i=1}^{N_c} y_i e_i \quad (2.6)$$

and, although  $e_i$  is a function of temperature only, the internal energy for a chemically reacting mixture depends also on the amount of each  $i^{th}$  species in the mixture.

Equally, the heat capacity at constant pressure can be derived directly from the first law of thermodynamics when heat is added at constant pressure and the definition of enthalpy is used:

$$c_{p_i} = \left( \frac{dh_i}{dT} \right)_{p=const} \quad (2.7)$$

therefore the absolute enthalpy of the  $i^{th}$  species reads:

$$h_i = \int_{T_{ref}}^T c_{p_i}(T) dT + (\Delta h_f)_i^{T_{ref}} \quad (2.8)$$

where the terms on the right-hand side represent the sensible and the formation contribution, respectively. The mixture absolute enthalpy can be evaluated by:

$$h = \sum_{i=1}^{N_c} \frac{\rho_i}{\rho} h_i = \sum_{i=1}^{N_c} y_i h_i \quad (2.9)$$

and it is a function of both the species absolute enthalpy and the mass fraction of each species in the mixture.

### Thermal equation of state

A perfect gas is a gas for which the intermolecular interactions are negligible compared to kinetic energy. The macroscopic thermodynamic properties of a gas are generated by the motion of the molecules of the mixture, therefore they can be influenced by the intermolecular forces. However, in case of not extremely high pressure (lower than  $\approx 100 \text{ MPa}$ ) and not very low temperature (higher than  $\approx 30 \text{ K}$ ) the molecules are sufficiently far off each other than the intermolecular forces can be neglected [37]. Under this condition (compatible with the applications of interest in the present work) the gas obeys to the so called perfect-gas equation of state:

$$p = \sum_{i=1}^{N_c} p_i = \sum_{i=1}^{N_c} \rho_i R_i T = \rho R T \quad (2.10)$$

where the Dalton's law has been applied to consider that the pressure of the gas mixture is made up by summing the partial pressure of every single species in the mixture. In Eq. (2.10),  $R$  is the mixture gas constant that can be derived by the universal gas constant ( $\mathcal{R} = 8314.51 \text{ J kmol}^{-1} \text{ K}^{-1}$ ):

$$R = \frac{\mathcal{R}}{\mathcal{M}} = \sum_{i=1}^{N_c} y_i R_i = c_p - c_v$$

where  $\mathcal{M}$  is the molecular mass of the mixture defined as follows:

$$\mathcal{M} = \frac{1}{\sum_{i=1}^{N_c} \frac{y_i}{\mathcal{M}_i}}$$

and the heat capacities of the mixture are obtained by the heat capacities and the mass fraction of the  $i^{th}$  species:<sup>1</sup>

$$c_v = \sum_{i=1}^{N_c} y_i c_{v_i}, \quad c_p = \sum_{i=1}^{N_c} y_i c_{p_i} \quad (2.11)$$

At this point, the heat capacity ratio can be introduced:

$$\gamma = \frac{c_p}{c_v} \quad (2.12)$$

It is worth noting that the quantities in Eq. (2.11) have commonly referred to as frozen heat capacities [37].

### Thermodynamic data

The thermodynamic properties of the chemical species are evaluated with the thermodynamic database used in the "Chemical Equilibrium and Applications" (CEA) computer program developed by Gordon and McBride [38]. This database contains data from several sources as: Chase et al. [39], Cox et al. [40], Gurvich et al. [41], and Marsh et al. [42] and McBride et al. [43].

**Data for individual species.** The non-dimensional thermodynamic functions: heat capacity at constant pressure, enthalpy, and entropy, are given (as functions of temperature) in the form of least-square coefficients. The general form of

---

<sup>1</sup>The adopted model considers only mixtures in thermal equilibrium and every contribution to the internal energy (such as the vibrational energy) is included into the  $c_{v_i}$  expression

these equations is as follows:

$$\begin{aligned}\frac{\tilde{C}_{p_i}}{\mathcal{R}} &= \sum_{j=-2}^4 a_j T^j \\ \frac{\tilde{H}_i}{\mathcal{R}T} &= \frac{\int \tilde{C}_{p_i} dT}{\mathcal{R}T} = \frac{\int \sum_{j=-2}^4 a_j T^j dT}{\mathcal{R}T} \\ \frac{\tilde{S}_i^*}{\mathcal{R}} &= \int \frac{\tilde{C}_{p_i}}{\mathcal{R}T} dT = \int \frac{\sum_{j=-2}^4 a_j T^j}{\mathcal{R}T} dT\end{aligned}\quad (2.13)$$

where, for each generic species  $i$ ,  $\tilde{C}_{p_i}$  ( $\text{J kmol}^{-1} \text{K}^{-1}$ ) is the molar heat capacity at constant pressure for standard-state,  $\tilde{H}_i$  ( $\text{J kmol}^{-1}$ ) is the standard-state molar enthalpy and  $\tilde{S}_i^*$  ( $\text{J kmol}^{-1} \text{K}^{-1}$ ), is the standard-state molar entropy. In Eqs. (2.13) the seven least-square coefficients  $a_i$ , as well as the two integration constant, are taken from the sources described above. Different temperature intervals are reproduced (200 K to 1000 K, 1000 K to 6000 K and, for some gases, 6000 K to 20 000 K). Generally, the three functions of Eqs. (2.13) are fit simultaneously and the fit is constrained to match the functions exactly at  $T = 298.15 \text{ K}$ . Thus, the least-square coefficients reproduce heats of formation at this temperature exactly.

**Mixture properties.** The mixture properties can be evaluated once the thermodynamic data for each species,  $i$ , are known. A general rule can be applied to connect a generic molar property ( $\Psi_i$ ) to its relative specific property ( $\psi_i$ ). Once the standard-state molar entropy in Eqs.(2.13) has been transformed in:

$$\tilde{S}_i = \tilde{S}_i^* - \mathcal{R} \ln X_i - \mathcal{R} \ln p$$

the rule can be applied considering  $\tilde{\Psi}_i$  instead of any of the three molar properties,  $\tilde{C}_{p_i}$ ,  $\tilde{H}_i$  and  $\tilde{S}_i$ :

$$\psi_i = \frac{1}{\mathcal{M}} \sum_{j=1}^{N_c} X_j \tilde{\Psi}_j \quad (2.14)$$

where  $X_j$  is the mole fraction of the  $j^{th}$  species in the mixture.

### 2.1.3 Transport properties

The additional fluid properties relationships needed to close the system of Eqs. (2.1) can be supplied by modeling the diffusion coefficients ( $\mathcal{D}_{im}$ ), the mixture viscosity ( $\mu$ ) and the mixture thermal conductivity ( $k$ ), the viscous stress tensor and the heat flux modeling (see Appendix A for details).

#### Effective diffusion coefficient

The diffusion term of the single species,  $i$ , needed in each the species continuity equations of Eqs. (2.1) can be rewritten as follows using Eq. (A.2):

$$\nabla \cdot (\rho y_i \mathbf{u}_i) = -\rho \mathcal{D}_{im} \nabla y_i = \mathbf{j}_i \quad (2.15)$$

In the present work, multi-component effects are taken into account by means of a diffusion model based on the effective, or average, diffusion coefficients that are defined as in [44]:

$$\mathcal{D}_{im} = \frac{1 - X_i}{\sum_{\substack{j,k=1 \\ j \neq k}}^{N_c} X_j / \mathcal{D}_{jk}} \quad (2.16)$$

where the term  $\mathcal{D}_{jk} = \mathcal{D}_{kj}$  is the binary diffusion coefficient ( $\mathcal{D}_{jj} = 0$ ) that will be described later on. With such an approximation the requirement of the diffusion mass fluxes summing to zero is not guaranteed. Therefore, a corrected

form for Eq. (2.15) is necessary [45]:

$$\mathbf{j}_{i,corr} = \mathbf{j}_i - y_i \sum_{j=1}^{N_c} \mathbf{j}_j \quad (2.17)$$

ensuring that the mass fluxes sum to zero by distributing the residual according to the species mass fraction.

### Viscosity and thermal conductivity

In order to obtain the transport properties of a gas mixture from the properties of the individual molecular constituent species, rigorous kinetic theory formulas can be derived directly from a solution of the Boltzmann equation using the classical Chapman-Enskog theory. However, approximations of the complete Chapman-Enskog formulas are often employed for practical uses. Indeed, considering the species generic property  $\psi_i$  (that could be either  $\mu_i$  or  $k_i$  in this case), the mixture generic property ( $\psi$ ) can be approximated using the following mixture rule [38]:

$$\psi = \sum_{i=1}^{N_c} \frac{X_i \psi_i}{\sum_j X_j \phi_{ij}} \quad (2.18)$$

where the term  $\phi_{ij} \neq \phi_{ji}$  is the interaction coefficient that will be discussed later on.

### Transport properties of the species

The transport properties of individual species are computed by using the CEA database where most of the thermal transport property data is taken from Svehla [46]. The viscosity for many species is determined by fitting experimental data to a theoretical form. This is obtained either by the Lennard-Jones potential or by the Stockmeyer potential for non polar and polar molecules, respectively [38].

The generic transport properties of the single species,  $i$ , is provided by the CEA database in form of least-square coefficients:

$$\ln \psi_i = a_1 \ln T + \frac{a_2}{T} + \frac{a_3}{T^2} + a_4 \quad (2.19)$$

where  $\psi_i$  can represent either the species viscosity ( $\mu_i$ ) or thermal conductivity ( $k_i$ ).

The effective binary diffusion coefficient (Eq. (2.16)) is not only a function of the species but it is also a function of the mixture, as it depends from all the other species mole fractions ( $X_i$ ). Therefore, it cannot be stored in a database but it has to be treated as a mixture property and calculated at run time. To calculate its value, the binary diffusion coefficients ( $\mathcal{D}_{ij}$ ) are needed. They are evaluated, for each couple of species  $i - j$ , using the following expression [46]:

$$\mathcal{D}_{ij} = \frac{3}{5} \frac{\mathcal{M}_i + \mathcal{M}_j}{\mathcal{M}_i \mathcal{M}_j} \frac{A_{12} \mathcal{R} T}{p} \mu_{ij} \quad (2.20)$$

where  $A_{12}$  is a function of the collision integrals and differs only slightly from unity and the binary interaction parameter  $\mu_{ij}$  is provided by the CEA database in the same form of Eq. (2.19).

The interaction coefficients in Eq. (2.18),  $\phi_{ij}$ , are provided by the CEA database too, where they are evaluated using the following expressions from Brokaw [47, 48, 49]:

$$\phi_{ij} = \frac{\mu_i}{\mu_{ij}} \frac{2\mathcal{M}_j}{\mathcal{M}_i + \mathcal{M}_j} \quad (2.21)$$

that defines the coefficients needed for the mixture viscosity evaluation, and:

$$\phi_{ij} = \frac{\mu_i}{\mu_{ij}} \frac{2\mathcal{M}_j}{\mathcal{M}_i + \mathcal{M}_j} + \left[ 1 + \frac{2.41(\mathcal{M}_i - \mathcal{M}_j)(\mathcal{M}_i - 0.142\mathcal{M}_j)}{(\mathcal{M}_i + \mathcal{M}_j)^2} \right] \quad (2.22)$$

that defines those for the mixture conductivity.

Possibly, not all the needed data are present in the CEA database. If data regarding the binary interaction parameter ( $\mu_{ij}$ ) and the interaction coefficients ( $\phi_{ij}$ ) for a specific couple of species are missing, a simplified expression is used to evaluate the missing interaction coefficients:

$$\phi_{ij} = \frac{1}{4} \left[ 1 + \left( \frac{\mu_i}{\mu_j} \right)^{\frac{1}{2}} \left( \frac{\mathcal{M}_j}{\mathcal{M}_i} \right)^{\frac{1}{4}} \right]^2 \left( \frac{2\mathcal{M}_j}{\mathcal{M}_i + \mathcal{M}_j} \right)^{\frac{1}{2}} \quad (2.23)$$

and the binary interaction parameters ( $\mu_{ij}$ ) is obtained by reversing Eq. (2.21). Differently, when the data for the species viscosity or thermal conductivity are not present, the species viscosity is calculated by means of the following approximate expression:

$$\mu_i = \frac{\alpha \sqrt{\mathcal{M}_i T}}{\Omega} \quad (2.24)$$

in which:

$$\alpha = 0.3125 \sqrt{\frac{10^5 K_b}{\pi N_A}} \quad \text{and} \quad \Omega = \ln \left( \frac{50 \mathcal{M}_i^{4.6}}{T^{1.4}} \right)$$

being  $K_b$  the Boltzmann constant and  $N_A$  the Avogadro number; and the species thermal conductivity is evaluated as follows:

$$k_i = \mu_i \frac{\mathcal{R}}{\mathcal{M}_i} [0.00375 + 0.00132(\hat{C}_{pi} - 2.5)] \quad (2.25)$$

where  $\hat{C}_{pi} = \tilde{C}_{pi}/\mathcal{R}$  is the adimensionalized specific heat.<sup>2</sup>

---

<sup>2</sup>Using S.I. units, the expressions (2.24) and (2.25) give viscosity and thermal conductivity in units of micropoise ( $\mu\text{P}$ ) and microwatts per centimeter-Kelvin ( $\mu\text{W cm}^{-1} \text{K}^{-1}$ ), respectively.

### 2.1.4 Turbulence modeling

So far, the presented gas-phase governing equations (Eq. (2.1)) strictly refer to laminar flows. Turbulence effects can be accounted for by expressing all quantities as the sum of mean and fluctuating part and relying on a turbulence model to obtain the value of the additional unknowns introduced by procedure. The turbulent model used in this work is the one-equation Spalart-Allmaras model [50]. The model, has been developed mainly for aerodynamic applications and basically solves a transport equation for the turbulence viscosity  $\nu_t$ .

#### The Spalart-Allmaras model

Turbulence effects are accounted for by modifying the transport properties of the mixture [51]. Viscosity, conductivity and diffusivity coefficients are evaluated as follows:

$$\mu = \mu_l + \mu_t \quad (2.26)$$

$$k = k_l + \frac{\mu_t c_p}{Pr_t} \quad (2.27)$$

$$\mathcal{D} = \mathcal{D}_l + \frac{\mu_t}{\rho Sc_t} \quad (2.28)$$

where the subscript “*l*” indicates the laminar transport properties,  $\mu_t$  is the turbulent viscosity,  $Pr_t$  and  $Sc_t$  are the turbulent Prandtl and Schmidt numbers, respectively. The Spalart-Allmaras turbulence model solves a transport equation:

$$\frac{\partial \tilde{\nu}}{\partial t} + \mathbf{v} \cdot \nabla \tilde{\nu} - \frac{1}{\sigma} \nabla \cdot [(\nu + \tilde{\nu}) \nabla \tilde{\nu}] - \frac{c_{b2}}{\sigma} (\nabla \tilde{\nu})^2 = c_{b1} \tilde{S} \tilde{\nu} - c_{w1} f_w \left( \frac{\tilde{\nu}}{d} \right)^2 \quad (2.29)$$

**Table 2.1** – Spalart-Allmaras coefficients and constants.

Coefficient	Definition	Constant	Value
$c_{w1}$	$\frac{c_{b1}}{\kappa} + \frac{1 + c_{b2}}{\sigma}$	$c_{b1}$	0.14
$f_{\nu 1}$	$\frac{\chi^3}{\chi^3 + c_{\nu 1}^3}$	$c_{b2}$	0.6
$f_{\nu 2}$	$1 - \frac{\chi}{+\chi f_{\nu 1}}$	$c_{\nu 2}$	7.1
$f_w$	$g \left[ \frac{1 + c_{w3}^6}{g^6 + c_{w3}^6} \right]^{1/6}$	$c_{w2}$	0.3
$\chi$	$\frac{\tilde{\nu}}{\nu}$	$c_{w3}$	2
$g$	$r + c_{w2}(r^6 - r)$	$\kappa$	0.41
$r$	$\frac{\tilde{\nu}}{\tilde{S}\kappa^2 y^2}$	$\sigma$	2/3
$\tilde{S}$	$S + \frac{\tilde{\nu}}{\kappa^2 y^2} f_{\nu 2}$		
$S$	$\sqrt{2\Omega_{ij}\Omega_{ij}}$		

where the last two terms on the left-hand side represent the turbulent diffusion, the first term on the right-hand side is the turbulence production and the second one is the turbulence destruction ( $d$  is the distance to the nearest wall). The variable  $\tilde{\nu}$  in Eq. (2.29) is related to the eddy viscosity through the relation:

$$\tilde{\nu} = \nu_t / f_{\nu 1}$$

and the used coefficients are defined as in Table 2.1, where  $\Omega_{ij} = \frac{1}{2}(\partial u_i / \partial x_j - \partial u_j / \partial x_i)$  is the halved vorticity tensor. Finally, it has to be noted that the wall

boundary condition is represented by  $\tilde{v} = 0$ .

## 2.2 Solid phase modeling

### 2.2.1 Solid-phase conservation equations

As for the gas phase, conservation equations can be written for the solid phase. If a generic ablative pyrolyzing material is considered, its internal density can vary because of in-depth processes (resin decomposition or solid-solid homogeneous reaction between the char components). This internal processes generate gaseous products that percolate through the porous material. For this reason, three different densities can be identified in a control volume inside the material: the solid material bulk density (that is the solid mass per total volume,  $\rho_s = M_s / V_{bulk}$ ), the pyrolysis gas density ( $\rho_g$ ) and the density ( $\rho_h$ ) of the gaseous products of the homogeneous solid-solid reaction that can occur in certain classes of ablative materials (e.g. post-pyrolytic homogeneous chemical reactions between the carbon and the silica in silica-phenolic materials). To facilitate the illustration of the governing equations, it is important to understand the material model used to characterize the state of the solid/gas mixture ( $\bar{\rho}$ ). It is assumed that all the pores are interconnected; therefore, the internal gases occupy all of the pore space and are free to flow through it. Consequently, the density of the solid/gas mixture is described by:

$$\bar{\rho} = \Phi_g \rho_g + \Phi_h \rho_h + \rho_s \quad (2.30)$$

where the terms  $\Phi_g$  and  $\Phi_h$  represent the volume fraction of the material occupied by the pyrolysis gas and by the solid-solid reaction gaseous products, respectively. The summation of the two volume fractions equals the porosity

of the porous solid:  $\Phi = V_{void}/V_{bulk} = \Phi_g + \Phi_h$ . Note that the internal gases, although generated by different phenomena, can interact with each other resulting in a single mixture. However, for the sake of simplicity, the two gases are considered here as single, separate, non-reactive and immiscible entities that flow through the material at the same velocity  $\mathbf{v}$ . Considering this, the continuity equation is formulated by summing the continuity equations for the two different phases:

$$\frac{\partial \bar{\rho}}{\partial t} + \nabla \cdot (\Phi_g \rho_g \mathbf{v} + \Phi_h \rho_h \mathbf{v}) = 0 \quad (2.31)$$

where the net source term due to the transformation of the solid phase into the gaseous one (pyrolysis gas or other products) is zero:  $\dot{w}_s + \dot{w}_g + \dot{w}_h = 0$ . Equation (2.31) can be further simplified by neglecting the mass of the gases at any point as being small compared to the mass of solid material ( $\bar{\rho} \simeq \rho_s$ ):

$$\frac{\partial \rho_s}{\partial t} + \nabla \cdot (\Phi_g \rho_g \mathbf{v} + \Phi_h \rho_h \mathbf{v}) = 0 \quad (2.32)$$

Next, assuming the gases to be inviscid and the pressure variations in the flow small, allows to formulate the energy conservation equation in terms of specific enthalpy by summing the energy equations of the two different phases:

$$\frac{\partial}{\partial t}(\rho_s h_s) + \nabla \cdot (\Phi_g \rho_g h_g \mathbf{v} + \Phi_h \rho_h h_h \mathbf{v}) - \nabla \cdot (k_s \nabla T) = 0 \quad (2.33)$$

where (i) the solid and gas have been considered in thermal equilibrium, (ii) no in-depth energy sources have been accounted for, and (iii) the internal gases have been assumed to pass immediately out through the char (zero residence time). In Eq. (2.33) the terms, from left to right, represent: the time variation of the material sensible energy, the energy entering the control volume due to the injection of pyrolysis gas and homogeneous solid-solid reactions gaseous products,

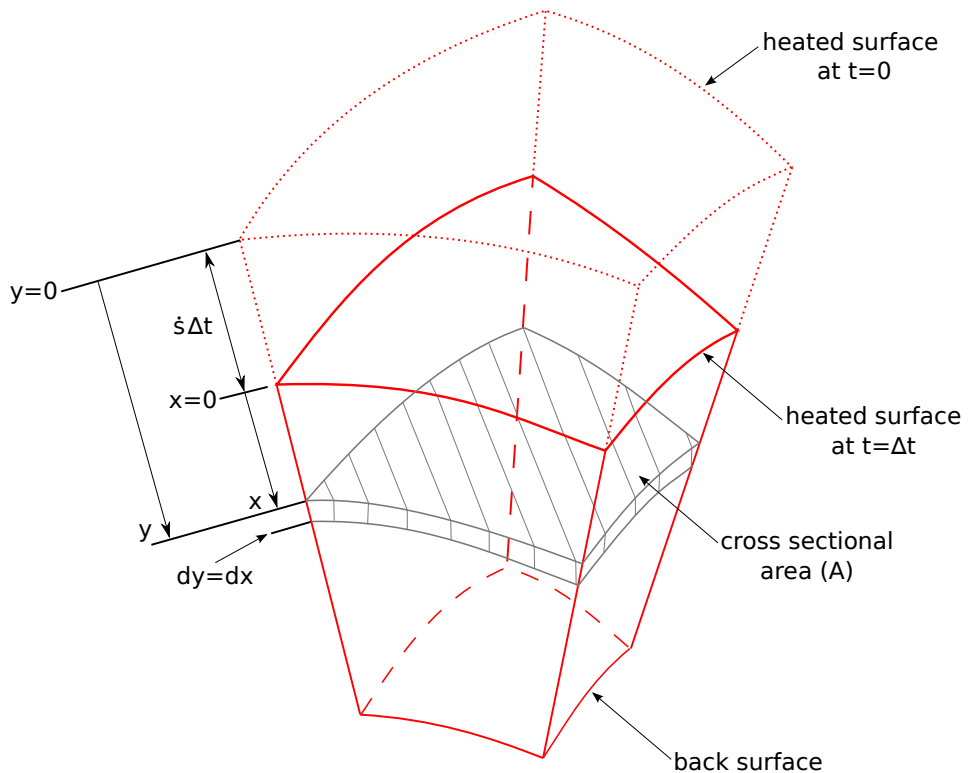


**Figure 2.1 – Coordinate system illustration.**

and the net heat conduction inside the material. As the surface of the ablative material recedes, it may be useful rewriting Eqs. (2.32) and (2.33) in a moving coordinate system. Considering, for the sake of simplicity the one-dimensional case, we can define two different reference frames: a moving and a fixed one, named  $x$  and  $y$ , respectively (Fig. 2.1). Note that, although the considered frames are one-dimensional, the cross-sectional area (perpendicular to the conduction direction) can vary in an arbitrary manner with the depth. This allows to account for non-planar surface in a simplified way. Therefore, considering the

following relations between the two reference frames:

$$\begin{aligned} y &= x + \frac{\partial y}{\partial t} \Big|_x \Delta t = x + \dot{s} \Delta t \\ \frac{\partial \cdot}{\partial x} \Big|_t &= \frac{\partial \cdot}{\partial y} \Big|_t \\ \frac{\partial \cdot}{\partial t} \Big|_x &= \frac{\partial \cdot}{\partial t} \Big|_y + \frac{\partial \cdot}{\partial y} \Big|_t \frac{\partial y}{\partial t} \Big|_x = \frac{\partial \cdot}{\partial t} \Big|_y + \frac{\partial \cdot}{\partial y} \Big|_t \dot{s} \end{aligned}$$

Equations (2.32) and (2.33) in the moving coordinate system read [52]:

$$\frac{\partial}{\partial t}(\rho_s A) = \dot{s} \frac{\partial}{\partial x}(\rho_s A) + \frac{\partial}{\partial x}(\dot{m}_g A + \dot{m}_h A) \quad (2.34a)$$

$$\frac{\partial}{\partial t}(\rho_s h_s A) = \frac{\partial}{\partial x} \left( A k_s \frac{\partial T_s}{\partial x} \right) + \dot{s} \frac{\partial}{\partial x}(\rho_s h_s A) + \frac{\partial}{\partial x}(\dot{m}_g h_g A + \dot{m}_h h_h A) \quad (2.34b)$$

where the gas mass flow rate term, defined as  $\dot{m}_{g,h} = \Phi_{g,h} \rho_{g,h} v$ , has been introduced. In Eq. (2.34a), the following contribution are accounted for (from left to right): time variation of solid bulk density, convective term due to coordinate motion ( $\dot{s}$  is the material recession rate), and mass flow rate due to the internal gas flow. The terms in Eq. (2.34a) (from left to right) represent: the time variation of the material sensible energy, the net heat conduction inside the material, the convected energy due to the coordinate motion and, finally, the energy entering the control volume due to the injection of pyrolysis gas and homogeneous solid-solid reactions gaseous products (considered immiscibles as previously).

### 2.2.2 Steady-state ablation approximation

When planar surfaces ( $A = \text{const}$ ) are considered, Eqs. (2.34) can be rewritten eliminating the cross-sectional area inside the derivative terms. Let us introduce, for reasons that will be clarified later, a coordinate  $\eta$  parallel to the previous one  $x$  but pointing in the opposite direction (outwards the material). Then, Eqs. (2.34) for a planar surface read:

$$\frac{\partial \rho_s}{\partial t} = -\dot{s} \frac{\partial \rho_s}{\partial \eta} - \frac{\partial}{\partial \eta} (\dot{m}_g + \dot{m}_h) \quad (2.35a)$$

$$\frac{\partial}{\partial t} (\rho_s h_s) = \frac{\partial}{\partial \eta} \left( k_s \frac{\partial T_s}{\partial \eta} \right) - \dot{s} \frac{\partial}{\partial \eta} (\rho_s h_s) - \frac{\partial}{\partial \eta} (\dot{m}_g h_g + \dot{m}_h h_h) \quad (2.35b)$$

Considering a planar surface allows to obtain a closed solution of Eq. (2.35b). In fact, by integrating Eq. (2.35b) between the gas–wall interface ( $w$ ) and a point inside the material (assuming adiabatic condition at the inner surface) where the material is still in the virgin state ( $in$ ) and, therefore, the terms  $(\dot{m}_g h_g)_{in}$  and  $(\dot{m}_h h_h)_{in}$  are null, yields the steady-state solution:

$$\dot{q}_{cond}^{ss} = (\dot{m}_g h_g)_w + (\dot{m}_h h_h)_w - \dot{s}(\rho_v h_v - \rho_c h_c) \quad (2.36)$$

where it has been assumed that the density of the solid material ( $\rho_s$ ) corresponds to the density of the charred material ( $\rho_c$ ) and to the density of the virgin material ( $\rho_v$ ) at the wall interface and at the back surface, respectively. Equation (2.36) represents the steady-state closed solution of Eq. (2.35b). In fact, differently from a classical heat conduction problem, the heat conduction in a system tied to a receding surface can reach the steady-state condition. This means that, if the considered material is thick enough, such that the temperature variation does not reach the bottom surface, the temperature profile inside the material does

not vary with time in the moving coordinate system.<sup>3</sup> Obviously, the steady-state ablation hypothesis is an approximation of the conductive heat flux, however it can be considered reasonably valid for low-conductivity materials or high ablation rates. Typically, for SRM nozzle applications which are characterized by high heating and recession rates and low-conductivity materials, the steady-state ablation permits to correctly evaluate the erosion rate level by decoupling the erosion process from the transient heating problem of the nozzle material.

At this point it is interesting to note that the steady-state hypothesis allows further consideration on the mass fluxes involved in the overall surface mass balance. In fact, by integrating the mass conservation equation (Eq. (2.35a)) between the back surface and the gas–solid interface of a generic planar pyrolyzing ablative material, and considering the steady-state solution, the general mass conservation equation in a moving coordinate system tied to the receding surface is [12, 29]:

$$\dot{m}_g + \dot{m}_h + \dot{m}_c = \rho_v \dot{s} \quad (2.37)$$

where the term  $\dot{m}_c$  represents the mass flow rate of the totally charred material at the surface. Therefore, considering that, the material recession rate is by definition:

$$\dot{s} = \frac{\dot{m}_c}{\rho_c} \quad (2.38)$$

the sum of the internal gas mass flow rates is a known fraction,  $\varphi$ , of the char mass flow rate:

$$\varphi = \frac{\dot{m}_g + \dot{m}_h}{\dot{m}_c} = \left( \frac{\rho_v}{\rho_c} - 1 \right) \quad (2.39)$$

Equation (2.39) allows the quantification of the total internal gas mass flow rate once the char mass flow rate, the virgin material density and the charred

---

<sup>3</sup>The steady-state solution exists only if the temperature rise does not reach the bottom surface.

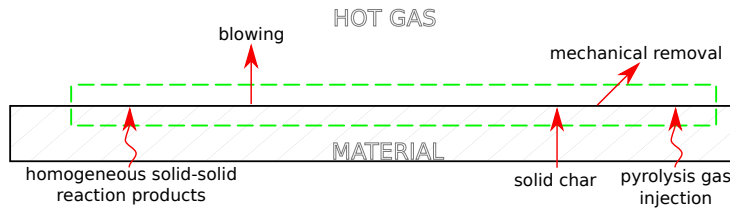


**Figure 2.2 – Overall mass fluxes over a generic ablating material.**

material density are known. In fact, when the steady-state condition is reached, the thickness of the charred material does not vary with time anymore.

## 2.3 Surface phenomena modeling for ablative materials

When focusing on the accurate resolution of the complex nozzle flow field, the gas-surface interaction has to be dealt with as a boundary condition which needs a specific modeling. Surface mass and energy balances over this kind of materials can be derived directly from the observation of the involved phenomena. The general form of these balances is derived in the following, whereas their application for each specific material analyzed in the present work will be presented in the next chapters.

### 2.3.1 Surface mass balance

As a generic ablative pyrolyzing material is exposed to severe thermal and chemical conditions, the mass fluxes entering and exiting the surface can be sketched as in Fig. 2.2, where a moving coordinate system tied to the moving surface has been assumed. The internal decomposition generates a pyrolysis gas and leaves a porous solid residual (char). The pyrolysis gas percolates through the porous

residual and reaches the surface. For certain classes of ablative materials, the material heating favors homogeneous solid-solid reactions between different components of the char (e. g. between the carbon and the silica in silica-phenolic composites), and so the generated gaseous products flow from the reaction zone towards the surface. Moreover, when surface material consumption occurs, a certain amount of solid char enters the control surface because of the surface motion. Once this char has entered the surface it can sublime, as well thermochemically react with some species present in the boundary layer. These processes generate gaseous products that enter the flowfield modifying the bulk gaseous mass next to the surface. As a result of this mass addition, the bulk gaseous mass next to the surface is convected away (blowing effect). Finally, the surface material can be removed by shear stresses or particle impingement (mechanical erosion). Under this condition, the overall surface mass balance can be written as follows:

$$\dot{m}_g + \dot{m}_s + \dot{m}_h = \dot{m}_f + \dot{m}_{blow} \quad (2.40)$$

where the terms on the left-hand side of Eq. (2.40) are the mass fluxes entering the surface due pyrolysis gas injection, solid surface motion, and the injection of the in-depth homogeneous solid-solid reaction products; while the terms on the right-hand side, exiting the surface, are due to mechanical ablation and blowing. A different view of the involved phenomena can be found by formulating the surface mass balances for the  $i^{th}$  gaseous species in the system. Fig. 2.3 shows the surface mass fluxes involved when a single gaseous species,  $i$ , is considered. The two gas injection contributions coming from the solid side are the same of Fig. 2.2. However, in this case, species production or consumption can occur at the wall because of several different phenomena. For this reason, in Fig. 2.3 three source terms, accounting for thermochemical ablation, sublimation and

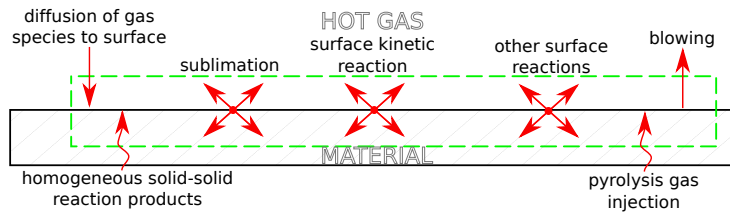


**Figure 2.3 – Gaseous species mass fluxes over a generic ablating material.**

reactions different from ablation (i.e. catalysis) have to be considered. Moreover, in the gas side, the injection of the gaseous products generated by the material consumption causes the blowing of the species away from the surface, whereas the concentration boundary layer, arising from the surface reactions, causes the diffusion of gas species towards and away from the surface.

To formulate the surface mass balances for each gaseous species  $i$ , it is convenient to start from the species continuity equations in its integral form (see Appendix A for its derivation). By limiting the thickness of the control volume to zero, one obtains an infinitely thin lamina. As the lateral surfaces of the volume go to zero, the surface integral reduces to two separate integrals on the upper and the lower surfaces of the lamina, denoted as “+” and “−”, and having two different outward facing normals:  $\mathbf{n}^+ = -\mathbf{n}^-$ , respectively [53]. In the limit as the volume goes to zero, the species continuity equations becomes ( $i = 1, \dots, N_c$ ):

$$\begin{aligned} \int_S [(\rho_i^+ (\mathbf{v}^+ - \mathbf{v}_s^+) - \rho^+ \mathcal{D}_{im}^+ \nabla y_i^+) + \\ - (\rho_i^- (\mathbf{v}^- - \mathbf{v}_s^-) - \rho^- \mathcal{D}_{im}^- \nabla y_i^-)] \cdot \mathbf{n}^+ dS = \\ = \lim_{V \rightarrow 0} \int_V \dot{w}_i dV - \lim_{V \rightarrow 0} \left( \frac{d}{dt} \int_V \rho_i dV \right) \quad (2.41) \end{aligned}$$

where the surfaces of the control volume have been considered movable ( $\mathbf{v}_s^+ = \mathbf{v}_s^- = \mathbf{v}_s$  for a thin lamina) and the Leibnitz Theorem has been applied ( $\psi$  is a

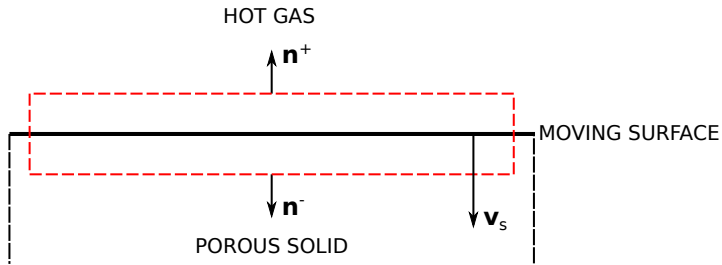


**Figure 2.4** – Thin lamina and corresponding outward facing normals.

generic variable):

$$\frac{d}{dt} \int_V \psi dV = \int_V \frac{\partial \psi}{\partial t} dV + \int_S \psi (\mathbf{v}_s \cdot \mathbf{n}) dS \quad (2.42)$$

Assuming that mass does not accumulate in the lamina as time proceeds and considering that:

$$\lim_{V \rightarrow 0} \int_V \dot{w}_i dV = \int_S \omega_i dS \quad (2.43)$$

where  $\omega_i$  is a source term per unit surface, Eq. (2.41) can be rewritten for any arbitrary lamina as ( $i = 1, \dots, N_c$ ):

$$[(\rho_i^+ (\mathbf{v}^+ - \mathbf{v}_s^+) - \rho^+ \mathcal{D}_{im}^+ \nabla y_i^+) - (\rho_i^- (\mathbf{v}^- - \mathbf{v}_s^-) - \rho^- \mathcal{D}_{im}^- \nabla y_i^-)] \cdot \mathbf{n}^+ = \omega_i \quad (2.44)$$

At this point, recalling the qualitative description of the involved phenomena at the material surface, it is possible to label the terms in Eq. (2.44). If we assume that the thin lamina corresponds to the surface of the ablating material, the upper surface and the lower surface can be located just outside (flowfield) and just inside (porous solid) of the surface, respectively. Consequently, the terms labeled with

the “+” sign are representative of the gas phase (Fig. 2.4). Differently, the terms labeled with the “−” sign are representative of the porous solid. Noting that the solid phase has zero velocity ( $\mathbf{v}^- = 0$  for the solid material), the velocity in the porous solid is that of the internal gases. Recalling the approximations taken in Section 2.2 for the internal gases, considered inviscid, the diffusive terms in the porous-solid side are null. Then, using the following positions:

$$\begin{aligned}\rho_{i_g}^- \mathbf{v}^- \cdot \mathbf{n}^+ &= \dot{m}_g y_{i_g} \\ \rho_{i_h}^- \mathbf{v}^- \cdot \mathbf{n}^+ &= \dot{m}_h y_{i_h}\end{aligned}$$

and considering that the gas velocities (flowfield, pyrolysis and the one generated from the internal homogeneous reactions) are much larger than the boundary velocity ( $\mathbf{v}_s$ ), Eq. (2.44) reads:

$$\begin{aligned}\rho \mathcal{D}_{im} \frac{\partial y_i}{\partial \eta} \Big|_w + \dot{m}_g y_{i_g} + \dot{m}_h y_{i_h} + \sum_{r=1}^{N_r} \omega_i^r + \sum_{r=1}^{\tilde{N}_r} \tilde{\omega}_i^r + \sum_{r=1}^{\hat{N}_r} \hat{\omega}_i^r &= \\ = (\rho v)_w y_{i_w} &\quad i = 1, \dots, N_c \quad (2.45)\end{aligned}$$

where  $\eta$  has been used instead of  $\mathbf{n}^+$  and the source term  $\omega$  has been decomposed in three different terms. The first three terms on the left-hand side of Eq. (2.45) are the mass fluxes of species  $i$  entering the surface due to diffusion, injection of pyrolysis gas and injection of the in-depth homogeneous solid-solid reaction products; whereas the last three terms are the source terms due to thermochemical ablation, sublimation and other surface reactions. The term on the right-hand side is the mass flux of species  $i$  exiting the surface because of the blowing effect. Eq. (2.45) represents the most general form of the surface mass balance over a decomposing ablative material and can be used in the following as a starting point in deriving the more specific one for each of the analyzed

materials.

At this point it is interesting to note that the overall surface mass balance (Eq. (2.40)) can be obtained by summing Eq. (2.45) over all species (considering also the contribution of the mechanical ablation not accounted for in the gaseous phase surface mass balance). In fact, noting that the overall contributions of both the diffusion and the reactions different than ablation are null since they do not adduce mass:

$$\sum_{i=1}^{N_c} \rho \mathcal{D}_{im} \frac{\partial y_i}{\partial \eta} \Big|_w = 0$$

$$\sum_{i=1}^{N_c} \sum_{r=1}^{N_r} \hat{\omega}_i^r = 0$$

and assuming the following positions:

$$\dot{m}_g = \sum_{i=1}^{N_c} \dot{m}_g y_{i_g} \quad (2.46a)$$

$$\dot{m}_h = \sum_{i=1}^{N_c} \dot{m}_h y_{i_h} \quad (2.46b)$$

$$\dot{m}_s = \sum_{i=1}^{N_c} \sum_{r=1}^{N_r} \omega_i^r + \sum_{i=1}^{N_c} \sum_{r=1}^{\tilde{N}_r} \tilde{\omega}_i^r \quad (2.46c)$$

$$\dot{m}_{blow} = \sum_{i=1}^{N_c} (\rho v)_w y_{i_w} \quad (2.46d)$$

Equation (2.40) is re-obtained.

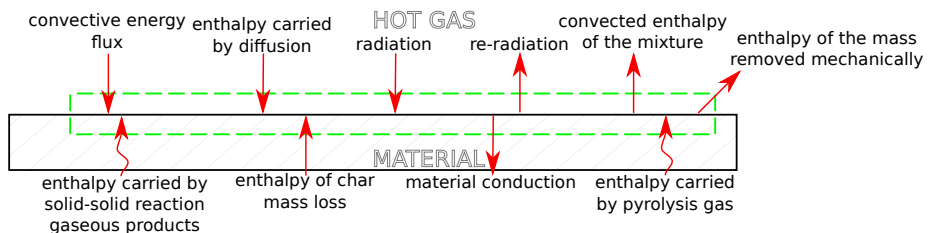


**Figure 2.5 – Overall energy fluxes over a generic ablating material.**

### 2.3.2 Surface energy balance

As done for the mass fluxes, a schematic of the energy fluxes entering and exiting the material surface, when thermochemical erosion occurs, is given in Fig. 2.5. When the reference system is tied to the receding surface, there are three energy fluxes entering the surface of a generic ablative material from the material side. The first two are due to the fact that the mass injections of the pyrolysis gas, and of the gaseous products of the in-depth solid-solid homogeneous reactions, carry a certain amount of enthalpy from the material interior up to surface; the third term accounts for the energy of the solid material entering the surface because of the surface regression. Concerning the energy fluxes exiting the surface from the material side, the only phenomenon to be accounted for is the solid material conduction. From the gas side, the terms that have to be accounted for are: convection, diffusion, radiation from the gas mixture, blowing, re-radiation from the wall and, finally, the energy that eventually will be carried away if mechanical removal occurs.

The surface energy balance can be derived as done for the surface mass balance (Eq. (2.45)). By starting from the energy conservation in its integral form (see Appendix A for its derivation), using the Leibnitz Theorem (Eq. (2.42)) and assuming that the viscous dissipation term ( $\nabla \cdot (\mathbb{T} \cdot \mathbf{v})$ ) is small because of the small Mach number next to the surface. The energy conservation rewritten for

the thin lamina surroundding the surface is:

$$[(\rho^+ \mathcal{E}^+ (\mathbf{v}^+ - \mathbf{v}_s) + p^+ \mathbf{v}^+ + \dot{\mathbf{q}}^+) + \\ - (\rho^- \mathcal{E}^- (\mathbf{v}^- - \mathbf{v}_s) + p^- \mathbf{v}^- + \dot{\mathbf{q}}^-)] \cdot \mathbf{n}^+ = 0 \quad (2.47)$$

Rearranging Eq. (2.47) one obtains:

$$(\rho^+ \mathcal{E}^+ + p^+) \mathbf{v}^+ \cdot \mathbf{n}^+ - (\rho^- \mathcal{E}^- + p^-) \mathbf{v}^- \cdot \mathbf{n}^+ + (\dot{\mathbf{q}}^+ - \dot{\mathbf{q}}^-) \cdot \mathbf{n}^+ = \\ = (\rho^+ \mathcal{E}^+ - \rho^- \mathcal{E}^-) \mathbf{v}_s \cdot \mathbf{n}^+ \quad (2.48)$$

At this point, considering the “+” and the “−” terms as representative of the gas and the porous-solid side, respectively; assuming negligible the boundary velocity ( $\mathbf{v}_s$ ) with respect to the gas velocity of both the flow-field mixture and the solid-side gases (pyrolysis and homogeneous reaction products); considering null the velocity  $v^-$  for the solid; using the definition of total specific enthalpy ( $h_0 = \mathcal{E} + p/\rho$ ) and approximating the total specific enthalpy with the static specific one (as the Mach number of both the flow-field mixture and the solid-side gases is small), the surface energy balance can be rewritten and three different contributions can be identified:

$$\text{flow field gas} + \text{solid} + \text{internal gases} = 0 \quad (2.49)$$

where:

- flow field gas =  $[(\rho \mathbf{v})_w h_w + \dot{\mathbf{q}}_w] \cdot \mathbf{n}^+ =$   
 $= (\rho v)_w h_w - k \frac{\partial T}{\partial n^+} \Big|_w - \sum_{i=1}^{N_c} h_{i_w} \rho \mathcal{D}_{im} \frac{\partial y_i}{\partial n^+} \Big|_w \quad (2.50)$

- solid =  $[\rho_s \mathbf{v}_s h_{s_w} - \dot{\mathbf{q}}_{cond}] \cdot \mathbf{n}^+ = -\rho_s v_s h_{s_w} + k_s \frac{\partial T_s}{\partial n^+} \Big|_w \quad (2.51)$

- internal gases =  $-[(\rho \mathbf{v})_g h_{g_w} + (\rho \mathbf{v})_h h_{h_w}] \cdot \mathbf{n}^+ =$   
 $= -(\rho v)_g h_{g_w} - (\rho v)_h h_{h_w} \quad (2.52)$

Finally, considering these contributions, the overall surface energy balances for such a generic ablative material can be written as follows:

$$\begin{aligned} k \frac{\partial T}{\partial \eta} \Big|_w + \sum_{i=1}^{N_c} h_{i_w} \rho \mathcal{D}_{im} \frac{\partial y_i}{\partial \eta} \Big|_w + \dot{q}_{rad_{in}} + \dot{m}_g h_{g_w} + \dot{m}_s h_{s_w} + \dot{m}_h h_{h_w} \\ = (\rho v)_w h_w + \dot{q}_{rad_{out}} + \dot{m}_f h_{f_w} + k_s \frac{\partial T_s}{\partial \eta} \Big|_w \quad (2.53) \end{aligned}$$

where the energy fluxes entering and exiting the surface are on the left-hand and on the right-hand side, respectively,  $\eta$  has been used instead of  $n^+$ , and the fail mass removal, as well as the radiative heat fluxes from and towards the wall, have been considered .

As described previously, the terms in Eq. (2.53) can be distinguished in two categories: the “gas-side terms” and the “solid-side terms”. In particular, since this work deals mainly with the description and the modeling of the gas-side phenomena, a further description of the solid-side terms is needed in order to describe how to account for these terms. For example, the last term  $k_s(\partial T_s / \partial \eta)$  on Eq. (2.53), that represents the solid conduction term (named  $\dot{q}_{cond}$  in the following), should be evaluated by a numerical or semi-analytical computational

solid mechanics (CSM) analysis by using Eq. (2.53) as the boundary condition, implying a coupled analysis of both the gas- and the material side. However, this kind of approach is impractical and cpu time demanding (even unfeasible for large time scale). Often, a radiative equilibrium solution [54] can be achieved by setting  $\dot{q}_{cond} = 0$ , while retaining all the other terms in Eq. (2.53). However, this is rarely a reasonable assumption for an ablating surface because the energy conduction in the material cannot be neglected. Fortunately, when dealing with an heated receding surface, further assumptions can be made on the conductive energy flux, helping in separating the resolution of the gas-side phenomena from that of the solid-side one. A good approximation of this term can be formulated by using the steady-state ablation hypothesis (Section 2.2.2) [55, 56]. By means of Eq. (2.36), Eq.(2.53) can be rewritten considering the steady-state heat conduction term, yielding:

$$\begin{aligned} k \frac{\partial T}{\partial \eta} \Big|_w + \sum_{i=1}^{N_c} h_{i_w} \rho \mathcal{D}_{im} \frac{\partial y_i}{\partial \eta} \Big|_w + \dot{q}_{rad_{in}} + \dot{m}_s h_{s_w} \\ = (\rho v)_w h_w + \dot{q}_{rad_{out}} + \dot{m}_f h_{f_w} - \dot{s}(\rho_{v_{in}} h_{v_{in}} - \rho_{c_w} h_{c_w}) \end{aligned} \quad (2.54)$$

where the terms related to the internal gas injection (pyrolysis or other) have disappeared.

---

# Numerical method

Navier-Stokes equations can be differently formulated depending on the numerical method used for their integration. In particular, in the present work, the numerical mathematical method known as the  $\lambda$ -scheme, is adopted [57]. A reformulation of the conservation equations, convenient to be used with this integration technique, is presented in this chapter. Moreover, the description of several boundary conditions, suitable for different applications of interest, is given.

## 3.1 Governing equations

The selected formulation considers the state variable listed in Table 3.1. Using these variables the Navier-Stokes equations (Eq. (2.1)) can be rewritten as follows

**Table 3.1** – State variables in the mathematical model.

Variable	Symbol	Units
Mass fraction	$y_i$	–
“Scaled” speed of sound <sup>1</sup>	$b$	[m s <sup>-1</sup> ]
Velocity	$\mathbf{v}$	[m s <sup>-1</sup> ]
Entropy	$s$	[J K <sup>-1</sup> ]

[58, 59, 60, 61]:

$$\left\{ \begin{array}{l} \frac{Dy_i}{Dt} = V_{y_i} \\ \frac{1}{c_1} \frac{Db}{Dt} + a \nabla \cdot \mathbf{v} - \frac{a}{\gamma R} \frac{Ds}{Dt} = V_b \\ \frac{D\mathbf{v}}{Dt} + \frac{a}{c_1} \nabla b - \frac{a^2}{\gamma R} \nabla s + \frac{a^2}{\gamma R} \sum_{i=1}^{N_c} Q_i \nabla y_i = \mathbf{V}_m \\ \frac{Ds}{Dt} = V_s \end{array} \right. \quad i = 1, \dots, N_c - 1 \quad (3.1)$$

in which the new terms that have been introduced are defined in Table 3.2, where  $g_i$  represents the Gibbs free energy per unit mass (chemical potential) of the species  $i$ . In Eq. (3.1) the diffusive and the source terms of each equation have been included in the terms named  $V_{y_i}$ ,  $V_b$ ,  $\mathbf{V}_m$  and  $V_s$ , defined as follows:

---

<sup>1</sup> $b = 2a/(\gamma - 1)$

**Table 3.2 – Euler equation abbreviation definitions.**

Name	Definition
$\beta$	$ac_1 \sum_{i=1}^{N_c} \left[ -\frac{e_i}{RT} + \frac{g_i}{RT} + \frac{1}{c_1} \frac{\partial(1/\delta)}{\partial y_i} - \left( \frac{a_2}{c_1} - \frac{1}{d_1(\gamma-1)} \right) \frac{\partial \ln(\gamma R)}{\partial y_i} \right] \frac{Dy_i}{Dt}$
$Q_i$	$s_i - \frac{\partial \ln(\gamma R)}{\partial y_i} c_p \left( \frac{1}{d_1} - \frac{2a_2}{d_1 a_1} \right) - 2 \frac{c_p}{d_1 a_1} \frac{\partial(1/\delta)}{\partial y_i}$
$d_1$	$1 + T \frac{\partial(\gamma R)}{\partial T}$
$a_1$	$\frac{1}{\delta} + \frac{2T}{d_1} \frac{\partial(1/\delta)}{\partial T}$
$a_2$	$\frac{T}{d_1} \frac{\partial(1/\delta)}{\partial T}$
$c_1$	$d_1 \delta a_1$
$\delta$	$\frac{\gamma-1}{2}$

$$\begin{aligned}
 V_{y_i} &= \frac{\tilde{w}_i}{\rho} - \frac{1}{\rho} \nabla \cdot \mathbf{j}_i \\
 V_b &= \frac{1}{c_1} \beta + \frac{a}{\gamma R} (\gamma - 1) V_s \\
 \mathbf{V}_m &= \frac{1}{\rho} \nabla \cdot \mathbb{T} \\
 V_s &= -\frac{1}{T} \sum_{i=1}^{N_c} g_i V_{y_i} + \frac{R}{p} (\nabla \cdot (\mathbb{T} \cdot \mathbf{v}) - \nabla \cdot \dot{\mathbf{q}})
 \end{aligned} \tag{3.2}$$

## 3.2 Non-dimensional form of governing equations

Defining a general variable  $\psi$ , its dimensionless value can be obtained dividing it by a reference value  $\psi_r$ . In Table 3.3 each variable and its corresponding reference

**Table 3.3 – Reference variables.**

Variable	Reference value	Variable	Reference value
Density	$\rho_r = p_r / (R_r T_r)$	Shear stress tensor	$S_r = p_r$
Pressure	$p_r$	Viscous stress tensor	$T_r = p_r$
Length	$l_r$	Viscosity	$\mu_r$
Molecular weight	$\mathcal{M}_r = \mathcal{M}_{N_2}$	Enthalpy	$h_r = p_r / \rho_r$
Gas constant	$R_r = \mathcal{R} / \mathcal{M}_{N_2}$	Internal energy	$e_r = p_r / \rho_r$
Temperature	$T_r$	Heat flux (per unit area)	$q_r = p_r v_r$
Velocity	$v_r = \sqrt{p_r / \rho_r}$	Mass flux (per unit area)	$\dot{m}_r = \rho_r v_r$
Time	$t_r = l_r / v_r$	Gamma	$\gamma_r$
Entropy	$s_r = R_r$	Specific heats	$c_{pr} = c_{vr} = (\gamma_r / \gamma_r - 1) R_r$
Sound speed	$a_r = v_r$	Chemical source	$\omega_r = \rho_r / t_r$
Conductivity	$k_r = (\mu_r c_{pr}) / Pr_r$	Diffusion coefficient	$\mathcal{D}_r = \mu_r / (Le_r Pr_r \rho_r)$

value are reported. Note that some variables in Table 3.3 have been expressed in terms of the non-dimensional reference parameters listed in Table 3.4. At this point, maintaining the same notation for any variable, but bearing in mind that from now on we will refer to its non-dimensional representation, Eqs. (3.1) hold exactly the same in non-dimensional variables but the constitutive equations have to be reformulated as follows:

$$\mathbb{T} = \frac{1}{Re_r} \mu \left[ -\frac{2}{3} (\nabla \cdot \mathbf{v}) \mathbb{I} + \nabla \mathbf{v} + (\nabla \mathbf{v})^T \right] \quad (3.3a)$$

$$\dot{\mathbf{q}} = -\frac{\gamma_r}{\gamma_r - 1} \frac{1}{Re_r Pr_r} k \nabla T - \frac{1}{Le_r Re_r Pr_r} \sum_{i=1}^{N_c} \rho \mathcal{D}_{im} h_i \nabla y_i \quad (3.3b)$$

$$\mathbf{j}_i = -\frac{1}{Pr_r Le_r Re_r} \rho \mathcal{D}_{im} \nabla y_i \quad (3.3c)$$

**Table 3.4** – Non-dimensional reference parameters.

Parameter	Definition
Reynolds number	$Re_r = \frac{\rho_r v_r l_r}{\mu_r}$
Prandtl number	$Pr_r = \frac{\mu_r c_{pr}}{k_r}$
Lewis number	$Le_r = \frac{k_r}{\rho_r c_{pr} \mathcal{D}_r}$

### 3.3 The $\lambda$ -scheme

Following the technique presented in [57, 62, 63] for two-dimensional inviscid flows and extended in [59], [61], and [64] for viscous, reacting, and three-dimensional flows, respectively, the quasi-linear form of the governing equations, written in terms of  $b$ ,  $\mathbf{v}$ ,  $s$  and  $y_i$ , can be reformulated using ideas based on the concept of characteristics.

Being  $\mathbf{n}$  and  $\boldsymbol{\tau}$  be a pair of unit vectors along the coordinate lines of a given curvilinear orthogonal grid in the physical plane  $(x,y)$  and let  $\mathbf{i}$  and  $\mathbf{j}$  be a pair of unit vectors of a Cartesian grid in the same plane.

$$\mathbf{v} = u \mathbf{n} + v \boldsymbol{\tau}$$

Now let be  $\alpha = \alpha(x, y)$  the angle between the two orthogonal reference frames, by applying the transformation matrix between the two systems one obtains:

$$\mathbf{n} = \cos \alpha \mathbf{i} + \sin \alpha \mathbf{j}, \quad \boldsymbol{\tau} = -\sin \alpha \mathbf{i} + \cos \alpha \mathbf{j}$$

and

$$d\mathbf{n} = \boldsymbol{\tau} d\alpha, \quad d\boldsymbol{\tau} = -\mathbf{n} d\alpha \quad (3.4)$$

We also consider a unit vector,  $\mathbf{k}$ , perpendicular to the plane of motion so that  $\mathbf{k} = \mathbf{i} \times \mathbf{j} = \mathbf{n} \times \boldsymbol{\tau}$ . The following identities are easily proven:

$$\nabla \cdot \mathbf{v} = \mathbf{n} \cdot \nabla u + \boldsymbol{\tau} \cdot \nabla v + \mathbf{k} \times \mathbf{v} \cdot \nabla \alpha \quad (3.5)$$

$$(\mathbf{v} \cdot \nabla) \mathbf{v} = (\mathbf{v} \cdot \nabla u) \mathbf{n} + (\mathbf{v} \cdot \nabla v) \boldsymbol{\tau} + (\mathbf{v} \cdot \nabla \alpha) (u \boldsymbol{\tau} - v \mathbf{n}) \quad (3.6)$$

Finally, let  $\mathbf{w}$  be an arbitrary *unit* vector. By using the definition of the substantial derivative and using the notation  $\psi_t$  to express the time derivative of a general variable  $\psi$ , a single scalar equation can be obtained if the third of Eqs. (3.1) is dot-multiplied by  $\mathbf{w}$ , and the result is added to the second of Eqs. (3.1) and to the sum of the first  $i$  equations multiplied by  $a/(\gamma R)Q_i$ :

$$\begin{aligned} & \frac{1}{c_1} b_t + \mathbf{w} \cdot \mathbf{v}_t - \frac{a}{\gamma R} s_t + \frac{a}{\gamma R} \sum_{i=1}^{N_c} Q_i y_{i,t} + \\ & + (\mathbf{v} + a\mathbf{w}) \cdot \frac{\nabla b}{c_1} - \frac{a}{\gamma R} (\mathbf{v} + a\mathbf{w}) \cdot \nabla s + \mathbf{w} \cdot [(\mathbf{v} \cdot \nabla) \mathbf{v}] + \\ & + \frac{a}{\gamma R} (\mathbf{v} + a\mathbf{w}) \cdot \sum_{i=1}^{N_c} Q_i \nabla y_i + a \nabla \cdot \mathbf{v} = V_b + \mathbf{w} \cdot \mathbf{V}_m + \frac{a}{\gamma R} \sum_{i=1}^{N_c} Q_i V_{y_i} \end{aligned} \quad (3.7)$$

**Table 3.5** – Abbreviation definitions for Eq. (3.9).

Name	Definition	Name	Definition	Name	Definition
$\rho_1$	$b + u$	$\Lambda_1$	$\mathbf{v} + a \mathbf{n}$	$F$	$a \mathbf{k} \times \mathbf{v} \cdot \nabla \alpha$
$\rho_2$	$b - u$	$\Lambda_2$	$\mathbf{v} - a \mathbf{n}$	$B$	$\mathbf{v} \cdot \nabla \alpha$
$\rho_3$	$b + v$	$\Lambda_3$	$\mathbf{v} + a \boldsymbol{\tau}$	$c_{12}$	$(1 - c_1)/c_1$
$\rho_4$	$b - v$	$\Lambda_4$	$\mathbf{v} - a \boldsymbol{\tau}$		

By using Eq. (3.5) and (3.6), Eq. (3.7) can be written in the form:

$$\begin{aligned}
& \frac{1}{c_1} b_t + \mathbf{w} \cdot \mathbf{v}_t - \frac{a}{\gamma R} s_t + \frac{a}{\gamma R} \sum_{i=1}^{N_c} Q_i y_{i,t} + \\
& + (\mathbf{v} + a \mathbf{w}) \cdot \left( \frac{\nabla b}{c_1} - \frac{a}{\gamma R} \nabla s + \frac{a}{\gamma R} \sum_{i=1}^{N_c} Q_i \nabla y_i \right) + \\
& + \mathbf{w} \cdot [(\mathbf{v} \cdot \nabla u) \mathbf{n} + (\mathbf{v} \cdot \nabla v) \boldsymbol{\tau} + (\mathbf{v} \cdot \nabla \alpha) (u \boldsymbol{\tau} - v \mathbf{n})] + \\
& + a (\mathbf{n} \cdot \nabla u + \boldsymbol{\tau} \cdot \nabla v + \mathbf{k} \times \mathbf{v} \cdot \nabla \alpha) = V_b + \mathbf{w} \cdot \mathbf{V}_m + \frac{a}{\gamma R} \sum_{i=1}^{N_c} Q_i V_{y_i}
\end{aligned} \tag{3.8}$$

Now, substituting  $\mathbf{w}$  with  $\pm \mathbf{n}$  and  $\pm \boldsymbol{\tau}$  successively, four equations are obtained from Eq. (3.8). These equations can be rewritten in a simpler and symmetric form by using the definitions in Table 3.5:

$$\begin{aligned}
& \left( \frac{1}{c_1} b_t \pm u_t - \frac{a}{\gamma R} s_t + \frac{a}{\gamma R} \sum_{i=1}^{N_c} Q_i y_{i,t} \right) + \\
& + \begin{Bmatrix} \Lambda_1 \\ \Lambda_2 \end{Bmatrix} \cdot \left( \nabla \begin{Bmatrix} \rho_1 \\ \rho_2 \end{Bmatrix} - \frac{a}{\gamma R} \nabla s + \frac{a}{\gamma R} \sum_{i=1}^{N_c} Q_i \nabla y_i + c_{12} \nabla b \right) + \\
& + a \boldsymbol{\tau} \cdot \nabla v \mp Bv + F = V_b \pm \mathbf{V}_m \cdot \mathbf{n} + \frac{a}{\gamma R} \sum_{i=1}^{N_c} Q_i V_{y_i} \tag{3.9a}
\end{aligned}$$

$$\begin{aligned}
& \left( \frac{1}{c_1} b_t \pm v_t - \frac{a}{\gamma R} s_t + \frac{a}{\gamma R} \sum_{i=1}^{N_c} Q_i y_{i,t} \right) + \\
& + \begin{Bmatrix} \Lambda_3 \\ \Lambda_4 \end{Bmatrix} \cdot \left( \nabla \begin{Bmatrix} \rho_3 \\ \rho_4 \end{Bmatrix} \frac{a}{\gamma R} \nabla s + \frac{a}{\gamma R} \sum_{i=1}^{N_c} Q_i \nabla y_i + c_{12} \nabla b \right) + \\
& + a \mathbf{n} \cdot \nabla u \pm Bu + F = V_b \pm \mathbf{V}_m \cdot \boldsymbol{\tau} + \frac{a}{\gamma R} \sum_{i=1}^{N_c} Q_i V_{y_i} \tag{3.9b}
\end{aligned}$$

Note that if the orthogonal frame is also Cartesian, then the terms  $F$  and  $B$  vanish because  $\nabla \alpha = 0$  everywhere in the flowfield. At this stage we may observe that the vectors  $\Lambda_i$  ( $i = 1, \dots, 4$ ) are two-dimensional generalizations of the characteristic slopes,  $\lambda_i$ , defined for one-dimensional flows [57]. Similarly, the scalars  $\rho_i$  are generalizations of the Riemann variables. Some additional manipulation, however, is necessary to bring the equations to a form closer to the one obtained for one-dimensional flows. We see, indeed, that Eqs. (3.9) are a redundant system since the mass fractions  $y_i$  and the entropy  $s$  are provided by the first ( $N_c - 1$  equations) and the last of Eqs. (3.1), respectively, and three independent unknowns only remains: the variable  $b$  and the two velocity components  $u$  and  $v$ . Following an idea of Butler [65], the four Eqs. (3.9) can

be recombined into three, taking advantage of the orthogonality of  $\mathbf{n}$  and  $\boldsymbol{\tau}$ . By summing together the four Eqs. (3.9), and subtracting the second of Eqs. (3.1) multiplied by 2 and the sum over  $i$  of the first of Eqs. (3.1) multiplied by  $2a/(\gamma R)Q_i$ , one obtains:

$$\begin{aligned} & \left( \frac{1}{c_1} b_t - \frac{a}{\gamma R} s_t + \frac{a}{\gamma R} \sum_{i=1}^{N_c} Q_i y_{i,t} \right) + \\ & + \frac{1}{2} \sum_{j=1}^4 \Lambda_j \cdot \left( \nabla \rho_j - \frac{a}{\gamma R} \nabla s + \frac{a}{\gamma R} \sum_{i=1}^{N_c} Q_i \nabla y_i + c_{12} \nabla b \right) + \\ & - \mathbf{v} \cdot \left( \frac{\nabla b}{c_1} - \frac{a}{\gamma R} \nabla s + \frac{a}{\gamma R} \sum_{i=1}^{N_c} Q_i \nabla y_i \right) + F = V_b + \frac{a}{\gamma R} \sum_{i=1}^{N_c} Q_i V_{y_i} \end{aligned} \quad (3.10)$$

then, by subtracting the second of Eqs. (3.9a) from the first:

$$\begin{aligned} & u_t + \frac{1}{2} \Lambda_1 \cdot \left( \nabla \rho_1 - \frac{a}{\gamma R} \nabla s + \frac{a}{\gamma R} \sum_{i=1}^{N_c} Q_i \nabla y_i + c_{12} \nabla b \right) + \\ & - \frac{1}{2} \Lambda_2 \cdot \left( \nabla \rho_2 - \frac{a}{\gamma R} \nabla s + \frac{a}{\gamma R} \sum_{i=1}^{N_c} Q_i \nabla y_i + c_{12} \nabla b \right) - B v = \mathbf{V}_m \cdot \mathbf{n} \end{aligned} \quad (3.11a)$$

**Table 3.6** – Abbreviation definitions for Eq. (3.12).<sup>2</sup>

Name	Definition	Name	Definition
$U_j$	$\frac{1}{2}\Lambda_j \cdot \left( \nabla \rho_j - \frac{a}{\gamma R} \nabla s + \frac{a}{\gamma R} \sum_{i=1}^{N_c} Q_i \nabla y_i + c_{12} \nabla b \right)$	$V_u$	$\mathbf{v}_m \cdot \mathbf{n}$
$U_5$	$\frac{1}{2}\mathbf{v} \cdot \left( \frac{\nabla b}{c_1} - \frac{a}{\gamma R} \nabla s + \frac{a}{\gamma R} \sum_{i=1}^{N_c} Q_i \nabla y_i \right)$	$V_v$	$\mathbf{v}_m \cdot \boldsymbol{\tau}$
$U_6$	$\mathbf{v} \cdot \nabla s$	$V'_b$	$V_b + \frac{a}{\gamma R} \sum_{i=1}^{N_c} Q_i V_{y_i}$
$U_{7,i}$	$\mathbf{v} \cdot \nabla y_i$		

and, similarly, by subtracting the second of Eqs. (3.9b) from the first, one obtains:

$$\begin{aligned}
 v_t + \frac{1}{2}\Lambda_3 \cdot \left( \nabla \rho_3 - \frac{a}{\gamma R} \nabla s + \frac{a}{\gamma R} \sum_{i=1}^{N_c} Q_i \nabla y_i + c_{12} \nabla b \right) + \\
 - \frac{1}{2}\Lambda_4 \cdot \left( \nabla \rho_4 - \frac{a}{\gamma R} \nabla s + \frac{a}{\gamma R} \sum_{i=1}^{N_c} Q_i \nabla y_i + c_{12} \nabla b \right) + B u = \mathbf{v}_m \cdot \boldsymbol{\tau}
 \end{aligned} \tag{3.11b}$$

Finally, the first ( $N_c - 1$  equations) and the fourth of Eqs. (3.1) are needed to close the system. Note that these equations, and Eqs. (3.10)-(3.11) are all expressed in gradient form. The importance of this formulation resides in the way all these equations can be discretized. In fact, by using the abbreviations in Table 3.6, the system can be expressed in a more compact manner:

---

<sup>2</sup> $j = 1, \dots, 4$

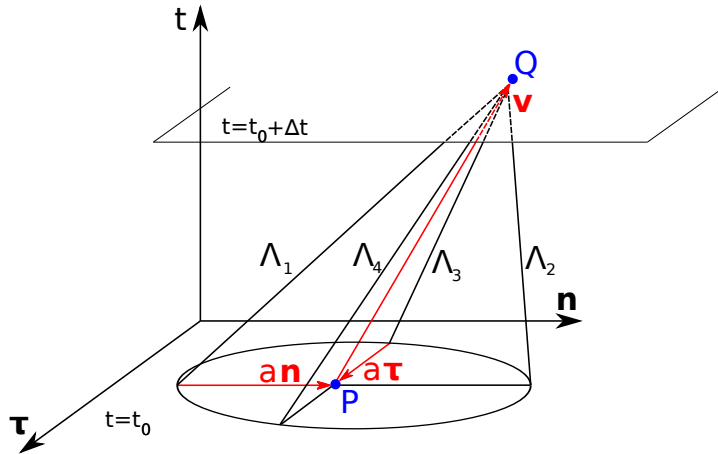


**Figure 3.1** – Mach conoid identifying the dependency domain of the point Q.

$$\left\{ \begin{array}{ll} y_{i,t} = -U_{7,i} + V_{y_i} & i = 1, \dots, N_c - 1 \\ b_t = c_1 \left( \frac{a}{\gamma R} s_t - \frac{a}{\gamma R} \sum_{i=1}^{N_c} Q_i y_{i,t} - \sum_{j=1}^4 U_j + 2U_5 - F + V'_b \right) \\ u_t = -U_1 + U_2 + B v + V_u \\ v_t = -U_3 + U_4 - B u + V_v \\ s_t = -U_6 + V_s \end{array} \right. \quad (3.12)$$

In this new system, local convective terms such as  $F$ ,  $B u$  e  $B v$ , and terms such as  $V'_b$ ,  $V_u$ ,  $V_v$ ,  $V_s$  and  $V_{y_i}$ , containing both diffusive and source terms, are present. All other terms containing space derivatives express differentiations of generalized Riemann variables along directions which lie on the surface of a Mach conoid or along the direction of  $v$  itself. Let a Mach conoid be drawn backwards in time from a generic point, Q, to be evaluated at time  $t + \Delta t$  (Fig. 3.1). Projecting

the conoid onto the physical plane at time  $t$ , a circle is the intersection of the conoid with the physical plane. The radius of the circle is the speed of sound and its center,  $P$ , is the origin of the  $\mathbf{v}$  vector ending at  $Q$ . According to the choice of  $\mathbf{n}$  and  $\tau$ , four points are identified on the circle as the origin of the lines defined by the vectors  $\Lambda_i$ . It is thus easy to identify from which computational cell the information proceeds, which is carried along a line parallel to one of the  $\Lambda_i$ . Each one of the terms contributing to the equations, thus, can be discretized using information related to its domain of dependence.

## 3.4 Solving technique

The technique adopted to numerically solve the two-dimensional, viscous, reacting, unsteady flow model is described here. To integrate the governing equations a finite-difference approach is used. The first step to be taken is the choice of a computational grid. Obviously, the grid has to be well adapted to the geometry of the rigid bodies in the problem: grids must be so chosen that any rigid body contour is described by a grid line. Experience dictates that more accurate results are obtained if the computational grid is orthogonal so that only orthogonal grids are used here. Moreover, the finite differencing is easier and more accurate if an equally-spaced Cartesian frame is adopted. Therefore, a curvilinear orthogonal grid in the physical space (obtained with conformal mapping) is transformed to a rectangular grid in the transformed space (Fig. 3.2) [66]. Because the finite difference calculations are performed on this rectangular grid, it is also called the computational space. Grid created in this way are called structured grids. Since it is often useful to have more nodes in some region of the flowfield (near walls), a first transformation (stretching) of the computational plane is performed: the computational grid is transformed to a new grid which is still Cartesian but no

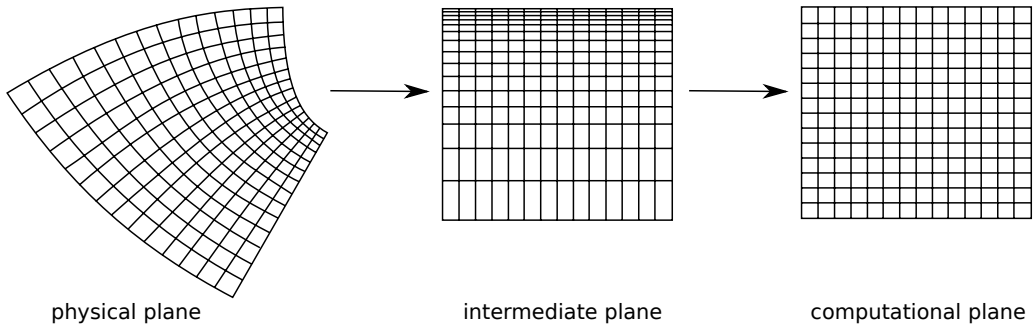


**Figure 3.2** – Plane transformations.

longer equally-spaced (clustering). This intermediate grid is finally transformed to the curvilinear grid in the physical space.

### 3.4.1 Equations in the computational plane

It is now necessary to transform the derivatives expressed in the physical plane into derivatives expressed in the computational plane (Fig. 3.2). The computational ( $\hat{x}, \hat{y}$ ) , intermediate ( $\zeta, \eta$ ), and physical planes ( $x, y$ ) can be defined by a complex variable:

$$\hat{z} = \hat{x} + i \hat{y}$$

$$\zeta = \xi + i \eta$$

$$z = x + i y$$

In the computational plane the flowfield is a box  $[0, 1] \times [0, 1]$  discretized with an equally-spaced Cartesian grid. The intermediate plane  $\zeta$  is obtained from the computational plane by stretching the coordinates  $\hat{x}$  and  $\hat{y}$ . The new grid is still Cartesian but no more equally-spaced. This stretching transformation is particularly easy since the transformation functions of the two coordinates are decoupled. To obtain the flowfield in the physical plane, where the grid is curvilinear orthogonal in order to be well adapted to the geometry of the body,

the transformation function  $z = z(\zeta)$  (where  $z$  is an analytical function) is needed. In two-dimensional problems a powerful tool to create orthogonal grids around difficult bodies is represented by conformal mapping [67, 68]. For an orthogonal frame obtained by conformal mapping of the intermediate frame  $\zeta$  onto the physical plane  $z$ , using the notations of [69]:

$$g = \frac{d\zeta}{dz} = Ge^{-i\alpha} = \xi_x + i\eta_x = -i\xi_y + \eta_y$$

$$\phi = \phi_1 + i\phi_2 = \frac{d \log g}{d\zeta} = \frac{G_\xi}{G} - i\alpha_\xi = -i\frac{G_\eta}{G} - \alpha_\eta = -\alpha_\eta - i\alpha_\xi$$

where  $\alpha$  is the same variable used in Eqs. (3.5) and (3.6), that is the angle between the two frames.

Now, noting that for a scalar  $\psi$  the following relation holds:

$$\nabla\psi = \psi_x \mathbf{i} + \psi_y \mathbf{j} = G(\psi_\xi \mathbf{n} + \psi_\eta \boldsymbol{\tau})$$

where  $\mathbf{n}$  and  $\boldsymbol{\tau}$  are now unit vectors along the coordinate lines  $\eta$  and  $\xi$ , respectively, the abbreviations in Table 3.6 and part of that in Table 3.5 can be expressed in terms of derivatives in the intermediate  $\zeta$  plane (Table 3.7). Then, noting that:

$$\psi_\xi = \psi_{\hat{x}} \hat{x}_\xi, \quad \psi_\eta = \psi_{\hat{y}} \hat{y}_\eta$$

and defining the quantities:

$$\lambda_1^x = G\hat{x}_\xi(u + a), \quad \lambda_2^x = G\hat{x}_\xi(u - a), \quad \lambda_3^x = G\hat{x}_\xi u$$

$$\lambda_1^y = G\hat{y}_\eta(v + a), \quad \lambda_2^y = G\hat{y}_\eta(v - a), \quad \lambda_3^y = G\hat{y}_\eta v$$

**Table 3.7** – Abbreviation definitions in the intermediate plane ( $\zeta$ ).

Name	Definition
$U_j$	$U'_j + U''_j \quad (j = 1, \dots, 5)$
$U'_1$	$\frac{G}{2}(u + a) \left[ (b + u)_\xi - \frac{a}{\gamma R} s_\xi + \frac{a}{\gamma R} \sum_{i=1}^{N_c} Q_i y_{i,\xi} + c_{12} b_\xi \right]$
$U''_1$	$\frac{G}{2} v \left[ (b + u)_\eta - \frac{a}{\gamma R} s_\eta + \frac{a}{\gamma R} \sum_{i=1}^{N_c} Q_i y_{i,\eta} + c_{12} b_\eta \right]$
$U'_2$	$\frac{G}{2}(u - a) \left[ (b - u)_\xi - \frac{a}{\gamma R} s_\xi + \frac{a}{\gamma R} \sum_{i=1}^{N_c} Q_i y_{i,\xi} + c_{12} b_\xi \right]$
$U''_2$	$\frac{G}{2} v \left[ (b - u)_\eta - \frac{a}{\gamma R} s_\eta + \frac{a}{\gamma R} \sum_{i=1}^{N_c} Q_i y_{i,\eta} + c_{12} b_\eta \right]$
$U'_3$	$\frac{G}{2} u \left[ (b + v)_\xi - \frac{a}{\gamma R} s_\xi + \frac{a}{\gamma R} \sum_{i=1}^{N_c} Q_i y_{i,\xi} + c_{12} b_\xi \right]$
$U''_3$	$\frac{G}{2}(v + a) \left[ (b + v)_\eta - \frac{a}{\gamma R} s_\eta + \frac{a}{\gamma R} \sum_{i=1}^{N_c} Q_i y_{i,\eta} + c_{12} b_\eta \right]$
$U'_4$	$\frac{G}{2} u \left[ (b - v)_\xi - \frac{a}{\gamma R} s_\xi + \frac{a}{\gamma R} \sum_{i=1}^{N_c} Q_i y_{i,\xi} + c_{12} b_\xi \right]$
$U''_4$	$\frac{G}{2}(v - a) \left[ (b - v)_\eta - \frac{a}{\gamma R} s_\eta + \frac{a}{\gamma R} \sum_{i=1}^{N_c} Q_i y_{i,\eta} + c_{12} b_\eta \right]$
$U'_5$	$\frac{G}{2} u \left[ b_\xi - \frac{a}{\gamma R} s_\xi + \frac{a}{\gamma R} \sum_{i=1}^{N_c} Q_i y_{i,\xi} + c_{12} b_\xi \right]$
$U''_5$	$\frac{G}{2} v \left[ b_\eta - \frac{a}{\gamma R} s_\eta + \frac{a}{\gamma R} \sum_{i=1}^{N_c} Q_i y_{i,\eta} + c_{12} b_\eta \right]$
$U_6$	$G(u s_\xi + v s_\eta)$
$U_{7,i}$	$G(u y_{i,\xi} + v y_{i,\eta}) \quad (i = 1, \dots, N_c - 1)$
$B$	$G(u \alpha_\xi + v \alpha_\eta)$
$F$	$-a G(v \alpha_\xi - u \alpha_\eta)$

and

$$R_1^x = b + u, \quad R_2^x = b - u$$

$$R_1^y = b + v, \quad R_2^y = b - v$$

the derivatives expressed in the intermediate plane  $\zeta = (\xi, \eta)$  in Table 3.7 can be finally transformed into derivatives expressed in the computational plane  $\hat{z} = (\hat{x}, \hat{y})$  (Table 3.8).

Finally, expressing in each equation the terms containing the same  $\lambda_j^{x,y}$  ( $j = 1, \dots, 3$ ), the following quantities can be defined:

$$\begin{aligned} f_1^x &= -\frac{\lambda_1^x}{2} \left[ (R_1^x)_{\hat{x}} - v \alpha_{\hat{x}} - \frac{a}{\gamma R} s_{\hat{x}} + \frac{a}{\gamma R} \sum_{i=1}^{N_c} Q_i y_{i,\hat{x}} + c_{12} b_{\hat{x}} \right] \\ f_2^x &= -\frac{\lambda_2^x}{2} \left[ (R_2^x)_{\hat{x}} + v \alpha_{\hat{x}} - \frac{a}{\gamma R} s_{\hat{x}} + \frac{a}{\gamma R} \sum_{i=1}^{N_c} Q_i y_{i,\hat{x}} + c_{12} b_{\hat{x}} \right] \\ f_3^x &= -\lambda_3^x (v_{\hat{x}} + u \alpha_{\hat{x}}) \\ f_4^x &= -\lambda_3^x s_{\hat{x}} \\ f_{5,i}^x &= -\lambda_3^x y_{i,\hat{x}}, \quad i = 1, \dots, N_c - 1 \end{aligned} \tag{3.13a}$$

**Table 3.8** – Abbreviation definitions in the computational plane ( $\hat{z}$ ).

Name	Definition
$U_j$	$U'_j + U''_j \quad (j = 1, \dots, 5)$
$U'_1$	$\frac{1}{2} \lambda_1^x \left[ (R_1^x)_{\hat{x}} - \frac{a}{\gamma R} s_{\hat{x}} + \frac{a}{\gamma R} \sum_{i=1}^{N_c} Q_i y_{i,\hat{x}} + c_{12} b_{\hat{x}} \right]$
$U''_1$	$\frac{1}{2} \lambda_3^y \left[ (R_1^x)_{\hat{y}} - \frac{a}{\gamma R} s_{\hat{y}} + \frac{a}{\gamma R} \sum_{i=1}^{N_c} Q_i y_{i,\hat{y}} + c_{12} b_{\hat{y}} \right]$
$U'_2$	$\frac{1}{2} \lambda_2^x \left[ (R_2^x)_{\hat{x}} - \frac{a}{\gamma R} s_{\hat{x}} + \frac{a}{\gamma R} \sum_{i=1}^{N_c} Q_i y_{i,\hat{x}} + c_{12} b_{\hat{x}} \right]$
$U''_2$	$\frac{1}{2} \lambda_3^y \left[ (R_2^x)_{\hat{y}} - \frac{a}{\gamma R} s_{\hat{y}} + \frac{a}{\gamma R} \sum_{i=1}^{N_c} Q_i y_{i,\hat{y}} + c_{12} b_{\hat{y}} \right]$
$U'_3$	$\frac{1}{2} \lambda_3^x \left[ (R_1^y)_{\hat{x}} - \frac{a}{\gamma R} s_{\hat{x}} + \frac{a}{\gamma R} \sum_{i=1}^{N_c} Q_i y_{i,\hat{x}} + c_{12} b_{\hat{x}} \right]$
$U''_3$	$\frac{1}{2} \lambda_1^y \left[ (R_1^y)_{\hat{y}} - \frac{a}{\gamma R} s_{\hat{y}} + \frac{a}{\gamma R} \sum_{i=1}^{N_c} Q_i y_{i,\hat{y}} + c_{12} b_{\hat{y}} \right]$
$U'_4$	$\frac{1}{2} \lambda_3^x \left[ (R_2^y)_{\hat{x}} - \frac{a}{\gamma R} s_{\hat{x}} + \frac{a}{\gamma R} \sum_{i=1}^{N_c} Q_i y_{i,\hat{x}} + c_{12} b_{\hat{x}} \right]$
$U''_4$	$\frac{1}{2} \lambda_2^y \left[ (R_2^y)_{\hat{y}} - \frac{a}{\gamma R} s_{\hat{y}} + \frac{a}{\gamma R} \sum_{i=1}^{N_c} Q_i y_{i,\hat{y}} + c_{12} b_{\hat{y}} \right]$
$U'_5$	$\frac{1}{2} \lambda_3^x \left[ \left( \frac{R_1^y + R_2^y}{2} \right)_{\hat{x}} - \frac{a}{\gamma R} s_{\hat{x}} + \frac{a}{\gamma R} \sum_{i=1}^{N_c} Q_i y_{i,\hat{x}} + c_{12} b_{\hat{x}} \right]$
$U''_5$	$\frac{1}{2} \lambda_3^y \left[ \left( \frac{R_1^x + R_2^x}{2} \right)_{\hat{y}} - \frac{a}{\gamma R} s_{\hat{y}} + \frac{a}{\gamma R} \sum_{i=1}^{N_c} Q_i y_{i,\hat{y}} + c_{12} b_{\hat{y}} \right]$
$U_6$	$\lambda_3^x s_{\hat{x}} + \lambda_3^y s_{\hat{y}}$
$U_{7,i}$	$\lambda_3^x y_{i,\hat{x}} + \lambda_3^y y_{i,\hat{y}} \quad (i = 1, \dots, N_c - 1)$
$B$	$\lambda_3^x \alpha_{\hat{x}} + \lambda_3^y \alpha_{\hat{y}}$
$F$	$\frac{1}{2} \left[ (\lambda_2^x - \lambda_1^x) v \alpha_{\hat{x}} - (\lambda_2^y - \lambda_1^y) u \alpha_{\hat{y}} \right]$

and

$$\begin{aligned}
f_1^y &= -\frac{\lambda_1^y}{2} \left[ (R_1^y)_{\hat{y}} + u \alpha_{\hat{y}} - \frac{a}{\gamma R} s_{\hat{y}} + \frac{a}{\gamma R} \sum_{i=1}^{N_c} Q_i y_{i,\hat{y}} + c_{12} b_{\hat{y}} \right] \\
f_2^y &= -\frac{\lambda_2^y}{2} \left[ (R_2^y)_{\hat{y}} - u \alpha_{\hat{y}} - \frac{a}{\gamma R} s_{\hat{y}} + \frac{a}{\gamma R} \sum_{i=1}^{N_c} Q_i y_{i,\hat{y}} + c_{12} b_{\hat{y}} \right] \\
f_3^y &= -\lambda_3^y (u_{\hat{y}} - v \alpha_{\hat{y}}) \\
f_4^y &= -\lambda_3^y s_{\hat{y}} \\
f_{5,i}^y &= -\lambda_3^y y_{i,\hat{y}}, \quad i = 1, \dots, N_c - 1
\end{aligned} \tag{3.13b}$$

in which either forward or backward upwind differences, according to the sign of  $\lambda_j^{x,y}$ , can be used to approximate the derivatives. At this point, Eqs. (3.12) can be rewritten in the computational plan as follows:

$$\left\{
\begin{array}{ll}
y_{i,t} = f_{5,i}^x + f_{5,i}^y + V_{y_i}, & i = 1, \dots, N_c - 1 \\
b_t = c_1 \left( f_1^x + f_2^x + f_1^y + f_2^y + V_b' + \frac{a}{\gamma R} s_t - \frac{a}{\gamma R} \sum_{i=1}^{N_c} Q_i y_{i,t} \right) \\
u_t = f_1^x - f_2^x + f_3^y + V_u \\
v_t = f_1^y - f_2^y + f_3^x + V_v \\
s_t = f_4^x + f_4^y + V_s
\end{array}
\right. \tag{3.14}$$

where the non-convective terms are still defined as in Eqs. (3.2) and Table 3.6 and, therefore, the diffusive term derivatives in the physical plan need to be transformed in the computational plan. The derivation of these derivatives is taken from [59] and [61] and, for the sake of brevity is reported in Appendix B.

### 3.4.2 Time-marching finite difference method

An explicit two-level (predictor-corrector) scheme [70, 57], patterned on the well-known MacCormack scheme and having second-order accuracy in both space and time, is adopted. The convective terms are discretized with upwind differences, either forward or backward according to the sign of  $\lambda_j^{x,y}$ . The diffusive terms are discretized explicitly by second-order central differences.

#### Predictor

Let define  $t = k\Delta t$ ,  $\hat{x} = n\Delta \hat{x}$ , and  $\hat{y} = m\Delta \hat{y}$ , then, knowing all the values at level  $k$ , solution at level  $k + 1/2$  (predictor) of a generic variable  $\psi$  is obtained as follows:

$$(\psi)_{nm}^{k+\frac{1}{2}} = (\psi)_{nm}^k + (\psi_t)_{nm}^k \Delta t / 2 \quad (3.15)$$

where the time derivative at level  $k$  can be evaluated using Eqs. (3.14). In the following, only the discretized form of  $f_1^x$  is shown since the other quantities  $f_p^q$  ( $p = 1, 2, 3, 4, 5$ ;  $q = x, y$ ) are discretized following the same logic. The  $f_1^x$  approximation at the first level (predictor) reads:

$$\begin{aligned} (f_1^x)_{nm}^k &= \\ &- \frac{1}{4\Delta \hat{x}} \left[ (\lambda_1^x)_{n'm}^k + (\lambda_1^x)_{n''m}^k \right] \left[ (R_1^x)_{n'm}^k - (R_1^x)_{n''m}^k \right] + \\ &+ \frac{1}{4\Delta \hat{x}} \left[ (\lambda_1^x)_{n'm}^k (v)_{n'm}^k + (\lambda_1^x)_{n''m}^k (v)_{n''m}^k \right] \left[ (\alpha)_{n'm}^k - (\alpha)_{n''m}^k \right] + \\ &+ \frac{1}{4\Delta \hat{x}} \left[ (\lambda_1^x)_{n'm}^k \left( \frac{a}{\gamma R} \right)_{n'm}^k + (\lambda_1^x)_{n''m}^k \left( \frac{a}{\gamma R} \right)_{n''m}^k \right] \left[ (s)_{n'm}^k - (s)_{n''m}^k \right] + \\ &- \frac{1}{4\Delta \hat{x}} \sum_{i=1}^{N_c} \left[ (\lambda_1^x)_{n'm}^k \left( \frac{aQ_i}{\gamma R} \right)_{n'm}^k + (\lambda_1^x)_{n''m}^k \left( \frac{aQ_i}{\gamma R} \right)_{n''m}^k \right] \left[ (y_i)_{n'm}^k - (y_i)_{n''m}^k \right] + \\ &- \frac{1}{4\Delta \hat{x}} \left[ (\lambda_1^x)_{n'm}^k (c_{12})_{n'm}^k + (\lambda_1^x)_{n''m}^k (c_{12})_{n''m}^k \right] \left[ (b)_{n'm}^k - (b)_{n''m}^k \right] \end{aligned} \quad (3.16)$$

where the index  $n'$  and  $n''$  are defined as follows:

$$(\lambda_1^x)_{nm}^k \geq 0 \Rightarrow \begin{cases} n' = n \\ n'' = n - 1 \end{cases} \quad (\lambda_1^x)_{nm}^k < 0 \Rightarrow \begin{cases} n' = n + 1 \\ n'' = n \end{cases}$$

The Eq. (3.16) is obtained from the first of Eqs. (3.13a) discretizing the spatial derivatives with upwind differences, either forward or backward according to the sign of  $(\lambda_1^x)_{nm}^k$ . The terms multiplying the space derivatives are substituted with their average value between the two nodes. A special treatment is needed when the sign of  $(\lambda_1^x)_{nm}^k$  changes between  $n'$  and  $n''$ . In that case the local value of  $(\lambda_1^x)_{nm}^k$  is used.

The diffusive terms, according to their nature, are discretized by central differences [71]. For example, the mass flux vector components  $j_{i1}$  and  $j_{i2}$ , that are the rewritten form in the computational plan of the mass flux vector components (see Appendix B for their derivation), are discretized as follows:

$$\begin{aligned} (j_{i1})_{nm}^k &= -\frac{(G)_{nm}}{Pr_r Re_r Le_r} (\rho)_{nm}^k (\mathcal{D})_{nm}^k (\hat{x}_\xi)_n \frac{(y_i)_{n'm}^k - (y_i)_{n''m}^k}{2\Delta\hat{x}} \\ (j_{i2})_{nm}^k &= -\frac{(G)_{nm}}{Pr_r Re_r Le_r} (\rho)_{nm}^k (\mathcal{D})_{nm}^k (\hat{y}_\eta)_m \frac{(y_i)_{nm'}^k - (y_i)_{nm''}^k}{2\Delta\hat{y}} \end{aligned}$$

and the divergence of the mass flux vector  $\mathbf{j}_i$  is:

$$\begin{aligned} (\nabla \cdot \mathbf{j}_i)_{nm}^k &= (G)_{nm} \left[ (\hat{x}_\xi)_n \frac{(j_{i1})_{n'm}^k - (j_{i1})_{n''m}^k}{2\Delta\hat{x}} - (j_{i1})_{nm}^k (\phi_1)_{nm} + \right. \\ &\quad \left. + (\hat{y}_\eta)_m \frac{(j_{i2})_{nm'}^k - (j_{i2})_{nm''}^k}{2\Delta\hat{y}} + (j_{i2})_{nm}^k (\phi_2)_{nm} \right] \quad (3.17) \end{aligned}$$

with:

$$\begin{cases} n' = n + 1 \\ n'' = n - 1 \end{cases} \quad \begin{cases} m' = m + 1 \\ m'' = m - 1 \end{cases}$$

Similarly, all the other diffusive terms are evaluated following the same logic. The terms which do not contain space derivatives, such as the chemical source term or the added term for axisymmetric problems (see Appendix C), are explicitly evaluated at level  $k$ .

To summarize, the time derivatives at level  $k$  can be evaluated using Eqs. (3.14) and expressions like Eqs. (3.16) and (3.17) for the convective terms and the diffusive terms, respectively. Finally, Eq. (3.15) can be used to obtain the values at level  $k + 1/2$ . Note that since the variable  $b$  is an implicit function of temperature, the value of  $T$  at level  $k + 1/2$  is obtained from the value of  $b$  at the same level using the Newton's iterative procedure. Then, from its knowledge, using the calculated value of  $(y_i)_{nm}^{k+1/2}$ , the ratio of specific heats  $(\gamma)_{nm}^{k+1/2}$  and the frozen speed of sound  $(a)_{nm}^{k+1/2}$  can be evaluated.

### Corrector

Solution at the second level  $k + 1$  (corrector) is obtained using Eq. (3.15), and substituting  $k$  by  $k + 1/2$ :

$$(\psi)_{nm}^{k+1} = (\psi)_{nm}^{k+\frac{1}{2}} + (\psi_t)_{nm}^{k+\frac{1}{2}} \Delta t / 2 \quad (3.18)$$

The time derivatives at level  $k + 1/2$ , needed to obtain the solution at level  $k + 1$ , are obtained from Eqs. (3.14) with  $F_p^q$  instead of  $f_p^q$ . The  $F_p^q$  are defined

as follows:

$$\begin{aligned}(F_p^x)_{nm}^{k+\frac{1}{2}} &= 2(f_p^x)_{nm}^{k+\frac{1}{2}} - (f_p^x)_{n'm}^k \\ (F_p^y)_{nm}^{k+\frac{1}{2}} &= 2(f_p^y)_{nm}^{k+\frac{1}{2}} - (f_p^y)_{nm'}^k\end{aligned}\quad (3.19)$$

where:

$$\begin{aligned}(\lambda_p^x)_{nm}^k > 0 \Rightarrow n' &= n - 1 & (\lambda_p^x)_{nm}^k < 0 \Rightarrow n' &= n + 1 \\ (\lambda_p^y)_{nm}^k > 0 \Rightarrow m' &= m - 1 & (\lambda_p^y)_{nm}^k < 0 \Rightarrow m' &= n + 1\end{aligned}$$

Consequently, the diffusive terms are evaluated with expressions like Eq. (3.17) with  $k + 1/2$  instead of  $k$ . In the discretized form of the equations, the metric terms are also present:  $(G)_{nm}$ ,  $(\alpha)_{nm}$ ,  $(\phi_1)_{nm}$ , and  $(\phi_2)_{nm}$ . Their expression in discrete form can be found in [59].

Thanks to Eq. (3.19), the technique is second-order accurate both in space and time even if two-nodes finite differences are being used. The time step  $\Delta t$  is determined from the CFL (Courant-Friedrick-Lowy) condition with a special correction for the viscous case. The time step is evaluated as follows:

$$\Delta t_e = \frac{c_s}{\hat{\lambda}_{max}}, \quad \hat{\lambda}_{max} = \max(\lambda_i^x \Delta \hat{x}, \lambda_i^y \Delta \hat{y}), \quad i = 1, \dots, 3 \quad (3.20)$$

where  $c_s$  is the Courant number of the scheme, limited to 2 as shown in [72] (a typical value is between 0.5 and 2.0). For viscous flows the stability analysis is more complex, and the following expression is used [73]:

$$\Delta t_v = \frac{c_s}{\tilde{\lambda}_{max}}, \quad \tilde{\lambda}_{max} = \max\left(\frac{8\Delta x^2}{Re_r}, \frac{\Delta y^2}{Re_r}\right) \quad (3.21)$$

where  $Re_r$  is the reference Reynolds number. The local time step  $\Delta t$  is therefore

evaluated as the smallest among Eqs. (3.20) and (3.21):

$$\Delta t = \min(\Delta t_e, \Delta t_v) \quad (3.22)$$

For transient problems, the time step must be the same everywhere and therefore the smallest  $\Delta t$  evaluated in the flowfield is used for every node. If steady-state solutions are sought, a way of reducing the computational time consists of using, for each node, the maximum time step permitted by the CFL conditions. A local time step, different for each node, is therefore used to speed-up convergence to the steady-state solution.

## 3.5 Boundary conditions

An appealing technique for specifying boundary conditions for hyperbolic systems is to use relations based on characteristic lines, i.e., on the analysis of the different waves crossing the boundary. It is well known that the Navier-Stokes equations are not hyperbolic as the addition of viscous terms changes the mathematical nature of the system by increasing its order. However, Navier-Stokes equations certainly propagate waves like Euler equations do and, from a physical point of view, Euler boundary conditions appear as first-order candidates to treat Navier-Stokes boundary conditions. However, Navier-Stokes equations require more boundary conditions than Euler equations. To build Navier-Stokes boundary conditions, the approach used here is to take those corresponding to Euler boundary conditions (the inviscid conditions) and to supply additional relations (the viscous conditions) which refer to viscous effects. The term viscous is used here to describe all diffusion processes which are specific to Navier-Stokes, i.e., viscous dissipation, thermal diffusion, species diffusion, etc. These additional conditions must have a negligible effect when the viscosity goes to zero and their

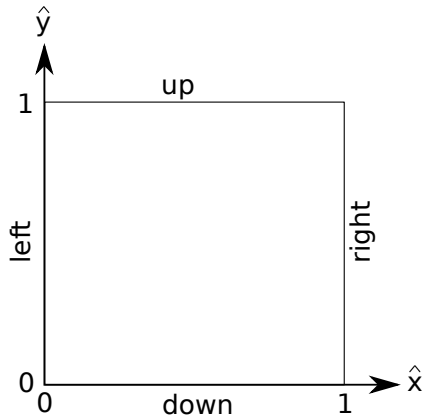


**Figure 3.3 – Computational plan and boundary definitions.**

implementation is not done at the same level as the inviscid conditions. The viscous conditions are used only to compute the viscous terms in the conservation equations at the boundary.

Boundary conditions must be applied at the four boundaries of the two-dimensional computational plane, which is a box  $[0, 1] \times [0, 1]$  (Fig. 3.3):

- Inflow:  $\hat{x} = 0$  (left)
- Outflow:  $\hat{x} = 1$  (right)
- Lower wall:  $\hat{y} = 0$  (down)
- Upper wall:  $\hat{y} = 1$  (up)

### 3.5.1 Inflow and outflow conditions

Both Eqs. (3.15) and (3.18), in addition to local terms, contain terms (the  $f_p^q$ ) which express physical contributions from one side or the other. Terms which

**Table 3.9** – Unknown signals for inflow and outflow boundary conditions at the left boundary ( $\hat{x} = 0$ ).

Condition	$\lambda_1^x$	$\lambda_2^x$	$\lambda_3^x$	Unknowns <sup>3</sup>	Unknown number
Supersonic inflow	<b>&gt;0</b>	<b>&gt;0</b>	<b>&gt;0</b>	$f_1^x, f_2^x, f_3^x, f_4^x, f_{5,i}^x$	$4 + (N_c - 1)$
Subsonic inflow	<b>&gt;0</b>	$< 0$	<b>&gt;0</b>	$f_1^x, f_3^x, f_4^x, f_{5,i}^x$	$3 + (N_c - 1)$
Supersonic outflow	$< 0$	$< 0$	$< 0$	---	0
Subsonic outflow	<b>&gt;0</b>	$< 0$	$< 0$	$f_1^x$	1

express contribution from outside, cannot be computed from inside the computational region and, therefore, need to be determined using some appropriate, model of the outer world. The inflow or outflow conditions are assigned to the left and right boundaries ( $\hat{x} = 0$  and  $\hat{x} = 1$ ). To assign inflow (or outflow) boundary conditions the first step is to identify which terms (corresponding to space derivatives in the  $\hat{x}$  direction) express the unknown contributions from outside, either at the left boundary, or at the right boundary. These unknowns correspond to the positive and the negative  $\lambda_j^x$  ( $j = 1, \dots, 3$ ) at the left and right boundaries, respectively. In Table 3.9 the three  $\lambda_j^x$  are shown at the left boundary for each possible inflow and outflow flow regime, the  $\lambda_j^x$  values coming from outside the computational region (positive values) are reported in bold face and, accordingly to that  $\lambda_j^x$  values, the corresponding unknowns  $f_p^x$  are listed. In the following the four conditions described in Table 3.9 are discussed for the left boundary ( $\hat{x} = 0$ ) since their extension to the right one can be easily derived.

### Supersonic inflow

In this case the condition  $u > a$  holds, as seen in Table 3.9 the corresponding unknowns are  $4 + (N_c - 1)$ . Therefore,  $4 + (N_c - 1)$  boundary conditions are

---

<sup>3</sup> $i = 1, \dots, N_c - 1$

assigned. A steady flow at the initial condition can be assumed:

$$\begin{cases} b_t = 0 \\ u_t = 0 \\ v_t = 0 \\ s_t = 0 \\ y_{i,t} = 0, \quad i = 1, \dots, N_c - 1 \end{cases} \quad (3.23)$$

If a planar flow and uniform in the  $\hat{y}$  direction is assigned, the simple condition  $f_1^x = f_2^x = f_3^x = f_4^x = f_{5,i}^x = 0$  is obtained by substituting Eq. (3.23) into Eqs. (3.14). If this is not the case, the unknown terms can be obtained in the same manner after the space derivatives in the  $\hat{y}$  direction have been evaluated.

### Subsonic inflow

In this case the condition  $a > u > 0$  holds, as seen in Table 3.9 the corresponding unknowns are  $3 + (N_c - 1)$  since the  $f_2^x$  can be correctly evaluated from inside the computational region. Assuming that the incoming flow is directed along the  $\hat{y} = cost$  lines and has defined values of total temperature, total pressure and species mass fractions, the conditions can be expressed in terms of time derivatives and the equation of state can be used to rewrite them in terms of  $b, u, v$  and  $s$ :

$$\begin{cases} (T_0)_t = \mathcal{F}(t) \\ (p_0)_t = \mathcal{G}(t) \\ y_{i,t} = \mathcal{Y}_i(t) \\ V_t = 0 \end{cases} \Rightarrow \begin{cases} (h_0)_t = Fbb_t + uu_t = \hat{\mathcal{F}}(t) \\ s_t = \hat{\mathcal{G}}(t) \\ y_{i,t} = \mathcal{Y}_i(t) \\ v_t = 0 \end{cases} \quad (3.24)$$

where

$$F = \frac{(\gamma - 1)/2}{\left[ 1 - \frac{\gamma + 1}{\gamma - 1} \frac{T \partial \gamma}{\gamma \partial T} \right]}$$

and where, assuming that  $\alpha = 0$  at the entry boundary, the relation  $v = V$  holds. As for the case of supersonic inflow, the unknowns signals can be evaluated once the value of the derivatives in the  $\hat{y}$  direction have been given or set to zero assuming uniformity in  $\hat{y}$  direction. Moreover, if steady flow at the initial condition is assumed,  $\mathcal{F}(t)$ ,  $\mathcal{G}(t)$ , and  $\mathcal{Y}_i(t)$  are set to zero in Eqs. (3.24).

### Supersonic outflow

In this case  $u < -a$  holds. As shown in Table 3.9 all the  $\lambda_j^x$  are all negative, that for the left boundary means that all the signals come from inside the computational region and therefore no boundary conditions are needed.

### Subsonic outflow

In this case  $-a < u < 0$  holds and the only unknown signal is  $f_1^x$  (Table 3.9). Therefore, a single condition is needed and a series of different choices can be done to evaluate the unknown signal.

#### Assigned pressure

The time derivative of the pressure can be assigned:  $p_t = \mathcal{F}(t)$ . This condition can be expressed in terms of  $b_t$ ,  $s_t$ , and  $y_{i,t}$  by means of the the expression of entropy and the equation of state:

$$\mathcal{F}(b_t, s_t, y_{i,t}) = \hat{\mathcal{F}}(t) \quad (3.25)$$

and, using the second of Eqs. (3.14),  $f_1^x$  can be easily evaluated from known quantities. If a constant pressure with time is assumed, then  $\mathcal{F}(t)$  is set to zero.

### Non-reflecting (radiative) condition

In this case, the signals coming from the outside are assumed to be zero [74] and the unknown signal is simply:

$$f_1^x = 0 \quad (3.26)$$

### Extrapolation

The two previous condition can be applied when there is a knowledge of the physical behavior of the investigated system at the boundary. Sometimes, when no data on the physical conditions are known for the boundary, a simpler boundary condition can be assumed considering that the boundary values of all the variables ( $b$ ,  $u$ ,  $v$ ,  $s$ , and  $y_i$ ) are simply the extrapolation of the corresponding values from inside the computational region. A typical case for which this condition applies is the exit condition for the subsonic boundary-layer of a supersonic flow.

### 3.5.2 Wall conditions

In assigning the wall conditions the nature of the  $\lambda$ -scheme can help and the boundary condition for the Navier-Stokes equations can be built by suppling additional relation to the Euler conditions that can be derived by analyzing the signal coming from outside the computational region as it has been done for the inflow/outflow conditions. These signals, that corresponds to the positive  $\lambda_j^y$  for the lower wall, and to the negative  $\lambda_j^y$  for the upper wall, are analyzed in the following for the lower wall but can be easily derived for the upper wall using the same logic. Obviously, in case of “non-conventional” computational domain, the wall condition can be assigned either to the left or right boundary as well as the inflow/outflow conditions can be assigned to either the upper or the lower wall.

---

<sup>4</sup> $i = 1, \dots, N_c - 1$

**Table 3.10** – Unknown signals for the wall condition at the lower boundary ( $\hat{y} = 0$ ).

Condition	$\lambda_1^y$	$\lambda_2^y$	$\lambda_3^y$	Unknowns <sup>4</sup>	Unknown number
Inviscid wall	$>0$	$<0$	$=0$	$f_1^y, f_3^y, f_4^y, f_{5,i}^y$	$3 + (N_c - 1)$

### Inviscid wall

To apply the described procedure, the first step to be done to build up the wall boundary condition for the Navier-Stokes equations is to derive the boundary condition for the particular case of the inviscid wall (Euler condition). For a rigid wall at steady-state condition, the normal velocity and its time derivative must be zero:  $v = v_t = 0$ . The  $\lambda_j^y$  values and the correspondent unknowns for this case are reported in Table 3.10. The value of  $f_1^y$  can be derived from the fourth of Eqs. (3.14) by using the condition on the normal velocity  $v_t = 0$ :

$$f_1^y = f_2^y - f_3^x \quad (3.27)$$

The other unknown signals, are easily derived by imposing  $\lambda_3^y = 0$ :

$$f_3^y = f_4^y = f_{5,i}^y = 0 \quad (3.28)$$

### Viscous wall (non-reacting)

An additional condition needs to be added to the inviscid wall condition in order to build up the final wall boundary condition for the Navier-Stokes equations. The additional condition that must be added to the flow tangency condition ( $v = 0$ ) is the typical no-slip condition at the wall:  $u = 0$ . Because of the existence of friction, in fact, the flow can no longer slip at the wall. Moreover, a

zero-pressure gradient at the wall is enforced:

$$\left. \frac{\partial p}{\partial y} \right|_w = 0 \quad (3.29)$$

In addition, because of energy transport by thermal conduction, an additional boundary condition involving temperature at the wall is needed. Different cases can be considered [37].

#### Assigned wall temperature

If the temperature distribution along the surface is known (i.e. from experimental values) the following boundary condition can be enforced:

$$T = T_w(\hat{x}) \quad (3.30)$$

where  $T_w(\hat{x})$  denotes the specified wall temperature along the surface (the  $\hat{y} = 0$  line in the computational plane). If a single constant value of the surface temperature is assigned, the boundary condition corresponds to that of isothermal wall.

#### Heat-transfer wall boundary condition

$$q_w = -k \left. \frac{\partial T}{\partial y} \right|_w \quad (3.31)$$

where  $q_w$  is the heat transfer (energy per second per unit area) into or out of the wall, and  $(\partial T / \partial y)_w$  is the normal temperature gradient existing in the gas immediately at the wall. In general, the wall heat transfer (and hence the wall-temperature gradient) are unknowns of the problem, and, therefore, in the most general case this boundary condition must be matched to a separate heat-conduction analysis describing the heat distribution within the surface material itself, and both the flow problem and the surface material problem must be solved

in a coupled way.

### Adiabatic wall

A special case of the above condition is the adiabatic wall condition, wherein by definition the heat transfer to the wall is zero and reads:

$$\left. \frac{\partial T}{\partial y} \right|_w = 0 \quad (3.32)$$

The resulting wall temperature, which comes out as part of the solution, is defined as the adiabatic wall temperature  $T_{aw}$ .

Although the choice of an appropriate boundary condition for temperature at the wall appears somewhat open-ended from the preceding discussion, the majority of high-speed viscous flow calculations assume one of the two extremes, that is, they either treat a uniform, constant-temperature wall or an adiabatic wall. However, for a detailed and accurate solution of many practical problems, a heat-transfer wall boundary condition must be employed along with a coupled solution of the heat-conduction problem in the surface material itself, or further assumptions need to be done in order to correctly evaluate the wall convective heat flux. When dealing with ablative materials, the use of the surface balances (Section 2.3) and of the steady-state ablation approximation (Section 2.2.2), allow the evaluation of the wall convective heat flux when a suitable ablation model is adopted. The detailed description of the ablative boundary condition will be the subject of discussion in the next two chapters.

### **Viscous wall (reacting)**

As for the non-reacting viscous wall, the standard, no-slip boundary conditions on velocity at the wall ( $u = 0$ ) hold for a chemically reacting viscous flow as well. For a constant-temperature wall with known temperature  $T_w$ , the particular

isothermal case of the boundary condition of assigned temperature holds as well. Differently, for an adiabatic wall, the diffusive heat flux generated by the species concentration gradient has to be accounted for, and Eq. (3.32) is substituted by:

$$\frac{\partial T}{\partial y} \Big|_w + \sum_{i=1}^{N_c} h_{iw} \rho \mathcal{D}_{im} \frac{\partial y_i}{\partial y} \Big|_w = 0 \quad (3.33)$$

where it can be noted that in a chemically reacting flow for an adiabatic wall the normal temperature gradient is not necessarily zero. Moreover, since the mass fractions  $y_i$  are dependent variables a boundary condition is needed as well as for  $u$ ,  $v$ , and  $T$  already discussed.

#### Fully-catalytic wall

When diatomic molecules are considered, this means that all atoms diffusing to the wall are recombined to form homogeneous, neutral diatoms. The boundary condition is simply the following:

$$y_{A_w} = 0 \quad (3.34)$$

where  $y_{A_w}$  is the mass fraction of atomic species at the surface. Using this model the atoms are imposed to recombine irrespective of the mass fraction that would be allowed to exist at local chemical equilibrium conditions (pressure and temperature at the wall).

#### Equilibrium catalytic wall

An equilibrium catalytic wall is one at which chemical reactions are catalyzed at an infinite rate, that is, the mass fractions at the wall are at their local equilibrium values at the local pressure and temperature at the wall. The boundary condition is simply as follows:

$$y_{i_w} = y_{i_{eq}} \quad (3.35)$$

where  $y_{i_{eq}}$  is the equilibrium mass fraction value of the  $i^{th}$  species at the wall pressure and temperature. Note that, if the wall temperature is sufficiently low, the equilibrium value of  $y_{A_w}$  is essentially zero. In this case the fully catalytic and the equilibrium catalytic wall conditions are exactly the same.

#### Partially catalytic wall

A partially catalytic wall is one at which chemical reactions are catalyzed at a finite rate. Let  $\dot{w}_c$  denote the catalytic rate at the surface (mass of species  $i$  per second per unit area); it is positive for species  $i$  consumed at the surface and negative for species  $i$  produced at the surface. At the surface, the amount of species  $i$  produced or destroyed as a result of the catalytic rate must be balanced by the rate at which species  $i$  is diffused to the surface. Hence:

$$\dot{w}_{c_i} = \rho D_{im} \frac{\partial y_i}{\partial y} \Big|_w \quad (3.36)$$

Equation (3.36) is the boundary condition for a surface with finite-rate catalytic. It dictates the gradient of the mass fraction at the surface.

#### Non-catalytic wall

A non-catalytic wall is one where no recombination occurs at the wall, that is,  $(\dot{w}_c)_i = 0$ . For this case, from (3.36):

$$\left( \frac{\partial y_i}{\partial y} \right)_w = 0 \quad (3.37)$$

The subjects of surface chemical reactions with the flow and the associated boundary conditions just discussed for a catalytic surface are serious matters for the analysis of chemically reacting viscous flows, because they can strongly affect the aerodynamic heating. The more complex case of a pyrolyzing and non-pyrolyzing ablating surface and the associated boundary conditions, that are

the main aims of the present work will be discussed in the next chapters.

### 3.5.3 Error accumulation on the boundaries

Several boundary condition models involve prescribing the invariance of some flow properties. Analytically, considering the generic property  $\psi$ , the two conditions  $\psi(\omega) = \text{const}$  and  $\partial\psi(\omega)/\partial t = 0$  (with  $\omega$  being the state vector), are equivalent. However, being  $\hat{\omega}$  the discrete approximation of  $\omega$ , the discrete time derivative:

$$\frac{\partial\psi(\hat{\omega})}{\partial t} = \frac{\partial\psi(\hat{\omega})}{\partial\omega} \frac{\partial\omega(\hat{\omega})}{\partial t}$$

cannot be considered generally equal to zero. Therefore, for each of the described cases (inflow, outflow, rigid wall), the problem of truncation errors accumulation in time can arise [57]. To avoid this problem, the boundary conditions must be enforced not only on space derivatives but also on variables themselves. For this reason, terms such as  $f_1^y$  in Eq. (3.27), re-evaluated at the boundaries, are used in Eq. (3.14) to update the boundary points themselves.

For example, the velocity in the direction normal to the wall,  $v$ , is originally equal to zero and, theoretically, it should remain equal to zero because Eq. (3.27) assures the vanishing of  $v_t$ . Similarly, for the inflow and outflow boundary conditions,  $T_0$  and  $p_0$  should remain constant because of Eq. (3.24), and  $p$  should remain constant because of Eq. (3.25). In practice, it may not be so because the updating of  $v$ ,  $T_0$ ,  $p_0$  and  $p$  is affected by almost imperceptible truncation errors in time. After a number of steps, one can observe a departure from the original values, producing an increase or decrease in total energy and/or a non-vanishing  $v$  (expressing an addition or loss of mass through the wall). It is necessary, therefore, to reset certain quantities to maintain  $T_0$ ,  $p_0$ ,  $p$  and  $v$  constant at the entry,

exit, and wall boundary, respectively. This can be done easily at the wall because  $v$  is one of the variables of the system while it can be a little more complicated for outflow or inflow conditions, where the conserved parameters  $(T_0, p_0, p)$  are a combination of the dependent variables. For example the task is accomplished, at the entrance, by computing:

$$\begin{cases} (h_0)^{k+1} = h_0 \\ (R_2^x)^{k+1} = (b)^{k+1} - (u)^{k+1} \end{cases} \quad (3.38)$$

Since  $h_0$  is a function of  $T_0$ , the system (3.38) can be used to obtain the corrected values of  $(b)^{k+1}$  and  $(u)^{k+1}$ . From these values and the knowledge of  $p_0$ , the corrected value of  $(s)^{k+1}$  can be obtained.

---

# **Ablation model for non-pyrolyzing carbon-based materials**

As described in the Introduction, pyrolyzing and non-pyrolyzing carbon-based materials share the same ablation mechanism that is the thermochemical oxidation by the gas phase. Therefore, although one of the main objectives of the present work is the development of boundary conditions for carbon-based pyrolyzing materials, the ablation modeling of the non-pyrolyzing ones has to be considered as a needed step. For this reason, the finite-rate ablative boundary condition for carbon-based non-pyrolyzing materials is described in detail in this chapter.

The ablation of a non-pyrolyzing carbon-based ablative material in nozzle environment has been the subject of many investigations. The principal outcomes of the experimental and numerical analysis over the years have been essentially two: the poor contribution of the mechanical erosion to the TPS consumption (especially in the throat region) and the strong effect of aluminum particles in

limiting the oxidizing species concentration in the combustion gases, and thus the thermochemical erosion. Therefore, to develop a macroscopic model able to predict the ablation of carbon-based non-pyrolyzing TPS in complex full-scale nozzle geometries, it is essential to rely on a suitable thermochemical ablation model. During the last years, several ablative boundary conditions of increasing complexity have been implemented in the code described in Chapter 3. Originally, Bianchi [25] developed an isothermal ablative boundary condition capable of modeling the ablation process in the diffusion limited regime and at a defined temperature. By means of the CEA code, the wall composition was calculated at the selected temperature and at different pressures. Once the CFD simulation was run, and the wall pressure (practically not affected by the wall ablation) was evaluated, a surface mass balance was solved to evaluate the solid material mass flow rate and hence the erosion rate. Subsequently, a more complex version of the equilibrium ablative boundary condition was set-up, and the hypothesis of isothermal ablation was taken apart [75]. In this version, the wall compositions were, again, evaluated preemptively but also the wall temperature was used as a parameter in the look-up tables generation. To calculate the additional unknown (the wall temperature) the solution of the surface energy balance, in addition to the surface mass balances, was implemented as a boundary condition. Finally, in the latest version, the surface equilibrium approximation was also discarded, and an accurate finite-rate ablative boundary condition was developed with the aim of evaluating the ablation rate in whatever ablation regime. This last version of the boundary condition is accurately described in the following together with its foremost validation test case.

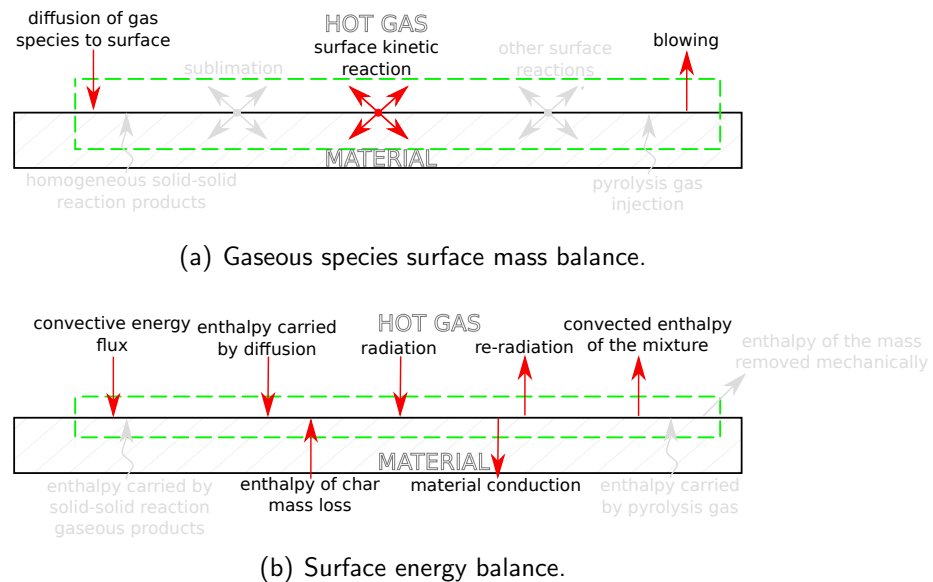


**Figure 4.1 – Surface balances for a carbon-based non-pyrolyzing material.**

## 4.1 Surface balances

Graphite and C-C are the two most common TPS materials used in solid rocket motor nozzles. As described in the Introduction, there are strong differences in the way that these materials withstand to the severe conditions experienced in rocket nozzles. Moreover they differ in both the manufacturing process and final thermo/mechanical characteristics. However, macroscopically and chemically speaking, they can be considered exactly the same material. With this assumption, the following discussion is considered valid for both graphite and C-C that can be generically referred to as non-pyrolyzing carbon-based ablative materials. Figure 4.1 shows the customized surface mass and energy balances for such a kind of material. In this case only the highlighted contributions need to be taken into account. The non-decomposing nature of the material allows to omit the terms related to the gaseous injection coming from the inside of the material. The mechanical removal is not considered because the CFD analysis deals with a

single phase flow and the material strength is sufficient to avoid the consumption by the shear forces. Among the wall source terms, only the one belonging to the surface heterogeneous reactions is active. The other two source terms are neglected since there are no reactions other than ablation and the sublimation has been shown to be not activated in practical rocket-motor environment [26].

With these assumptions the surface species mass balance reads:

$$\rho \mathcal{D}_{im} \frac{\partial y_i}{\partial \eta} \Big|_w + \sum_{r=1}^{N_r} \omega_i^r = (\rho v)_w y_{i_w} \quad i = 1, N_c \quad (4.1)$$

and the surface energy balances is:

$$\begin{aligned} k \frac{\partial T}{\partial \eta} \Big|_w + \sum_{i=1}^{N_c} h_{i_w} \rho \mathcal{D}_{im} \frac{\partial y_i}{\partial \eta} \Big|_w + \dot{q}_{rad_{in}} + \dot{m}_s h_{s_w} = \\ = (\rho v)_w h_w + \dot{q}_{rad_{out}} - \dot{m}_s (h_{s_{in}} - h_{s_w}) \end{aligned} \quad (4.2)$$

where the steady-state conduction has been slightly modified with respect to Eq. (2.54) by taking into account Eq. (2.38), and by considering that there is no difference between the virgin and the char state for a non-pyrolyzing material.<sup>1</sup> By summing Eq. (4.1) over all the species in the mixture, one obtains the overall surface mass balance for this kind of material:

$$\dot{m}_s = \sum_{i=1}^{N_c} \sum_{r=1}^{N_r} \omega_i^r = (\rho v)_w \quad (4.3)$$

## 4.2 Thermochemical ablation model

To account for the heterogeneous surface chemical reaction source term in Eq. (4.1), a finite-rate model has been implemented. These reactions are de-

---

<sup>1</sup> $\rho v_{in} = \rho c_w$

**Table 4.1** – Kinetic data for heterogeneous surface reactions. [19]

Surface reaction	$A_i$	$E_i, \text{ kJ mol}^{-1}$	$b$	$n$
$\text{C}_s + \text{H}_2\text{O} \rightarrow \text{CO} + \text{H}_2$	$4.80 \times 10^5$	288	0.0	0.5
$\text{C}_s + \text{CO}_2 \rightarrow 2\text{CO}$	$9.00 \times 10^3$	285	0.0	0.5
$\text{C}_s + \text{OH} \rightarrow \text{CO} + \text{H}$	$3.61 \times 10^2$	0.0	-0.5	1.0

scribed by the multiple oxidizing species reaction mechanisms (MOS) [19], which is a semi-global heterogeneous reaction mechanism for carbon oxidation consisting of the three reactions listed in Table 4.1. The validity of the approximation of considering only these three principal reactions grounds on the fact that, as it will be shown in the following, other possible oxidizing species such as NO, O, and  $\text{O}_2$  are present in very low concentrations in typical propellant combustion products; for this reason, their erosion contribution can be neglected.

With this mechanism, the rate of consumption of carbon by the generic oxidizing species,  $i = \text{H}_2\text{O}, \text{CO}_2, \text{OH}$ , can be expressed as:

$$\dot{m}_i = \sum_{r=1}^{N_r} \omega_i^r = p_i^n A_i T_w^b \exp(-E_i / \mathcal{R} T_w) \quad (4.4)$$

where  $p_i$  is the partial pressure of the oxidizing species  $i$ ,  $T_w$  is the wall temperature and  $n$  is the overall reaction order of the heterogeneous reaction.  $A_i$  and  $E_i$  are the pre-exponential factor and the activation energy of the heterogeneous reaction, respectively. The kinetic parameters of Eq. (4.4) for the three reactions are taken from [19] and are listed in Table 4.1. Therefore, the total erosion rate of carbon due to the surface heterogeneous reactions can be evaluated as:

$$\dot{m}_s = \dot{m}_{\text{H}_2\text{O}} + \dot{m}_{\text{CO}_2} + \dot{m}_{\text{OH}} = \rho_s \dot{s} \quad (4.5)$$

## 4.3 Numerical procedure

In all the calculations the nozzle is characterized by subsonic inflow boundary conditions describing the combustion gases (total temperature and total pressure are enforced together with the flow direction and chemical equilibrium composition), supersonic outflow, symmetry axis and solid wall.

A typical time step of the algorithm procedure used to calculate the nozzle erosion by means of the surface balances described in Section 4.1 can be summarized as follows:

1. The wall pressure is calculated from the flow field assuming zero-pressure gradient at wall;
2. The mass flow rate  $\dot{m}_i$  for each species  $i$  is computed from Eq. (4.4) using the calculated wall pressure and the wall temperature of the previous step;
3. The total mass flow rate is calculated using Eq.(4.5);
4. The wall temperature is updated by Eq. (4.2) using a Newton's iterative procedure.

At each time step, the wall temperature, the solid mass flow rate, and the wall chemical composition are updated, together with the flow-field solution, until a steady-state condition is reached. The convergence criterion to steady-state is the drop of the residual by five orders of magnitude. It has to be noted that there is no connection between the CFD simulation and a specific material density. The erosion rate evaluation is, in fact, obtained in the post processing by means of Eq. (4.5) using the calculated value of the solid mass flow rate and the density of the material of interest. Therefore, a single numerical simulation can represent different scenarios, depending on the density of the chosen kind of material (pyrolytic graphite, C-C, etc. . . ).

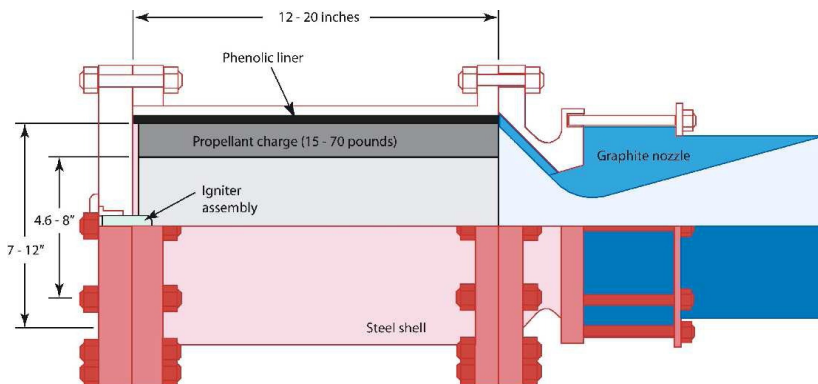


**Figure 4.2 – 70 pounds BATES motor [77].**

## 4.4 Bates motor test

To validate the thermo-chemical ablation model, an experimental test case has been selected and reproduced. Calculated recession rates have been compared with the experimental data from Geisler [76] and Geisler and Beckman [77].

### 4.4.1 Input data

The nozzle geometry employed is the one used in the Ballistic Test and Evaluation System (BATES) rocket motor and sketched in Fig. 4.2. The BATES motor was developed in the early 60s and has become a standard for measuring and comparing solid propellant performance in the United States [77]. The nozzle material is bulk graphite with a density of  $1.83 \text{ g cm}^{-3}$ . Since comprehensive data on the effective nozzle geometry were not available, the geometry shown in Fig 4.3 has been rebuilt on the basis of the main geometric parameters (throat radius, overall dimensions, and divergence angle) reported in [77]. As seen, the adopted grid geometry has been modified with respect to the real nozzle geometry, the conical converging section with an angle of  $45^\circ$  has been substituted by a parabolic curve, which becomes parallel to the nozzle axis at the inlet section so

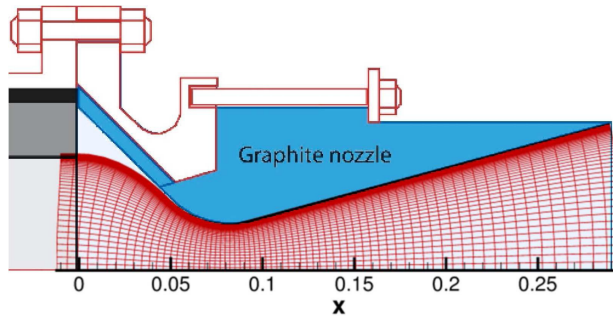


**Figure 4.3 – Adopted nozzle grid.**

that an axial inlet velocity profile can be assigned. However, since the length of the wall is important, because it affects the boundary-layer thickness and hence the heat and mass transfer rate, the total wall length of the parabolic curve as been imposed to match the length of the  $45^\circ$  cone. The computational domain is discretized into  $60 \times 70$  grid points in the axial and radial directions, respectively (Fig. 4.3). In the radial direction, the mesh is clustered near the nozzle surface to ensure a value of  $y^+$  less than 1.0 all along the nozzle length to accurately capture the near-wall phenomena.

The hot exhaust gas flowing in the nozzle consists of the combustion products of typical metallized and non-metallized AP/HTPB (ammonium perchlorate / hydroxyl-terminated polybutadiene) composite propellants. Five different test cases, with wide variations of aluminum content and flame temperature of the propellant exhaust have been selected. The inlet conditions for the CFD simulations, shown in Table 4.2, reproduce exactly the chamber conditions of the experimental test cases. However, since a single-phase treatment is used in the model, all the  $\text{Al}_2\text{O}_3$  present in the combustion products has been assumed to be in the gas phase. Finally, it has to be noted that both the radiative heat flux, from and towards the wall, in Eq. (4.3) have been considered negligible in the present analysis. In fact, the mean chamber pressure has a value comparable with

**Table 4.2** – Input conditions for the five validation test cases [77].

$y_{CO}$	$y_{CO_2}$	$y_{HCl}$	$y_{H_2}$	$y_{H_2O}$	$y_{N_2}$	$y_{Al_2O_3}$	$p_c$ , bar	$T_c$ , K	Al%
0.175	0.04	0.24	0.02	0.145	0.10	0.28	69	3580	15
0.18	0.025	0.23	0.02	0.105	0.10	0.34	69	3655	18
0.20	0.015	0.195	0.02	0.07	0.10	0.40	69	3715	21
0.20	0.005	0.190	0.02	0.045	0.10	0.44	69	3750	24
0.20	0.005	0.190	0.02	0.025	0.10	0.46	69	3745	27

that of a full-scale solid rocket motor and in that applications the radiation is usually one order of magnitude less than convection in that applications [15, 16].

#### 4.4.2 Results and discussion

At first, to ensure that the presented results are grid independent, the CFD solution has been verified by a grid convergence analysis on three grid levels for one of the validation test cases. Three different meshes have been adopted to perform such an analysis. In addition to the  $60 \times 70$  mesh described previously, a doubled and a halved mesh have been generated. The obtained erosion rates are compared in Table 4.3 for three different nozzle locations:  $x = 7.35$  cm (peak erosion rate),  $x = 8.21$  cm (throat section),  $x = 9.58$  cm (beginning of the conical diverging section). The quantitative analysis of solutions obtained on three grid levels confirms that the spatial order of accuracy is close to the formal value of 2. This confirms the asymptotic behavior of the numerical error and thus gives a good confidence on the error estimate. The discrepancy between the throat erosion rate obtained by means of the Richardson extrapolation [73] and the one evaluated with the medium grid ( $60 \times 70$ ) is less than 2%; therefore, the medium grid has been selected for the validation and analysis test cases.

The computed erosion rate distributions along the nozzle length as a function

**Table 4.3** – Erosion rate at three different locations for three different refined meshes [27].

Grid	$\dot{s}$ , mm s <sup>-1</sup> ( $x = 7.35$ cm)	$\dot{s}$ , mm s <sup>-1</sup> ( $x = 8.21$ cm)	$\dot{s}$ , mm s <sup>-1</sup> ( $x = 9.58$ cm)
30×35	0.294022	0.261987	0.167377
60×70	0.301885	0.273677	0.173536
120×140	0.304005	0.277737	0.174986

of the aluminum content of the propellant are plotted, together with the experimental data measured at the throat, in Fig. 4.4. Both, the equilibrium and the finite-rate ablative boundary condition (described previously) have been used by Bianchi [26, 27] to run these simulations and validate the two different ablation models. The erosion rates at the throat computed with the surface equilibrium assumption show an excellent agreement with the experimental data, except for the propellant with the minimum aluminum content. This trend has been explained in [26], noting that the 15% aluminum propellant exhibits a rather low wall temperature (Fig. 4.5), where the influence of chemical kinetics can be important, which would explain the overestimate of the erosion rate computed with the surface equilibrium. For this reason, the results obtained with the finite-rate ablation model are in better agreement with the experimental data for this lower aluminized propellant. Moreover, Fig. 4.5 clearly shows that the erosion predictions with the finite-rate model are exactly like their surface equilibrium counterparts for the higher aluminum content propellants. The finite-rate erosion in the case of 15% aluminum propellants is lower than the corresponding surface equilibrium erosion, resulting in a better agreement with the experimental data. In particular, for the 15% aluminum propellant, the equilibrium model provides a 12% overestimation compared to the 1% underestimation provided

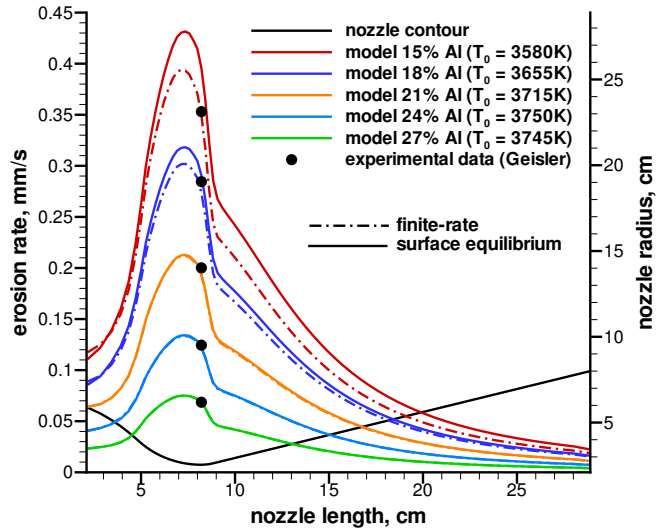


**Figure 4.4 –** Erosion rate distribution for propellants with different aluminum content [27].

by the finite-rate model. The comparison between the experimental and the computed erosion rates at the throat is also reported in Table 4.4 for both the surface equilibrium and the finite-rate model.

The finite-rate ablation model has finally shown a good capability of reproducing the flow/surface interaction in case of carbonaceous non-pyrolyzing ablative materials over a wide range of chamber condition, thus it will be applied with reasonable confidence in the following to calculate the nozzle erosion in case of carbonaceous pyrolyzing ablative materials.

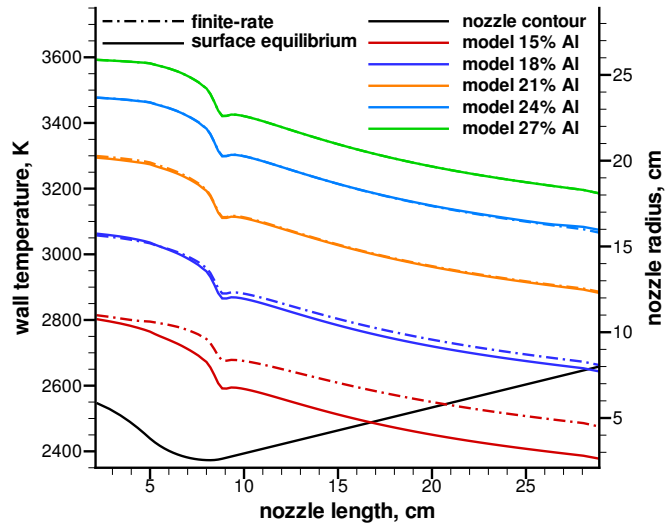


**Figure 4.5** – Wall temperature distribution for propellants with different aluminum content [27].

**Table 4.4** – Erosion rate and percentual error at the throat section using the equilibrium and the finite-rate ablation model.

Al,%	$\dot{s}_{exp}, \text{mm s}^{-1}$	$\dot{s}_{eq}, \text{mm s}^{-1}$ ( <i>error%</i> )	$\dot{s}_{f-r}, \text{mm s}^{-1}$ ( <i>error%</i> )
15	0.3531	0.3958	0.3497
18	0.2845	0.2907	0.2737
21	0.2000	0.1943	0.1926
24	0.1245	0.1226	0.1218
27	0.0686	0.0684	0.0684

---

# Ablation model for pyrolyzing carbon-based materials

The study of pyrolyzing ablative TPS materials requires to take into account the pyrolysis gas injection. In fact, once the pyrolysis gas has been injected into the nozzle flow, it alters the wall gas composition and, in turn, influences the erosion rate. Thus, the pyrolysis gas injection needs to be accurately modeled to correctly predict the gas-surface interaction over such a material. In this chapter carbon-based pyrolyzing materials will be presented and modeled. The material decomposition model and the pyrolysis gas model are presented in the first part of the chapter. Subsequently, the customized surface balances, the ablation model and a validation test case are presented and discussed.

## 5.1 Resin pyrolyzation modeling

The carbon-based pyrolyzing materials are particular pyrolyzing materials whose reinforcing fibers are composed by carbon. However, the following discussion

can be considered valid for a general pyrolyzing material, composed by a resin filler and a reinforcing materials. The resin is the component that undergoes decomposition when is heated, and from its decomposition the pyrolysis gas is generated. Since the resin does not entirely decompose, a certain amount of it remains together with the reinforcing material to form the char. For this reason, many pyrolyzing char-forming materials are represented assuming a three-component model [12]. In such a model, the resin is considered to consist of two decomposing component, the first that totally decomposes (A) and the second, only partially decomposing, having a non-zero final density after the decomposition (B). Finally, the third component (R) represents the reinforcing material that does not undergo decomposition (silica or carbon in the present analysis).

In a general thermal response code that uses a three-component model [12], the instantaneous density of each component can be calculated using the following relation:

$$\frac{\partial \rho_i}{\partial t} = -\beta_i \exp(-E_{a,i}/RT_w) \rho_{0,i} \left( \frac{\rho_i - \rho_{r,i}}{\rho_{0,i}} \right)^{\psi_i}, \quad i = A, B, R \quad (5.1)$$

where the subscripts 0 and *r* indicate the initial and the final density of the component (known from experimental data), respectively, and the pre-exponential factor  $\beta$ , the activation energy  $E_a$  (in  $\text{J mol}^{-1}$ ) and the reaction order  $\psi$  are specific for each of the material components. By means of Eq. (5.1) the instantaneous density of each component can be determined, and the density of the whole composite material can be calculated as:

$$\rho = \Gamma_V(\rho_A + \rho_B) + (1 - \Gamma_V)\rho_R \quad (5.2)$$

being  $\Gamma_V$  the volumetric fraction of the material occupied by the resin, that is

related to the mass fraction of the resin in the material ( $\Gamma_M$ ) by means of the following relation:

$$\Gamma_M = \frac{\Gamma_V (\rho_{0,A} + \rho_{0,B})}{\rho_{0,R} (1 - \Gamma_V) + \Gamma_V (\rho_{0,A} + \rho_{0,B})} \quad (5.3)$$

As described in Section 2.2.2, in the present work a simplified model that relies on the steady-state ablation approximation has been used to manage the solid-side terms that cannot be directly calculated from the CFD simulation. Taking advantage from this hypothesis, further considerations can be made on the decomposition of the material. When the material reaches the steady-state temperature profile, in fact, the density profile of the material does not change with time anymore and each point at a fixed distance from the receding surface shows a constant triplet of component densities. For these reason, the char zone and the pyrolysis zone of the material (see Fig. 1.4(b) in the Introduction) have a fixed thickness with time and the internal gas mass flow rates can be calculated by reversing Eq. (2.39) once the virgin and the charred density of the material have been calculated using Eq. (5.2). However, the charred material density is directly linked to the pyrolysis gas mass flow rate (that is generated by the material decomposition).

If homogeneous solid-solid in-depth reactions are neglected (assumption true for carbon-based material and reasonably valid for the silica-based materials) the only gas coming from the in-depth of the material is the pyrolysis gas. During the decomposition of a pyrolyzing material, the gaseous pyrolysis products rise the pressure inside the char, forcing these products to flow through this porous media. Of course, the residence time of the pyrolysis gas inside the material and the chemical interactions between the pyrolysis gas and the char can modify the composition and the properties of both the char and the gas [78]. However, in the present model, the pyrolysis gas composition is calculated in a simplified, as

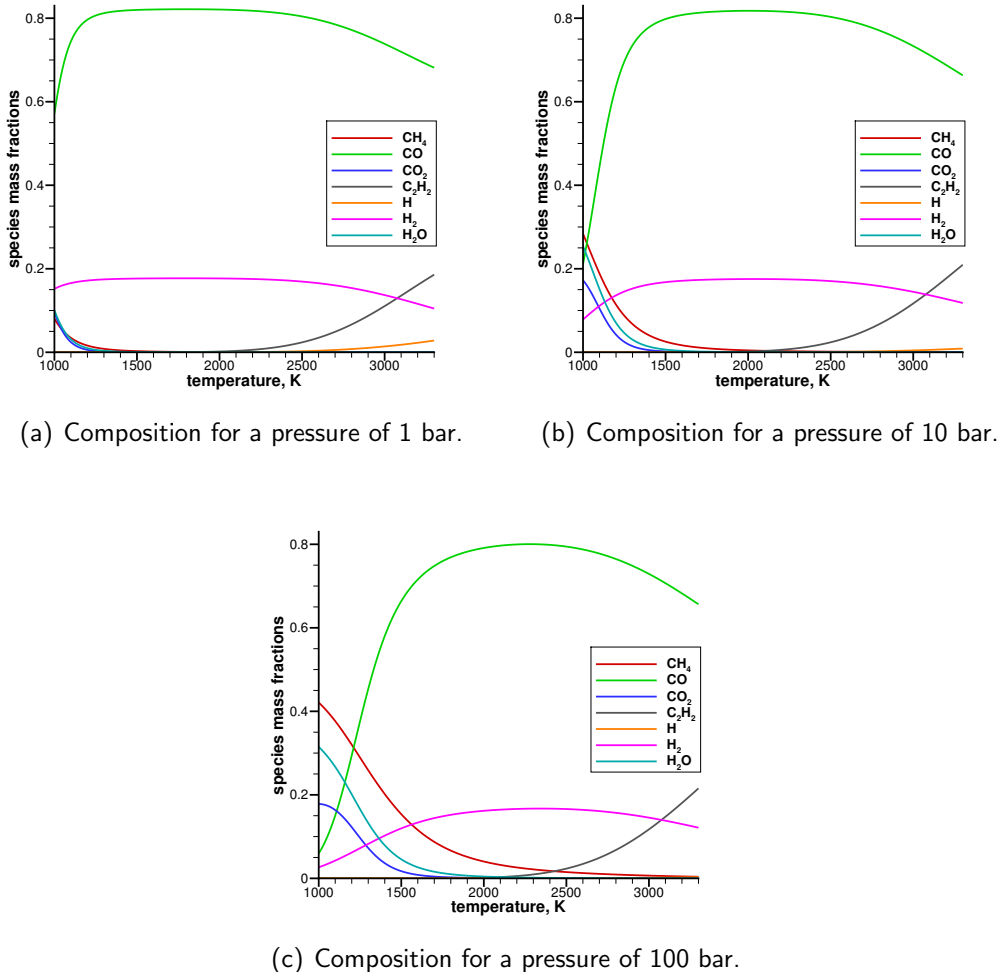


**Figure 5.1** – Calculated pyrolysis gas composition as a function of temperature for different pressure values.

well as reasonable, manner [79]. In fact, this gas is considered to be in chemical equilibrium at the wall temperature and pressure. Under this hypothesis, its composition can be calculated by a chemical equilibrium code [38] and stored in a database at different values of pressure and temperature. Attention should be paid to the fact that, although the pyrolysis gas is injected into the boundary layer at a well defined composition, the injected species modify the mixture composition at the wall and thus influence the surface mass and energy balances.

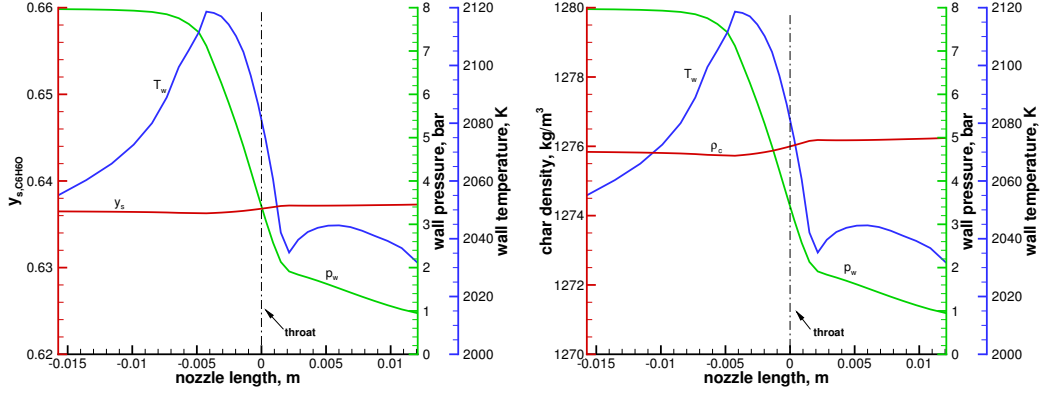
The elemental composition of the phenolic resin matrix, to be used in the chemical equilibrium code, has been calculated starting from a simple phenol molecule ( $C_6H_5OH$ ). Considering that the product of the phenolic resin decomposition are the pyrolysis gas and a solid carbonaceous residual, the two resin components (A and B) can be modeled assuming that the partially decomposing component (B) is pure carbon. With this hypothesis, the charred material density ( $\rho_c$ ) can be evaluated from Eq. (5.2) assuming that all the carbon resulting in the solid state from the equilibrium calculation of  $C_6H_5OH$  at the selected conditions (wall temperature and pressure) belongs to the “B” component, whose density can be calculated as:

$$\rho_{r,B} = (\rho_{0,A} + \rho_{0,B}) y_{s,C_6H_5OH} \quad (5.4)$$

where the solid carbon mass fraction is represented by  $y_{s,C_6H_5OH}$ . Obviously, since the equilibrium calculation is affected by the ambient conditions (Fig. 5.1), the solid carbon content, and thus the charred material density, are affected by the ambient conditions too. Therefore, the char density is allowed to vary along the nozzle, so that the  $\varphi$  ratio (Eq. (2.39)) takes different values at each wall station along the nozzle profile. However, the variation of the solid carbon residual along the nozzle wall is really small for the practical conditions of interest (Fig. 5.2) that, if specific data on each resin component are unavailable for the analyzed material, using a single value for  $\varphi$  to compute the pyrolysis gas mass flow rate all along the nozzle does not lead to significant errors.

## 5.2 Surface balances

For the surface balances over a pyrolyzing carbon-based ablating surface, all the considerations made for the non-pyrolyzing case (Chapter 4) are still valid.



(a) Solid carbon mass fraction, wall pressure and wall temperature along the nozzle. (b) Char density, wall pressure and wall temperature along the nozzle.

**Figure 5.2 – Examples of solid carbon mass fraction and char density calculated for a generic nozzle.**

Figure 5.3 shows the surface balances over this kind of material. The highlighted terms are the same of the non-pyrolyzing case with the exception of a further term related to the pyrolysis gas injection. Therefore, the gaseous species mass balance over such a surface reads as in [80]:

$$\rho \mathcal{D}_{im} \left. \frac{\partial y_i}{\partial \eta} \right|_w + \varphi \dot{m}_c y_{i_g} + \sum_{r=1}^{N_r} \omega_i^r = (\rho v)_w y_{i_w} \quad i = 1, N_c \quad (5.5)$$

where the pyrolysis gas injection term has been rewritten using the char mass flow rate using Eq. (2.39). The surface energy balance is:<sup>1</sup>

$$\begin{aligned} k \left. \frac{\partial T}{\partial \eta} \right|_w + \sum_{i=1}^{N_c} h_{i_w} \rho \mathcal{D}_{im} \left. \frac{\partial y_i}{\partial \eta} \right|_w + \dot{q}_{rad_{in}} + \dot{m}_c h_{c_w} \\ = (\rho v)_w h_w + \dot{q}_{rad_{out}} - \dot{s}(\rho_{v_{in}} h_{v_{in}} - \rho_{c_w} h_{c_w}) \end{aligned} \quad (5.6)$$

<sup>1</sup>In case of carbon-phenolic the surface material is in the charred state, therefore the subscripts "c" and "s" are equivalent.

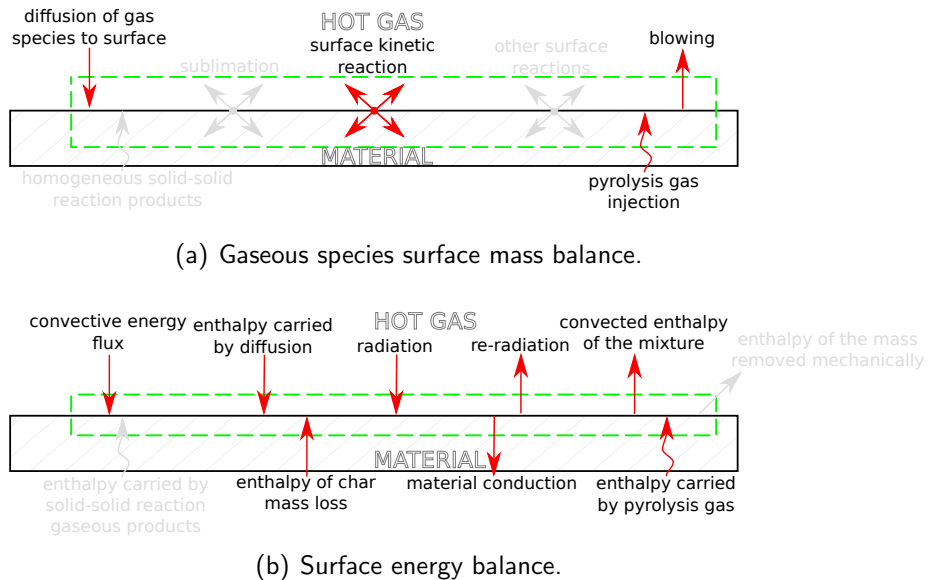


**Figure 5.3 –** Surface balances for a carbon-based pyrolyzing material.

where no terms related to the enthalpy injected by the pyrolysis gas appear because of the equation simplification obtained using the steady-state ablation approximation (see Eq. (2.54)). At this point, considering the definition of  $\varphi$  (Eq. (2.39)) and the definition of the erosion rate (Eq. (2.38)), reported here for the sake of convenience:

$$\varphi = \frac{\dot{m}_g + \dot{m}_h}{\dot{m}_c} = \left( \frac{\rho_v}{\rho_c} - 1 \right) \quad \dot{s} = \frac{\dot{m}_c}{\rho_c}$$

and, defining  $\dot{m}_{tot} = \dot{m}_c + \dot{m}_g$  ( $\dot{m}_h = 0$  for the carbon-phenolic), the erosion rate for a pyrolyzing material can be rewritten as:

$$\dot{s} = \frac{\dot{m}_c}{\rho_c} = \frac{\dot{m}_{tot}}{\rho_v} = \frac{\dot{m}_c(1 + \varphi)}{\rho_v} \quad (5.7)$$

and, considering the overall surface mass balance obtained by summing Eq. (5.5) over  $i$ , the final form of the surface energy balance reads:

$$k \frac{\partial T}{\partial \eta} \Big|_w + \sum_{i=1}^{N_c} h_{i_w} \rho D_{im} \frac{\partial y_i}{\partial \eta} \Big|_w + \dot{q}_{rad,in} = \dot{q}_{rad,out} - \dot{m}_c [(1 + \varphi)(h_{v_{in}} - h_w)] \quad (5.8)$$

### 5.3 Numerical procedure

The numerical procedure for the evaluation of the erosion rate in case of pyrolyzing ablative material is very similar to the one described in the previous chapter for the non-pyrolyzing one. Again, the nozzle is characterized by subsonic inflow boundary conditions describing the flow of the combustion gases (total temperature and total pressure are enforced together with the flow direction and chemical composition), supersonic outflow, symmetry axis and solid wall. The description of a general time step of the algorithm is therefore quite unmodified with respect to the one given in Section 4.3. Differences in the procedure are due only to the calculation of the pyrolysis gas composition and charred material density. The pyrolysis gas composition is calculated as described in Section 5.1 by means of the CEA code and stored in a database, together with the solid carbon residual from the resin decomposition, using pressure and temperature as parameters. At each time step, using the wall temperature and pressure of the previous time step, the pyrolysis gas composition and the solid carbon residual are extracted from the table, the char density is evaluated using Eq. (5.2) and the  $\varphi$  value to be used in Eq. (5.5) is determined.

It is worth noting that, differently from the non-pyrolyzing material case, the solution of Eq. (5.7) is intimately connected to the input set of material parameters (by assigning either a single constant value of  $\varphi$  or the material component

**Table 5.1** – Test conditions [81].

Test no.	Prop.	$t_b$ , s	$\bar{p}_c$ , MPa	AI%	$\rho_v$ , g cm $^{-3}$
#22	MOD. 8	11.52	4.73	16	1.51
#8	JPL-612	12.03	4.86	18	1.50

densities and by calculating the local  $\varphi$  using the decomposition model). In fact, the pyrolysis gas injection, whose amount is defined by  $\varphi$ , has a direct effect on both the char density and the pyrolysis gas mass flow rate, and an indirect one, that is caused by the wall composition modification, on the char mass flow rate. Therefore, the results of a single CFD simulation can be used exclusively to evaluate the erosion rate of the material whose specific data have been used as input for the simulation.

## 5.4 RSRM subscale nozzle test

In order to validate the ablation model for carbon-based pyrolyzing materials, an experimental work carried out during the 80s at the NASA Jet Propulsion Laboratory to study several new candidate materials for nozzle of the Space Shuttle Reusable Solid Rocket Motor (RSRM) [81, 82], has been numerically reproduced.

### 5.4.1 Input data

As reported in [81], the test motor is a double-length BATES chamber, 0.305 m in diameter and 1.026 m long. The propellant grain was composed by two 0.513 m long by 0.305 m diameter cartridges. The nominal test nozzle initial throat diameter is 55.8 mm with an initial expansion ratio of 6.1:1. Numerical investigation has addressed two of the experimental test cases that use the FM-5055 carbon-

**Table 5.2** – Chamber temperature and species mass fractions for two test cases.

Test no.	#22	#8
$T_c$ , K	3485	3383
$\text{Al}_2\text{O}_3$	0.3008	0.3219
$\text{AlCl}$	0.0110	0.0234
CO	0.2131	0.2656
$\text{CO}_2$	0.0298	0.0151
Cl	0.0227	0.0143
H	0.0016	0.0015
$\text{H}_2$	0.0170	0.0243
$\text{HCl}$	0.1929	0.1832
$\text{H}_2\text{O}$	0.1125	0.0643
$\text{N}_2$	0.0888	0.0829
OH	0.0098	0.0035

phenolic material [81]. In Table 5.1, the test identification number, the propellant name, the burning time, the chamber pressure, the propellant aluminum content and the virgin TPS density are listed for the two experiment test cases. The two test cases use two different propellants: 86% solids loaded AP/PBAN with 16% aluminium and 86% solids loaded AP/HTPB with 18% aluminum, respectively named as propellant MOD. 8 and propellant JPL-612 in Table 5.1. The nozzle inlet compositions and temperature have been derived from chemical equilibrium calculations [38], by imposing the chamber pressure and the total enthalpy conservation and starting from the propellant formulation described in [81]. The chamber temperatures and the inlet compositions of the two test cases are shown in Table 5.2.

Since the analyzed wall material is a decomposing material, a further datum is necessary to correctly predict the pyrolysis gas mass flow rate: the char density (see Eq. (2.39)). Unfortunately, there are uncertainties on this datum. In fact, because this material has undergone several changes during the years, univocal values for the char densities have not been found [83, 84, 85]. Since also the

virgin densities from the [83, 84, 85] were not in agreement with those given in [81] and reported in Table 5.1, the choice of evaluating the  $\varphi$  value directly from the data (virgin density and char density) of each reference [83, 84, 85], and then using the higher and the lower  $\varphi$  to perform the numerical simulations, has been made. The two obtained bounding values of  $\varphi=0.383$  and  $\varphi=0.145$  have been derived from [83] (virgin density  $1400\text{ kg m}^{-3}$ , char density  $1012\text{ kg m}^{-3}$ ) and [85] (virgin density  $1459\text{ kg m}^{-3}$ , char density  $1275\text{ kg m}^{-3}$ ), respectively. Again, the radiative heat fluxes have been considered negligible with respect to the other heat fluxes of Eq. (5.8) and, therefore, they have not been considered in the analysis. The adopted grid geometry has been modified with respect to the real nozzle geometry. The experimental nozzles, in fact, are submerged. Because the role of the submerged part of the nozzle is not important for the present study, the considered geometry starts at the nose point. The initial part of the nose has been reproduced using a parabolic curve up to the point of  $45^\circ$  inclination. This curve becomes parallel to the nozzle axis at the inlet section so that an axial inlet velocity profile can be assigned. As the length of the wall affects the boundary-layer thickness and hence the heat and mass transfer rate, the total wall length of the parabolic curve is equal to that of the original nozzle wall.

### 5.4.2 Results and Discussion

An original  $70\times 80$  grid has been generated (Fig. 5.4). Cell clustering in the axial and radial directions ensures a good resolution of the nozzle convergent part and a value of  $y^+$  less than 1.0, respectively. To ensure grid independent results, a grid convergence analysis has been carried out. Table 5.3 shows the calculated mass flow rate of ablated material for three different grid sizes at three different locations. The quantitative analysis of solutions obtained on three grid

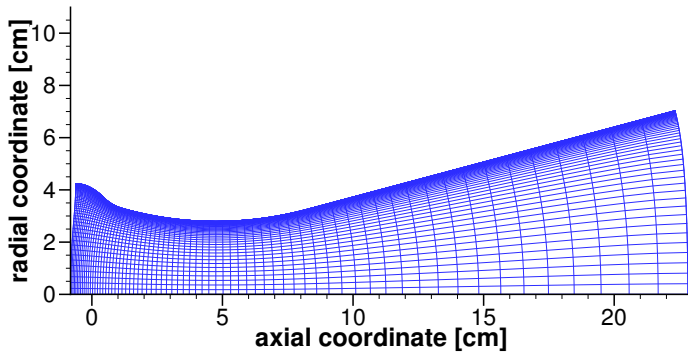


**Figure 5.4** – Nozzle geometry and selected mesh.

levels confirms that the spatial order of accuracy is close to the formal value of 2. The discrepancy between the throat mass flow rate obtained by means of the Richardson extrapolation [73] and the one evaluated with the medium grid ( $70 \times 80$ ) is less than 1.5%; therefore, the medium grid has been considered suitable for the present analysis.

In Fig. 5.5, the erosion rate for tests number 22 and 8 in case of  $\varphi=0$  (carbon–carbon),  $\varphi=0.383$  and  $\varphi=0.145$  are compared with the experimental values. Material decomposition (pyrolysis gas injection) has a strong influence on the erosion rate: the higher the pyrolysis mass injection, the higher the erosion rate. In fact, by using the same virgin material density but considering different values of  $\varphi$ , the higher the  $\varphi$  value the lower the char density and, hence, the higher the

**Table 5.3** – Mass flow rate at three different locations for three different refined meshes.

Grid	$\dot{m}_{tot}$ , $\text{kg m}^{-2} \text{s}^{-1}$ ( $x = 2.86 \text{ cm}$ )	$\dot{m}_{tot}$ , $\text{kg m}^{-2} \text{s}^{-1}$ ( $x = 4.75 \text{ cm}$ )	$\dot{m}_{tot}$ , $\text{kg m}^{-2} \text{s}^{-1}$ ( $x = 16.77 \text{ cm}$ )
$35 \times 40$	0.665609	0.619398	0.111301
$70 \times 80$	0.702249	0.64768	0.111928
$140 \times 160$	0.711420	0.653563	0.112173

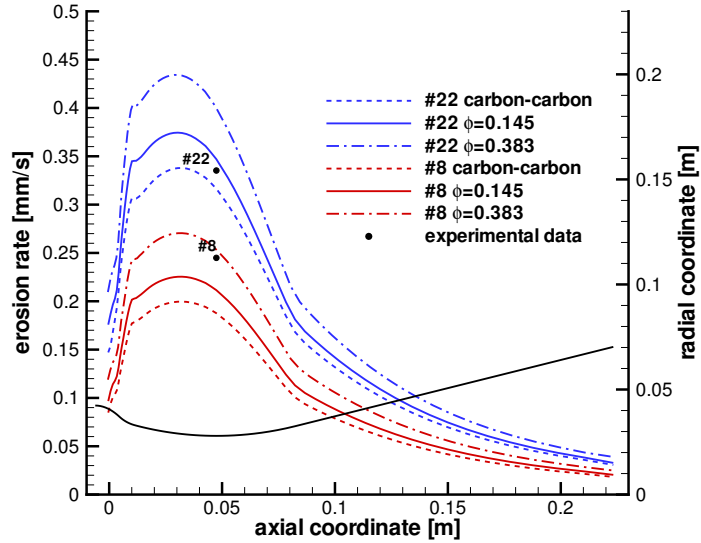


**Figure 5.5** – Erosion rate for tests #22 and #8 in case of different value of  $\varphi$ .

erosion rate. Furthermore, as shown in Fig. 5.6, the higher the erosion rate, the lower the wall temperature. This is in agreement with the fact that, although non-pyrolyzing materials (e.g. carbon-carbon, graphite, etc...) are known to better resist to erosion, they normally need a back-up insulator to prevent the overheating of the underlying structure. On the contrary, the choice of using a stand-alone pyrolyzing material is frequent in the nozzle sections where the erosion is not so high and where, in order to reduce the total mass, the use of both primary ablative material and back-up insulator is considered an excessively conservative option.

The agreement with the experimental results in Fig. 5.5 is quite good. As shown, the different  $\varphi$  values reflect quite different erosion rates and it can be stated that the pyrolysis gas injection has to be considered properly. The use of a non-pyrolyzing material model, in fact, can lead to the underestimation of the erosion rate, especially in the case of pyrolyzing material of high resin content

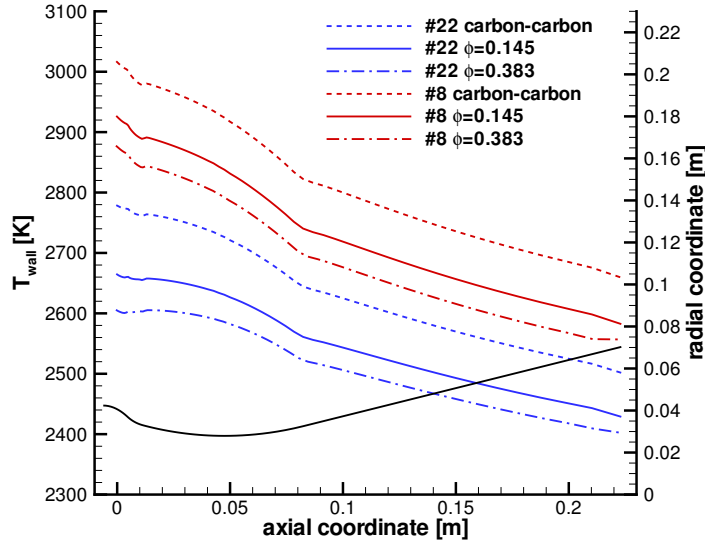


**Figure 5.6** – Wall temperature for tests #22 and #8.

(high value of  $\varphi$ ).

Unfortunately, as seen in Fig. 5.5, there is no single value of  $\varphi$  that seems to be in better agreement with the experimental values. However, an important uncertainty on the input data, especially for small size motor as the simulated one, has not been analyzed yet: the combustion efficiency. For this reason, a sensitivity analysis has been carried out to investigate the effect of varying the chamber temperature, which can be influenced by parameters such as the combustion efficiency [4]. Although combustion efficiency is related to both the combustion gas composition and temperature ( $c^* = \sqrt{RT_c}/\Gamma$ ), here the assumption that the chamber temperature variation is the only responsible of the lower combustion efficiencies has been made. Hence, to analyze its influence on the final erosion rate value, further simulations have been performed for the test cases 8 and 22 by using the same chamber composition and pressure as listed in Table 5.2 but considering combustion efficiencies of 0.97 and 0.95. It is worth to remind that,

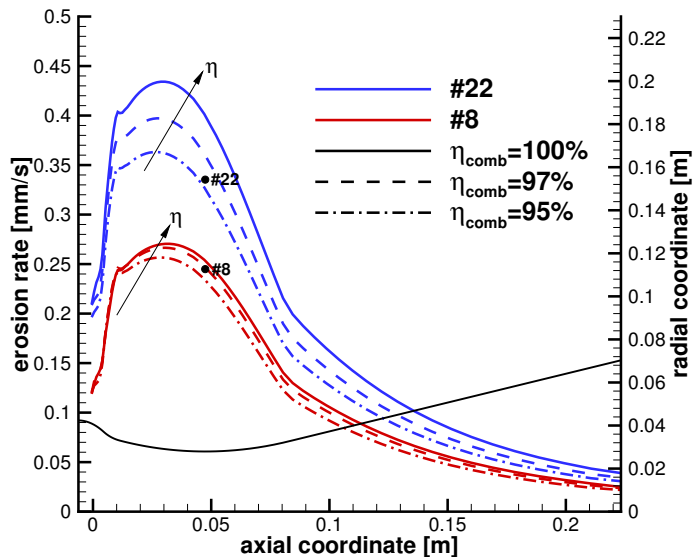


**Figure 5.7** – Erosion rate for  $\varphi = 0.383$  in case of different combustion efficiency.

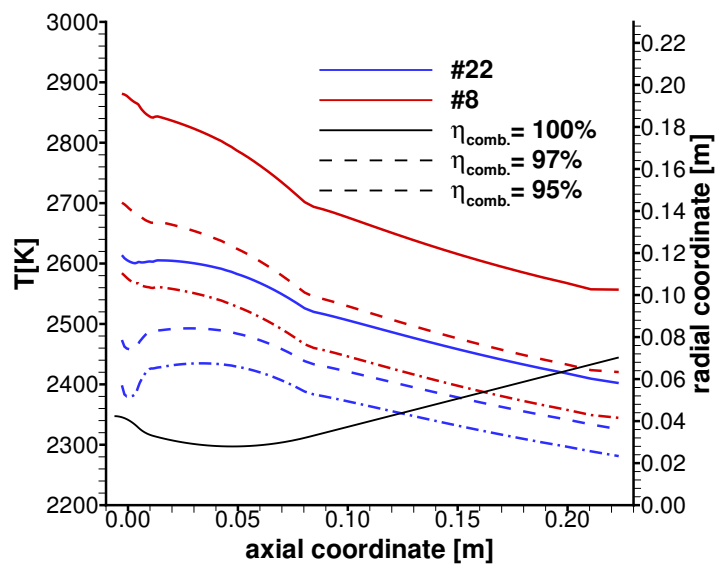


**Figure 5.8** – Wall temperature variation for  $\varphi = 0.383$  in case of different combustion efficiency.

**Table 5.4** – Percentage variation of mass blowing rate,  $\dot{m}_{tot} = \dot{m}_c + \dot{m}_g$ , and wall temperature at the throat section for test cases #22 and #8 in case of different values of combustion efficiency ( $\eta_{comb}$ ).

Test no.	$\varphi$	$\eta_{comb}$	$\Delta T_w, \%$	$\Delta \dot{m}_{tot}, \%$
22	0.383	1.00	0.00	0.00
22	0.383	0.97	-3.86	-10.00
22	0.383	0.95	-5.99	-18.50
8	0.383	1.00	0.00	0.00
8	0.383	0.97	-5.85	-2.57
8	0.383	0.95	-9.32	-7.71

because of the different erosion rates, the two analyzed test cases show fairly different wall temperatures also in the case of 100% efficiency (Fig. 5.6). A lower combustion efficiency reflects a chamber temperature reduction which in turn produces a decrease in the wall temperature. Figure 5.7 shows that the effect of such a wall temperature reduction on the erosion rate is stronger for the test case characterized by a lower wall temperature. For these test cases, in fact, the erosion process is highly influenced by the chemical kinetics of the surface reactions (see Table 5.4) because of the lower wall temperature. Hence, although the wall temperature variation is smaller for the test no. 22 than for test no. 8 (see Fig. 5.8 and Table 5.4), this temperature variation strongly modifies the kinetic parameters. Thus, it can be observed that for low values of the wall temperature, the reaction rates drive the erosion process as experienced for non-pyrolyzing material [27].

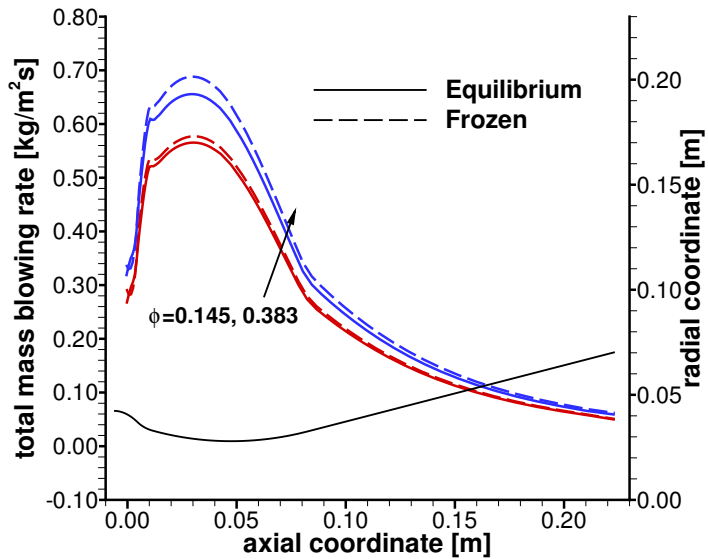
Another uncertainty is related to the pyrolysis gas composition and to its influence on the erosion rate. To correctly evaluate the pyrolysis gas composition at the injection into the boundary layer, chemical and transport models need to be formulated. In fact, the pyrolysis gas is actually subjected to modifications while it flows through the material. Nevertheless, as explained, in the present model a simplified approach has been chosen and the pyrolysis gas is assumed to be

**Table 5.5** – Relative percent change (with respect to the case of equilibrium pyrolysis gas composition) of the total mass blowing rate at the throat section in case of frozen and equilibrium pyrolysis gas composition.

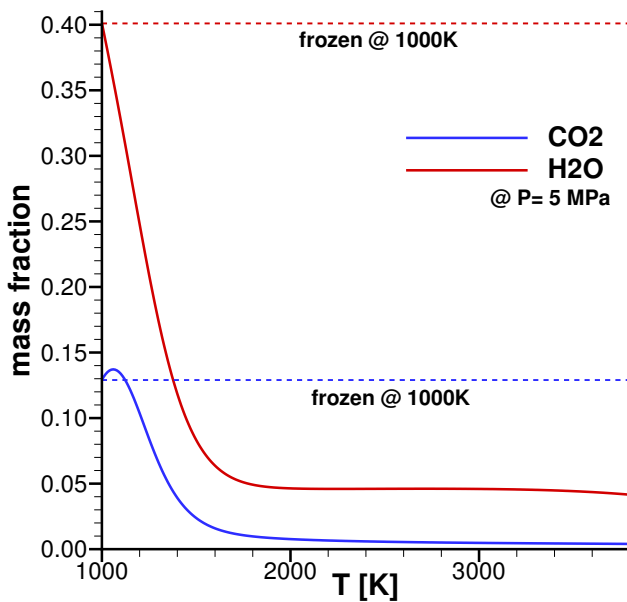
Test no.	$\varphi$	$\Delta\dot{m}_{tot,\%}$
22	0.145	+2.14
22	0.383	+4.97
8	0.145	+1.73
8	0.383	+4.93

in equilibrium at the local wall conditions. The effect of considering a different assumption than equilibrium for evaluating the composition of the pyrolysis gas is shown in Fig. 5.9, where results obtained by a standard equilibrium and a frozen pyrolysis gas composition are compared for the test case 22. The frozen composition has been evaluated at  $T = 1000$  K (at which the phenolic resin can be supposed to be totally decomposed, [86]) and  $p = 5$  MPa (approximately twice the throat wall pressure for every test cases) and is hence independent from the surface conditions. As shown in Fig. 5.10, the frozen pyrolysis gas composition has values of oxidizing species mass fractions different from equilibrium values. Figure 5.9 and Table 5.5 indicate that the higher the value of  $\varphi$  the higher the modification of the mass blowing rate when assuming frozen pyrolysis gas composition. In fact, as the frozen composition has higher mass fractions of the two major oxidizing species (Fig. 5.10), the mass flow rate of these oxidizing species is much higher in case of high  $\varphi$  values than in case of low  $\varphi$  values. These considerations lead to the conclusion that, when the selected material has a high value of  $\varphi$ , the right evaluation of the pyrolysis gas composition could be relevant for the correct determination of the erosion rate value.

So far, because of the uncertainty on the material data, only constant  $\varphi$  values have been tested. In [85] some information are given regarding to the compo-



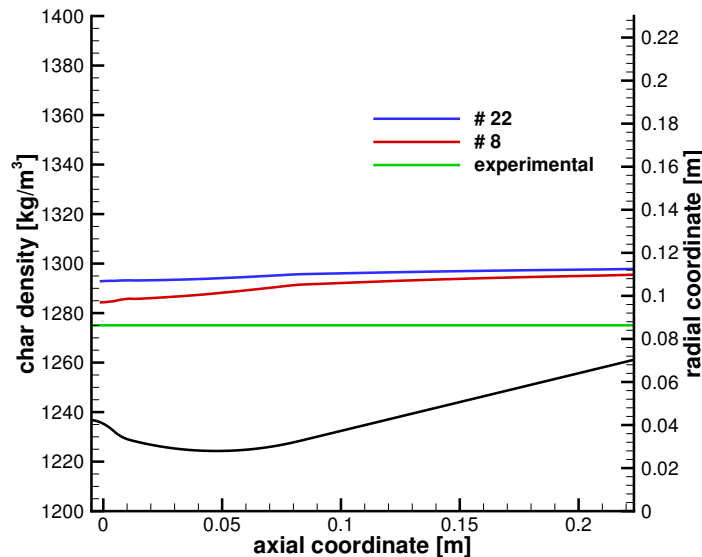
**Figure 5.9** – Total mass blowing rate variation in case of frozen pyrolysis gas for case test #22.



**Figure 5.10** – Example of pyrolysis gas mass fractions of the two major oxidizing species in case of equilibrium and frozen composition.

**Table 5.6 –** Material data from [85].

$\rho_{0,A}$ , kg m <sup>-3</sup>	$\rho_{0,B}$ , kg m <sup>-3</sup>	$\rho_{0,R}$ , kg m <sup>-3</sup>	$\Gamma_V$
324.21	973.12	1541.88	0.338

**Figure 5.11 –** Comparison between calculated and experimental char density from [85] (labeled as experimental) for inlet conditions of case test #22 and #8.

sition of FM-5055. Unfortunately, these information could not have been used directly for the validation test case because of the disagreement between the virgin material density from [85] ( $1459 \text{ kg m}^{-3}$ ) and the one from [81] from which the experimental data have been taken (see Table 5.1). Therefore, the choice of taking only the char density reported in [85] and evaluate the constant  $\varphi$  value using the virgin density of Table 5.1 was judged as the best one when the main output of the analysis was the erosion rate. However, an analysis to verify the decomposition model is still to be done and the virgin density and the resin volumetric fraction given in [85], and listed in Table 5.6, can be used to perform

this analysis. By using these data, other two simulations have been run by using the decomposition model. Results on erosion rates for both the test cases are not reported as they practically overlap those obtained for the lowest  $\varphi$  value in the previous analysis. The obtained char densities are shown in Fig. 5.11. As seen the model gives slightly variable char densities along the nozzle wall, and both the test cases give a results in encouraging agreement with the actual char density reported in [85].

As a final consideration, it can be stated that the developed model can be considered usable for the evaluation of the erosion rate, the pyrolysis gas mass flow rate and the char density, when the hypothesis of steady-state ablation is applicable and a sufficient amount of data on the carbon-based pyrolyzing material are available.

## Ablation model for pyrolyzing silica-based materials

As described in the Introduction, the erosion process of silica-based TPS materials is quite different from that of carbon-based materials. When the surface temperature does not reach the silica melting temperature, the material can lose mass only because of the following processes:

- resin decomposition (pyrolysis);
- homogeneous reactions between silica fibers and residual carbon (in the solid phase) deriving from the resin decomposition;
- oxidation of the residual carbon exposed to the gas phase at the surface.

However, when melting of silica takes place, the latter two mass losses mentioned above can be considered negligible and an estimate of the erosion rate can be evaluated by taking into account only the fail mass removal of both the liquid-silica layer formed by the surface melting and the carbon residual from the resin

decomposition. In this scenario, the surface boundary condition for silica-based materials can be formulated using appropriately modified surface mass and energy balances.

In this chapter, the modeling of silica-based materials is presented. Considering that the decomposition model is still the same of the carbon-based pyrolyzing materials, no further discussion is presented on the material internal behavior. The surface balances and the ablation model are presented in the first part of the chapter. After that, the validation test case is introduced and the obtained results are discussed.

## 6.1 Surface balances

Assuming that the only mechanism that causes the ablation of a melted silica-based material is the mechanical removal of the melted layer exposed to the hot gas (referred to as “fail” in the following), the mass fluxes over such a surface can be schematized as in Fig. 6.1(a). Therefore by customizing Eq. (2.40) one obtains the overall surface mass balance for the pyrolyzing silica-based material:<sup>1</sup>

$$\dot{m}_g + \dot{m}_c = (\rho v)_w + \dot{m}_{f,\text{SiO}_2} + \dot{m}_{f,C} \quad (6.1)$$

where the last two terms on the right-hand side are the fail mass flow rates of the silica fibers and of the carbon residual from the resin decomposition, respectively. At this point, if this carbon residual is assumed to have a negligible strength and flow away together with the silica reinforcement, the driving factor of the surface material removal can be assumed to be only the fail removal of the melted silica. With this assumption, the two fail mass flow rate contributions in Eq. (6.1)

---

<sup>1</sup>In case of silica-phenolic the surface material is in the charred state, therefore the subscripts “c” and “s” are equivalent.

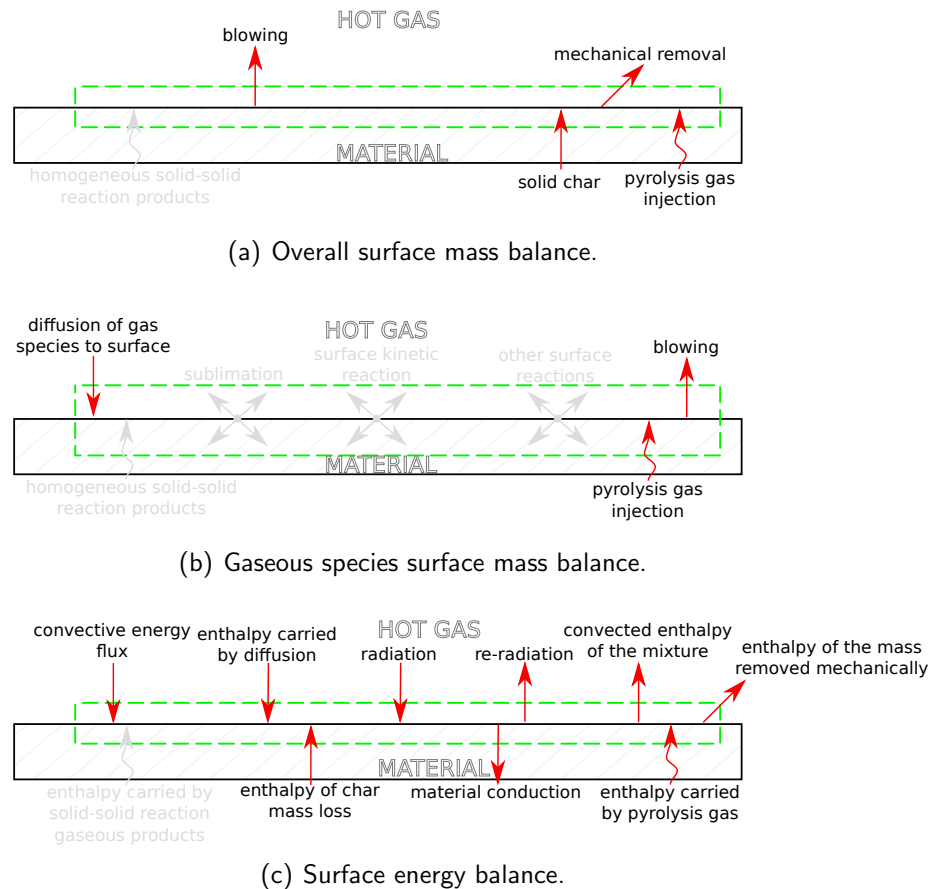


**Figure 6.1** – Surface balances for a silica-based pyrolyzing material.

need no longer to be distinguished and can be referred to as a general term  $\dot{m}_f$ . Therefore, the solid char entering the surface at steady-state equals the melted mass removed from the surface:

$$\dot{m}_c = \dot{m}_f \quad (6.2)$$

and the overall surface mass balance for this kind of material reads:

$$\dot{m}_g = (\rho v)_w \quad (6.3)$$

in which the blowing term equals the pyrolysis gas injection (note that corresponds to the summation of Eq. (2.45) over  $i$ , when only the highlighted fluxes of Fig. 6.1(b) are considered).

Considering Eq. (6.2) and the heat fluxes highlighted in Fig. 6.1(c), the surface energy balance in case of steady-state ablation, Eq. (2.54), can be customized for the silica-based material:

$$\begin{aligned} k \frac{\partial T}{\partial \eta} \Big|_w + \sum_{i=1}^{N_c} h_{i_w} \rho \mathcal{D}_{im} \frac{\partial y_i}{\partial \eta} \Big|_w + \dot{q}_{rad_{in}} + \dot{m}_f h_{c_w} \\ = (\rho v)_w h_w + \dot{q}_{rad_{out}} + \dot{m}_f h_{f_w} - \dot{s}(\rho_{v_{in}} h_{v_{in}} - \rho_{c_w} h_{c_w}) \end{aligned} \quad (6.4)$$

where the term  $\dot{m}_f h_{f_w}$  on the right-hand side is the enthalpy carried away by the mechanical removal of the surface melted material and differs from the  $\dot{m}_f h_{c_w}$  on the left-hand side which is the enthalpy, carried on by the char (silica plus carbon) in the solid state, that is entering the control surface from the solid material side. Finally, redefining the erosion rate as:

$$\dot{s} = \frac{\dot{m}_f}{\rho_c} = \frac{\dot{m}_{tot}}{\rho_v} = \frac{\dot{m}_f(1 + \varphi)}{\rho_v} \quad (6.5)$$

where the definition of  $\dot{m}_{tot} = \dot{m}_f + \dot{m}_g$  has been used, Eq. (6.4) can be rearranged in a more appealing form if Eq. (6.3) and Eq. (2.39) are taken into account:

$$\begin{aligned} k \frac{\partial T}{\partial \eta} \Big|_w + \sum_{i=1}^{N_c} h_{i_w} \rho \mathcal{D}_{im} \frac{\partial y_i}{\partial \eta} \Big|_w + \dot{q}_{rad_{in}} \\ = \dot{q}_{rad_{out}} + \dot{m}_f h_{f_w} - \dot{m}_f [(1 + \varphi)(h_{v_{in}}) - \varphi h_w] \end{aligned} \quad (6.6)$$

## 6.2 Ablation model

At this point, further considerations regarding the fail mass removal are necessary. Due to the assumption of the common removal of the liquid silica and solid carbon, the surface mass balance, Eq. (6.3), does not permit the direct evaluation of the fail mass removal ( $\dot{m}_f$ ) as, for example, is done for the char mass flow rate in case of carbon-based materials by means of the thermochemical ablation model. Therefore, unless a specific relation between the liquid silica layer removal and the viscous stress acting on the surface is found, a further assumption is necessary. In particular, a sudden removal of this liquid layer, that is supposed to flow away as soon as it is formed, is assumed. As a consequence, the surface is considered as isothermal at the silica melting temperature (1996 K). Else, in fact, the sub-surface temperature could reach a value higher than the melting value, and this is in contradiction with the assumed hypothesis of sudden removal. Considering these hypothesis, the evaluation of the erosion rate comes directly from the resolution of Eq. (6.4).

It has to be noted that, as opposed to the carbon-based material case, the evaluation of the char enthalpy in the liquid state ( $h_{f_w}$ ) is needed in this case. Despite the fact that the solid carbon does not undergo phase change and no enthalpy variation occurs between a layer just below the surface and the surface itself, once the silica melting takes place a small but non-negligible gap in its enthalpy occurs (Fig. 6.2). As previously described, the charred material is composed of a mix of silica and carbon, and its enthalpy has to be evaluated correctly. By using the same decomposition model that has been described for the carbon-based material case, the char enthalpy for the present material can be evaluated as:

$$h_c = \frac{1 - \Gamma_M}{1 - \Gamma_M(1 - y_{s,C_6H_5OH})} h_{SiO_2} + \frac{\Gamma_M y_{s,C_6H_5OH}}{1 - \Gamma_M(1 - y_{s,C_6H_5OH})} h_{s,C_6H_5OH} \quad (6.7)$$

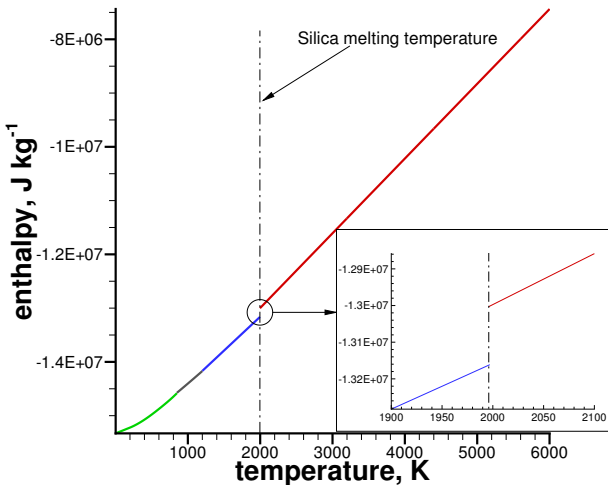


**Figure 6.2 – Variation of silica enthalpy with temperature.**

where, as in Eq. (5.4), the subscript “*s*, C<sub>6</sub>H<sub>5</sub>OH” indicates the solid carbon residual from the resin decomposition.

### 6.3 Numerical procedure

The numerical procedure for the evaluation of the ablation rate in case of silica-phenolic uses the described ablation model, decomposition model and pyrolysis model. As for the case of carbon-based materials, the nozzle is characterized by subsonic inflow boundary conditions describing the flow of the combustion gases (total temperature and total pressure are enforced together with the flow direction and chemical composition), supersonic outflow and symmetry axis. Differently, in this case the solid wall boundary condition is an isothermal condition at the silica melting temperature (1996 K). However, in a real situation the wall is not isothermal and a certain surface temperature profile along the nozzle is established once the steady state has been reached. Therefore, in a generic

point along the nozzle the wall temperature can be lower than the silica melting temperature. In order to detect such a condition in the present model, a check on the convective heat flux has been introduced in the procedure, and the general time step of the algorithm procedure can be synthesized as follows:

1. The wall pressure is calculated from the flow field assuming zero-pressure gradient at the wall;
2. Assuming isothermal wall temperature the conductive heat flux is evaluated;
  - 2a. If the wall conductive heat flux is positive (from the gas to the surface), the decomposition model is activated to determine the char density (Eq. (5.2)) and the char enthalpy (Eq. (6.7)). Then, the local value of  $\varphi$  has been evaluated and the procedure goes to step 3;
  - 2b. If the wall conductive heat flux is negative, that is obviously a non-physical solution, no melting of the surface silica occurs, the ablation is switched off, simple isothermal wall condition without any mass flow is considered for that nozzle station and the step 3 is not performed for that point;
3. The fail mass flow rate is evaluated by means of Eq. (6.6).

At each time step, the fail mass flow rate, and the wall chemical composition (modified by the injection of the pyrolysis gas) are updated until a steady-state condition is reached considering as a convergence parameter the drop-down of the residual by five orders of magnitude. It is worth noting that, differently than the thermochemical ablation model for carbon-based material, this ablation model has a sort of on/off switching condition. This condition implies that, when the

ablation model is switched off, no further consideration of the wall conditions can be made and both, the solid conductive heat flux and the pyrolysis gas mass flow rate cannot be evaluated since the steady-state ablation approximation cannot longer be useful when no ablation occurs.

## 6.4 Arc-plasma silica-phenolic nozzle test

The ablative boundary condition for silica-based materials developed in the present study is validated by comparison with results of an experimental work carried out during the 70s at the Nasa Lewis Research Center to investigate the effect of off-optimum rocket engine operating conditions on silica-phenolic ablative material performance [11].

Since the test procedure is more exotic than the conventional solid rocket firing used as validation tests for the carbon-base materials, a further description of the experimental setup and of the applied test procedure is useful. In this experimental campaign, an arc-plasma generator has been used as the energy source with the objective of simulating the combustion products of a  $\text{N}_2\text{O}_4 - 50\% \text{N}_2\text{H}_4 / 50\% \text{UMDH}$  mixture with mixture ratios varying from pure oxidizer to nearly pure fuel and different characteristic velocities. In a rocket engine, the characteristic velocity is an easy-to-measure indicator of overall combustion efficiency. So that, it has been employed as a guide for selecting simulation gas energy content for “off-optimum” conditions. The characteristic velocity is defined as follows:

$$c^* = \frac{p_c A_{th}}{\dot{m}_{th}} \quad (6.8)$$

where  $p_c$  is the chamber pressure,  $A_{th}$  the throat area and  $\dot{m}_{th}$  the throat mass flow rate. The ratio of measured-to-ideal  $c^*$  for equilibrium isentropic flow is referred to as combustion efficiency ( $c^*/c_{opt}^*$ ).

The correspondence between the plasma generator test conditions (chemical composition and enthalpy) and the liquid propellant rocket conditions (local mixture ratio and overall  $c^*$ ) is not obvious. In a rocket engine, off-optimum conditions result from a number of non-ideal events which include incomplete mixing and non-adiabatic combustion. For the arc-plasma generator, however, all chemical species are completely mixed and are effectively in overall thermodynamic equilibrium, but their compositions and energy content may be varied over wide ranges independently. In the experimental investigation, the "off-optimum" rocket operating conditions simulated by the arc-plasma generator were defined consistently with the following assumptions about flow in the rocket nozzle:

- The relation between characteristic velocity and total temperature is defined by one-dimensional isentropic flow of the optimum rocket mixture ratio ( $O/F=2.0$ ).
- "Off-optimum" characteristic velocities are simulated by adjusting the total temperature of the arc heated gases.
- Local mixture ratios at the boundary layer edge in the rocket nozzle are in thermodynamic equilibrium and are at the total temperature defined by the above assumptions.

The fact that the first assumption acts as the basis to relate simulation gas energy content directly to rocket engine performance is emphasized in [11]. Moreover, since simulation test ablation data must be taken in terms of stream energy, it is the only basis for directly relating the measurements to an anticipated rocket engine performance. Therefore, the most fruitful and meaningful use of the arc-plasma generator data is to utilize it in combination with the accurately known surface boundary conditions to adequately characterize the important ablative

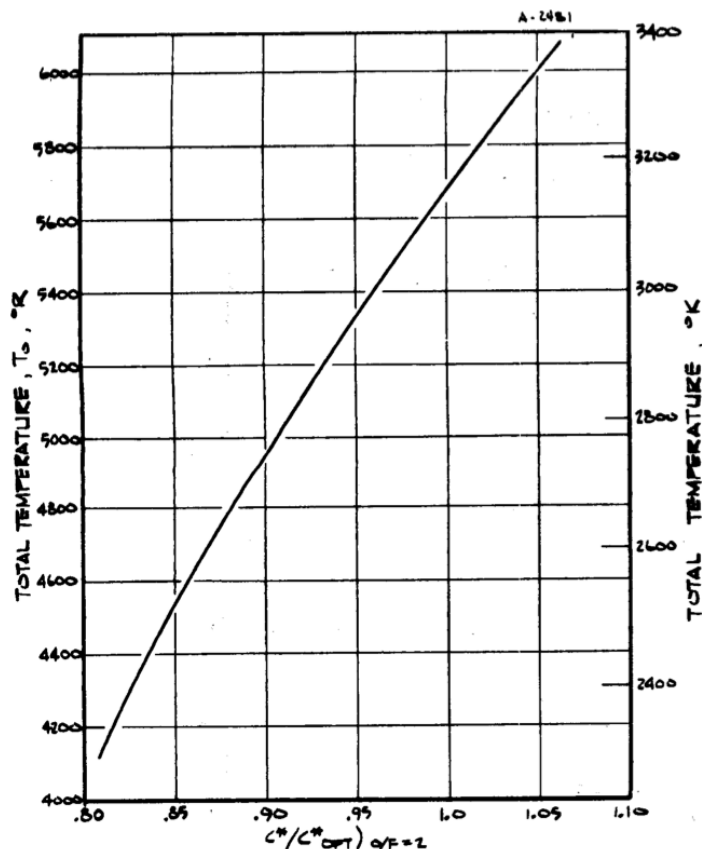


**Figure 6.3 –** Characteristic velocity ratio ( $c^*/c^*_{opt}$ ) as a function of temperature for  $O/F=2.0$  and  $p_c = 7.1$  bar [11].

phenomena and then, to utilize this basic understanding to predict the rocket engine performance.

For purposes of establishing the chamber-temperature range-of-interest, characteristic velocity ratios ranging from 0.85 to 1.0 are considered and the desired chamber temperature range is obtained from a  $(c^*/c^*_{opt})|_{O/F=2}$  temperature plot (Fig. 6.3).<sup>2</sup> Then, the experiments were conducted over a wide range of mixture ratio ( $0.38 \leq O/F \geq \infty$ ) and chamber temperature (within the selected range). The resulting data may be correlated with such fundamental parameters

<sup>2</sup> $(c^*/c^*_{opt})|_{O/F=2}$  is the actual to optimum velocity ratio for the  $O/F=2$  mixture.

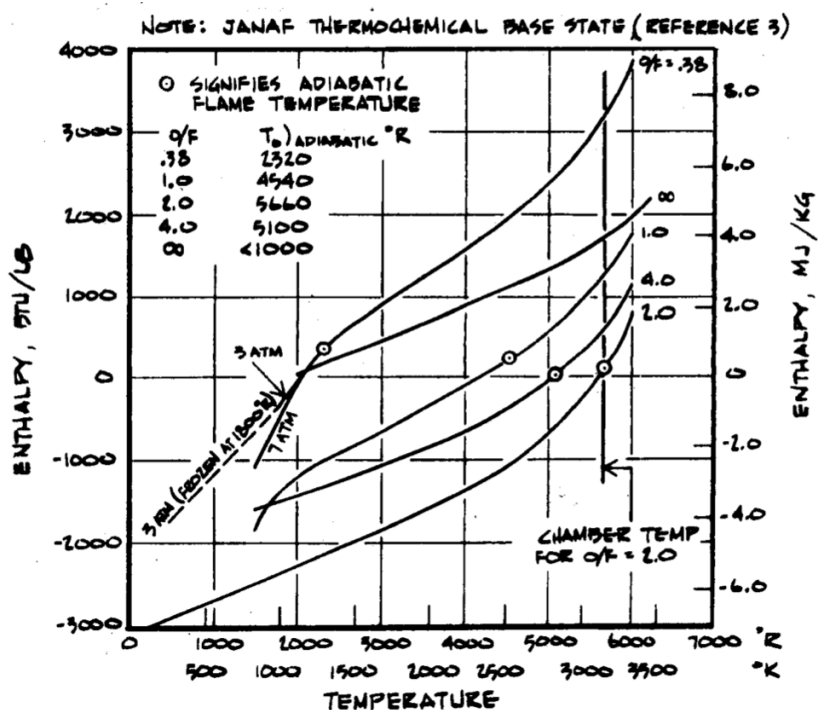


**Figure 6.4 –** Enthalpy-temperature characteristics for various oxidizer to fuel ratio [11].

as chemical composition and enthalpy or with more gross parameters such as characteristic velocity ratio. The desired levels of the various simulation parameters are achieved by introducing a specially tailored gas mixture to an arc-plasma generator, by dissipating the appropriate amount of electrical energy to increase the gas total enthalpy to correspond to that in the rocket engine, and then by expanding this high temperature gas mixture through an ablative material test nozzle.

The total enthalpy variation with total temperature is shown for each mixture ratio in Fig. 6.4. From this graph, the total enthalpy range corresponding to the selected temperature range can be easily derived for each of the selected mixture ratios. Then, Fig. 6.4, in conjunction with Fig. 6.3 enables relating the total enthalpy for each mixture ratio to the characteristic velocity ratio for

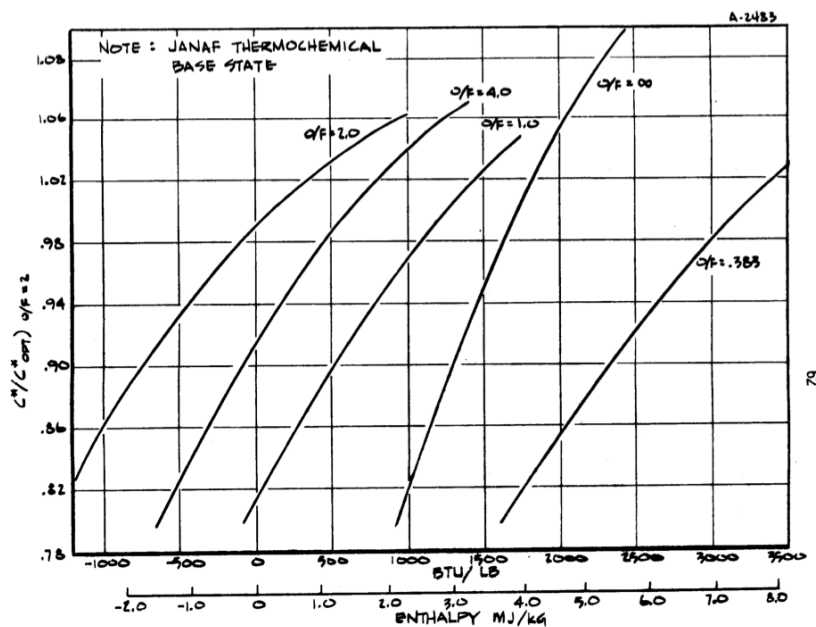


**Figure 6.5 –** Enthalpy of off-optimum mixture ratio required to produce temperature corresponding to indicated characteristic velocity ratio for  $O/F=2.0$  [11].

$O/F = 2.0$  (Fig. 6.5). This latter step allows the classification of the results for each experimental test ( $O/F - T_c$  couple) in terms of the corresponding characteristic velocity ratio of the  $O/F=2.0$  mixture ( $(c^*/c^*_{opt})_{O/F=2}$ ) having the same temperature as the experimental one. Finally, to reproduce the selected conditions the elemental mass fractions corresponding to the simulated  $O/F$  ratio (ranging from 0.38 to  $\infty$ ) were injected in the chamber and, taking into account the initial enthalpy of the injected mixture, a proper amount of energy was provided by means of the arc generator to reach a selected total enthalpy of the mixture (depending upon the simulated characteristic velocity ratio). A nominal maximum chamber pressure of 6.8 bar was achieved in all tests and the tests were terminated when chamber pressure had decayed to one-half its initial value as a consequence of the nozzle erosion. It has to be noted that, although efforts were made in order to respect the selected temperature range, for same

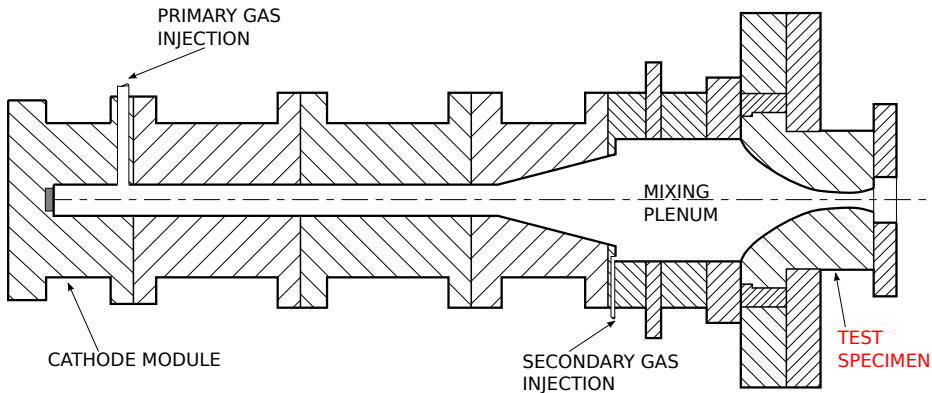


**Figure 6.6** – Schematic assembly of arc plasma generator and silica-phenolic nozzle (test specimen)[11].

experimental test case the reached temperature exceed the upper bound of the range. As a consequence, an  $(c^*/c_{opt}^*)_{O/F=2}$  higher than 1 is obtained for these test cases.

#### 6.4.1 Input data

The test specimen is a 7.3 cm long, 0.38 cm throat radius nozzle (labeled as test specimen at the right hand of the test structure shown in Fig. 6.6). Thanks to the meticulous work done by the researchers, all data needed for the present purpose can be easily drawn from [11]. Among the several O/F values experimentally tested, the attention has been focused here on optimum and fuel-rich off-optimum conditions, which are typically used for practical rocket engine applications. Therefore, a subset of the experimental tests has been selected and numerically reproduced to validate the ablative boundary condition for silica-based materials. Several factors have been accounted for in the selection: erosion occurrence, final eroded profile symmetry, supplied energy fluctuations and researcher comments on the specific test. The selected input conditions corresponding to three different O/F values are listed in Table 6.1 together with

**Table 6.1** – silica-phenolic validation test cases input conditions and species mass fractions.

Test no.	1129	1339	1145
O/F	2	1	0.38
$p_c$ , bar	5.7	6.3	6.1
$T_c$ , K	3062	2534	3167
$(c^*/c_{opt}^*)_{O/F=2}$	0.992	0.865	1.005
CO	8.48e-2	2.07e-1	3.35e-1
CO <sub>2</sub>	9.68e-2	3.45e-2	8.00e-5
H	9.60e-4	3.80e-4	6.27e-3
H <sub>2</sub>	6.32e-3	3.78e-2	8.75e-2
H <sub>2</sub> O	3.09e-1	2.26e-1	8.80e-4
NO	1.26e-2	1.10e-4	---
N <sub>2</sub>	4.28e-1	4.94e-1	5.68e-1
O	5.33e-3	---	---
OH	3.34e-2	1.03e-3	5.00e-5
O <sub>2</sub>	2.30e-2	---	---
HCN	---	---	1.21e-3
HNC	---	---	1.21e-3

the original test number from [11] and the corresponding characteristic velocity ratio which is also varying. It has to be noted that, although in [11] the total chamber temperature is a given datum, during the test campaign it was actually derived from the total enthalpy of the flow, that is in fact the actual measured data. For this reason, time-enthalpy plots in [11] have been considered as more reliable data and have been used to calculate the time-averaged value of the test total enthalpy from which, by means of chemical equilibrium calculations [38], the total chamber temperatures and gas composition listed in Table 6.1 have been derived. Since the developed boundary condition applies only to the case of steady-state ablation, both the time-averaged pressure and total enthalpy have been calculated over the actual erosion period (individuated in [11] as the time for which the chamber pressure departed from its nominal value). As a consequence, also the experimental steady-state erosion rate has been obtained by dividing the total erosion by the erosion time.

**Table 6.2** – MXS-89 material component characteristics [10].

$\rho_{0,A}$ , kg m <sup>-3</sup>	$\rho_{0,B}$ , kg m <sup>-3</sup>	$\rho_{0,R}$ , kg m <sup>-3</sup>	$\Gamma_M$
324.21	973.12	1927.02	0.305

All the input data regarding the ablative material (MXS-89) composition that are needed to apply the decomposition model described previously are listed in Table 6.2. Since in the experimental campaign the chamber pressure was fairly lower than the other test cases presented so far, omitting the evaluation of the radiative heat flux cannot be considered a reasonable choice here. However, the accurate evaluation of the radiation implied a strong modification of the code and was far beyond the scope of the present work. Therefore a simplified treatment of the radiative heat flux has been sought in order to account for it in the surface energy balance. In particular, considering the gas emissivity, very low with respect to the TPS's one, the incoming radiative heat flux (from the gas to the wall) has been considered of secondary importance and, therefore, neglected. For this reason the wall radiative heat flux (directed from the wall to the gas) has been considered in the surface energy balance Eq. (6.6) and a further datum as the wall emissivity, necessary to the heat flux evaluation, was needed.<sup>3</sup> Unfortunately, a single value of the emissivity has not been found in literature for the analyzed material. As a consequence, a typical value of 0.85 for silica has been applied in all the performed simulations. It has to be noted that several simplifications have been introduced by using this radiative heat flux modeling. In fact, the radiative heat flux emitted from the ablative wall has been considered totally absorbed by the nozzle flow before reaching the opposite wall of the nozzle. This allowed to eliminate the possible mutual

---

<sup>3</sup>The wall radiative heat flux is evaluated as  $\dot{q}_{rad,out} = \sigma \varepsilon_w T_w$ , where  $\sigma = 5.670\,373 \times 10^8 \text{ W m}^{-2} \text{ K}^{-4}$  is the Stefan-Boltzmann constant and  $\varepsilon_w$  is the wall emissivity.

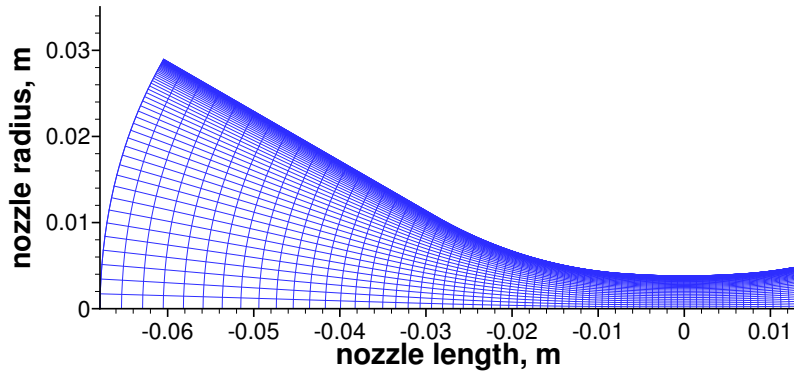


**Figure 6.7** – Nozzle geometry and selected mesh.

radiation between facing internal walls that could have been otherwise complicate the model. Moreover, because of the high nozzle mass flow rate, this relatively small amount of energy emitted from the wall, and absorbed by the gas, has not been considered in the gas energy conservation equation. Theoretically this simplification should not introduce significative errors, and has been already used in similar problem [24], unless the emitted radiation is absorbed in a very thin gas layer, significantly influencing the temperature distribution into the boundary layer and, consequently, the convective heat flux.

#### 6.4.2 Results and discussion

An original  $70 \times 60$  grid has been generated (Fig. 6.7). Cell clustering in the radial direction has been imposed to ensure a good resolution of the flow region next to the wall and a value of  $y^+$  less than 1.0. Because of the nature of this simplified ablation model, that considers an isothermal wall at the silica melting temperature, the discussion upon the simulation results cannot be as extended as in the previous validation test cases. As explained, in fact, only the fail mass flow rate of the surface material has been considered, and for the nozzle

sections where no erosion occurs, no further consideration can be done inasmuch the steady-state ablation approximation is unusable. However, for the region in which the surface material melts, the erosion rate, the char mass flow rate and the pyrolysis gas mass flow rate can be evaluated.

The obtained erosion rate profiles are shown together with the throat erosion rate experimental value in Fig. 6.8. As seen, the numerical results agree reasonably well with the experimental data for the three simulated O/F ratios ( $O/F=2$ , 1, and 0.38, corresponding to the test cases number 1129, 1339 and 1145, respectively) which are characterized by different combustion efficiencies. The numerical simulations seem to correctly represent the erosion rate variation and only a slight departure from the experimental erosion rates has been found. The result for  $O/F=2$  (which corresponds to the optimum) gives a percentage error of less than 1%, the one for  $O/F=0.38$  underestimates the experimental values by about 13% and, finally, the one for  $O/F=1$  presents a null erosion rate against an experimental value of  $0.0037 \text{ mm s}^{-1}$ .

Finally, it can be asserted that the developed boundary condition has shown good prediction capacity in evaluating the silica-phenolic erosion rate when the environmental condition are such that the silica melting occurs. Obviously, this is just a small range of possible operative conditions and, if other ablation mechanisms take place, a more detailed ablation model must be developed, and surface melting rate should be accounted for as well as the diffusion of the oxidizing species inside the melt layer and the possible internal mechanisms different than the resin decomposition. Nevertheless, because of the nature of these other silica-phenolic ablation mechanisms, that are mainly sub-superficial, the present model can be considered as one of the best approximations that can be done as long as coupling with a detailed transient computation of the in-depth material evolution is not considered.

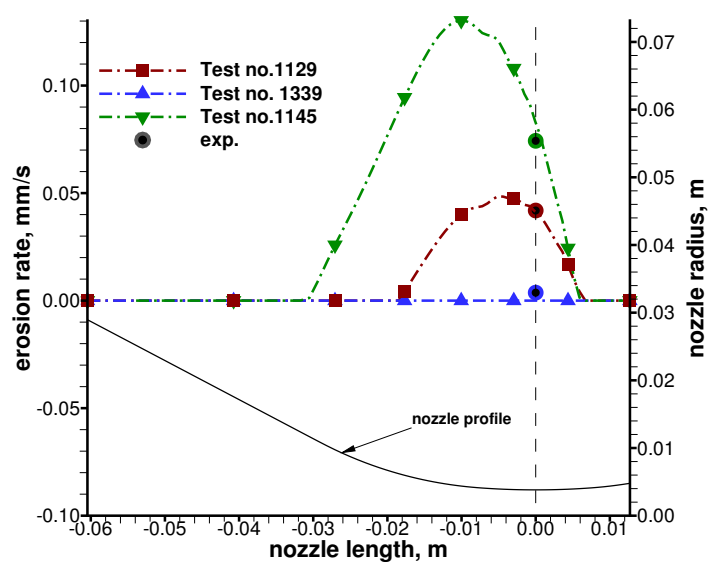


**Figure 6.8 – Erosion rate distributions and experimental data (exp.) at the throat section.**

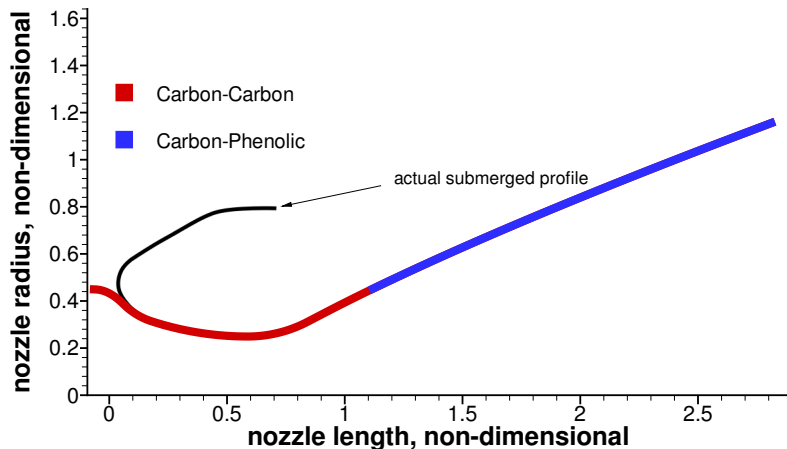
## **Part II**

# **Application Results**

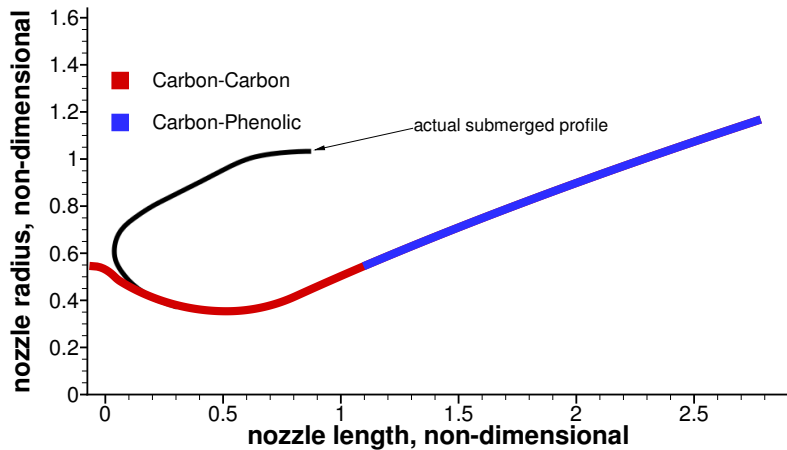
---

## Zefiro 9 and Zefiro 23 nozzle erosion analysis

As described in the Introduction the use of different ablative materials as liners for different parts of the nozzle is a common practice. Non-pyrolyzing, highly densified and more expensive materials such as carbon-carbon composites are usually adopted for the high heat transfer regions, such as the throat. The regions downstream of the throat are characterized by less heat transfer and erosion. As a consequence, different, lower density and less expensive pyrolyzing materials are generally used. In this chapter, the presented model is applied with the purpose of simulating the erosion behavior of a full-scale solid rocket motor with a composite nozzle characterized by the use of pyrolyzing and non-pyrolyzing carbon-based ablative materials. Data provided by Avio Group S.p.A. have been used to study the complete nozzle erosion of Zefiro 9 and Zefiro 23, the European Vega launcher 3<sup>rd</sup> and 2<sup>nd</sup> stage solid rocket motors, respectively. The obtained simulation results are then compared against the post-firing experimental profiles by applying the shape-change strategy developed in [28].



(a) Zefiro 9.



(b) Zefiro 23.

**Figure 7.1 – Zefiro 9 and Zefiro 23 liner materials.**

## 7.1 Input data

The two motors share the same architecture for the nozzle thermal protection system (Fig. 7.1). After a first carbon-carbon ablative liner for the Integral Throat/Entrance (ITE), a second carbon-carbon liner is used, which constitutes the After Throat Divergent (ATD). Downstream of the ATD, two subsequent ablative liners of carbon-phenolic are used for the forward divergent thermal protection system. These two liners are made of the same ablative material: carbon-

phenolic. The carbon-carbon material used for the ITE and ATD has a density of  $\approx 1.90 \text{ g cm}^{-3}$ , while the carbon-phenolic has a density of  $\approx 1.50 \text{ g cm}^{-3}$  and a  $\varphi$  ratio of  $\approx 0.12$  (low resin content). Because of the proprietary nature of the data, in some cases only approximate or non-dimensional values are given. As shown in (Fig. 7.1), the adopted nozzle entrance profile has been modified with respect to the real geometry using a parabolic curve, which becomes parallel to the nozzle axis at the inlet section. The shape of the nozzle entrance has a very small effect on the flowfield due to the low flow velocity at the inlet. This modification has been made because both motors have a submerged-nozzle configuration but the submerged nose erosion is beyond the scope of the present analysis. Because the length of the wall affects the boundary-layer thickness, and hence the heat and mass transfer rate, the total wall length of the parabolic curve is equal to that of the real entrance profile, which is assumed to start at the stagnation point.

Figure 7.3 shows the numerical grid and the pressure field at the mean chamber pressure for the two nozzles. The different expansion ratio of the two nozzles can be noted. The non-dimensional pressure-time traces is shown in Fig. 7.2. Zefiro 9 and Zefiro 23 have a mean chamber pressure of approximately 50 bar and 60 bar, respectively. The burning time is approximately 130 s for Zefiro 9 and 80 s for Zefiro 23. The numerical grid discretizes the computational domain contoured by the nozzle of the two motors. The hot exhaust gas flowing in the nozzle consists of the combustion products of metallized AP/HTPB composite propellants. As in [28], and in the validation test cases of Chapters 4 and 5, all the  $\text{Al}_2\text{O}_3$  present in the exhaust gas is assumed to be in the gas-phase and mechanical erosion contribution is neglected. The computational domain is subdivided into  $170 \times 100$  and  $140 \times 100$  grid points in the axial and radial directions for Zefiro 9 and Zefiro 23, respectively (Fig. 7.3). The meshes have

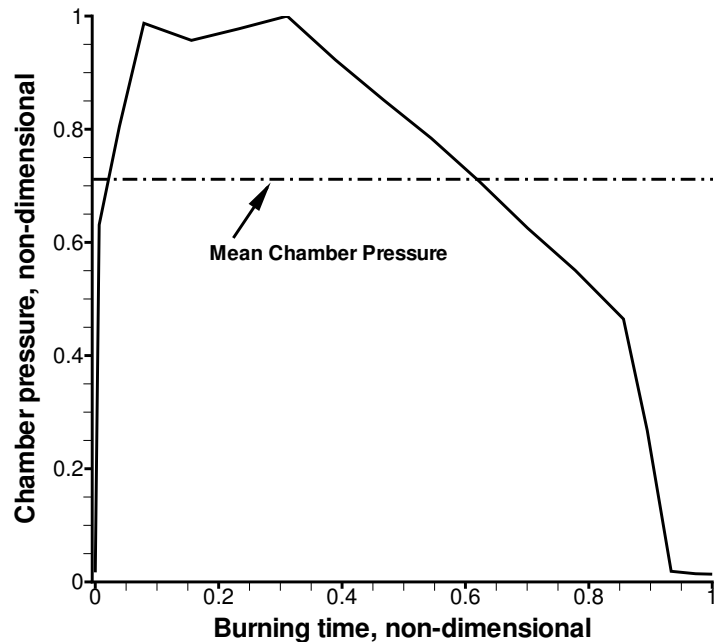
**Table 7.1** – Throat erosion rate of Zefiro 9 and Zefiro 23 for three different refined meshes.

Nozzle	Grid	$\dot{s}_{tot}$ , mm s <sup>-1</sup>
Zefiro 9	85×50	0.179
	170×100	0.188
	340×200	0.190
Zefiro 23	70×50	0.206
	140×100	0.215
	280×200	0.218

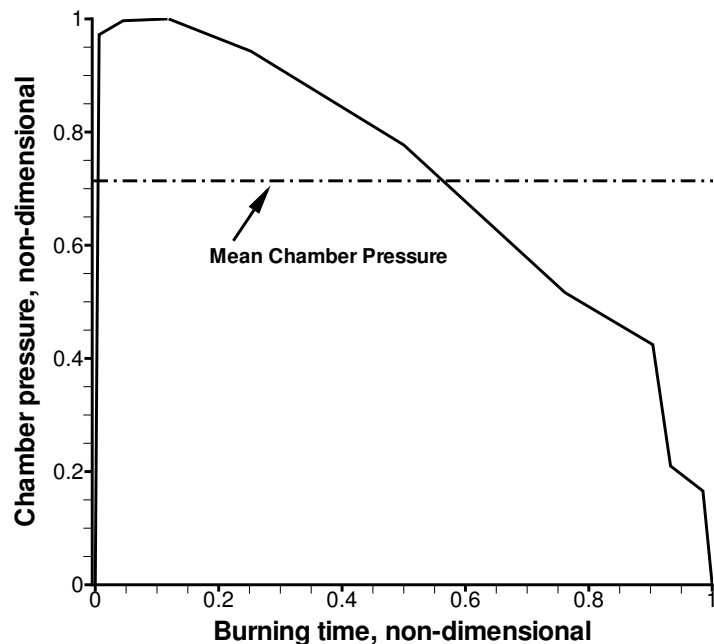
been verified by a grid convergence analysis (the quantitative analysis of solutions obtained on three grid levels confirms that the spatial order of accuracy is close to the formal value of 2 for both the nozzles, see Table 7.1) and are stretched in the radial direction such to ensure a value of  $y^+$  less than 1.0 at the wall-adjacent cell all along the nozzle length to accurately describe the boundary layer. Both the medium meshes ( Zefiro 9 and Zefiro 23) show a difference less than 2.0% with respect to the erosion rate obtained by means of the Richardson extrapolation [73] and, therefore, have been considered suitable for the present analysis. All the computations presented are at the steady-state condition obtained by iterating in time until residuals drop by five orders of magnitude.

## 7.2 Simulation results

As the nozzle thermal protection system is made of two different materials, different boundary-conditions are imposed at the surface. To describe the carbon-carbon ablation, the finite-rate ablation model for non-pyrolyzing ablative material, described in Chapter 4, is used. Differently, for the carbon-phenolic part, the model described in Chapter 5 that account for the pyrolysis gas injection, is

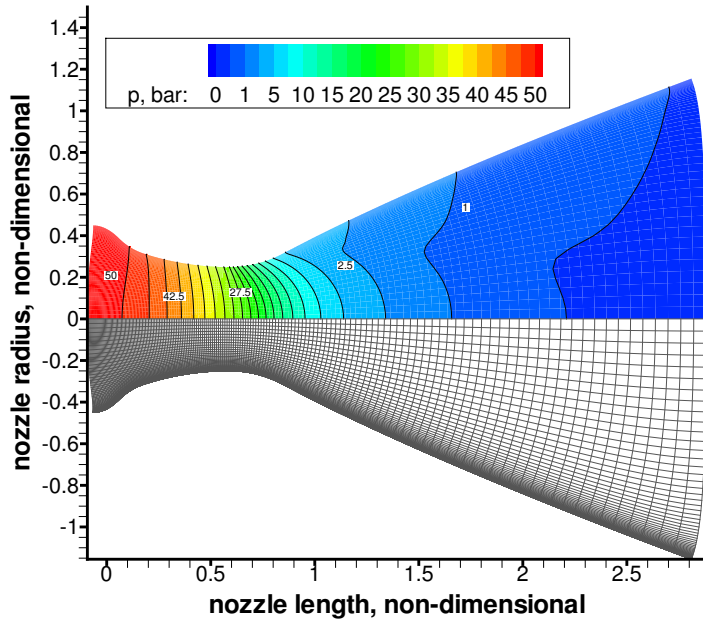


(a) Zefiro 9.

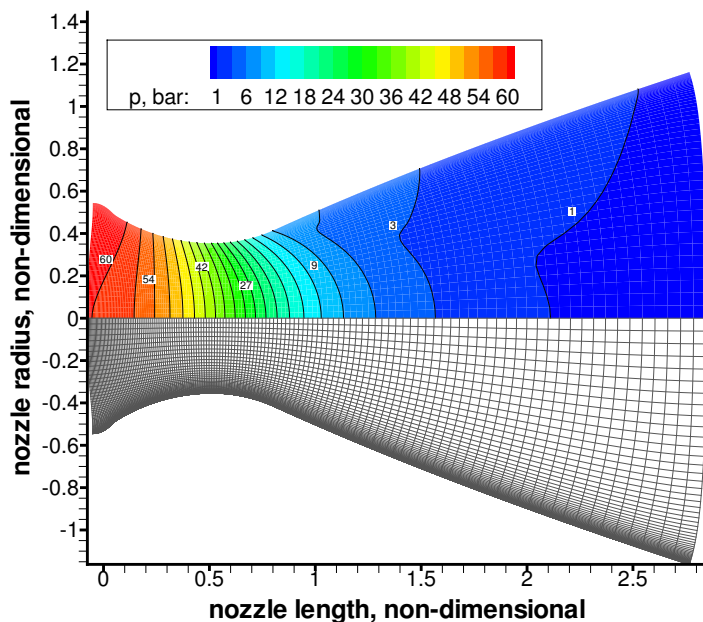


(b) Zefiro 23.

**Figure 7.2 – Time-pressure trace.**



(a) Zefiro 9.

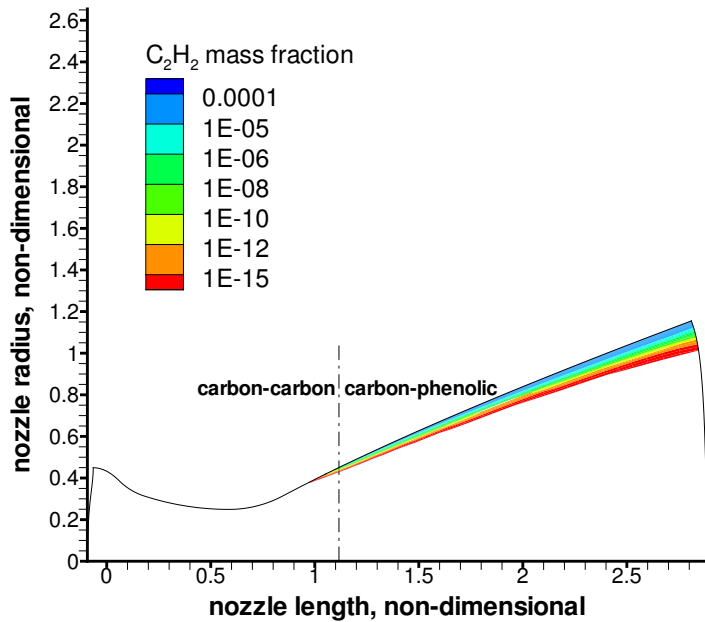
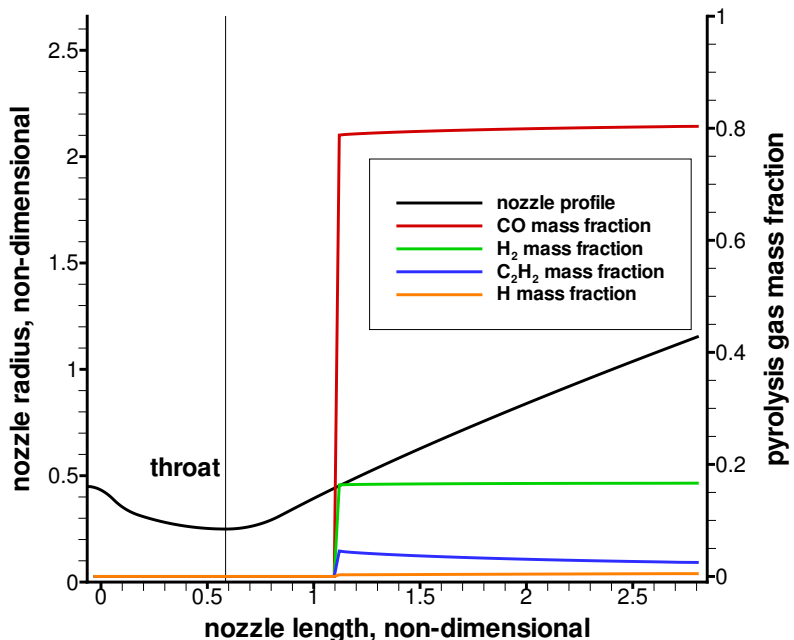


(b) Zefiro 23.

**Figure 7.3 – Zefiro 9 and Zefiro 23 pressure field (average pressure condition) and numerical grid.**

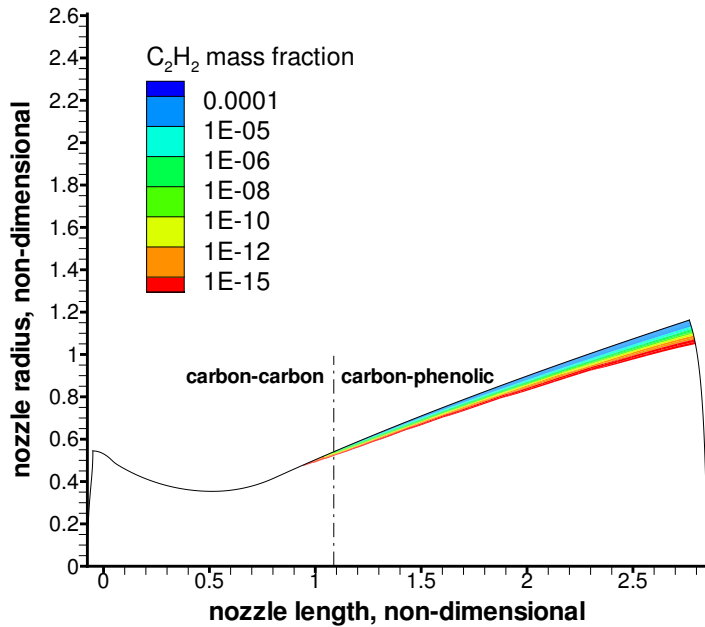
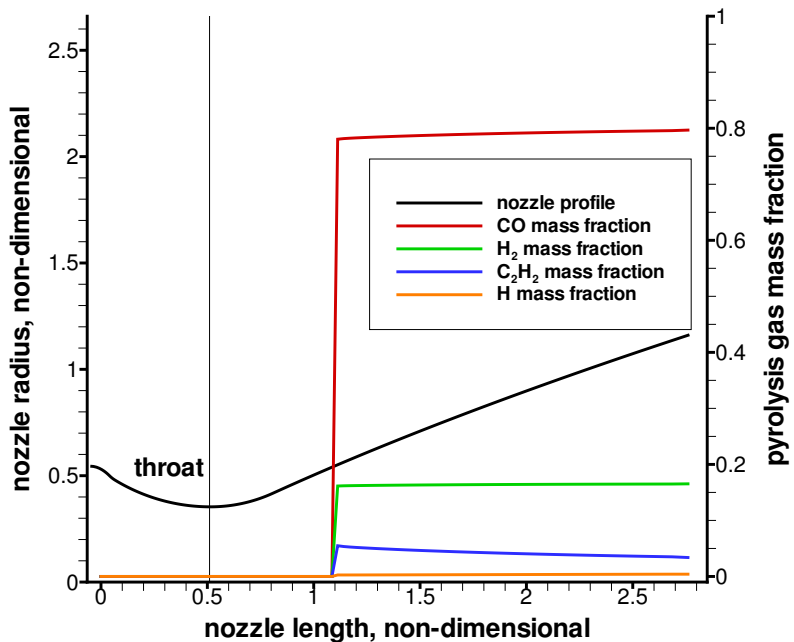
employed. Since the char density of the carbon-phenolic is known, the decomposition model that uses a constant value of the  $\varphi$  ratio is applied (Section 5.1). Due to the injection of the pyrolysis gas at the material-change point, the chemical composition of the wall mixture of gases is modified. Figures 7.4 and 7.5 show the mass fraction field of  $C_2H_2$  and the pyrolysis gas composition at the surface (only major species are shown) for the two motors. The species  $C_2H_2$  is only present in the pyrolysis gas, so it represents a tracer species which can help to visualize the pyrolysis gas diffusion in the boundary layer. As shown in Figs. 7.4(a) and 7.5(a),  $C_2H_2$  is diffusing downstream of the first pyrolysis gas injection point. A very small concentration of  $C_2H_2$  is also present upstream of the first injection point, due to diffusion in the subsonic boundary layer. The pyrolysis gas, as shown in Figs. 7.4(b) and 7.5(b), is mainly composed of CO and  $H_2$ , with a minor amount of  $C_2H_2$  and H, for the present surface temperature and pressure conditions. Because oxidizing species presence is negligible in the pyrolysis gas, its injection in the boundary layer can help reducing the char erosion rate, as it blows the oxidizing species present in the flowfield away from the surface. However this effect is minimal, as will be shown later.

Figure 7.6 shows the various heat flux contributions along the nozzle length. Because the surface energy balance is imposed at the surface (Eq. (4.2) for carbon-carbon and Eq. (5.8) for carbon-phenolic), the sum of the various contributions is zero. The chemical heat flux can be obtained if the diffusive mass flux calculated from the species surface mass balance (Eq. (4.1) for the non-pyrolyzing material or Eq. (5.5) for the pyrolyzing one) is substitute in the surface energy balance (Eq. (4.3) for the non-pyrolyzing and Eq. (5.8) for the pyrolyzing mate-

(a) Zefiro 9  $C_2H_2$  mass fraction field.

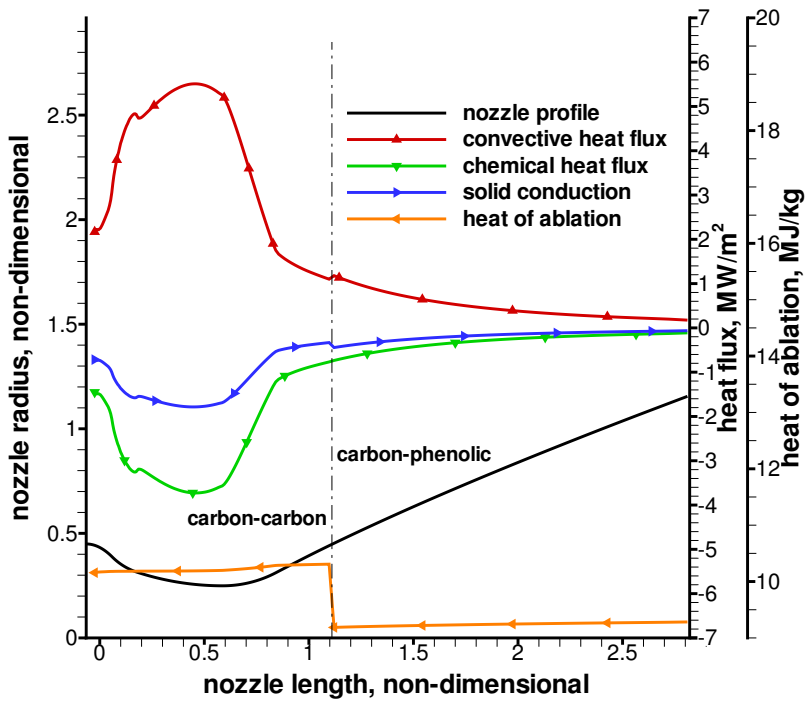
(b) Zefiro 9 wall pyrolysis gas composition distribution along the nozzle length.

**Figure 7.4** –  $C_2H_2$  mass fraction field and pyrolysis gas composition for Zefiro 9 (average pressure condition).

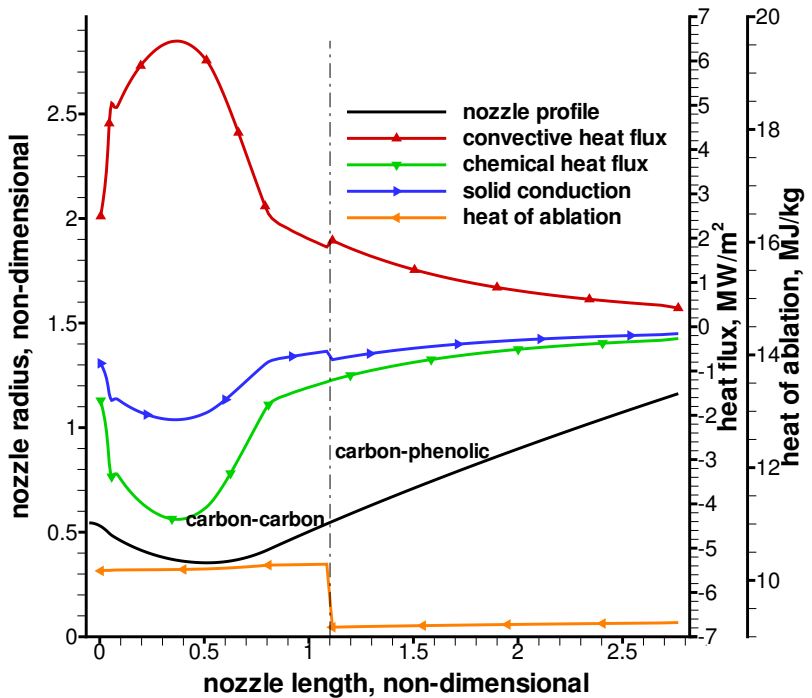
(a) Zefiro 23  $\text{C}_2\text{H}_2$  mass fraction field.

(b) Zefiro 23 wall pyrolysis gas composition distribution along the nozzle length.

**Figure 7.5 –  $\text{C}_2\text{H}_2$  mass fraction field and pyrolysis gas composition for Zefiro 23 (average pressure condition).**



(a) Zefiro 9.



(b) Zefiro 23.

**Figure 7.6 – Wall heat fluxes and heat of ablation (average pressure condition).**

rial, respectively):<sup>1</sup>

$$\dot{q}_{chem} = \sum_{i=1}^{N_c} \sum_{r=1}^{N_r} \omega_i^r h_{i_w} - \dot{m}_s h_{s_w} = \dot{m}_{tot} \Delta H_{abl} \quad (7.1)$$

where the subscript “tot” indicate either the solid mass flow rate or the sum of solid and pyrolysis gas mass flow rates if non-pyrolyzing or pyrolyzing materials are considered, respectively. The term

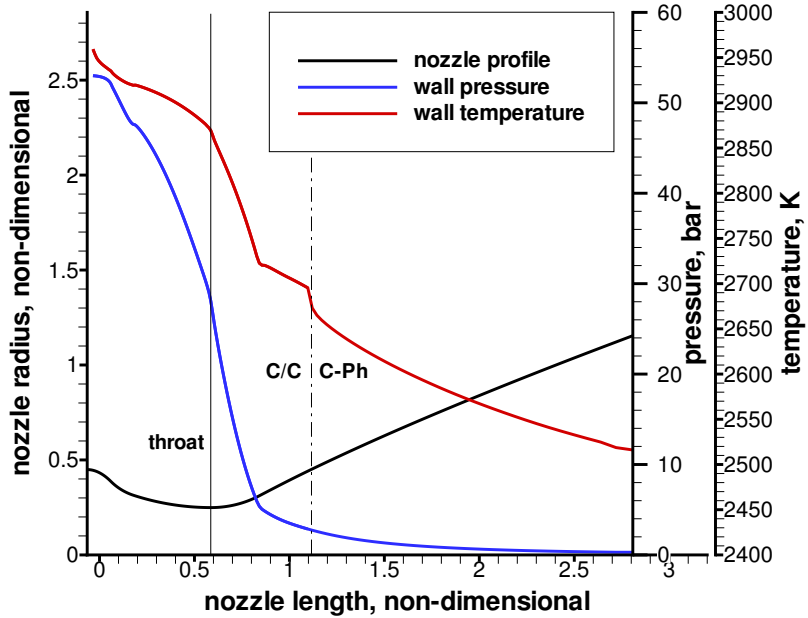
$$\Delta H_{abl} = \frac{\dot{m}_s}{\dot{m}_{tot}} \sum_{i=1}^{N_c} \sum_{r=1}^{N_r} \frac{\omega_i^r}{\dot{m}_s} h_{i_w} - h_{s_w} \quad (7.2)$$

is the so-called heat of ablation, which is the difference between the enthalpies of the species created or consumed by the surface ablation process and the enthalpy of the solid material per unit mass of material ablated. As shown in Fig. 7.6, a large part of the incoming convective heat flux is absorbed by the endothermic surface ablation process and the remaining part is conducted into the material. The heat of ablation is positive due the endothermic nature of the surface heterogeneous reactions.

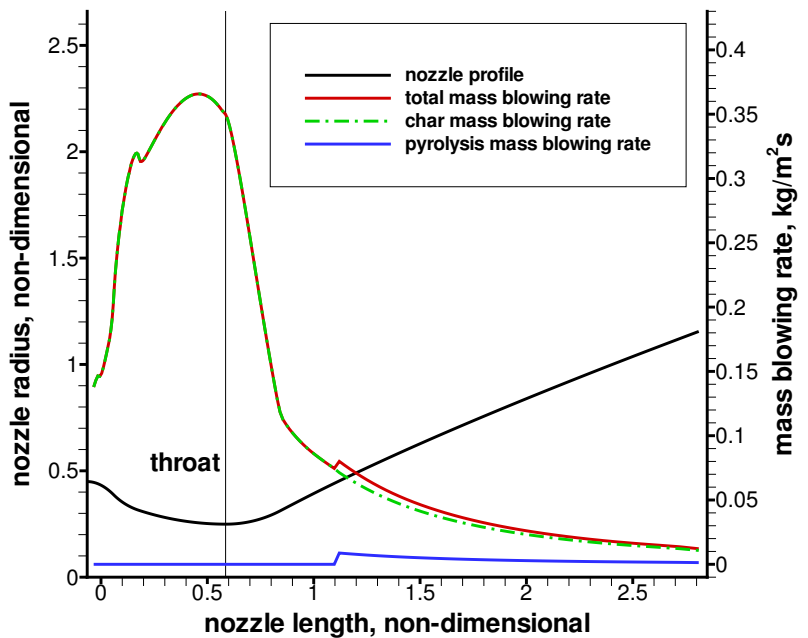
Figures 7.7 and 7.8 show pressure, temperature, and ablation mass rate distributions along the nozzle length for the two motors. Wall pressure is unaffected by the pyrolysis gas injection, while wall temperature shows a drop at the material change section. The temperature drop is similar for the two motors, even if Zefiro 23 is characterized by a slightly higher wall temperature, due to the higher average chamber pressure. The abrupt change of slope of the pressure and temperature distributions is due to the change of curvature of the nozzle profile between the throat and the diverging section, which is almost conical for both motors. The total ablation mass blowing rate, which is the sum of the char

---

<sup>1</sup>The subscript “s” here represents either the solid mass flow rate of charred or non-charred material in case of pyrolyzing and non-pyrolyzing material, respectively.

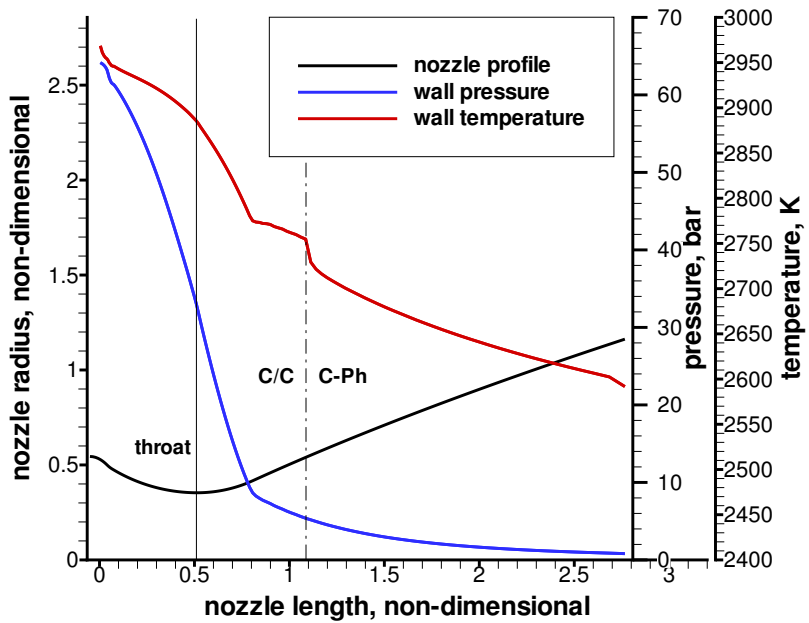


(a) Zefiro 9 surface pressure and temperature distributions along the nozzle length

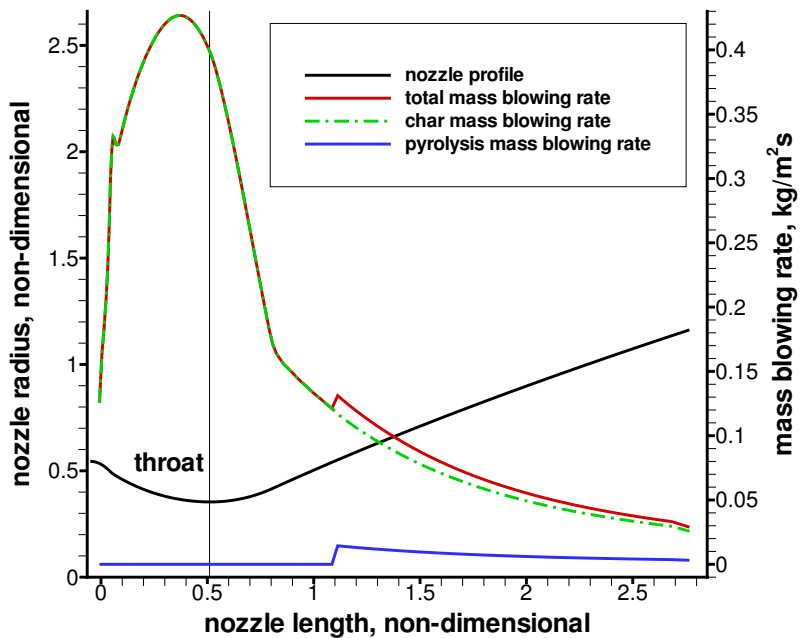


(b) Zefiro 9 ablation mass rates distributions along the nozzle length

**Figure 7.7** – Surface pressure, temperature, and ablation mass rates distributions for Zefiro 9 (average pressure condition).



(a) Zefiro 23 surface pressure and temperature distributions along the nozzle length

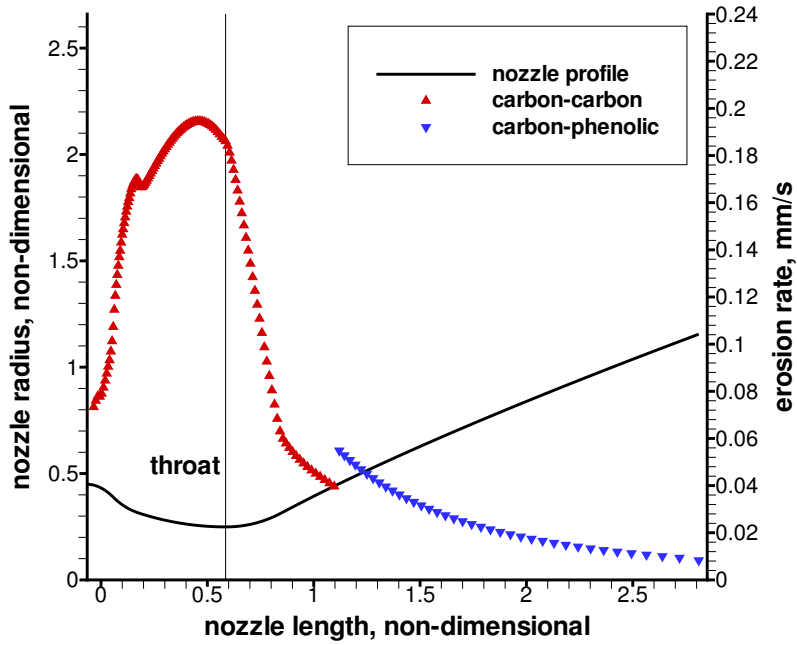


(b) Zefiro 23 ablation mass rates distributions along the nozzle length

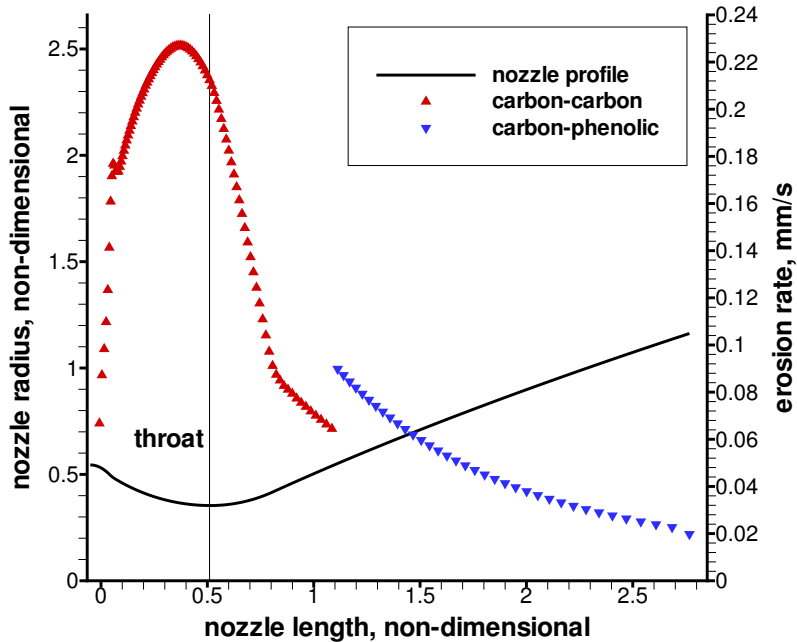
**Figure 7.8** – Surface pressure, temperature, and ablation mass rates distributions for Zefiro 23 (average pressure condition)

blowing rate and the pyrolysis blowing rate, shows a sudden increase, due to the injection of the pyrolysis gas, at the material change section. The char blowing rate, instead, is essentially unaffected by the pyrolysis injection. Actually the char blowing rate is slightly decreasing due to the pyrolysis gas injection but the effect is so small, due to the limited amount of pyrolysis injection (small  $\varphi$  ratio), that it cannot be detected in the figure. The total mass blowing rate difference corresponding to the material change is  $\approx 0.01 \text{ kg m}^{-2} \text{ s}^{-1}$  for Zefiro 23 and  $\approx 0.06 \text{ kg m}^{-2} \text{ s}^{-1}$  for Zefiro 9. Such a difference is higher for Zefiro 23 because the material change occurs in a nozzle section having a lower expansion ratio than that of Zefiro 9. Because the material density is also changing, the difference in terms of erosion rate is higher, as shown in Fig. 7.9, with  $\approx 0.025 \text{ mm s}^{-1}$  for Zefiro 23 and  $\approx 0.015 \text{ mm s}^{-1}$  for Zefiro 9. Such a difference can produce a step between the two materials of the order of few millimeters at the end of the burning time.

The comparison between the predicted and measured final nozzle profile after the motor firing is shown in Fig. 7.10 for the two motors. Four different sets of experimental measurements are available, one for each ablative liner: carbon-carbon ITE, carbon-carbon ATD, first carbon-phenolic forward divergent and second carbon-phenolic forward divergent (same material but different fiber orientation, which was not modeled in the present work). The predicted final nozzle shape has been computed according to two different approaches: neglecting and considering the effect of nozzle shape change. In both the erosion is assumed to occur normal to the local surface; this means that a point in the converging section is shifted downstream, while a point in the diverging section is shifted upstream by the erosion process. The shape change effect is accounted for coupling the CFD and the nozzle recession using a loosely coupled technique. This means that the CFD simulations are started with the initial unablated shape, and the



(a) Zefiro 9



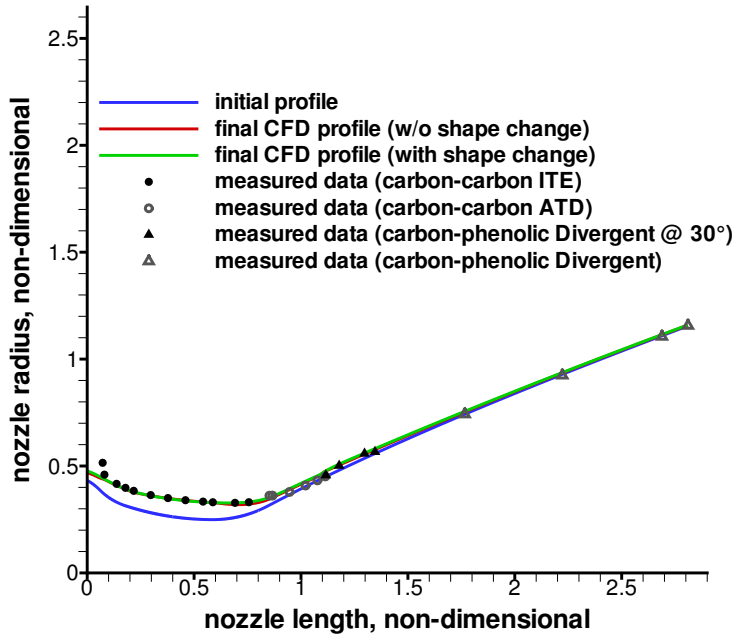
(b) Zefiro 23

**Figure 7.9** – Erosion rate distribution along the nozzle length for Zefiro 9 and Zefiro 23 (average pressure condition).

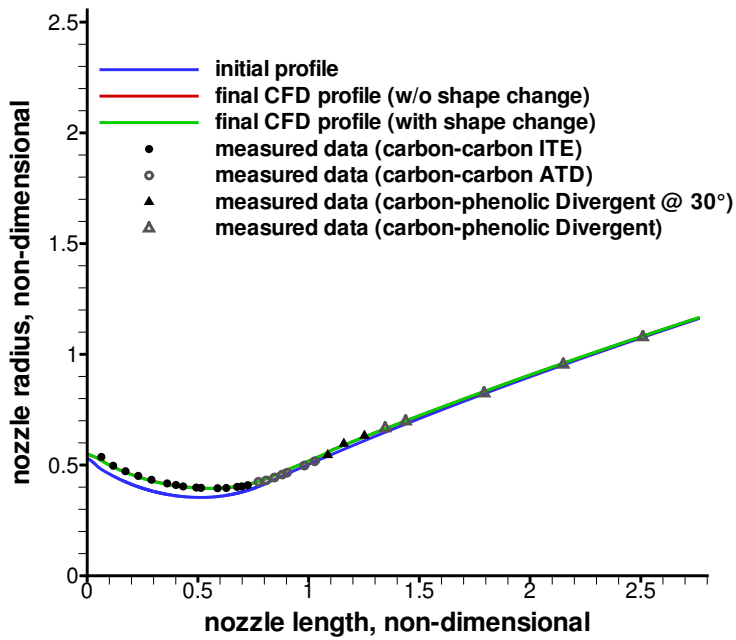
surface erosion rate is computed; after that, the shape evolution model is run for a portion of the burning time, chosen to ensure that a predetermined maximum recession level is not exceeded. Then, a new CFD grid is generated using the re-ceded shape, and a new CFD solution using this grid is computed. Subsequently, the erosion rate distribution is updated, and the procedure is repeated until the total burning time is reached. Each CFD computation is performed at the mean chamber pressure of the corresponding time step. A maximum time step of 20 s has been selected for both motors, because it assures that the amount of recession never exceeds 5% of the throat radius. Seven time steps have been considered for Zefiro 9 and four time steps for Zefiro 23.

Figures 7.11 and 7.12 show a detail of the predicted and measured final profiles for the different ablative liners for Zefiro 9 and Zefiro 23, respectively. The model is fully capable of predicting not only the throat erosion rate but also the axial shifting of the throat and the flattening of the whole throat region. Looking at Figs. 7.11(a) and 7.12(a), in fact, it can be seen that the final eroded profile in the throat region is flatter than the initial profile and the throat has been shifted downstream by the prolonged erosion process. Such an axial shifting and flattening of the throat region cannot be properly evaluated without taking into account the coupling of the eroding nozzle profile and the CFD solution. Neglecting such coupling can lead to errors in the estimation of the throat erosion, which is a key parameter for motor performance prediction [28]. The agreement with the measured eroded profile is very good regardless of the shape change for Zefiro 23, while the shape change affects a bit more the solution obtained for Zefiro 9. The reason why the shape change is important for Zefiro 9 and negligible for Zefiro 23 is due to the combinations of two effects. The first one is the longer burning time and the smaller dimensions of Zefiro 9, which clearly enhance the shape-change phenomena; the second one is the abrupt slope

change of the erosion curve for Zefiro 9 due to the strong change of curvature radius at the throat location. Such an abrupt change of the erosion curve is not present on Zefiro 23, because the curvature change upstream/downstream the throat is milder [28]. Results of the diverging part (Figs. 7.11(b) and 7.12(b)) show a good reproduction of the eroded profile for the carbon-phenolic forward divergent for both motors, provided that the measuring points are sufficiently far from a material change, which would need much more modeling efforts to be properly characterized also because of the complex flow structure around the step [87]. The computed solutions, however, fail to reproduce the erosion of most of the carbon-carbon ATD which, according to the experimental data, is almost non-eroding. The ATD erosion prediction is similar for both motors showing a good agreement with the measurements for the measuring points closer to the throat, but departing from the experimental data for the remaining measuring points. This aspect has to be further analyzed, looking in more details into the experimental data, as the fact that these measuring points have not much receded from their original positions, does not necessarily imply that they did not experience any significant erosion. However, the model has proven a good capability in reproducing the nozzle erosion in a real full-scale application and the obtained encouraging results suggest that it can be reasonably considered as a prediction approach for future analysis.

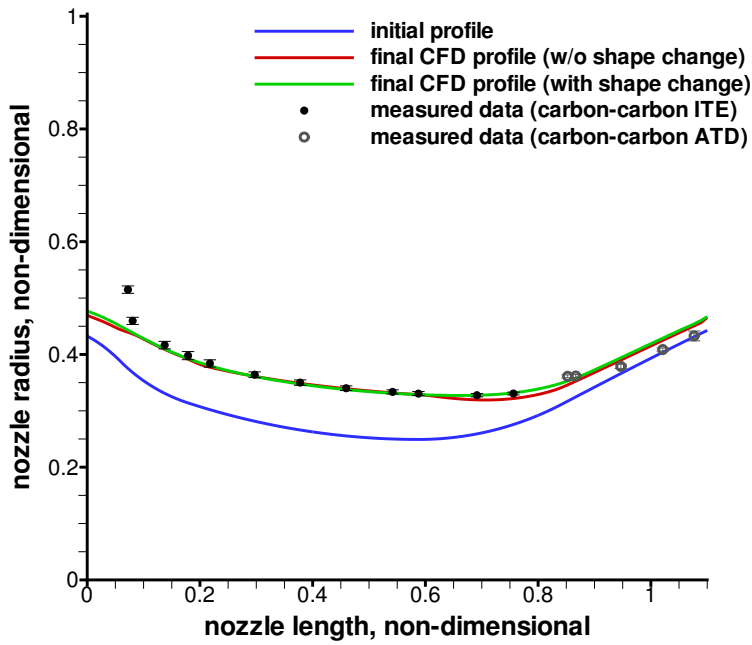


(a) Zefiro 9

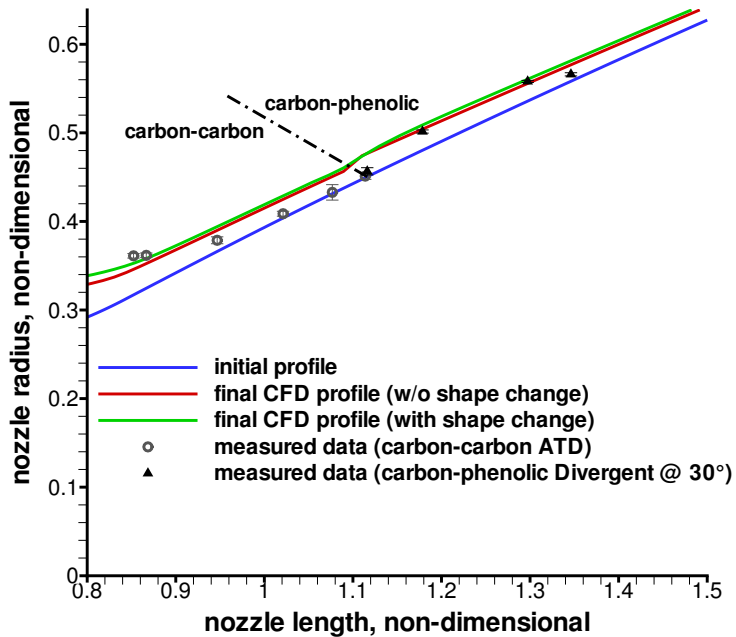


(b) Zefiro 23

Figure 7.10 – Predicted and measured nozzle profiles for Zefiro 9 and Zefiro 23.

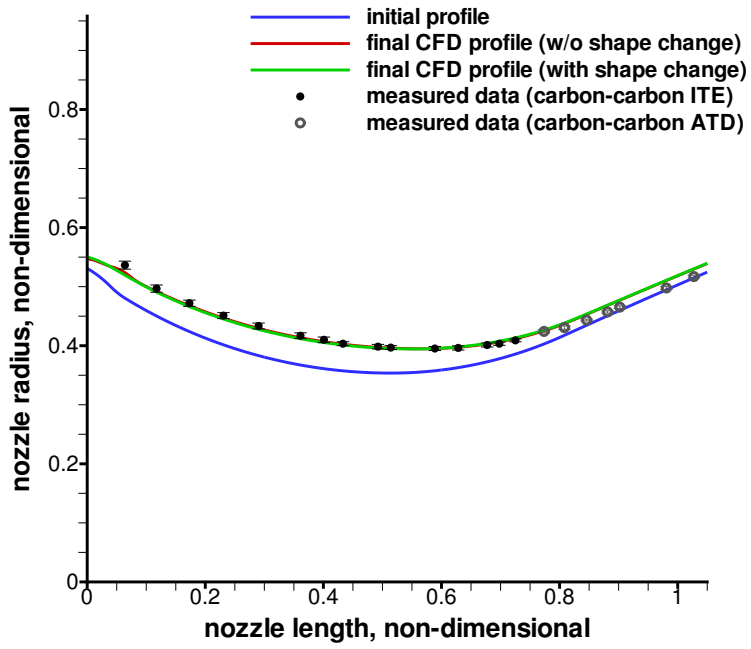


(a) ITE and ATD ablative liners

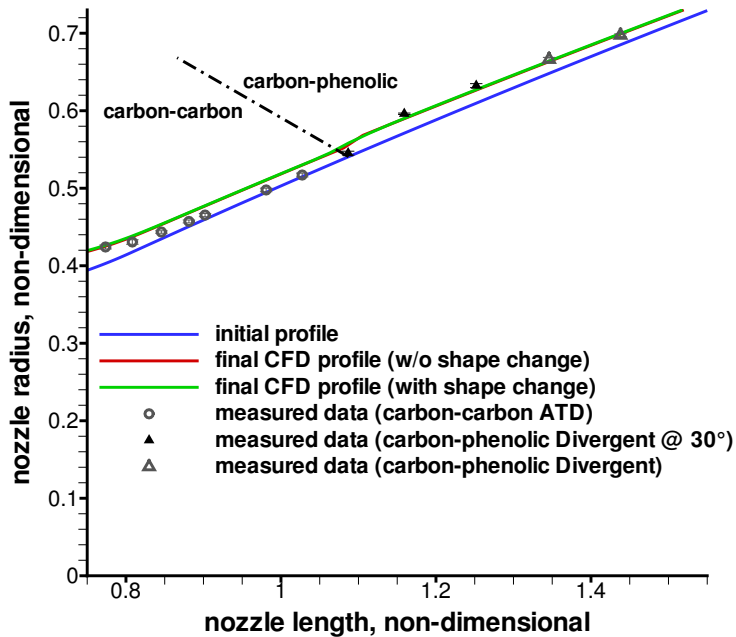


(b) ATD and Divergent ablative liners

**Figure 7.11** – Detail of predicted and measured (error bars are reported) profiles for Zefiro 9.



(a) ITE and ATD ablative liners



(b) ATD and Divergent ablative liners

**Figure 7.12** – Detail of predicted and measured (error bars are reported) profiles for Zefiro 23.

---

## Ablation in oxygen/methane thruster environment

Oxygen/methane liquid rocket engines have recently gained interest for various space applications, from launch systems, such as boosters and upper stages, to space propulsion [88, 89, 90]. Methane as a fuel can provide a higher specific impulse than other hydrocarbons; moreover, differently than oxygen/hydrogen propellant combination, oxygen/methane can be considered space storable and is favored by a higher density [91]. In developing these kinds of engines, attention should be paid to reduce costs and system complexity and to improve reliability. For example, looking at the class of low-pressure/low-thrust upper-stage and deep-space engines, passive cooling systems, such as radiative or ablative, have gained interest in these kinds of applications [92, 93]. Therefore, understanding of the behavior of this kind of thermal protection system (TPS) in oxygen/methane combustion products environment can be of relevant importance in developing oxygen/methane thruster.

In this chapter, the ablation models for carbon- and silica-based ablative mate-

rials are used to perform a preliminary analysis on ablative material behavior in oxygen/methane thruster environment.

## 8.1 Input Data

The thrust chamber reported in Fig. 8.2 represents the test geometry. The thrust chamber includes of a cylindrical chamber and a converging-diverging nozzle with a contraction and expansion ratio of approximately 2.4 and 1.4, respectively. The reason for such a relatively small expansion ratio has to be found in the fact that a truncated nozzle profile has been chosen, since the primary objective of the present study is analyzing the ablative chamber and throat behavior.

After a literature review [94, 95], three different ablative materials have been selected for the present analysis: carbon-carbon (C-C), carbon-phenolic (C-Ph) and silica-phenolic (Si-Ph). Tables 8.1 and 8.2 show the chosen virgin densities, decomposing material component densities and the virgin material resin mass fractions. Considering that the two pyrolyzing materials (carbon-phenolic and silica-phenolic) are composed of the same phenolic resin, the decomposing components in Table 8.2 ( $\rho_A$  and  $\rho_B$ ) are identical.

Figure 8.1 shows the normalized oxidizing species mass fractions as a function of the O/F ratio. Six different O/F values have been considered, starting from 2.8 and going toward richer mixtures. The O/F=2.8 has been selected as it is the value where the maximum specific impulse typically occurs [96]. The inlet conditions have been derived from chemical equilibrium calculations [38], by imposing the chamber pressure ( $\approx 10$  bar) and oxygen and methane as reactants in the selected mixture ratio. A first equilibrium calculation has been performed without any constraint on the number of products, and a set of most significant species has been selected; subsequently, the number of allowed species in the

**Table 8.1** – Ablative material characteristics.

Material	Type	$\rho_v, \text{ kg m}^{-3}$
C-C	non-decomposing	1900
C-Ph	decomposing	1460
Si-Ph	decomposing	1741

**Table 8.2** – Decomposing material component characteristics.

Material	$\rho_A, \text{ kg m}^{-3}$	$\rho_B, \text{ kg m}^{-3}$	$\rho_R, \text{ kg m}^{-3}$	$\Gamma_m$
C-Ph	324	973	1564	0.347
Si-Ph	324	973	2066	0.315

equilibrium calculation has been reduced to eight species, verifying that the effect of this reduction was negligible both in terms of chamber temperature and thermodynamic properties variations.

## 8.2 Simulation results

The input conditions that have been obtained for the selected O/F values have been used to perform a wide investigation on ablative material response. The O/F=2.8 chamber condition has been set as the reference one (referred to as nominal in the following) and has been used for a first investigation. A grid sensitivity analysis, to ensure grid independent results, has been performed first. The obtained throat erosion rate for a carbon-carbon nozzle are shown in Table 8.4. The quantitative analysis of solutions obtained on the three grid levels confirms that the spatial order of accuracy is close to the formal value of 2. The discrepancy between the throat mass flow rate obtained by means of the Richardson extrapolation [73] and the one evaluated with the medium grid ( $100 \times 80$ ) is less than 2.5%; therefore, the medium grid has been considered suitable for the

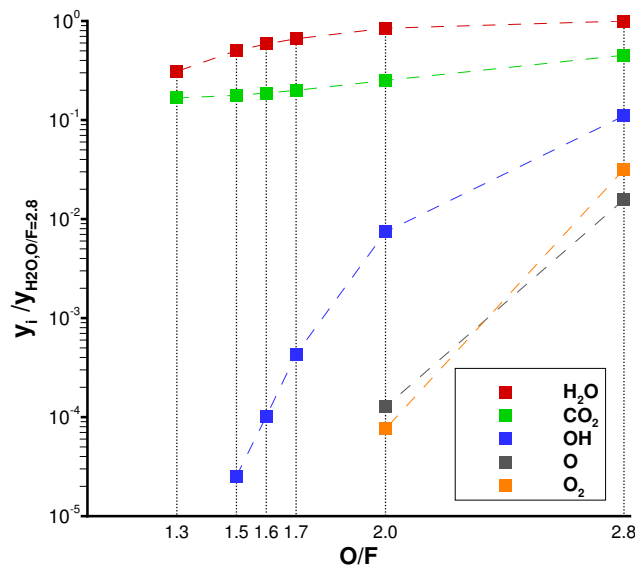


**Figure 8.1** – Oxidizing species mass fractions (normalized with respect to the  $\text{H}_2\text{O}$  mass fraction at  $\text{O}/\text{F}=2.8$ ).

**Table 8.3** – Chamber temperatures at different  $\text{O}/\text{F}$  values for the nominal chamber pressure.

$\text{O}/\text{F}$	2.8	2	1.7	1.6	1.5	1.3
$T_c, \text{ K}$	3239	2698	2255	2076	1883	1464

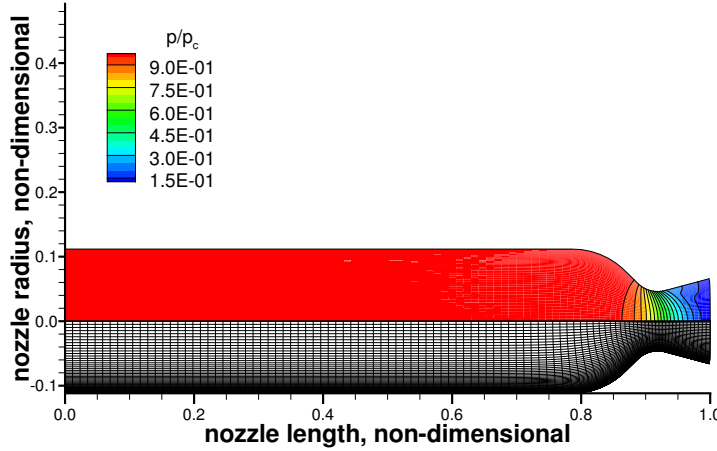


**Figure 8.2** – Pressure field and adopted grid.

present analysis. Cell clustering in the radial directions has been used to ensure a good resolution of the near-wall phenomena as well as a  $y^+$  value less than 1 (Fig. 8.3). Figure 8.2 shows, together with the adopted grid, the non-dimensional pressure field obtained for the nominal condition in case of carbon-carbon material. Note that this single simulation can be considered as representative of all the analyzed ablative materials since the pressure field is not affected by the surface phenomena (this is true also for the wall pressure, Fig. 8.4(a)). The effect of the surface ablation is instead evident in the wall temperature trend depicted in Fig. 8.4(b), where carbon-carbon and carbon-phenolic show a

**Table 8.4** – Throat erosion rate for three different refined meshes.

Grid	$\dot{s}_{tot}, \text{mm s}^{-1}$
$50 \times 40$	0.0570
$100 \times 80$	0.0601
$200 \times 160$	0.0611

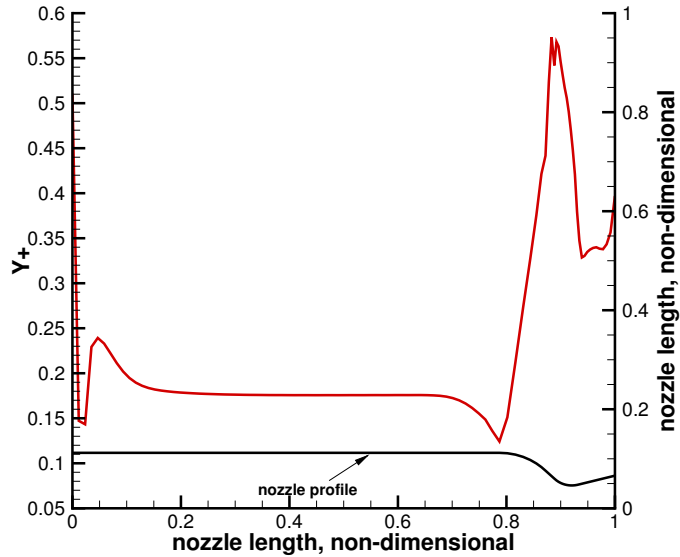
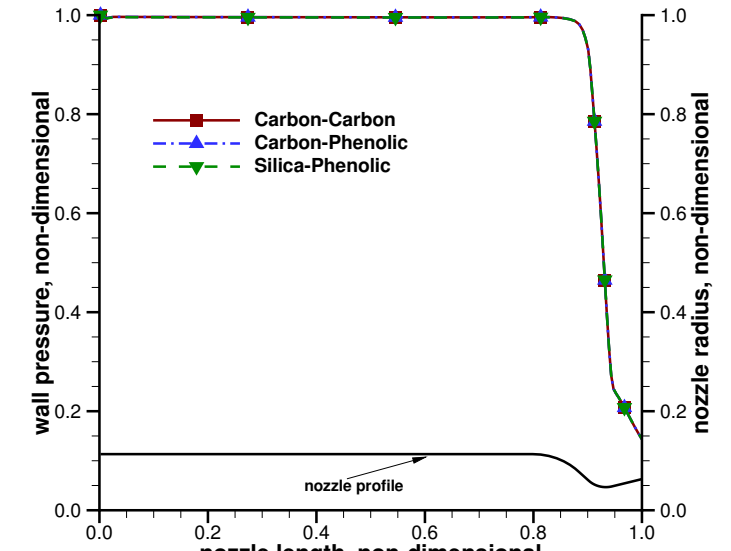
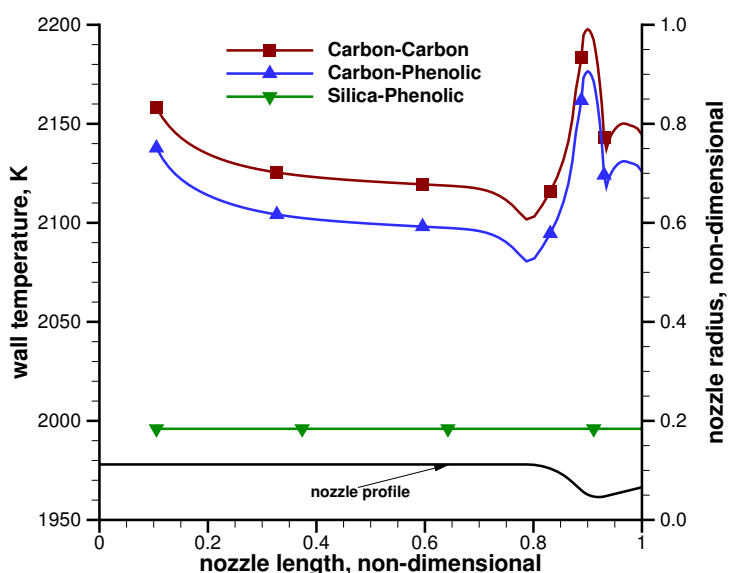


**Figure 8.3 –  $y^+$  profile along the nozzle wall.**

similar profile whereas silica-phenolic, by virtue of its isothermal boundary condition, presents a constant temperature value of 1996 K. At this point, it might be necessary to stress that the simplified treatment of the combustion products adopted for the present analysis does not allow an accurate resolution of the complex chemical field next to the injector plate. However, the influence of such a phenomena on the TPS ablative behavior can be considered of minor importance. Accordingly, in the following figures the results are plotted starting from a distance of one chamber radius from the injector plate, since upstream to this point they cannot be considered representative as the combustion process is not modeled. It has also to be noted that, because of non-disclosure restrictions, all the presented non-dimensional results are normalized with respect to the corresponding throat value that has been obtained from the simulation at the nominal chamber condition in case of C-C wall.



(a) Pressure.



(b) Temperature.

**Figure 8.4** – Wall pressure and temperature for the three selected ablative materials ( $O/F=2.8$ ).

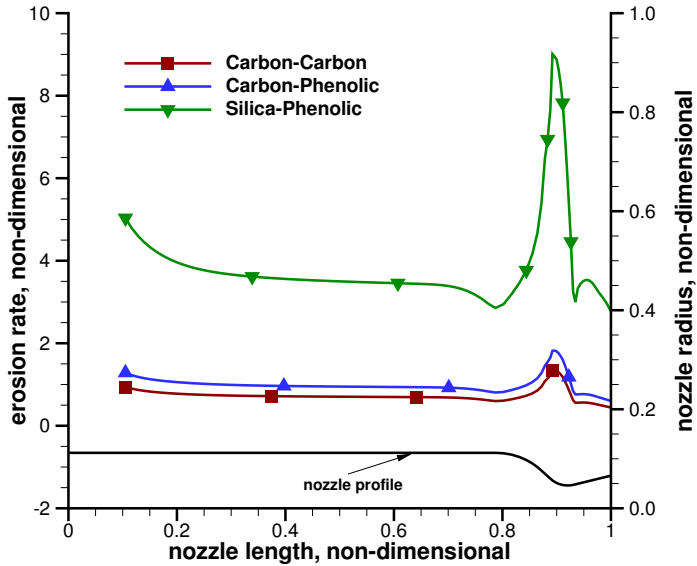


**Figure 8.5 – Erosion rate for the three selected ablative materials ( $O/F=2.8$ ).**

The nominal ( $O/F=2.8$ ) erosion rate values are plotted in Fig. 8.5, where the direct correspondence between these profiles and the wall temperature profiles (Fig. 8.4(b)) is evident in case of carbon-based materials (carbon-carbon and carbon-phenolic). A thorough analysis of the involved processes can be carried out by analyzing the mass flow rate entering the flow from the wall. Figure 8.6 shows the char mass flow rate (due to thermochemical ablation) together with the pyrolysis gas mass flow rate (null for carbon-carbon), revealing that the actual char mass flow rate for the carbon-phenolic is lower than the carbon-carbon (92% of the carbon-carbon value at the throat section). This is due to the blockage effect of the pyrolysis gas injection which is also responsible for the lower surface temperature of carbon-phenolic. Finally, considering that the erosion rate depicted in Fig. 8.5 can be obtained simply dividing the char mass flow rate by the char density (Eq. (5.7)), the higher erosion rate for carbon-

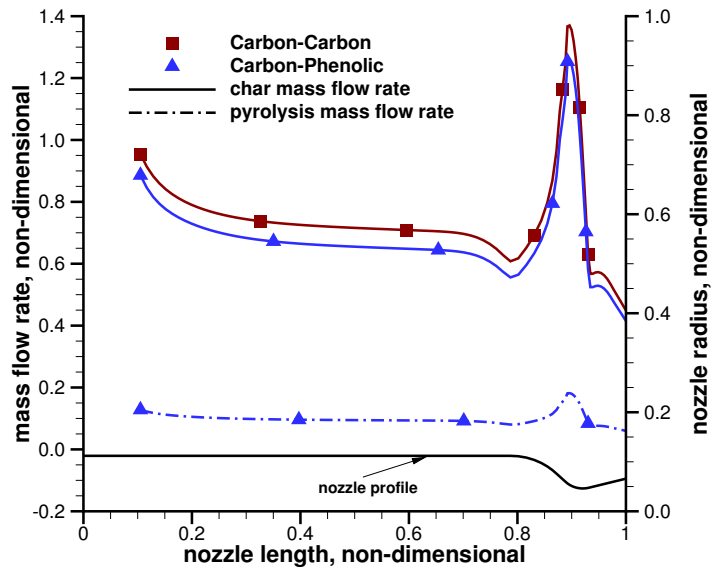


**Figure 8.6** – Wall mass flow rate for the carbon-based materials ( $O/F=2.8$ ).

phenolic (136% of the carbon-carbon value at the throat section) has to be related to the lower char density of the pyrolyzing material. It is important to stress the fact that the erosion for carbon-based materials is in the kinetic-limited regime for this condition, as the oxidizing species are far from being completely consumed at the surface (except for OH) as seen in Fig. 8.7. This is due to the high concentration of the oxidizing species in the combustion products of oxygen/methane mixtures which would make unacceptable the adoption of a diffusion-limited ablation model.

Differently, the reason of the fairly higher erosion rate of silica-phenolic in Fig. 8.5 has to be sought both in the lower wall temperature of 1996 K (silica melting temperature), which enhances the wall convective heat flux (Fig. 8.8), and in the very poor heat absorption of the silica melting if compared to the heat absorbed by the thermochemical erosion of carbon.

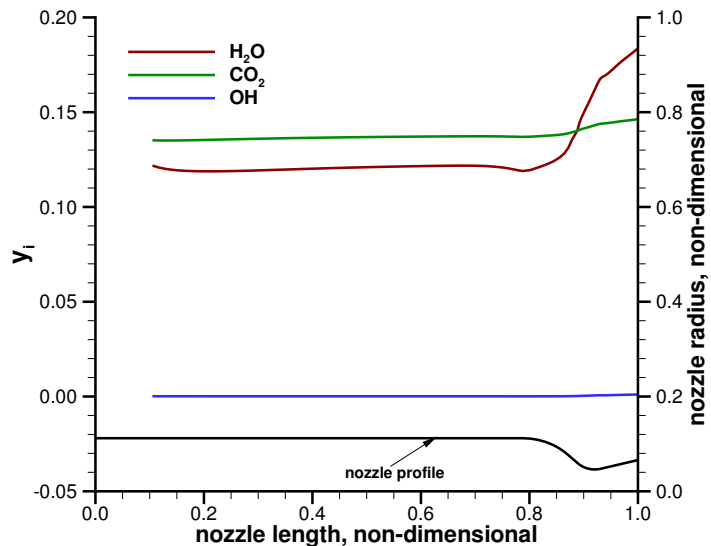


**Figure 8.7** – Oxidizing species wall mass fractions for carbon-carbon ( $O/F=2.8$ ).

After this first set of simulations, carried out at the nominal chamber conditions, the effect of shifting the chamber conditions towards a less harsh environment has been analyzed. Figures 8.9–8.11 show the nozzle erosion rates that have been obtained varying the  $O/F$  value according to Table 8.3. Note that for carbon-carbon and carbon-phenolic only four out of six  $O/F$  values have been analyzed, whereas for silica-phenolic all the  $O/F$  values have been used. As seen, an evident reduction of the erosion rate corresponds to the lowering of the mixture ratio. Actually, this behavior has to be related to the diminishing of the oxidizing species mass fractions and the total chamber temperature (Fig. 8.1 and Table 8.3). In analyzing these results, it should be noted that the chamber temperature variation for the lowest  $O/F$  values ( $O/F=1.5$  and  $O/F=1.3$ ) is so strong that its value drops below the silica melting temperature (1996 K). For this reason, the two lowest  $O/F$  values experience a null erosion rate in

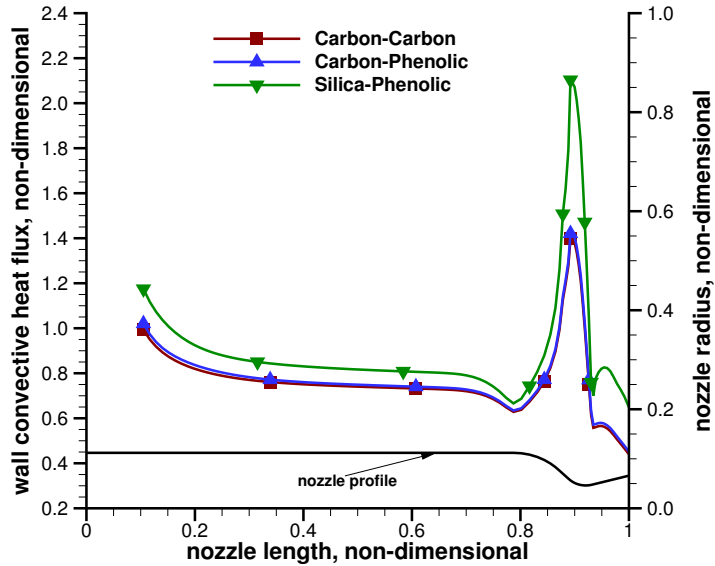


**Figure 8.8** – Wall convective heat flux for the three selected ablative materials ( $O/F=2.8$ ).

case of silica-phenolic (Fig. 8.11) while they show a small but non-null value when carbon-carbon and carbon-phenolic are used. Differently, for  $O/F$  values higher than 1.5, the silica-phenolic wall basically shows the same behavior of the carbon-based materials.

Figures 8.12(a) and 8.12(b) show the carbon-based materials (carbon-carbon and carbon-phenolic) wall temperatures and char mass flow rates, respectively. It is interesting to note that the char mass flow rate is immediately affected by the  $O/F$  reduction while the surface temperature, even if decreasing, seems to be less sensitive to the initial  $O/F$  reduction. This behavior is due to the fact that, in case of kinetic-limited erosion regime, the heterogeneous surface reactions are strongly dependent on the wall temperature. Consequently, even a small variation of the wall temperature can significantly modify the erosion rate. At the same time, a lower erosion rate implies a lower heat absorption by the surface reactions

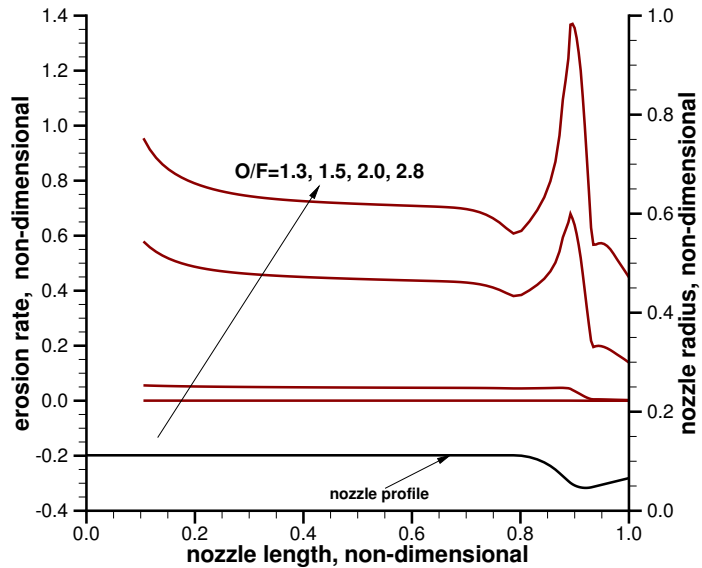


**Figure 8.9** – Erosion rate in case of carbon-carbon with varying O/F.

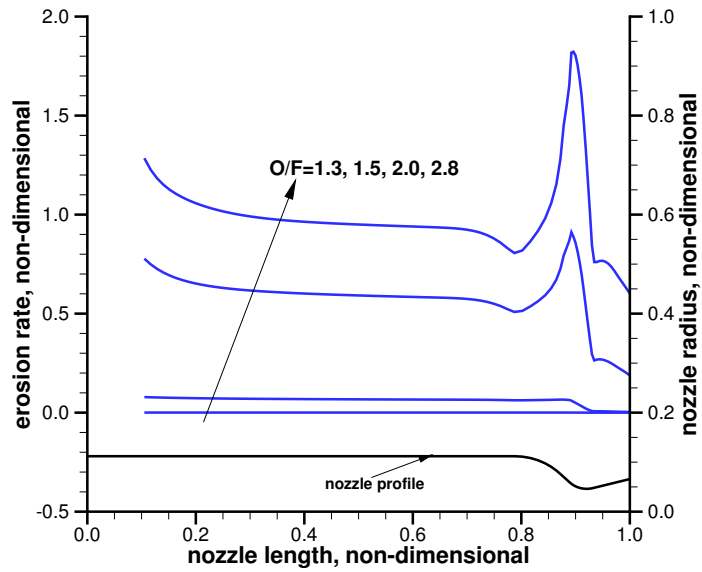


**Figure 8.10** – Erosion rate in case of carbon-phenolic with varying O/F.

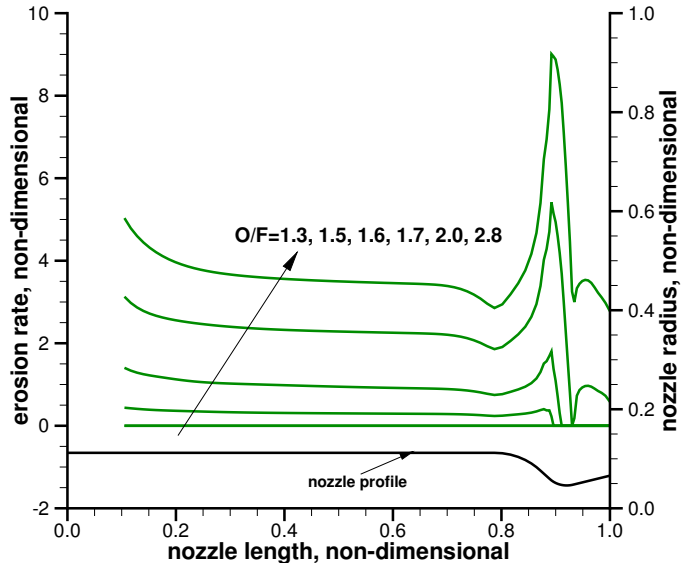
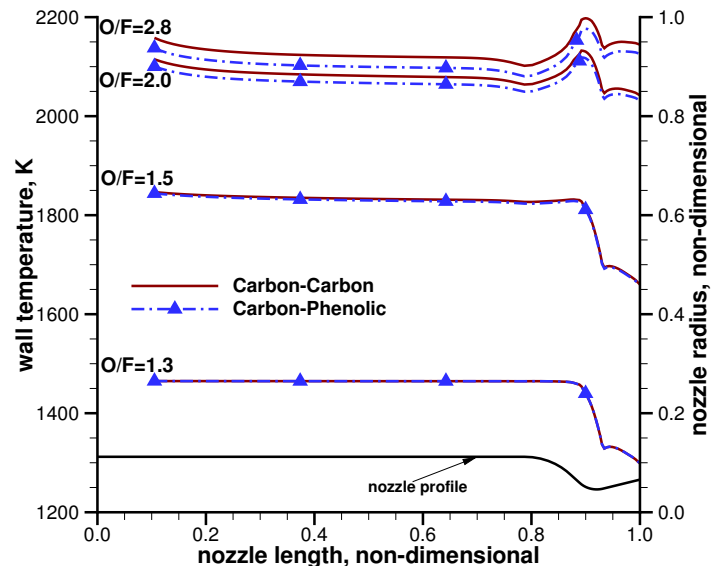


**Figure 8.11** – Erosion rate in case of silica-phenolic with varying O/F.

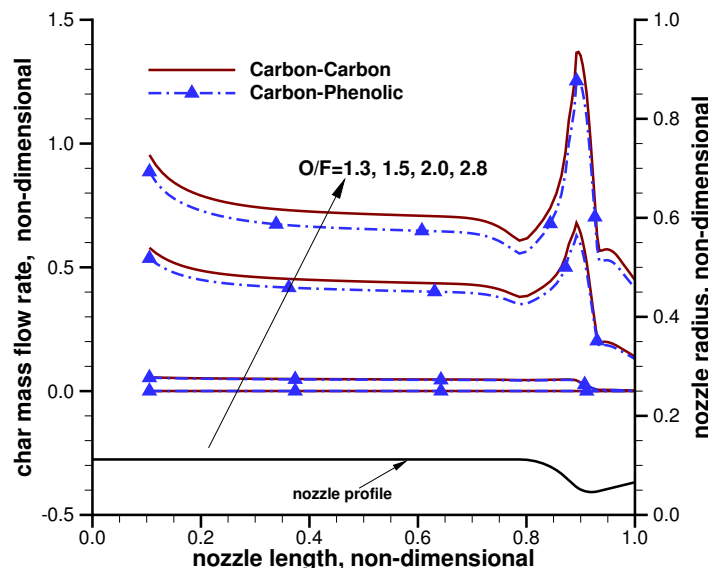
which actually counteracts the wall temperature reduction induced by the O/F shifting. At the lowest O/F value the chamber temperature reduction is such that a practically non-eroding condition is attained. It is also interesting to note that the difference between carbon-carbon and carbon-phenolic results is reduced with the O/F shifting, due to the reduction of the pyrolysis gas injection which diminishes its blockage effect.

**Table 8.5** – Percentage erosion rate peak (with respect to the zero emissivity case) for different materials and wall emissivities.

Material	$\epsilon = 0.50$	$\epsilon = 0.85$
C-C	$\dot{s} = 69\%$	$\dot{s} = 53\%$
C-Ph	$\dot{s} = 70\%$	$\dot{s} = 56\%$
Si-Ph	$\dot{s} = 77\%$	$\dot{s} = 61\%$



(a) Temperature.

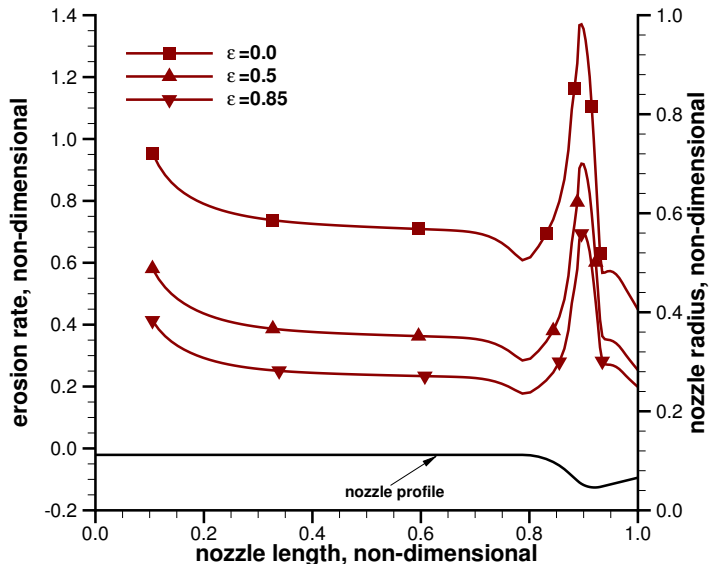


(b) Char mass flow rate.

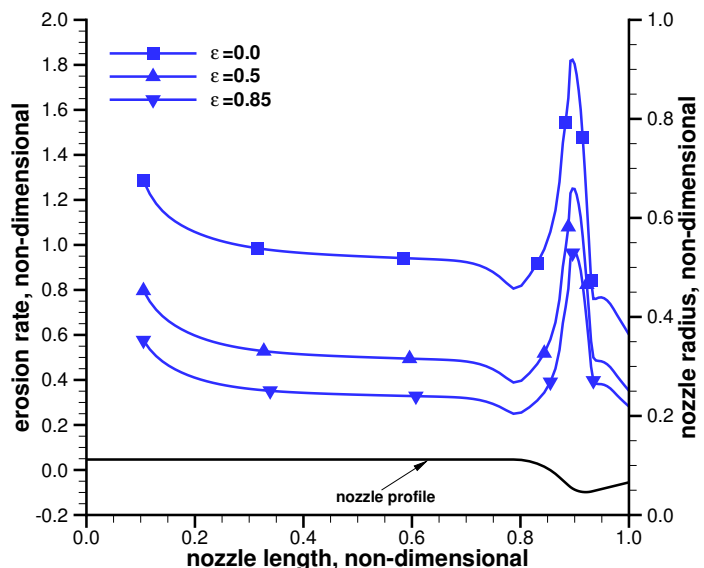
**Figure 8.12** – Wall temperature and char mass flow rate for carbon-based materials with varying O/F.

So far, all the presented results have been obtained neglecting the wall radiative contribution in the surface balance by setting a zero material emissivity. However, due to the high emissivities of carbon and silica, the wall radiative heat flux can have a significant effect on the surface energy balance, especially when the convective heat flux is not particularly high due to a low chamber pressure. For this reason, two different reasonable values of wall emissivity have been chosen for the present analysis:  $\varepsilon = 0.5$  and  $\varepsilon = 0.85$ . Figures 8.13 and 8.14 illustrate the obtained erosion rate values for different wall emissivities in case of the nominal chamber conditions ( $O/F=2.8$ ). Obviously, as pointed out in Chapter 6 this simplified modeling of the radiation contribution is far beyond to be complete and has to be used consciously. However, some interesting results of this analysis can be highlighted. As seen, a strong reduction of the erosion rate is obtained for all the materials when this radiative heat flux is considered. For the carbon-based materials the erosion rate peak value is strongly reduced (Table 8.5) and, for the highest emissivity case, a value comparable with that of the cylindrical chamber in case of zero emissivity is obtained (Fig. 8.13). Similarly, in case of silica-phenolic a strong reduction of the peak value has been found (Table 8.5), however the region far from the throat are those showing the most interesting behavior as for the highest emissivity case no erosion occurs in that region (Fig. 8.14). Looking accurately at these profiles, a difference between the carbon-based and the silica-based materials can be pointed out. In case of carbon-carbon and carbon-phenolic (Fig. 8.13), in fact, the surface temperature for the nominal O/F value has the typical shape, with a visible peak slightly upstream of the throat, that has been shown in Figs. 8.4(b) and 8.12(a). Therefore the radiative heat flux, directly related to the fourth power of the surface temperature, has itself a peak in this region and its contribution to the surface energy balance is here intensified. As a result, the erosion rate reduction is enhanced in the throat region as the wall

emissivity is increased. This trend is more evident when the variation of the erosion rate with respect to the peak value is analyzed (Fig. 8.15). As seen, for the carbon-based materials the difference between the local and the peak value of the erosion rate is reduced when the emissivity is enhanced. Differently, in case of silica-phenolic, for which the surface temperature is at a constant value, the peaked profile of the erosion rate becomes more evident as the material emissivity is increased and this local-to-peak variation remains constant with varying the emissivities (Fig. 8.16). This peculiar behavior leads to the interesting results plotted in Fig. 8.17, where a value of 0.85 has been assumed for the emissivity of both materials, showing that the erosion rate in the nozzle can be minimized by using a combination of two different materials (carbon-carbon and silica-phenolic) in different regions of the nozzle.



(a) carbon-carbon.



(b) carbon-phenolic.

**Figure 8.13** – Erosion rate in case of carbon-based materials with varying emissivities.

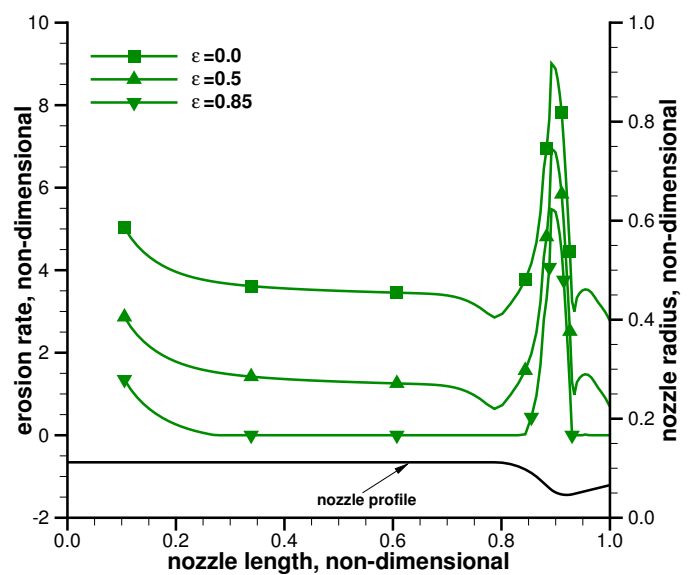
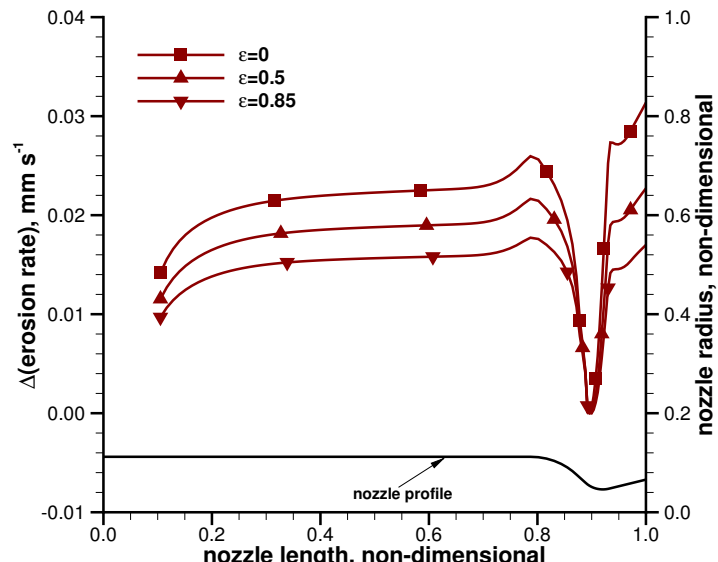
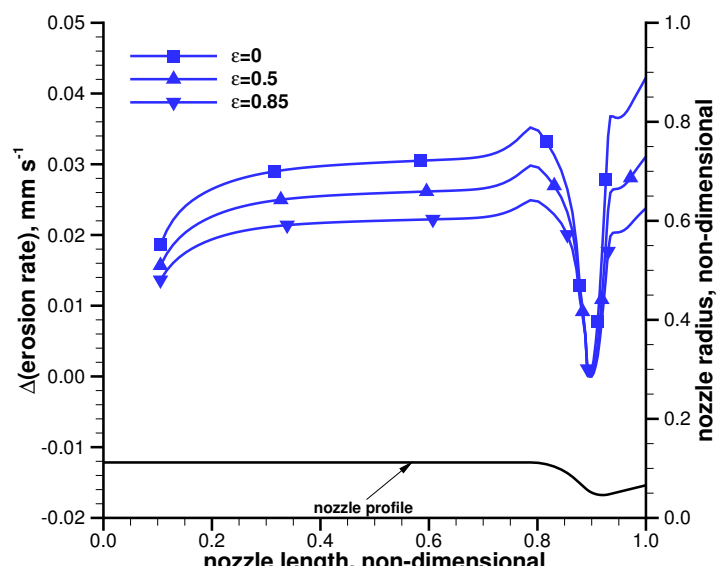


**Figure 8.14** – Erosion rate in case of silica-phenolic with varying emissivities.



(a) carbon-carbon.



(b) carbon-phenolic.

**Figure 8.15** – Peak-to-local erosion rate variation in case of carbon-based materials with varying emissivities.

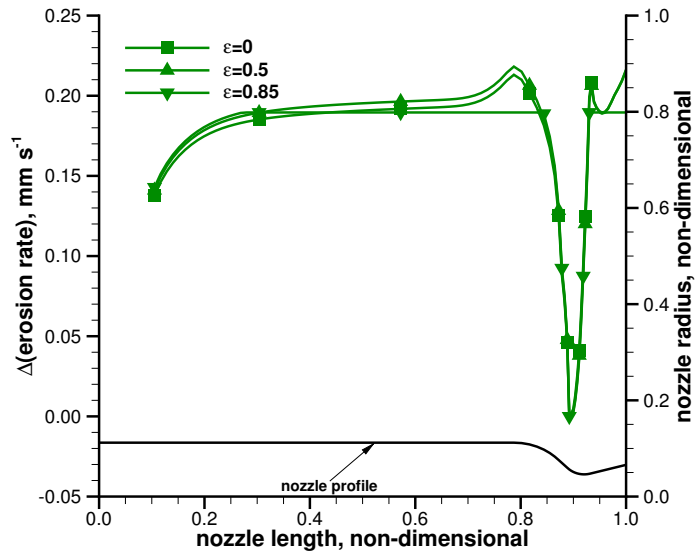


**Figure 8.16** – Peak-to-local erosion rate variation in case of silica-phenolic with varying emissivities.

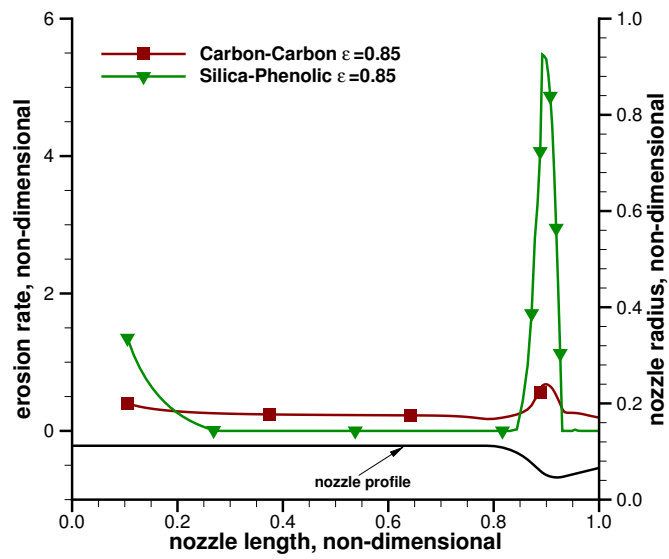


**Figure 8.17** – Erosion rate for carbon-carbon and silica-phenolic with radiative wall.

---

## Coupled flow/material transient analysis

As described in Section 2.2.2, the steady-state ablation is a reasonable assumption for low-conductivity materials or, as it generally happens in solid rocket nozzles due to the high heating rates, at high ablation rates. When the steady-state condition is reached the temperature profile and the erosion rate do not change with time provided that the boundary conditions are not changing. Such an approximation permits to decouple the erosion process from the transient heating problem of the nozzle material and to express the solid conductive heat flux in the surface energy balance (Eq. (2.54)) in a closed way. However, assuming steady-state ablation, no information is available on the time needed to reach such a condition. A transient period is in fact always present during which the surface material heats up prior to start being thermochemically (in case of carbon-based) or mechanically (in case of silica-based) eroded. During this transient the surface temperature rises from an initial value to the steady-state value and so does the erosion rate. In case of pyrolyzing materials, during this transient

---

phase the rate of advance of the pyrolysis zone (Fig. 1.4(b)) is much higher than that of the receding surface, producing a growth of the char zone thickness and thus causing a higher value of  $\varphi$  than its steady-state value (Eq. (2.39)).

For carbon-based materials, at low surface temperatures the erosion rate is predominantly determined by the chemical kinetics and hence is much lower than the steady-state value which is, on the contrary, predominantly determined by the diffusion process of oxidizing species. This transient phase is responsible for the delay in the onset of erosion typical of solid rocket nozzles [77, 97]. Such a delay is clearly affected by the heating process in the nozzle material and hence it depends on parameters such as material properties as well as exhaust gas properties, which affect the heating of the surface material. Usually propellants with a higher aluminum content approach the steady-state condition faster than the ones with a lower aluminum content [15]. This is explained by the faster surface temperature rise for propellants with higher aluminum content which are characterized by higher flame temperatures. Since the surface temperature rises more rapidly for propellants with higher aluminum content, the kinetic-limited time interval is reduced and the recession approaches the steady-state diffusion-limited value faster.

The study of the interaction between the high-temperature, high-velocity combustion gas flow and the nozzle ablative protection material in solid rocket motors coupled with the transient heat conduction response of the nozzle is addressed in this chapter. This allows evaluating the transient nature of the recession process and in particular to study the coupled heating/erosion problem by removing the steady-state ablation approximation. Specifically, the transient response of a graphite nozzle for different kinds of metallized propellants is addressed in this analysis to assess the importance of the material transient heating on the nozzle erosion response and to identify the driving parameters which control the erosion

delay.

## 9.1 Surface balances

Even when steady-state ablation approximation (Section 2.2.2) is removed, the mass balance at the gas/solid interface of a non-pyrolyzing carbon-based ablative material is unmodified with respect to Eq. (4.3), as reported here for the sake of convenience:

$$\rho \mathcal{D}_{im} \left. \frac{\partial y_i}{\partial \eta} \right|_w + \sum_{r=1}^{N_r} \omega_i^r = (\rho v)_w y_{i_w} \quad i = 1, N_c \quad (9.1)$$

Differently, the surface energy balance differs from Eq. (4.2) for the last term on the right-hand side (that has to be expressed in a more general form) and reads:

$$k \left. \frac{\partial T}{\partial \eta} \right|_w + \sum_{i=1}^{N_c} h_{i_w} \rho \mathcal{D}_{im} \left. \frac{\partial y_i}{\partial \eta} \right|_w + \dot{m}_s h_{s_w} = (\rho v)_w h_w + k_s \left. \frac{\partial T_s}{\partial \eta} \right|_s \quad (9.2)$$

or, in a more compact form:

$$k \left. \frac{\partial T}{\partial \eta} \right|_w = \dot{m}_s \Delta H_{abl} + \dot{q}_{cond} \quad (9.3)$$

where the definitions of the heat of ablation (Eq. (7.2)) and the surface mass balance (Eq. (9.1)) have been used.

## 9.2 Heat conduction in the solid phase

It is assumed that heat conduction into the nozzle material is dominant in the direction normal to the local surface. Although temperature gradients exist along the nozzle wall, they are generally small if compared to the heat conduction in

the wall normal direction and represent a second order effect, which has not been accounted for in the present analysis. In a moving local coordinate system tied to the receding surface, the temperature distribution for a non-planar surface of non-decomposing material such as graphite is governed by the following equation [52]:

$$\rho_s \frac{\partial h_s}{\partial t} = \frac{1}{A} \frac{\partial}{\partial \eta} \left( k_s A \frac{\partial T_s}{\partial \eta} \right) - \rho_s \dot{s} \frac{\partial h_s}{\partial \eta} \quad (9.4)$$

that is a customized form of Eq. (2.35b). The terms in Eq. (9.4) represent, from left to right, the sensible energy accumulation, the net conduction, and the net energy convected as a consequence of coordinate motion. The specific heat and thermal conductivity of the nozzle protection materials may experience a significant variation in the temperature range in which they usually operate and therefore, in Eq. (9.4), they are allowed to vary with temperature.

### 9.2.1 Finite-difference method for the in-depth solution

In order to describe the coupling procedure, it is useful to introduce the adopted thermal response code named: Implicit Thermal Ablation Computational Tool (ImpACT). Since the objective is to let the reader familiarize with this approach, only a brief description of the numerical procedure is given here. We will refer to the less complex case of planar surface and constant material properties, the added complexity due to the variable area and variable properties somewhat complicates the algebra of the difference form of the equation but the solution philosophy remains the same. A thorough description of the code implementation and validation can be found in [25].

Considering the in-depth energy balance in the moving coordinate system, expressed by Eq. (9.4), and assuming planar surface (constant area) and constant

properties yields:

$$\frac{\partial T}{\partial t} = \alpha \frac{\partial^2 T}{\partial x^2} + \dot{s} \frac{\partial T}{\partial x} \quad (9.5)$$

where the variable “x” represents the distance from the moving surface in the one-dimensional problem and  $\alpha = k_s / (\rho_s c_p)$  is the thermal diffusivity.

The solution procedure is based on a finite-difference approach. The material is discretized in nodes (elements) and the nodal positions are specified by defining the total number of nodes and their thickness. The following principles of nodal sizing are applied:

- The nodes have a fixed size.
- When necessary a node is dropped to account for the surface recession.
- The nodes are dropped from the back (non-ablating surface) face of the material.

Supposing the domain being rectangular with  $x$  ranging from  $x_{min}$  to  $x_{max}$  and time,  $t$ , ranging from 0 to  $\mathcal{T}$ . Divide  $[0, \mathcal{T}]$  into  $M$  equally spaced intervals at  $t$  values indexed by  $m = 0, 1, \dots, M$ , and  $[x_{min}, x_{max}]$  into  $N$  intervals at  $x$  values indexed by  $n = 1, \dots, N + 1$ . The length of these intervals is  $\Delta t$  in the time direction and  $\Delta x$  in the spatial direction. The implicit finite-difference scheme is based on the Crank-Nicholson algorithm, which has the virtue of being unconditionally stable and is second order accurate in both  $x$  and  $t$  directions. The first step is to approximate the partial derivatives of  $T$  at each gridpoint by

finite-difference expressions. Derivatives in Eq. (9.5) are expressed as follows:

$$\frac{\partial T}{\partial t} = \frac{T'_n - T_n}{\Delta t}$$

$$\frac{\partial T}{\partial x} = \frac{(T'_{n+1} - T'_{n-1}) + (T_{n+1} - T_{n-1})}{4\Delta x}$$

$$\frac{\partial^2 T}{\partial x^2} = \frac{(T'_{n+1} - 2T'_n + T'_{n-1}) + (T_{n+1} - 2T_n + T_{n-1})}{2\Delta x^2}$$

where the superscript  $T'$  indicates the temperature value at the new time  $t' = t + \Delta t$ . Then, substituting these expressions into the energy balance (Eq. (9.5)), one obtains the energy balance rewritten in a finite-difference form (see Appendix D). The system expressing the energy balance at each node (from the surface to the back face) can be rewritten in the so-called tri-diagonal matrix form as:

$$\begin{bmatrix} B_1 & C_1 & 0 & \dots & \dots & \dots & 0 \\ A_2 & B_2 & C_2 & \ddots & & & \vdots \\ 0 & A_3 & B_3 & C_3 & \ddots & & \vdots \\ \vdots & \ddots & \ddots & \ddots & \ddots & \ddots & \vdots \\ \vdots & & \ddots & A_{N-1} & B_{N-1} & C_{N-1} & 0 \\ \vdots & & & \ddots & A_N & B_N & C_N \\ 0 & \dots & \dots & \dots & 0 & A_{N+1} & B_{N+1} \end{bmatrix} \begin{Bmatrix} T'_1 \\ T'_2 \\ T'_3 \\ \vdots \\ T'_{N-1} \\ T'_N \\ T'_{N+1} \end{Bmatrix} = \begin{Bmatrix} D_1 \\ D_2 \\ D_3 \\ \vdots \\ D_{N-1} \\ D_N \\ D_{N+1} \end{Bmatrix} \quad (9.6)$$

where both the elements in the coefficient matrix and the elements in the right-hand side vector are functions of known quantities (as the solution at the previous time step,  $s$ ,  $\Delta t$ ,  $\Delta x$ ,  $\alpha$ ) and boundary conditions (see Appendix D for details),

only.<sup>1</sup> With this in mind, it may be seen that, beginning with the last node, the highest-indexed unknown temperature may be eliminated from each equation in turn (this is the standard first step in the routine reduction of a tri-diagonal matrix). The resulting simpler set of equations is the following:

$$\begin{bmatrix} B_1^* & 0 & \dots & \dots & \dots & \dots & 0 \\ A_2^* & B_2^* & \ddots & & & & \vdots \\ 0 & A_3^* & B_3^* & \ddots & & & \vdots \\ \vdots & \ddots & \ddots & \ddots & \ddots & & \vdots \\ \vdots & & \ddots & A_{N-1}^* & B_{N-1}^* & \ddots & \vdots \\ \vdots & & & \ddots & A_N^* & B_N^* & 0 \\ 0 & \dots & \dots & \dots & 0 & A_{N+1}^* & B_{N+1}^* \end{bmatrix} \begin{Bmatrix} T'_1 \\ T'_2 \\ T'_3 \\ \vdots \\ T'_{N-1} \\ T'_N \\ T'_{N+1} \end{Bmatrix} = \begin{Bmatrix} D_1^* \\ D_2^* \\ D_3^* \\ \vdots \\ D_{N-1}^* \\ D_N^* \\ D_{N+1}^* \end{Bmatrix} \quad (9.7)$$

Where the coefficients  $A_n^*$ ,  $B_n^*$ , and  $D_n^*$ , defined in Table 9.1, are functions of the coefficients of Eq. (9.5). At this point, looking at the first equation of Eq. (9.7), it can be noted that, since it represents the surface node, it involves the boundary condition at the gas/surface boundary. Considering that the boundary condition is given in terms of conductive heat flux, the conductive heat flux at the new time step can be expressed as a function of known terms and surface temperature at the new time step  $T'_1$  (see Appendix D for details):

$$\dot{q}'_{cond} = A_s T'_1 + B_s \quad (9.8)$$

Since  $T'_1 = T_w$ , Eq. (9.8) represents the sought relation between  $\dot{q}_{cond}$  and  $T_w$  implied by the in-depth solution.

---

<sup>1</sup>The surface recession rate,  $\dot{s}$ , is treated in an explicit manner. This causes little error since the energy term involving  $\dot{s}$  are small compared to the other energy terms.

**Table 9.1** – Coefficient definitions.

Position	Node no.	Coefficient	Definition
Surface	$n = 1$	$B_1^*$	$B_1 - C_1 A_2^* / B_2^*$
		$D_1^*$	$D_1 - C_1 D_2^* / B_2^*$
Interior	$n = 2, \dots, N$	$A_n^*$	$A_n$
		$B_n^*$	$B_n - C_n A_{n+1}^* / B_{n+1}^*$
		$D_n^*$	$D_n - C_n D_{n+1}^* / B_{n+1}^*$
Back	$n = N + 1$	$A_{N+1}^*$	$A_{N+1}$
		$B_{N+1}^*$	$B_{N+1}$
		$D_{N+1}^*$	$D_{N+1}$

**Table 9.2** – Nozzle conditions assumed in the analysis.

$T_{aw}, \text{K}$	$h_c, \text{kW m}^{-2} \text{K}^{-1}$	$\Delta H_{abl}, \text{MJ kg}^{-1}$
3600	10	2000

### 9.2.2 Simplified analysis of TPS transient behavior

After that the accuracy of the material response model was verified (see Appendix D for details), an analysis to simulate a nozzle environment and to study the effect of both the material properties and the erosion rate on the material thermal response has been carried out. A simplified transfer coefficient energy boundary condition, obtained from Eq. (9.3), has been applied to a semi-infinite graphite slab:

$$h_c (T_{aw} - T_w) = \rho_s \dot{s} \Delta H_{abl} + \dot{q}_{cond} \quad (9.9)$$

where  $h_c$  and  $T_{aw}$  represent the heat transfer coefficient and the adiabatic wall temperature, respectively. Based on previous CFD calculations, the representative values reported in Table 9.2 have been assumed for the nozzle conditions. Different constant erosion rates ( $\dot{s}$ ) and solid thermal conductivities ( $k_s$ ) have

**Table 9.3** – Test matrix assumed in the analysis.

Test no.	$k_s, \text{W m}^{-1} \text{K}^{-1}$	$\dot{s}, \text{mm s}^{-1}$
01	10	0.00
02	10	0.25
03	10	0.50
04	10	1.00
05	100	0.00
06	100	0.25
07	100	0.50
08	100	1.00

been selected for the analysis. The surface material is graphite with a density of  $1830 \text{ kg m}^{-3}$  and an initial temperature ( $T_0$ ) of 300 K. The specific heat of graphite as a function of temperature has been taken from the CEA species thermodynamics [98] (Fig. 9.1). Note that, typically, the thermal conductivity of graphite and carbon-carbon [99] can vary one order of magnitude in the temperature range of 300 K–3000 K (Fig. 9.1), for this reason two different constant values have been selected in the analysis. Table 9.3 reports the conditions for each of the eight tests performed. Figure 9.2 shows the effect of the erosion rate and thermal conductivity on the transient heating solution. The wall temperature histories of Fig. 9.2(a) show that the higher the erosion rate and the lower the thermal conductivity, the faster the material reaches the steady-state. The erosion rate level can significantly affect the steady state solution while the thermal conductivity can only affect the time needed to reach the steady-state solution but not the solution itself. At increasing levels of erosion rate, the wall temperature is reduced and this is due to the combined effects of two phenomena: the heat absorption by the heterogeneous surface reactions in Eqs. (9.9), and the convection energy term in the in-depth energy balance, Eq. (9.4). A

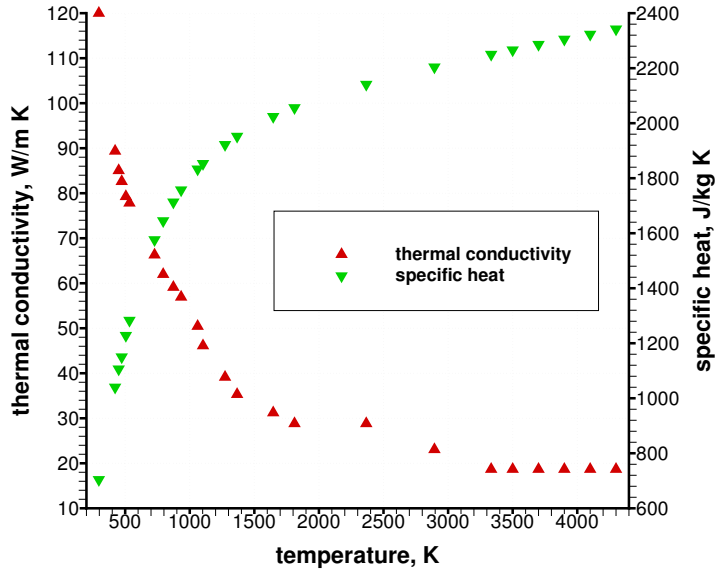
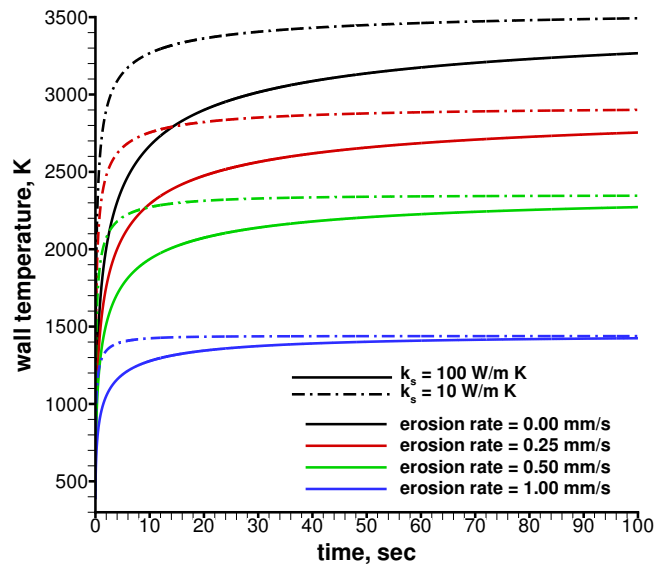


Figure 9.1 – Material thermophysical properties.

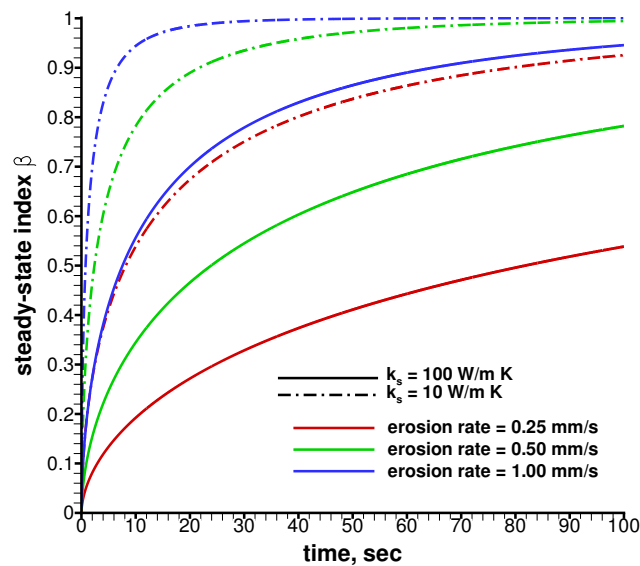
useful measure of the approach to steady-state is provided by the variable:

$$\beta = \frac{\rho_s \dot{s} (h_w - h_0)}{\dot{q}_{\text{cond}}}$$

comparing the amount of solid convection pick-up to the amount of energy conducted into the solid. This term is initially zero and approaches unity in the steady-state as shown in Fig. 9.2(b). Without surface recession, there is no steady-state solution. Results show how the transient material heating before reaching the steady-state is significantly influenced by the material thermal conductivity.



(a) Wall temperature history of graphite.



(b) Dimensionless steady-state index as a function of time.

**Figure 9.2** – Graphite transient heating solutions for different erosion rates and thermal conductivities.

### 9.3 Coupling Technique

The coupling between the flow solver and the material response code has to be time accurate as the heating history of the material affects the flow solution and vice-versa. Due to large differences in the characteristic times associated with the flow and the material solutions, code coupling is performed via a loosely coupled technique where each flow simulation is a steady-state computation while the material heat conduction process is transient. The Navier-Stokes equations are solved via the CFD code and the transient heat conduction equation (Eq. (9.4)) is solved by the ImpACT code.

The balances in Eqs. (9.1) and (9.2) represent a common boundary condition for both the flow field and the material code and hence have to be solved either in the flow code or in the material response code. As the only information coming from the material response in Eqs. (9.1) and (9.2) is the rate of heat conduction into the nozzle material, the gas/solid interface balance equations are iteratively solved in the flow code (together with the Navier-Stokes equations) in an iterative fashion using the information on the rate of heat conduction coming from the material code. When a steady-state flow solution is obtained, the time-dependent material response simulation can advance in time up to the next time step using the newly predicted wall temperatures and erosion rates. The last term on the right-hand side of Eq. (9.2) represents the mechanism which joins the material response solution with the flow field solution. Based on the previously evaluated erosion rate level, the temperature profile inside the material, the back-surface boundary condition, and the selected time step, the material response code is able to express the unknown rate of heat conduction into the nozzle material as

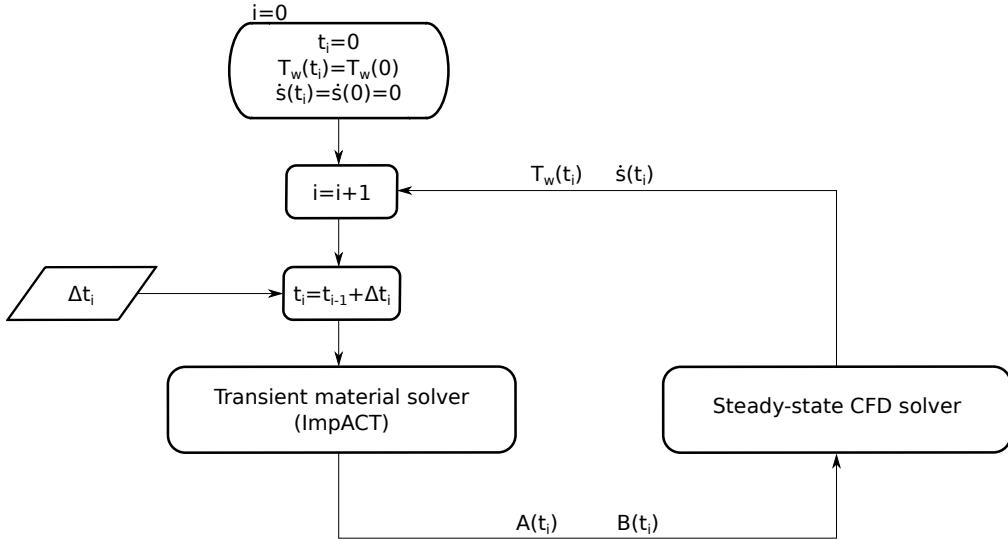


**Figure 9.3 – Schematic of the coupling technique.**

a function of the unknown wall temperature:

$$k_s \frac{\partial T_s}{\partial \eta} \Big|_s = \dot{q}_{\text{cond}} = A_s T_w + B_s \quad (9.10)$$

where  $A_s$  and  $B_s$ , already described previously, represent coefficients which depend on the transient heating history of the material, on the material erosion rate and thermal properties, and on the time step as well.<sup>2</sup> The schematic diagram depicted in Fig. 9.3 describes the loosely coupled technique. Two different levels of time increment are defined: a fine and a coarse one. The coupled transient solution starts from the material response code using the initial condition (a constant temperature of 300 K and no erosion rate) and the coarse time increment is used to obtain the first values of  $A_s$  and  $B_s$  for each axial section of the nozzle. Subsequently, this information is used to compute a steady-state CFD solution while the material response code is paused. The erosion rate and wall

<sup>2</sup>The most general case of non-constant properties is considered in this case.

temperature distributions obtained from the CFD solution are used as input for the material response code which is run again over the first (coarse) time step using the fine time steps and assuming a linear variation of the wall temperature and the erosion rate from the initial values to the ones calculated by the CFD code. Subsequently the process is repeated to advance to the second time step. First, new values of  $A_s$  and  $B_s$  using a single (coarse) time increment are evaluated via the material code and then used to perform a second steady-state CFD simulation to evaluate the new wall temperature and erosion rate values. Once this second CFD solution is available, the material code is run again over the time step separating the two CFD solutions using the fine time steps and assuming a linear variation of the wall temperature and the erosion rate. The procedure is repeated to advance the coupled flow/material solution in time until a selected simulation time has been reached. The time steps where the CFD solution is updated (coarse) are selected such to ensure that neither the wall temperature nor the erosion rate exceed a maximum allowable variation.

## 9.4 Analysis of Coupled Solutions

The described coupling procedure has been applied to couple the CFD code and the material response code in order to predict the temperature and erosion rate histories of graphite nozzles for different propellant combinations.

### 9.4.1 Input data

The thermophysical properties of the graphite used in the transient heat conduction calculation are the same as shown in Fig. 9.1. The nozzle geometry used in the analysis is the one of the BATES motor, already described in Section 4.4 and sketched here in Fig. 9.4. The analysis has been conducted on an axisymmetric

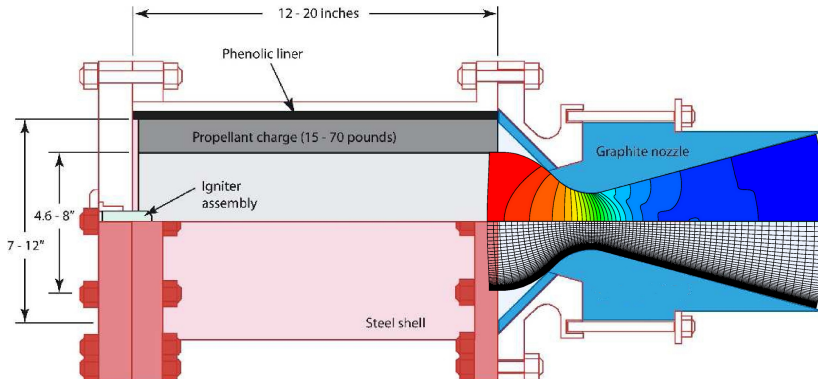


**Figure 9.4 –** BATES motor configuration [77] with CFD pressure field and nozzle grid.

**Table 9.4 –** Mass fractions, pressure, temperature, and aluminum content for propellants A and B.

Prop.	$y_{CO}$	$y_{CO_2}$	$y_{HCl}$	$y_{H_2}$	$y_{H_2O}$	$y_{N_2}$	$y_{Al_2O_3}$	$p_c, \text{bar}$	$T_c, \text{K}$	Al%
A	0.175	0.040	0.240	0.020	0.145	0.100	0.280	69	3580	15
B	0.200	0.005	0.190	0.020	0.025	0.100	0.460	69	3745	27

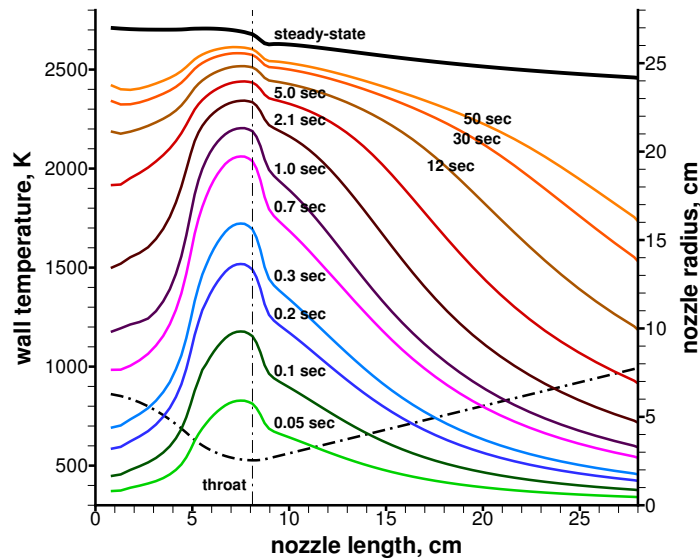
graphite nozzle considered at an initial temperature of  $T_w = 300 \text{ K}$ . Two different AP/HTPB aluminized propellants (named A and B) have been selected which are characterized by a different aluminum content. The propellant characteristics are listed in Table 9.4, for a selected chamber pressure of 69 bar. As seen, the different aluminum content generates fairly different flame temperatures and water vapor mass fractions. The chamber pressure is assumed to be constant during the entire test duration as the modeling of the motor ignition transient has been considered out of the purpose of this study.

#### 9.4.2 Simulation results

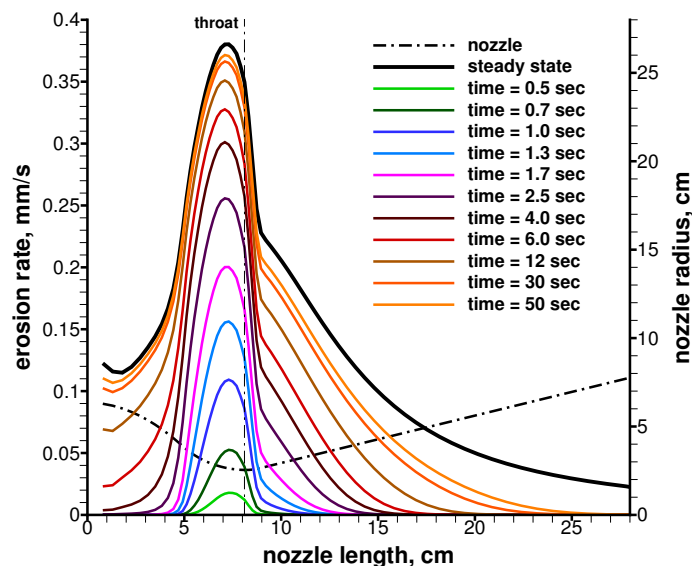
Figure 9.5 shows the coupled flow field and transient heat conduction solutions for propellant A together with the steady-state solution (obtained using the steady-state ablation approximation). The wall temperature is initially increasing rapidly

with time, especially in the throat region, where it exceeds 2000 K after less than one second of exposure. The temperature rise is not so quick for the nozzle sections away from the throat, due to the reduced convective heat flux in these regions. The erosion rate shows a similar behavior, however the difference between the throat behavior and the sections away from the throat is more evident, as there are clearly sections which are basically non-eroding due to insufficient heating, and where the steady-state condition is far from being reached. It is worth noting that the wall temperature in the throat region, after a very quick rise in the first few seconds of exposure, slowly tends towards the steady state condition. This is due to the fact that, as the wall temperature is increased, the convective heating is obviously reducing. Moreover, when the nozzle starts being thermochemically eroded, it absorbs energy and this slows down the nozzle heating process.

Figure 9.6 shows the results obtained for propellant B. The wall temperature rise is similar for the two propellants. However, due to the higher flame temperature, for propellant B the nozzle initial heating is slightly quicker. It can be also noted that propellant B, although heating faster, results to be less close to the steady-state solution than propellant A after the same period of time. This is explained by the effect of the erosion rate which, due to the much higher water vapor content, is much higher for propellant A than for B (at steady-state the erosion rate of propellant A is five times that of propellant B). As previously discussed, the higher the erosion rate, the faster the steady-state condition is attained. The erosion rate distribution history of propellant B shows a peculiar behavior which was not triggered for propellant A. Although the erosion rate distribution tends to reach the steady-state value as time elapses, propellant B shows a non-monotonic behavior as the erosion rate value in the throat region exceeds the steady-state value after a few seconds from initial exposure. This

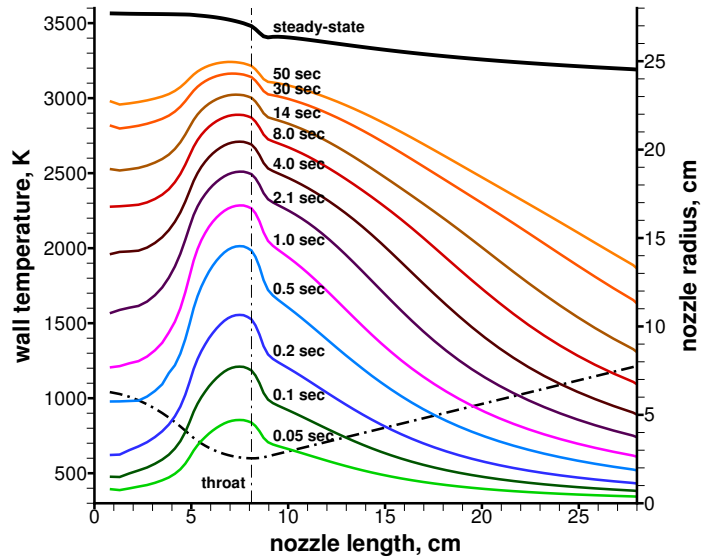


(a) Wall temperature distributions for various times.

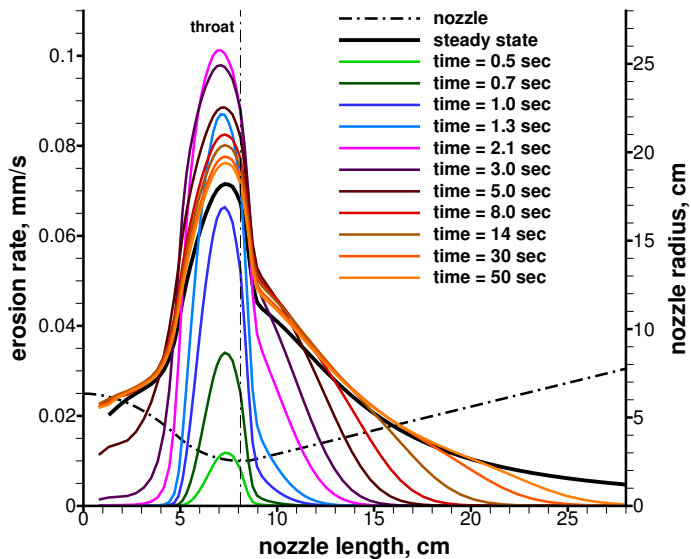


(b) Erosion rate distributions for various times.

**Figure 9.5 –** Coupled Flow field and transient heat conduction solutions for aluminized propellant A for various times (not all the solutions are shown).



(a) Wall temperature distributions as a function of time.



(b) Erosion rate distributions as a function of time.

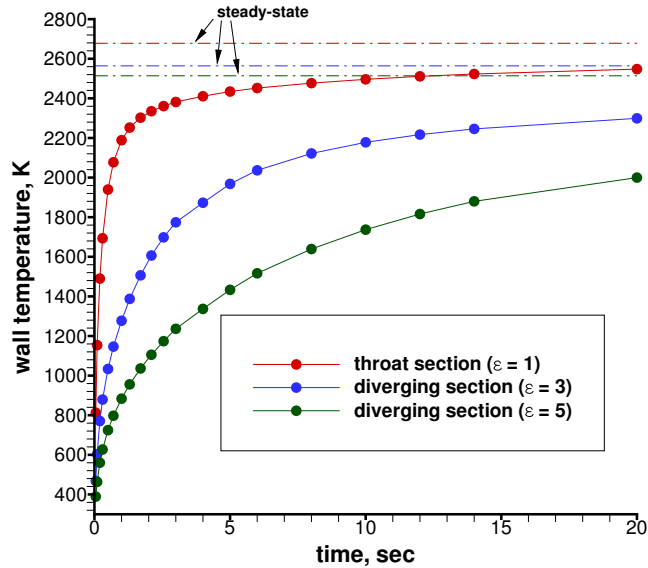
**Figure 9.6** – Coupled Flow field and transient heat conduction solutions for aluminized propellant B for various times (not all the solutions are shown).

**Table 9.5** – Percentage error on the throat temperature between standard and halved time steps for propellants A and B.

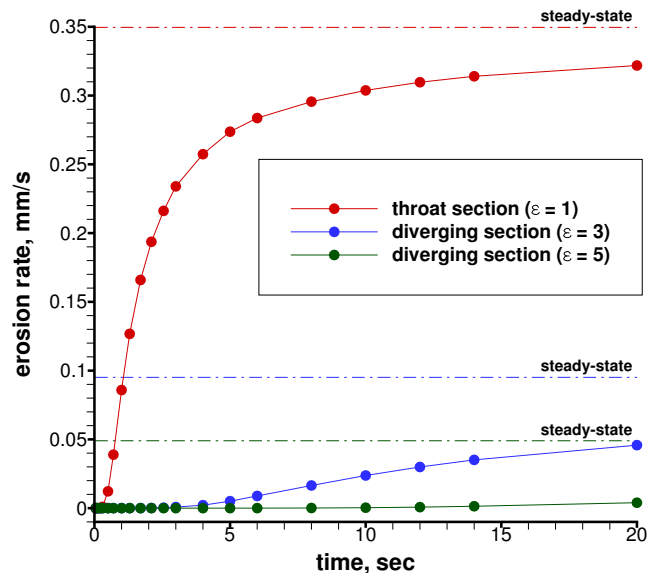
Prop.	0.1 s	0.3 s	0.7 s	1.3 s	2.1 s	3.0 s
A	14.3%	5.0%	1.9%	0.3%	0.1%	0.1%
B	16.4%	6.0%	2.3%	0.6%	0.3%	0.5%

behavior, which can be spotted by looking at Fig. 9.6(b), will be discussed in the following focusing on the throat section.

In order to verify the accuracy of the obtained results, the time steps selected for the first three seconds of exposure, which are characterized by high variations over time, have been halved. For each time step, a new CFD simulation is performed. A comparison of the error on the wall temperature at the throat location for the two propellants using the reference time steps and the halved ones is shown in Table 9.5. As seen, the error between the two time steps decreases to less than 1% at 1.3 seconds from exposure. In the following figures, for increased accuracy, results obtained with the halved time steps (up to 3 s) are presented. Figure 9.7 shows, for propellant A, the transient distributions at three different nozzle sections (the throat and two diverging sections at expansion ratio of 3 and 5, respectively) of the wall temperature and erosion rate. At the throat location, both the wall temperature and the erosion rate rise rapidly in the first few seconds of exposure and then tend more slowly to the steady-state. For the two sections downstream of the throat, the initial transient is longer and the steady-state condition, especially for the farther section from the throat, is far from being attained. The erosion regime for propellant A is kinetic-limited as the most important oxidizing species, water vapor, is not completely consumed at the throat location, as shown in Fig. 9.8(a) where water vapor mass fraction at the surface, and wall convective heat flux are shown at same three nozzle sections. For the kinetic-limited condition, the erosion rate is directly related to the

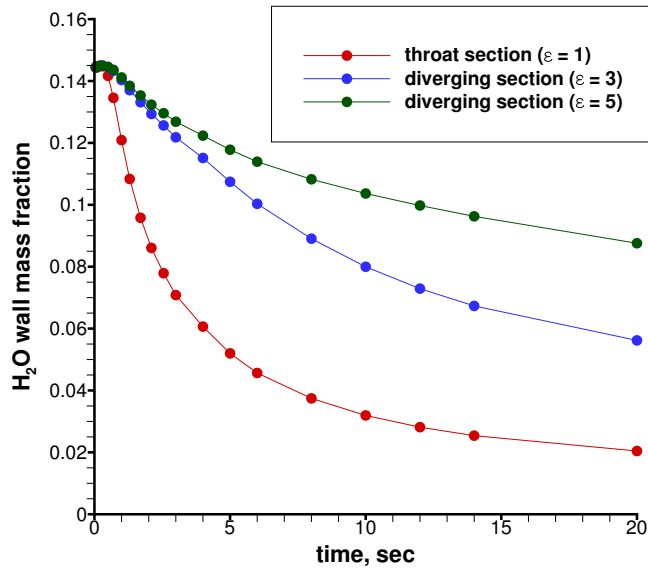


(a) Wall temperature as a function of time.

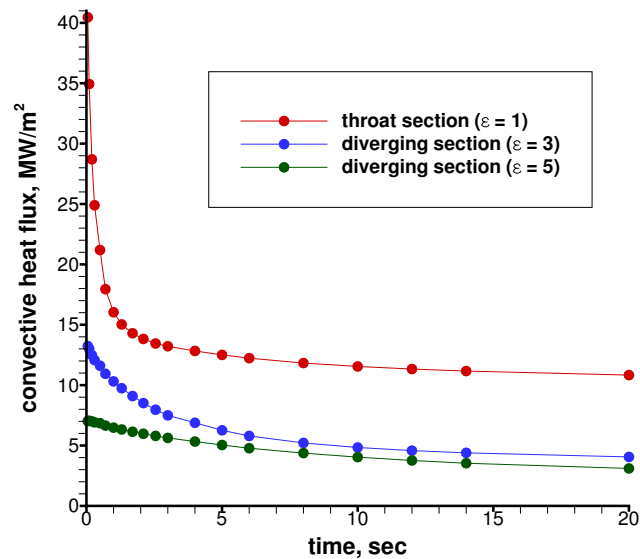


(b) Erosion rate as a function of time.

**Figure 9.7** – Transient distributions for aluminized propellant A at three different nozzle sections.



(a) Wall water vapor mass fraction as a function of time.



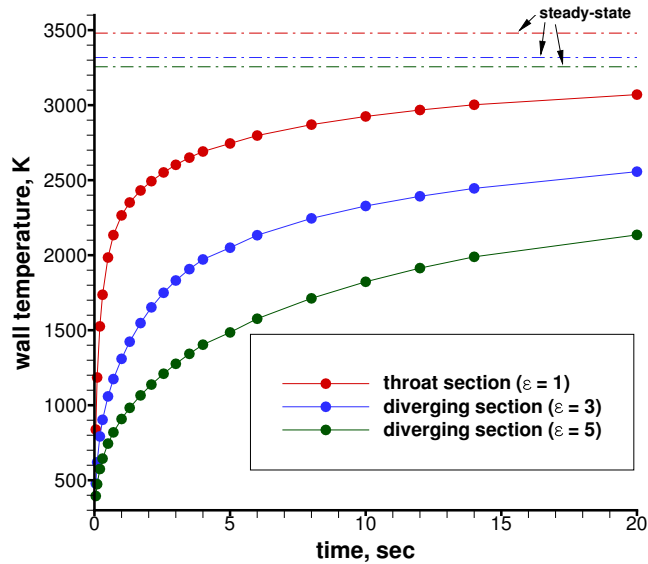
(b) Wall convective heat flux as a function of time.

**Figure 9.8** – Transient distributions for aluminized propellant A at three different nozzle sections.

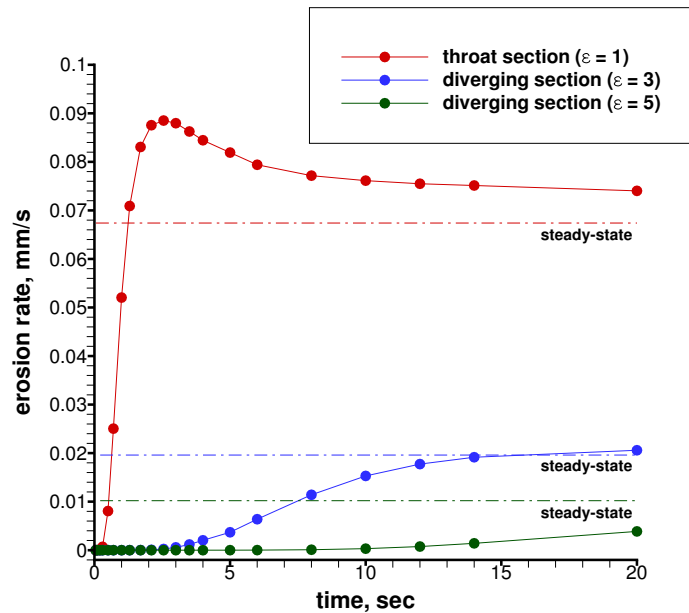
surface temperature and therefore they tend towards the steady-state solution in the same manner. After 20 seconds from exposure, the throat wall temperature reaches 95% of the steady-state value, while the erosion rate reaches 92%. Figures 9.9 and 9.10 show the same results for propellant B, which is characterized by behaviors similar to those of propellant A. However, there are also some peculiarities which are characteristic of propellant B only.

The most significative is the non-monotonic increase of the throat erosion rate (Fig. 9.9(b)) that shows a maximum 30% higher than the steady-state value at approximatively 2.5 s from initial exposure. At this early time, the wall temperature at the throat is about 2500 K, which is almost 1000 K lower than the steady-state temperature. However at this same time, as shown in Fig. 9.10(a), the water vapor has already been completely consumed at the surface, meaning that a diffusion-limited condition, at least for the throat region, has been reached. This permits to explain the overshoot of the steady-state erosion rate at 2.5 seconds: with the erosion in the diffusion-limited regime and a wall temperature much lower than steady-state, in fact, the boundary-layer is denser and thinner and this enhances the diffusion fluxes generating higher erosion levels. This does not happen for propellant A, as it lies in the kinetic-limited regime for all the duration of the heating process. Figure 9.11 shows the temperature profile in the graphite nozzle at the throat location at various times for the two propellants. Due to the high heating rates there are large temperature gradients in the temperature profiles. However, due to the relatively high thermal conductivity of graphite, there is also a significant temperature rise inside the material and at a distance of 1 cm from the gas/solid interface, the temperature reaches 1000 K in less than 10 seconds for propellant A. The in-depth temperature rise is even faster for propellant B, due to the higher wall temperature.

Finally, Figs. 9.12 and 9.13 show a comparison of the throat transient heating

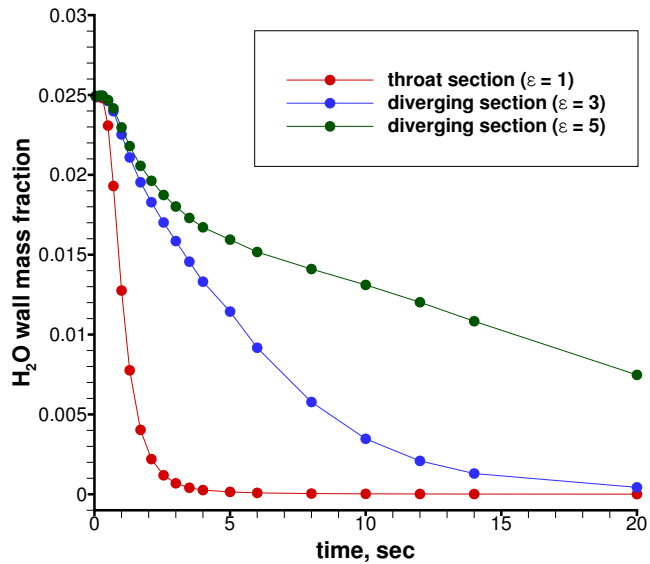


(a) Wall temperature as a function of time.

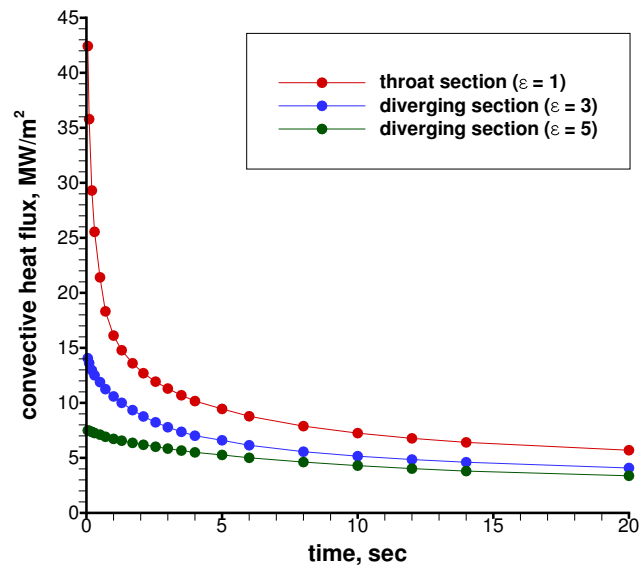


(b) Erosion rate as a function of time.

**Figure 9.9** – Transient distributions for aluminized propellant B at three different nozzle sections.

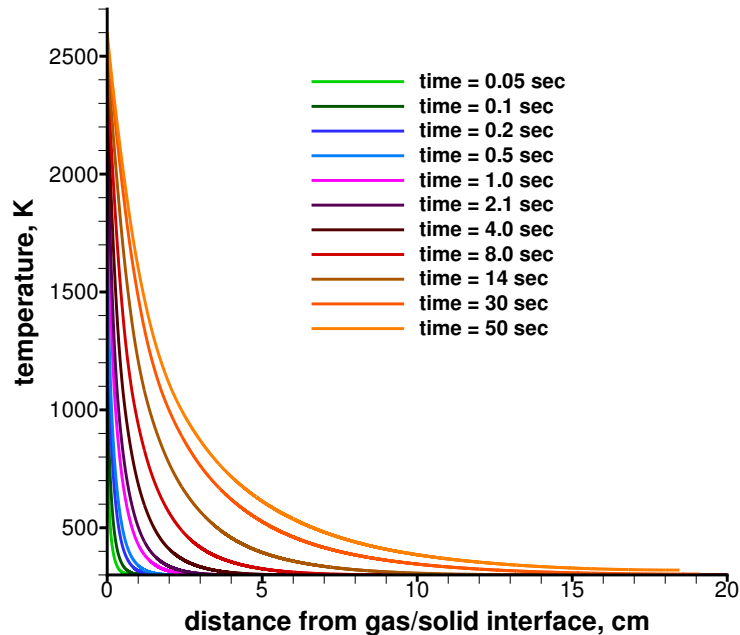


(a) Wall water vapor mass fraction as a function of time.

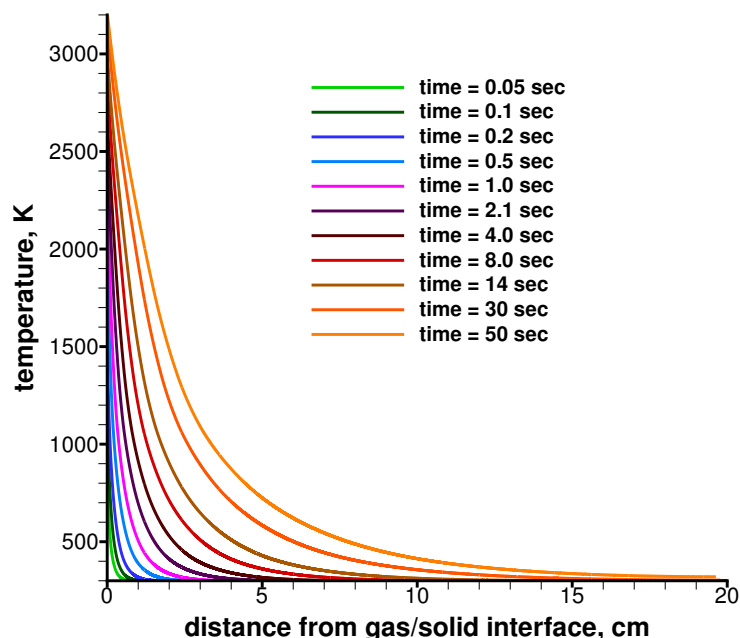


(b) Wall convective heat flux as a function of time.

**Figure 9.10** – Transient distributions for aluminized propellant B at three different nozzle sections.

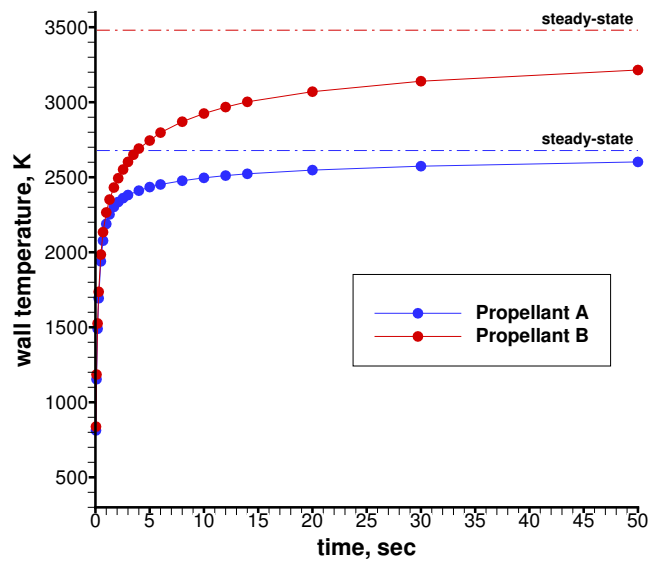


(a) Propellant A.

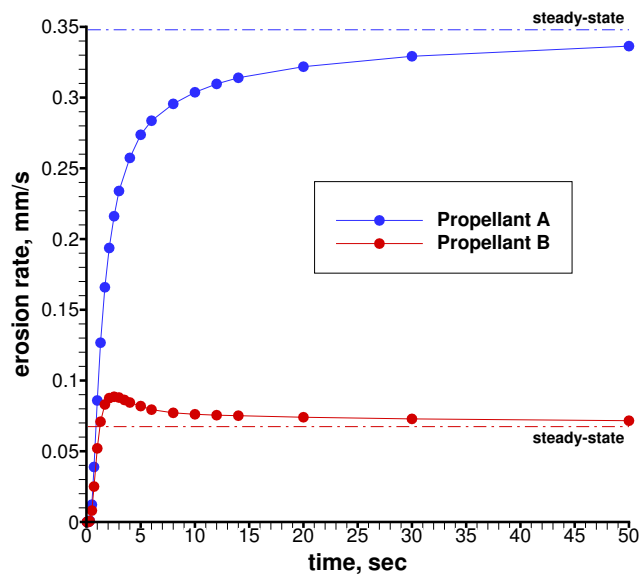


(b) Propellant B.

**Figure 9.11** – Temperature distributions in the solid material at throat for various times.

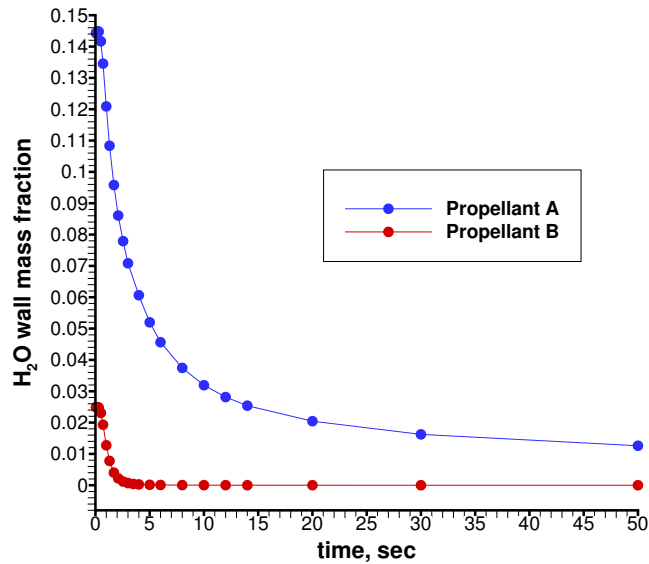


(a) Wall temperature as a function of time.

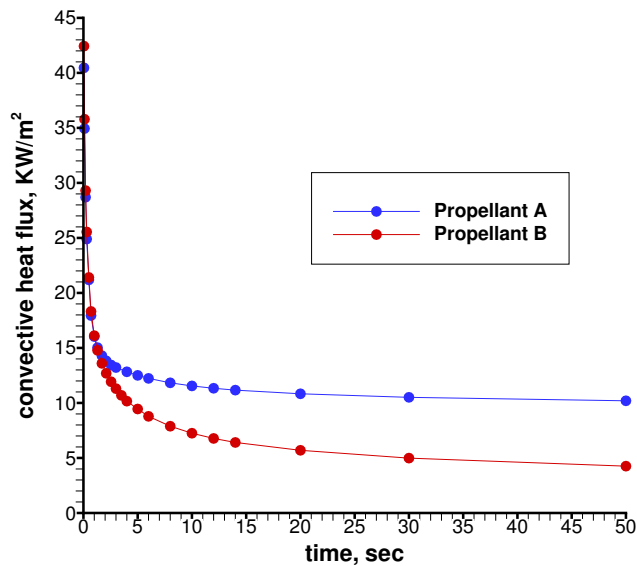


(b) Erosion rate as a function of time.

**Figure 9.12 – Transient distributions for propellant A and B at the throat section.**



(a) Wall water vapor mass fraction as a function of time.



(b) Wall convective heat flux as a function of time.

**Figure 9.13 – Transient distributions for propellant A and B at the throat section.**

and erosion between propellant A and B. As shown in Fig. 9.12(a), propellant B temperature is increasing more and faster than propellant A due to the higher flame temperature which also enhances the heating rate. However, despite its higher temperature rise, propellant B is somewhat slower in reaching out the steady-state condition and this is due to the much lower erosion rate which extends the time lapse needed to reach steady-state. Propellant A erosion rate is shown to approach the steady-state from lower values, while the opposite holds for propellant B. Due to its lower water vapor content, propellant B is quickly reaching a diffusion-limited regime, and 95% of the freestream water vapor mass fraction is consumed at the throat surface after 2.5 seconds of exposure. Differently, propellant A is clearly kinetic-limited and after 2.5 seconds of exposure the water vapor which has been consumed at the throat surface is less than 50%. Concluding, it can be stated that the developed loose coupling procedure has been tested and verified. The procedure gives encouraging preliminary results for future studies on the erosion onset in rocket nozzles. Importantly, it confirms the trend to approach the steady-state solution as time passes. It has to be stressed that a strong influence of the propellant composition on the transient erosion has been found. Differently aluminized propellants have shown different behavior in approaching the steady-state solution. Basically, it has been found to be due to the combustion temperature and the oxidizing species content, highly different between the two analyzed propellants, that cause the establishment of two different erosion regimes. For the present calculations, the erosion rate reaches the 90% of the steady-state value after less than 15 s of exposure. However, it is worth noting that caution has to be used in interpreting these results as a confirmation of the validity of the steady-state approach in a more general way. In fact, the main objective of this analysis was the verification and testing of the loose coupling approach. As pointed out in Section 9.2.2 the material prop-

erties have been found to have a strong influence on the time needed to reach the steady-state erosion. This fact has to be properly taken into account when accurate reproductions of experimental test results are sought, since the precise evaluation of the material properties to be used in the simulations is mandatory. It has to be noted that, has shown in Chapter 7, full-size nozzles normally use different TPS liners to protect different parts of the nozzle. As pyrolyzing materials are used in regions far from the throat, where the steady-state has been found far from being reached in the present coupled calculation for the graphite nozzle, the very low conductivity of these materials surely favors the attainment of the steady-state in a lower time (possibly comparable with the throat region one). For these reasons, the use of the steady-state ablation approximation for a steady-state uncoupled CFD simulation can still be considered the the best and fastest way to obtain quick and useful results when studying the behavior of the nozzle TPS material.

---

## **Conclusions**

The major aim of this work was the development of a comprehensive model that would allow the study of the behavior of different ablative materials in rocket nozzle environment accounting for surface ablation, pyrolysis gas injection and resin decomposition. The TPS material consumption represents a major issue in rocket prediction performance since the throat enlargement influences the nozzle mass flow rate and, in turn, the equilibrium chamber pressure. For this reason, a better prediction of the TPS behavior when it is exposed to the nozzle flow environment would permit a much accurate evaluation of the pressure-time trace and, more generally a good prediction of the overall rocket performance.

Typically, during the TPS design for a nozzle development, both experimental and simplified numerical analyses are used in an iterative process accounting for a large amount of constraints that are sometimes counteracting. The entire process is such a specific one that it is a common practice to strongly rely on empirical correlations. In particular, the estimate of the ablative material erosion rate,

whose determination is fundamental for the correct TPS design and performance prediction, is usually obtained from surface mass and energy balances based on bulk mass/energy transfer coefficients derived from semi-empirical correlations. Therefore, they need to be accurately calibrated relying on the availability of existing experimental data that are, unfortunately, specific for a particular combination of a wide set of parameters among which chamber pressure, nozzle size, propellant combination and TPS material type. As a consequence, the extension of such models and the helpfulness of these data in developing new technological applications are not so straightforward and, commonly, a large amount of expensive experimental tests have to be performed before acquiring the needed knowledge on the particular behavior of the TPS in the conditions of interest.

As a matter of fact, even if nowadays CFD is a common practice in nozzle applications, CFD codes rarely contain the correct surface boundary conditions to cope with ablation. Most codes, in fact, use simplistic boundary conditions (constant prescribed temperature or heat flux and zero mass transfer) and cannot be realistically used for TPS design and analysis. In this context, the present work has indicated that an accurate knowledge of the involved phenomena, in combination with a sharp individuation of the driving phenomena, allows to build up a theoretical/numerical framework capable of accounting for complex gas-surface interaction physics in a quite smart, simple and “computationally sustainable” way.

To pursue the objective of developing a reliable way to study the TPS behavior in nozzle environment, a CFD code, with an already implemented ablative boundary condition for the particular case of carbon-based non-pyrolyzing ablative TPS, has been used as the ground for the implementation of ablative boundary conditions for carbon- and silica-based pyrolyzing ablative TPS. The surface mass and energy balances have been derived for the pyrolyzing material of interest

in the particular case of steady-state ablation, when the mass flow of the pyrolysis gas can be related to the mass flow rate of the ablated material. The analyzed pyrolyzing TPS share the same resin filler, that is the phenolic resin. A specific decomposition and pyrolysis gas generation model has been developed and implemented. This model gives particular attention to the evaluation of the pyrolysis gas elemental composition and its compatibility with the residual part of the resin that remains, together with the fibers, to form the charred materials upon which the ablation model is applied. Since the highly different phenomena involved in case of carbon- or silica-based ablation the two ablation models rely on thermochemical or mechanical ablation, respectively. For the carbon-based materials (both pyrolyzing and non-pyrolyzing) a finite rate model for the carbon oxidation has been used. The model considers three major oxidizing species that are typically present in the combustion products:  $H_2O$ ,  $CO_2$  and  $OH$ . This allows to determine the nozzle erosion in whatever ablation regime: diffusion or kinetically limited. Differently, when the silica-based materials are considered, the surface melting has been considered the driving phenomenon of the erosion process. If the surface temperature overcomes the silica fiber melting temperature, the ablation model is switched on and the fail mass flow rate of the melted silica, that cause the TPS material consumption, is calculated by means of a customized surface energy balance.

A validation test case has been presented for each of the ablative boundary conditions implemented in the CFD code. After a necessary presentation of the boundary condition for non-pyrolyzing carbon-based materials and the description of its validation test case, the validations for the case of pyrolyzing TPSs has been described. The obtained erosion rates agree in an encouraging manner with the experimental measurements and suggest that the evaluation of the pyrolysis gas mass flow rate can be accurately accounted for by means of the

steady-state ablation approximation provided that the correct knowledge of the charred material density is given. The pyrolysis gas has shown its capacity of restraining the char mass flow rate thanks to its blockage effect, especially when material with high resin content are considered. However the lower density of the charred surface, with respect to that of a non-pyrolyzing material, leads to significantly higher erosion rate when the two materials are exposed to the same environmental conditions. Among these calculations, verifications of the implemented decomposition model have been performed showing a good capacity in reproducing the final charred material density when the data on the pyrolyzing material components are known.

A similar validation analysis has been carried out for the developed erosion model for silica-based pyrolyzing material. Despite the inherent simplification of isothermal surface, simulation results have shown a good agreement with the measured erosions in three different chamber conditions. Because of the nature of the silica-phenolic erosion phenomenon, the lowering of the chamber temperature has been found to be a deterrent for the material erosion up to the point that, practically, no erosion occurs when the surface temperature does not exceed the silica melting temperature.

Two different application test cases of the developed models have been studied. First, a thorough erosion analysis of the carbon-based nozzles of the 2<sup>nd</sup> and the 3<sup>rd</sup> stages of the European Vega launcher has been performed. The comparison of the predictions with the experimental measurements obtained from static firing tests shows a good reproduction of the eroded profile for both motors. The results demonstrate the applicability of the present model as a predictive tool in a full-scale application.

Subsequently, an analysis of the TPSs behavior in oxygen/methane environment has been performed. The cylindrical combustion chamber and the nozzle have

been analyzed for a wide range of chamber conditions, corresponding to several different mixture ratio. The carbon-based materials have shown a lower erosion rate, in both the chamber and the nozzle of the test geometry, for the nominal mixture ratio condition and null wall radiative heat flux. The responses of the analyzed materials at different mixture ratios have shown similar behaviors. Moving down from the nominal mixture ratio value, a reduction of the erosion rate has been found, suggesting as feasible the use of chemical film cooling to help the wall material in withstanding the harsh condition at which it is exposed. The reduction of the erosion rate due to the wall radiative heat flux has been found to be stronger for the silica-based materials than for carbon-based materials. In particular, both in the cylindrical chamber and in the last diverging part of the nozzle the erosion rate is reset for the silica-phenolic, whereas is still non-null for the carbon-based materials. However, the silica-based material erosion in the throat region was still high, and the insertion of a throat insert should be considered in order to limitate the erosion in that region.

Finally, the CFD code has been coupled to a thermal response code to study the coupled heating/erosion problem removing the classical use of the steady-state ablation approximation. Simulations have been performed for a non-pyrolyzing graphitic nozzle and for two different metallized propellants characterized by a wide variation of the aluminum content. Results have shown that the wall temperature at the throat location increases very quickly (for the analyzed conditions, 2000 K are exceeded in less than one second of exposure). After a quick initial rise, the wall temperature increases more slowly with time heading towards the steady-state condition. However, this transient phase has been found to be highly dependent on the material thermal properties, suggesting that when less conductive pyrolyzing materials are used, the steady-state could be reached much faster. The erosion rate build-up is characterized by a time delay during

which the erosion rate is only a fraction of its steady-state value. An interesting outcome of the analysis is also that, when the recession is diffusion-limited, the erosion rate can temporarily exceed the steady-state value due to the higher diffusion fluxes experienced in the colder boundary-layer with respect to those at steady-state. Differently, when the erosion is kinetic-limited, the erosion rate increases with the wall temperature and hence tends to steady-state monotonically. These transient analysis has confirmed the validity of the steady state approach although the strong influence of both the propellant composition and the material thermal properties on the time needed to reach the steady state has been found.

## Future works

On the whole, the developed model can be considered an important step towards the final objective of supporting the ablative nozzles analysis with reliable and accurate CFD models, based on the comprehensive reproduction of the physical phenomena occurring over different kinds of TPS ablative materials. Obviously, a lot of work is still to be done and improvements and modifications to the present model can be made. For example, the modeling of the TPS material roughness, arising because of non-homogeneous erosion rate over the surface, can be considered by modifying the turbulence model to account for its effect on the convective heat flux. The radiative heat flux towards the wall, due to the presence of highly emitting condensed Alumina particles, can modify the material behavior. Even without discarding the simplification of considering a single phase model, this phenomenon could be considered in a simplified way to understand its effect on the material erosion. Among the possible modifications, a proactive collaboration with the experimentalists is suggested to consider

the implementation of different models for the thermochemical ablation and the material decomposition, specifically developed for the strong variable pressure and temperature conditions encountered in rocket nozzles. Finally, considering the developed loose coupling technique and its results, the analysis of the transient behavior of the erosion phenomenon results an interesting open field that should be investigated to acquire a stronger consciousness of the simplifications introduced by using a simplifying hypothesis such as the steady-state ablation approximation.



---

## References

- [1] Kowal, T. J., "Thermal Protection System (Heat Shield) Development - Advanced Development Project," NASA Report JSC-CN-21831, 2010, Commercial Human Spaceflight Symposium, Houston, Texas, October 13-14 2010.
- [2] Bianchi, S., Serraglia, F., Giliberti, F., and Betti, F., "Vega Solid Rocket Motors Development and Qualification," AIAA Paper 2010-7084, 2010, 46th AIAA/ASME/SAE/ASEE Joint Propulsion Conference and Exhibit, Nashville, TN, July 25-28, 2010.
- [3] Ellis, R. A. and Jr., R. B. K., *Solid Rocket Motor Nozzles*, No. SP-8115, 1975.
- [4] Sutton, G. P. and Biblarz, O., *Rocket Propulsion Elements*, Wiley-Interscience, New York, 7th ed., 2001.

- [5] Swope, L. W. and Berard, M. F., "Effect of Solid-Rocket Propellant Formulations and Exhaust-Gas Chemistries on the Erosion of Graphite Nozzles," *AIAA Solid Propellant Rocket Conference*, Palo Alto, CA., Jan.1964.
- [6] Klager, K., "The Interaction of the Efflux of Solid Propellants with Nozzle Materials." *Propellants and Explosives*, Vol. 2, 1977.
- [7] Geisler, R. L., "The relationship between solid propellant formulation variables and nozzle recession rates," Presented at the JANNAF Rocket Nozzle Technology Subcommittee Workshops, July 12-13, 1978, Lancaster, CA.
- [8] Geisler, R. L., "A Global View of the Use of Aluminum Fuel in Solid Rocket Motor," AIAA Paper 2002-3748, 2002, 38th AIAA/ASME/SAE/ASEE Joint Propulsion Conference and Exhibit, Indianapolis, IN, July 07-10, 2002.
- [9] Hsieh, C.-L. and Seader, J. D., "Similarity Analysis for the Surface Ablation of Silica-Reinforced Composite," *Journal of Spacecraft and Rockets*, Vol. 10, No. 12, 1973, pp. 799–802.
- [10] Clark, K. J., Flood, D. T., Moyer, C. B., and Rindal, R. A., "Experimental and Theoretical Analysis of Ablative Material Response in a Liquid-Propellant Rocket Engine: Final Report," NASA Critical Report CR-72301, 1967.
- [11] Wool, M. R., Moyer, C. B., Powars, C. A., and Rindal, R. A., "Ablative Response of a Silica Phenolic to Simulated Liquid Propellant Rocket Engine Operating Conditions," NASA Critical Report CR-72701, 1971.
- [12] Kendall, R. M., Barlett, E. P., Rindal, R. A., and Moyer, C. B., "An Analysis of the Chemically Reacting Boundary Layer and Charring Ablator. Part I: Summary Report," NASA Critical Report CR-1060, 1968.

- [13] Delaney, L. J., Eagleton, L. C., and Jones, W. H., "A Semiquantitative Prediction of the Erosion of Graphite Nozzle Inserts," *AIAA Journal*, Vol. 2, No. 8, 1964, pp. 1428–1433.
- [14] McDonald, A. J. and Hedman, P. O., "Erosion of Graphite in Solid-Propellant Combustion Gases and Effects on Heat Transfer," *AIAA Journal*, Vol. 3, No. 7, 1965, pp. 1250–1257.
- [15] Kuo, K. K. and Keswani, S. T., "A Comprehensive Theoretical Model for Carbon-Carbon Composite Nozzle Recession," *Combustion Science and Technology*, Vol. 42, No. 3-4, 1985, pp. 145–164.
- [16] Kuo, K. K. and Keswani, S. T., "Validation of an Aerothermochemical Model for Graphite Nozzle Recession and Heat-Transfer Processes," *Combustion Science and Technology*, Vol. 47, No. 3-4, 1986, pp. 177–192.
- [17] Acharya, R. and Kuo, K. K., "Effect of Pressure and Propellant Composition on Graphite Rocket Nozzle Erosion Rate," *Journal of Propulsion and Power*, Vol. 23, No. 6, 2007, pp. 1242–1254.
- [18] Acharya, R. and Kuo, K. K., "Effect of Reaction Kinetic Schemes on Graphite Rocket Nozzle Erosion Rates," *International Journal of Energetic Materials and Chemical Propulsion*, Vol. 9, 2010, pp. 111.
- [19] Bradley, D., Dixon-Lewis, G., din Habik, S. E., and Mushi, E., "The Oxidation of Graphite Powder in Flame Reaction Zones," *Symposium (International) on Combustion*, Vol. 20, No. 1, 1985, pp. 931 – 940, Twentieth Symposium (International) on Combustion.
- [20] Chelliah, H., Makino, A., Kato, I., Araki, N., and Law, C., "Modeling of Graphite Oxidation in a Stagnation-Point Flow Field Using Detailed Homogeneous and Semiglobal Heterogeneous Mechanisms with Comparisons

- to Experiments," *Combustion and Flame*, Vol. 104, No. 4, 1996, pp. 469 – 480.
- [21] Acharya, R. and Kuo, K. K., "Numerical Simulation of Graphite Nozzle Erosion with Parametric Analysis," AIAA Paper 2010-6846, 2010.
- [22] Thakre, P., *Chemical Erosion of Graphite and Refractory Metal Nozzles and its Mitigation in Solid-Propellant Rocket Motors*, Ph.D. thesis, The Pennsylvania State University, University Park, Pennsylvania, 2008.
- [23] Thakre, P. and Yang, V., "Chemical Erosion of Carbon-Carbon/Graphite Nozzles in Solid-Propellant Rocket Motors," *Journal of Propulsion and Power*, Vol. 24, No. 4, 2008, pp. 822–833.
- [24] Thakre, P. and Yang, V., "Effect of Surface Roughness and Radiation on Graphite Nozzle Erosion in Solid Rocket Motors," *Journal of Propulsion and Power*, Vol. 28, No. 2, 2012, pp. 448–451.
- [25] Bianchi, D., *Modeling of Ablation Phenomena in Space Applications*, Ph.D. thesis, University of Rome "La Sapienza", Rome, Italy, 2007.
- [26] Bianchi, D., Nasuti, F., and Martelli, E., "Coupled Analysis of Flow and Surface Ablation in Carbon-Carbon Rocket Nozzles," *Journal of Spacecraft and Rockets*, Vol. 46, No. 3, 2009, pp. 492–500.
- [27] Bianchi, D., Nasuti, F., and Martelli, E., "Thermochemical Erosion Analysis for Graphite/Carbon-Carbon Rocket Nozzles," *Journal of Propulsion and Power*, Vol. 27, No. 1, 2011, pp. 197–205.
- [28] Bianchi, D. and Nasuti, F., "Analysis of Carbon-Carbon Nozzle Erosion with Shape-Change Effects in Full-Scale Solid-Rocket Motors," *Journal of Propulsion and Power*, Vol. 28, No. 4, 2012, pp. 820–830.

- [29] Chen, Y. and Milos, F., "Navier-Stokes Solutions with Finite Rate Ablation for Planetary Mission Earth Reentries," *Journal of Spacecraft and Rockets*, Vol. 42, No. 1, 2005, pp. 197–205.
- [30] Blumenthal, J. L., A. Burns, E., and Santy, M. J., "Kinetic Studies of High-Temperature Carbon-Silica Reactions in Charred Silica-Reinforced Phenolic Resins," *AIAA Journal*, Vol. 4, No. 6, 1966, pp. 1053–1057.
- [31] Cohz, S. N., Hamilton, J. V., Ladacki, M., and Samuel, N., "Heat of Pyrolysis of Resin in Silica-Phenolic Ablator," *AIAA Journal*, Vol. 4, No. 10, 1966, pp. 1798–180.
- [32] Romie, F. E., "Carbon-silica reaction in silica-phenolic composites," *AIAA Journal*, Vol. 5, No. 8, 1967, pp. 1511–1513.
- [33] Rindal, R. A. and Moyer, C. B., "Comment on Carbon-Silica Reaction in Silica-Phenolic Compositei," *AIAA Journal*, Vol. 6, No. 5, 1968, pp. 991–992.
- [34] Cagliostro, D. E., Goldstein, H., and Parker, J. A., "Silica Reinforcement and Char Reactions in the Apollo Heat Shield," *Journal of Spacecraft and Rockets*, Vol. 9, No. 5, 1972, pp. 346–350.
- [35] Joatton, R. C., "Formulation of the Surface Ablation of a Silica-Nylon-Phenol Material," *Journal of Spacecraft and Rockets*, Vol. 8, No. 5, 1971, pp. 527–529.
- [36] Hsieh, C.-L. and Seader, J. D., "Surface Ablation of Silica-Reinforced Composites," *AIAA Journal*, Vol. 11, No. 8, 1973, pp. 1181–1187.
- [37] Anderson, Jr., J. D., *Hypersonic and High-Temperature Gas Dynamics*, AIAA Education Series, Reston, Virginia, 2nd ed., 2006.

- [38] McBride, B. J. and Gordon, S., *Computer Program for Calculation of Complex Chemical Equilibrium Compositions and Applications: I. Analysis*, National Aeronautics and Space Administration, Lewis Research Center, Cleveland, Ohio 44135-3191, October 1994, NASA Reference Publication, RP-1311.
- [39] Chase, M. W., Davies, C. A., Downey, J. R., Frurip, D. J., McDonald, R. A., and Syverud, A. N., "JANNAF Thermodynamic Tables (Third ed., Pts. I-II)," *Journal of Physical and Chemical Reference Data*, Vol. 14, Suppl. 1, Americal Chemical Society, Washington, DC., 1985.
- [40] Cox, J. D., *CODATA Key Values for Thermodynamics*, Hemisphere Publishing Corp., New York, 1989.
- [41] Gurvich, L. V., Veyts, I. V., and Alcock, C. B., *Thermodynamic Properties of individual Substances*, Vol.1, Pts. 1-2, Fourth ed., Hemisphere Publishing Corp., New York, 1989.
- [42] Marsh, K. N., Das, A., Frenkel, M., Gadalla, N. M., and Wilhoit, R. C., *TRC Thermodynamic Tables, Non-Hydrocarbons (Vols. I-VIII) and Hydrocarbons (Vols. I-XII)*, Thermodynamics Research Center, Texas A&M University, College Station, TX, 1988.
- [43] McBride, B. J., Gordon, S., and Reno, M. A., "Thermodynamic Data for Fifty Reference Elements," NASA TP 3287, 1993.
- [44] Bird, R. B., Stewart, W. E., and Lightfoot, E. D., *Transport Phenomena*, John Wiley and Sons, Inc., 1960.
- [45] Sutton, K. and Gnoffo, P. A., "Multi-Component Diffusion With Application to Computational Aerothermodynamics," AIAA Paper 1998-2575,

- 1998, 7th AIAA/ASME Joint Thermophysics and Heat Transfer Conference, Albuquerque, New Mexico, June 15-18, 1998.
- [46] Hirschfelder, J., Curtiss, C., and Bird, R., *Theory of Gases and Liquids*, John Wiley and Sons, Inc, Reston, Virginia, 1954.
- [47] Brokaw, R. S., "Thermal Conductivity of Gas Mixtures in Chemical Equilibrium," *The Journal of Chemical Physics*, Vol. 32, No. 4, 1960.
- [48] Brokaw, R. S., "Approximate Forumlas for the Viscosity and Thermal Conductivity of Gas Mixtures," *The Journal of Chemical Physics*, Vol. 29, No. 2, 1958.
- [49] Brokaw, R. S., "Alignment Charts for Transport Properties, Viscosity, Thermal Conductivity, and Diffusion Coefficients for Nonpoalr Gases and Gas Mixtures at Low Density," *NASA-TR-R-81*, 1960.
- [50] Spalart, P. R. and Allmaras, S. R., "A One-Equation Turbulence Model for Aerodynamic Flow," *La Recherche Aerospatiale*, Vol. 1, 1994, pp. 5–21.
- [51] Kim, S., "Numerical Investigation of Chemical Reaction-Turbulence Interaction in Compressible Shear Layer," *Combustion and Flames*, Vol. 101, 1995, pp. 197–208.
- [52] Moyer, C. B. and Rindal, R. A., "An Analysis of the Chemically Reacting Boundary Layer and Charring Ablator. Part II: Finite Difference Solution for the In-Depth Response of Charring Materials Considering Surface Chemical Energy Balances," NASA Critical Report CR-1061, 1968.
- [53] Keenan, J. A., *Thermo-Chemical Ablation of Heat Shields Under Earth Reentry Conditions*, Ph.D. thesis, North Carolina State University, Raleigh, North Carolina, 1994.

- [54] Chen, Y. K. and Henline, W. D., "Hypersonic Nonequilibrium Navier-Stokes Solutions over an Ablating Graphite Nosetip," *Journal of Spacecraft and Rockets*, Vol. 31, No. 5, 1994.
- [55] Gupta, R. N., "Aerothermodynamic Analysis of Stardust Sample Return Capsule with Coupled Radiation and Ablation," *Journal of Spacecraft and Rockets*, Vol. 37, No. 4, 2000.
- [56] Bhutta, B. A. and Lewis, C. H., "Low-to-High Altitude Predictions of Three-Dimensional Ablative Hypersonic Flowfields," *Journal of Spacecraft and Rockets*, Vol. 30, No. 4, 1993.
- [57] Moretti, G., "A Technique for Integrating Two-Dimensional Euler Equations," *Computer and Fluids*, Vol. 15, No. 1, 1987, pp. 59–75.
- [58] Valorani, M., *Combustione ad Alta Velocit: Simulazione Numerica con Formulazione Quasilineare*, Ph.D. thesis, University of Rome “La Sapienza”, Rome, Italy, 1991, in Italian.
- [59] Nasuti, F., *Analisi Numerica di Fenomeni di Separazione in Ugelli Propulsivi*, Ph.D. thesis, University of Rome “La Sapienza”, Rome, Italy, 1995, in Italian.
- [60] Lentini, D., "A quasi-linear formulation for chemically reacting compressible mixtures of imperfect gases," *Acta Astronautica*, Vol. 62, No. 23, 2008, pp. 177 – 184.
- [61] Martelli, E., *Studio della Fluidodinamica Interna di Ugelli Propulsivi di Tipo Dual Bell*, Ph.D. thesis, University of Rome “La Sapienza”, Rome, Italy, 2006, in Italian.

- [62] Moretti, G., "A numerical analysis of muzzle blast precursor flow," *Computers and Fluids*, Vol. 10, No. 1, 1982, pp. 51 – 86.
- [63] Moretti, G., Marconi, F., and Onofri, M., "Shock-boundary layer interaction by shock fitting," *Thirteenth International Conference on Numerical Methods in Fluid Dynamics*, edited by M. Napolitano and F. Sabetta, Vol. 414 of *Lecture Notes in Physics*, Springer Berlin / Heidelberg, 1993, pp. 345–349.
- [64] Valorani, M. and Favini, B., "On the numerical integration of multi-dimensional, initial boundary value problems for the Euler equations in quasi-linear form," Vol. 14, John Wiley & Sons, Inc., 1998, pp. 781–814.
- [65] Butler, D. S., "The numerical solution of hyperbolic systems of partial differential equation in three independent variables," *Proc. R. Soc.*, , No. 255A, 1960, pp. 232–252.
- [66] Nasuti, F., "Multi-Block Shock-Fitting Technique to Solve Steady and Unsteady Compressible Flows," *2nd International Conference on Computational Fluid Dynamics*, edited by S. Armfield, P. Morgan, and K. Srinivas, Springer-Verlag, Berlin, 2003, pp. 217–222.
- [67] Moretti, G., "Orthogonal Grids around Difficult Bodies," *AIAA Journal*, Vol. 30, No. 4, 1992, pp. 933–938.
- [68] Nasuti, F., Onofri, M., and Valorani, M., "Orthogonal Grid Generation for Internal Flows by Conformal Mapping," *Numerical Methods in Laminar and Turbulent Flow*, Vol. VIII–1, Pineridge Press, Swansea, UK, 1993, pp. 1359–1369.
- [69] Moretti, G., "Analisi Matematica," Hoepli, Milano, 1981, II ed.

- [70] Moretti, G., "The  $\lambda$ -scheme," *Comput. Fluids*, Vol. 7, 1979, pp. 191–205.
- [71] Moretti, G., F., M., and Onofri, M., "Shock Boundary Layer Interactions Computed by a Shock Fitting Technique," *Lecture Nn in Physics*, Vol. 414, Springer-Verlag, Berlin, 1993, pp. 345–349.
- [72] Gabutti, B., "On Two Upwind Finite-Difference Scheme for Hyperbolic Equations in Non-Conservative Form," *Computer and Fluids*, Vol. 11, 1983, pp. 207–230.
- [73] Roache, P. J., "Computational Fluid Dynamics," Hermosa Publishers, 1976, Albuquerque, NM, USA.
- [74] Thompson, K. W., "Time Dependent Boundary Conditions for Hyperbolic Systems," *Journal of Computational Physics*, Vol. 68, 1987, pp. 1–24.
- [75] Bianchi, D., Nasuti, F., and Martelli, E., "Coupled Analysis of Flow and Surface Ablation in Carbon-Carbon Rocket Nozzles," AIAA Paper 2008–3912, 2008, 40th AIAA Thermophysics Conference, Seattle, Washington, June 23-26, 2008.
- [76] Geisler, R. L., "The prediction of graphite rocket nozzle recession rates," Presented at the JANNAF Propulsion Meeting, New Orleans, LA, May 1981. CPIA Publication 342.
- [77] Geisler, R. L. and Beckam, C. W., "The History of the Bates Motors at the Air Force Rocket Propulsion Laboratory," AIAA Paper 1998–3981, 1998, 34th AIAA/ASME/SAE/ASEE Joint Propulsion Conference and Exhibit, Cleveland, OH, July 13-15, 1998.
- [78] Venkatachari, B. S., Cheng, B., and Koomullil, R., "Uncertainty Analysis of Surface Ablation," AIAA Paper 2009–261, 2009, 47th AIAA Aerospace

- Sciences Meeting including The New Horizons Forum and Aerospace Exposition, Orlando, Florida, Jan. 5-8, 2009.
- [79] Chen, Y. and Milos, F., "Effects of Non-equilibrium Chemistry and Darcy-Forchheimer Flow of Pyrolysis Gas for a Charring Ablator," AIAA Paper 2011-3122, 2011, 42nd AIAA Thermophysics Conference, Honolulu, Hawaii, June 27-30, 2011.
- [80] Milos, F. and Rasky, D. J., "Review of Numerical Procedures for Computational Surface Thermochemistry," *Journal of Thermophysics and Heat Transfer*, Vol. 8, No. 1, 1994, pp. 24–34.
- [81] Powers, L. B., Bailey, R. L., and Morrison, B. H., "Shuttle Solid Rocket Motor Nozzle Alternate Ablative Evaluation," AIAA Paper 1981-1461, 1981, 17th AIAA/SAE/ ASME Joint Propulsion Conference, Colorado Springs, Colorado, July 27-29, 1981.
- [82] Powers, L. B. and Bailey, R. L., "Shuttle Subscale Ablative Nozzle Tests," *Journal of Spacecraft and Rockets*, Vol. 19, No. 2, 1982, pp. 104–112.
- [83] McManus, H. and Springer, G., "High Temperature Thermomechanical Behavior of Carbon-Phenolic and Carbon-Carbon Composites, II. Results," *Journal of Composite Materials*, Vol. 26, No. 2, 1992, pp. 230–255.
- [84] Keyhani, M., "Verification of Thermal Analysis Codes for Modeling Solid Rocket Nozzles," NASA Critical Report CR-195248, 1993.
- [85] Williams, S. D. and Curry, D. M., "Thermal Protection Materials: Thermophysical Property Data," NASA Reference Publication RP-1289, 1992.

- [86] McManus, H. and Springer, G., "High Temperature Thermomechanical Behavior of Carbon-Phenolic and Carbon-Carbon Composites, I. Analysis," *Journal of Composite Materials*, Vol. 26, No. 2, 1992, pp. 230–255.
- [87] Daimon, Y., Shimada, T., Tsuboi, N., Takaki, R., Fujita, K., and Takekawa, K., "Evaluation of Ablation and Longitudinal Vortices in Solid Rocket Motor by Computational Fluid Dynamics," 42nd AIAA/ASME/SAE/ASEE Joint Propulsion Conference and Exhibit, Sacramento, CA, July 2006.
- [88] Haeseler, D., Gotz, A., Mading, C., Roubinski, V., Gorokhov, V., and Khrissanfov, S., "Testing of LOX-Hydrocarbons Thrust Chambers for Future Reusable Launch Vehicles," AIAA Paper 2002-3845, 2002, 38th AIAA/ASME/SAE/ASEE Joint Propulsion Conference and Exhibit, Indianapolis, Indiana, July 7-10, 2002.
- [89] Preclik, D., Hagemann, G., Knab, O., Mading, C., Haeseler, D., Haidn, O., Woschnak, A., and DeRosa, M., "LOX/Hydrocarbon Preparatory Thrust Chamber Technology Activities in Germany," AIAA Paper 2005-4555, 2005, 41st AIAA/ASME/SAE/ASEE Joint Propulsion Conference and Exhibit, Tucson, Arizona, July 10-13, 2005.
- [90] Arione, L., Ierardo, N., Rudnykh, M., Caggiano, G., Lobov, S., Shostak, A., De Lillis, A., and D'Aversa, E., "Development status of the LM10-MIRA LOX-LNG Expander Cycle Engine for the LYRA Launch Vehicle," Proceedings of space propulsion 2010, 2010.
- [91] Preuss, A., Preclik, D., Mading, C., Gorgen, J., Soller, S., Haidn, O., Oschwald, M., Clauss, W., Arnold, R., and Sender, J., "LOX/Methane Tech-

- nology Efforts for Future Liquid Rocket Engines," Proceedings of space propulsion 2008, 2008.
- [92] Neil, T., Judd, D., Veith, E., and Rousar, D., "Practical Uses of Liquid Methane in Rocket Engine Applications," *Acta Astronautica*, Vol. 65, 2009, pp. 696–705.
- [93] Judd, D. C., Buccella, S., M, A., Hewitt, R., McLaughlin, B., Hart, G., and Veith, E., "Development Testing of LOX/Methane Engine for In-Space Propulsion," AIAA Paper 2006–5079, 2006, 42nd AIAA/ASME/SAE/ASEE Joint Propulsion Conference & Exhibit, Sacramento, California, July 9-12, 2006.
- [94] Squire, T., Milos, F., and Hartlieb, G., "Aerospace Materials Property Database (TPSX)," *Journal of Spacecraft and Rockets*, Vol. 46, No. 3, 2009, pp. 733–736.
- [95] Williams, S. D. and Curry, D. M., "Thermal protection materials: Thermophysical property data," NASA Reference Publication RP-1289, 1992.
- [96] Urbano, A. and Nasuti, F., "Parametric Analysis of Cooling Properties of Candidate Expander Cycle Fuels," AIAA Paper 2012–1148, 2012, 50th AIAA Aerospace Sciences Meeting, Nashville, Tennessee, January 9-12, 2012.
- [97] Evans, B., Kuo, K. K., Ferrera, P. J., Moore, J. D., Kutzler, P., and Boyd, E., "Nozzle Throat Erosion Characterization Study Using a Solid-Propellant Rocket Motor Simulator," AIAA Paper 2007–5776, 2007, 43rd AIAA/ASME/SAE/ASEE Joint Propulsion Conference & Exhibit, Cincinnati, Ohio, July 8-12, 2007.

- [98] Gordon, S. and McBride, B. J., "Computer Program for Calculation of Complex Chemical Equilibrium Compositions and Applications," NASA RP 1311, 1994.
- [99] Taylor, R. E., Groot, H., and Shoemaker, R. L., "Thermophysical Properties of Fine Weave Carbon/Carbon Composites," AIAA Paper 81-1103, June 1981, 16th AIAA Thermophysics Conference, Palo Alto, CA, June 23-25, 1981.
- [100] Nasuti, F., *Analisi Numerica di Fenomeni di Separazione in Ugelli Propulsivi*, 1995, PhD Thesis (in Italian), Dept. of Mechanics and Aeronautics, Univ. of Rome "La Sapienza", Rome, Italy.

# Derivation of the flow-field governing equations

## Continuity equation

A material control volume ( $\hat{V}$ ) is a time varying volume defined by a closed boundary surface ( $\hat{S}$ ) and containing the same portions of fluids at all times. Since the fluid elements cannot enter or leave this volume, each point of the surrounding surface moves at the local velocity  $\mathbf{v}$ . In a multi-species fluid, considering a volume containing only the species  $i$ , the local velocity of the surface is  $\mathbf{v}_i$  and is defined as:

$$\mathbf{v}_i = \mathbf{v} + \mathbf{u}_i \quad (\text{A.1})$$

where  $\mathbf{v}$  is the local mixture velocity and  $\mathbf{u}_i$  is the local diffusion velocity of the species  $i$ , here approximated using the Fick's law:

$$\mathbf{u}_i = -\frac{\mathcal{D}_{im} \nabla y_i}{y_i} \quad (\text{A.2})$$

and  $\mathcal{D}_{im}$  is the multicomponent diffusion coefficient. For this mixture, the continuity equation for each species  $i$  reads:

$$\frac{d}{dt} \int_V \rho_i dV = \dot{w}_i \quad (\text{A.3})$$

where the right-hand side represents a general source term of the species. Then, using the Reynolds transport theorem to write Eq. (A.3) in a fixed volume ( $V$ ) and applying the divergence theorem (noting that  $\mathbf{v} \cdot \mathbf{n} = \mathbf{n} \cdot \mathbf{v}$ ) to the left-hand side of Eq. (A.3):

$$\frac{d}{dt} \int_V \rho_i dV = \int_V \frac{\partial \rho_i}{\partial t} dV + \int_S \rho_i \mathbf{v}_i \cdot \mathbf{n} dS = \int_V \left( \frac{\partial \rho_i}{\partial t} + \nabla \cdot (\rho_i \mathbf{v}_i) \right) dV \quad (\text{A.4})$$

and considering that Eq. (A.4) applies to an arbitrary volume, the integrand must be zero and the species continuity equation in its conservation form reads:

$$\frac{\partial \rho_i}{\partial t} + \nabla \cdot (\rho_i \mathbf{v}_i) = \dot{w}_i \quad i = 1, \dots, N_c - 1 \quad (\text{A.5})$$

where only  $N_c - 1$  equations are needed, since the  $N_c^{th}$  is the definition of the mixture density:

$$\rho = \sum_{i=1}^{N_c} \rho_i y_i = \sum_{i=1}^{N_c} \rho_i \quad (\text{A.6})$$

Moreover, considering that:

$$\sum_{i=1}^{N_c} \dot{w}_i = 0, \quad \sum_{i=1}^{N_c} \mathbf{u}_i = 0 \quad (\text{A.7})$$

and using the definition of the mass-weighted average flow velocity of the mixture:

$$\mathbf{v} = \sum_{i=1}^{N_c} \mathbf{v}_i y_i \quad (\text{A.8})$$

by summing Eq. (A.5) over all the species, one obtains:

$$\frac{\partial \rho}{\partial t} + \nabla \cdot (\rho \mathbf{v}) = 0 \quad (\text{A.9})$$

that is the conservation form of the mixture continuity equation.

## Momentum balance

By definition, the momentum balance asserts that the time variation of the momentum of a material control volume ( $\hat{V}$ ) equals the sum of the volumetric and surface forces acting on the volume and on its surface. The integral form of the momentum balance for that volume is readily formulated:

$$\frac{d}{dt} \int_{\hat{V}} \rho \mathbf{v} dV = \int_{\hat{V}} \rho \mathbf{F} dV + \int_{\hat{S}} \mathbf{n} \cdot \mathbf{S} dS \quad (\text{A.10})$$

in which the term  $\mathbf{S}$  represents the stress tensor and, if the volumetric forces ( $\mathbf{F}$ ) are neglected, one obtains:

$$\frac{d}{dt} \int_{\hat{V}} \rho \mathbf{v} dV = \int_{\hat{S}} \mathbf{n} \cdot \mathbf{S} dS \quad (\text{A.11})$$

Assuming the hypothesis of Newtonian fluid, for which a linear relationship between stress and strain rate is valid, the stress tensor can be split into the contribution of pressure forces and viscous stresses:

$$\mathbf{S} = -p \mathbb{I} + \mathbf{T} \quad (\text{A.12})$$

where the viscous stress tensor, by means of the Stokes hypothesis that connect the viscosity coefficient and the second viscosity coefficient ( $3\lambda + 2\mu = 0$ ), can

be written as:

$$\mathbb{T} = -\frac{2}{3}\mu(\nabla \cdot \mathbf{v})\mathbb{I} + \mu \left[ \nabla \mathbf{v} + (\nabla \mathbf{v})^T \right] \quad (\text{A.13})$$

At this point, by applying the Reynolds transport theorem and the divergence theorem (bearing in mind that  $\rho \mathbf{v} \mathbf{v} \cdot \mathbf{n} = \mathbf{n} \cdot \rho \mathbf{v} \mathbf{v}$ ), the momentum balance reads:

$$\int_V \frac{\partial(\rho \mathbf{v})}{\partial t} dV + \int_V \nabla \cdot [(\rho \mathbf{v}) \mathbf{v}] dV - \int_V \nabla \cdot \mathbf{S} dV = 0 \quad (\text{A.14})$$

that must applies to any arbitrary volume, giving:

$$\frac{\partial(\rho \mathbf{v})}{\partial t} + \nabla \cdot [(\rho \mathbf{v}) \mathbf{v}] - \nabla \cdot \mathbf{S} = 0 \quad (\text{A.15})$$

which is the conservation form of the differential momentum balance.

## Conservation of energy

Following the energy conservation principle, that states that the total time energy variation in a material control volume is equal to the sum of the heat transfer rate entering through the surface and the total work made by the forces acting on the volume and on the surface, the integral form of the conservation of energy is:

$$\frac{d}{dt} \int_{\hat{V}} \left( e + \frac{(\mathbf{v} \cdot \mathbf{v})}{2} \right) \rho dV = \int_{\hat{S}} (\mathbf{n} \cdot \mathbf{S}) \cdot \mathbf{v} dS - \int_{\hat{S}} \dot{\mathbf{q}} \cdot \mathbf{n} dS \quad (\text{A.16})$$

where the volumetric heating and the radiative heating have been neglected. On the left-hand side integrand of Eq. (A.16) there is the total specific energy per unit of volume ( $\mathcal{E} = e + |v|^2/2$ ), composed by the internal specific energy ( $e$ ) and the kinetic specific energy  $|v|^2/2$ ; whereas the term  $\dot{\mathbf{q}}$  represents the heat

flux vector, composed by the conductive and the diffusive heat flux, defined as:

$$\dot{\mathbf{q}} = -k\nabla T + \sum_{i=1}^{N_c} \rho_i \mathbf{u}_i h_i \quad (\text{A.17})$$

where the diffusion velocity is defined as in Eq. (A.2),  $k$  is the thermal conductivity of the mixture and  $h_i$  the enthalpy of the  $i^{\text{th}}$  species. By applying the Reynolds transport theorem and the divergence theorem,<sup>1</sup> Eq. (A.16) can be rewritten for a fixed volume ( $V$ ):

$$\int_V \frac{\partial(\rho\mathcal{E})}{\partial t} dV + \int_V \nabla \cdot (\rho\mathcal{E}\mathbf{v}) dV = \int_V \nabla \cdot (\mathbf{S} \cdot \mathbf{v}) dV - \int_V \nabla \cdot \dot{\mathbf{q}} dS \quad (\text{A.18})$$

and, since this must hold for any volume:

$$\frac{\partial(\rho\mathcal{E})}{\partial t} + \nabla \cdot (\rho\mathcal{E}\mathbf{v}) = \nabla \cdot (\mathbf{S} \cdot \mathbf{v}) - \nabla \cdot \dot{\mathbf{q}} \quad (\text{A.19})$$

which is the conservation form of the differential conservation of energy.

---

<sup>1</sup> $\rho\mathcal{E}\mathbf{v} \cdot \mathbf{n} = \mathbf{n} \cdot \rho\mathcal{E}\mathbf{v}$ ;  $(\mathbf{n} \cdot \mathbf{S}) \cdot \mathbf{v} = \mathbf{n} \cdot (\mathbf{S} \cdot \mathbf{v})$  and  $\dot{\mathbf{q}} \cdot \mathbf{n} = \mathbf{n} \cdot \dot{\mathbf{q}}$

---

## Diffusive terms in the computational plan

The transformation from the physical to the computational plan of the diffusive terms in Eq. 3.14 is presented here. In the physical plan, the terms including both diffusive and source terms are:

$$\begin{aligned}
 V_b' &= V_b + \frac{a}{\gamma R} \sum_{i=1}^{N_c} Q_i V_{y_i} = \frac{1}{c_1} \beta + \frac{a}{\gamma R} (\gamma - 1) V_s + \frac{a}{\gamma R} \sum_{i=1}^{N_c} Q_i V_{y_i} \\
 V_u &= \mathbf{V}_m \cdot \mathbf{n} = \frac{1}{\rho} (\nabla \cdot \mathbb{T}) \cdot \mathbf{n} \\
 V_v &= \mathbf{V}_m \cdot \boldsymbol{\tau} = \frac{1}{\rho} (\nabla \cdot \mathbb{T}) \cdot \boldsymbol{\tau} \\
 V_s &= -\frac{1}{T} \sum_{i=1}^{N_c} \tilde{\mu}_i V_{y_i} + \frac{R}{p} (\nabla \cdot (\mathbb{T} \cdot \mathbf{v}) - \nabla \cdot \dot{\mathbf{q}}) \\
 V_{y_i} &= \frac{\dot{w}_i}{\rho} - \frac{1}{\rho} \nabla \cdot \mathbf{j}_i
 \end{aligned} \tag{B.1}$$

with:

$$\mathbb{T} = \frac{1}{Re_r}\mu \left[ -\frac{2}{3}(\nabla \cdot \mathbf{v})\mathbb{I} + \nabla \mathbf{v} + (\nabla \mathbf{v})^T \right] \quad (\text{B.2a})$$

$$\dot{\mathbf{q}} = -\frac{\gamma_r}{\gamma_r - 1} \frac{1}{Re_r P_r} k \nabla T - \frac{1}{Le_r Re_r Pr_r} \sum_{i=1}^{N_c} \rho \mathcal{D}_{im} h_i \nabla y_i \quad (\text{B.2b})$$

$$\mathbf{j}_i = -\frac{1}{Pr_r Le_r Re_r} \rho \mathcal{D}_{im} \nabla y_i \quad (\text{B.2c})$$

To complete the transformation from the physical plane to the computational plane the diffusive terms must be transformed in terms of derivatives in the computational plane. It is therefore necessary to express  $\nabla \cdot \dot{\mathbf{q}}$ ,  $\nabla \cdot \mathbf{j}_i$ ,  $(\nabla \cdot \mathbb{T}) \cdot \mathbf{n}$ ,  $(\nabla \cdot \mathbb{T}) \cdot \boldsymbol{\tau}$ , and  $\Phi = \nabla \cdot (\mathbb{T} \cdot \mathbf{v}) = \nabla \mathbf{v} : \mathbb{T}$  in the computational plane.

The following expressions are taken from [100] and [61]. At first,  $\nabla \mathbf{v}$  is evaluated:

$$\begin{aligned} \nabla \mathbf{v} &= G(\mathbf{v}_\xi \mathbf{n} + \mathbf{v}_\eta \boldsymbol{\tau}) = \\ &= G[(u\mathbf{n} + v\boldsymbol{\tau})_\xi \mathbf{n} + (u\mathbf{n} + v\boldsymbol{\tau})_\eta \boldsymbol{\tau}] = \\ &= G[(u_\xi - v\alpha_\xi)\mathbf{n} \mathbf{n} + (u_\eta - v\alpha_\eta)\mathbf{n} \boldsymbol{\tau} + (v_\xi + u\alpha_\xi)\boldsymbol{\tau} \mathbf{n} + (v_\eta + u\alpha_\eta)\boldsymbol{\tau} \boldsymbol{\tau}] \end{aligned}$$

now letting:

$$\begin{aligned} e_{11} &= G(u_\xi - v\alpha_\xi) = G(\hat{x}_\xi u_{\hat{x}} + v\phi_2) \\ e_{12} &= \frac{1}{2}G(u_\eta + v_\xi - v\alpha_\eta + u\alpha_\xi) = \frac{1}{2}G(\hat{y}_\eta u_{\hat{y}} + \hat{x}_\xi v_{\hat{x}} + v\phi_1 - u\phi_2) \\ e_{22} &= G(v_\eta + u\alpha_\eta) = G(\hat{y}_\eta v_{\hat{y}} - u\phi_1) \end{aligned}$$

The following expressions hold:

$$\nabla \mathbf{v} + (\nabla \mathbf{v})^T = 2[e_{11}\mathbf{n} \mathbf{n} + e_{12}(\mathbf{n} \boldsymbol{\tau} + \boldsymbol{\tau} \mathbf{n}) + e_{22}\boldsymbol{\tau} \boldsymbol{\tau}] \quad (\text{B.3})$$

$$\nabla \cdot \mathbf{v} = e_{11} + e_{22} \quad (\text{B.4})$$

therefore we can express the viscous stress tensor from Eq. (B.2a):

$$\mathbb{T} = T_{11}\mathbf{n}\mathbf{n} + T_{12}(\mathbf{n}\boldsymbol{\tau} + \boldsymbol{\tau}\mathbf{n}) + T_{22}\boldsymbol{\tau}\boldsymbol{\tau}$$

where:

$$\begin{aligned} T_{11} &= \frac{2\mu}{3Re_r}(2e_{11} - e_{22}) \\ T_{12} &= \frac{2\mu}{3Re_r}e_{12} \\ T_{22} &= \frac{2\mu}{3Re_r}(2e_{22} - e_{11}) \end{aligned}$$

finally obtaining, using (3.4):

$$\begin{aligned} \nabla \cdot \mathbb{T} &= \nabla \cdot [T_{11}\mathbf{n}\mathbf{n} + T_{12}(\mathbf{n}\boldsymbol{\tau} + \boldsymbol{\tau}\mathbf{n}) + T_{22}\boldsymbol{\tau}\boldsymbol{\tau}] = \\ &= G [T_{11\xi}\mathbf{n} + T_{11}(\alpha_\xi\boldsymbol{\tau} + \alpha_\eta\mathbf{n}) + T_{12\xi}\boldsymbol{\tau} + \\ &\quad + T_{12\eta}\mathbf{n} + 2T_{12}(\alpha_\eta\boldsymbol{\tau} - \alpha_\xi\mathbf{n}) + T_{22\eta}\boldsymbol{\tau} - T_{22}(\alpha_\xi\boldsymbol{\tau} + \alpha_\eta\mathbf{n})] = \\ &= G [\hat{x}_\xi T_{11\hat{x}} + \hat{y}_\eta T_{12\hat{y}} - (T_{11} - T_{22})\phi_1 + 2T_{12}\phi_2] \mathbf{n} + \\ &\quad + G [\hat{x}_\xi T_{12\hat{x}} + \hat{y}_\eta T_{22\hat{y}} - (T_{11} - T_{22})\phi_2 + 2T_{12}\phi_1] \boldsymbol{\tau} \quad (\text{B.5}) \end{aligned}$$

and from the symmetry of  $\mathbb{T}$ :

$$\nabla\mathbf{v} : \mathbb{T} = \frac{1}{2}(\nabla\mathbf{v} + \nabla\mathbf{v}^T) : \mathbb{T} = T_{11}e_{11} + 2T_{12}e_{12} + T_{22}e_{22}$$

from which we obtain the expression of  $\Phi$ :

$$\Phi = \frac{\mu}{Re_r} \left[ 2(e_{11}^2 + 2e_{12}^2 + e_{22}^2) - \frac{2}{3}(e_{11} + e_{22})^2 \right] \quad (\text{B.6})$$

Finally, we obtain the heat flux vector (B.2b) and the mass flux vector (B.2c)

and their divergence. The heat flux vector  $\dot{\mathbf{q}}$  becomes:

$$\begin{aligned}\dot{\mathbf{q}} &= \dot{q}_1 \mathbf{n} + \dot{q}_2 \boldsymbol{\tau} \\ \dot{q}_1 &= -G \left[ \frac{\gamma_r}{\gamma_r - 1} \frac{k}{Re_r Pr_r} \hat{x}_\xi T_{\hat{x}} + \frac{1}{Le_r Re_r Pr_r} \sum \rho \mathcal{D} \hat{x}_\xi h_i y_{i,\hat{x}} \right] \\ \dot{q}_2 &= -G \left[ \frac{\gamma_r}{\gamma_r - 1} \frac{k}{Re_r Pr_r} \hat{y}_\eta T_{\hat{y}} + \frac{1}{Le_r Re_r Pr_r} \sum \rho \mathcal{D} h_i \hat{y}_\eta y_{i,\hat{y}} \right]\end{aligned}$$

and its divergence, using (3.4):

$$\begin{aligned}\nabla \cdot \dot{\mathbf{q}} &= \nabla \cdot \dot{q}_1 \cdot \mathbf{n} + \nabla \cdot \dot{q}_2 \cdot \boldsymbol{\tau} + \dot{q}_1 \nabla \cdot \mathbf{n} + \dot{q}_2 \nabla \cdot \boldsymbol{\tau} = \\ &= G(\dot{q}_{1\xi} + \dot{q}_{2\eta} + \dot{q}_1 \alpha_\eta + \dot{q}_2 \alpha_\xi) = \\ &= G(\hat{x}_\xi \dot{q}_{1\hat{x}} + \hat{y}_\eta \dot{q}_{2\hat{y}} - \dot{q}_1 \phi_1 + \dot{q}_2 \phi_2)\end{aligned}\tag{B.7}$$

The mass flux vector  $\mathbf{j}_i$  is:

$$\begin{aligned}\mathbf{j}_i &= j_{i1} \mathbf{n} + j_{i2} \boldsymbol{\tau} \\ j_{i1} &= -\frac{G}{Pr_r Re_r Le_r} \rho \mathcal{D} \hat{x}_\xi y_{i,\hat{x}} \\ j_{i2} &= -\frac{G}{Pr_r Re_r Le_r} \rho \mathcal{D} \hat{y}_\eta y_{i,\hat{y}}\end{aligned}$$

and its divergence:

$$\nabla \cdot \mathbf{j}_i = G(\hat{x}_\xi j_{i1\hat{x}} + \hat{y}_\eta j_{i2\hat{y}} - j_{i1} \phi_1 + j_{i2} \phi_2)\tag{B.8}$$

The terms  $V'_b$ ,  $\mathbf{V}_m$ ,  $V_s$ , and  $V_{y_i}$  can be finally evaluated in the computational plane  $\hat{z}$  with the use of Eqs. (B.5), (B.6), (B.7) and (B.8).

---

## Two-Dimensional axisymmetric problems

The same two-dimensional equations (3.1) can be used for axisymmetric problem with the addition of some terms; therefore the effect of axisymmetry is treated as a source term. The axisymmetric operators (gradient, divergence, etc.), denoted with  $(\cdot)_a$ , can be expressed as a function their planar counterpart, denoted with  $(\cdot)_p$ . Following the work presented [100] and [61], the final results are shown here.

We now introduce three unit vectors  $\mathbf{i}$ ,  $\mathbf{j}$ , and  $\mathbf{k}$  along the axial, radial, and azimuthal direction, respectively, to define a Cartesian frame in the physical plane. Using the relations between planar and axisymmetric operators, the equations of motion (3.1) remain unchanged for the axisymmetric problem, except for the second of (3.1), which has the added term  $\frac{a}{y}(\mathbf{v} \cdot \mathbf{j})$  on the right-end side, and the source terms, whose expression is illustrated below. In the computational

plane, the second of (3.14) becomes:

$$(b_t)_a = (b_t)_p + c_1 A$$

where:

$$A = a e_{33} \quad (C.1)$$

$$e_{33} = \frac{\mathbf{v} \cdot \mathbf{j}}{y} = \frac{u \sin \alpha + v \cos \alpha}{y}$$

Now the viscous terms must be derived for the axisymmetric case. Noting that:

$$(\nabla \mathbf{v})_a = (\nabla \mathbf{v})_p + e_{33} \mathbf{k} \mathbf{k}$$

the (B.3-B.4) become:

$$\begin{aligned} (\nabla \mathbf{v} + \nabla \mathbf{v}^T)_a &= (\nabla \mathbf{v} + \nabla \mathbf{v}^T)_p + 2e_{33} \mathbf{k} \mathbf{k} \\ (\nabla \cdot \mathbf{v})_a &= (\nabla \cdot \mathbf{v})_p + e_{33} \end{aligned}$$

consequently we can express  $\mathbb{T}$  from Eq. (3.3a):

$$\mathbf{T} = (T_{11})_a \mathbf{n} \mathbf{n} + (T_{12})_a (\mathbf{n} \boldsymbol{\tau} + \boldsymbol{\tau} \mathbf{n}) + (T_{22})_a \boldsymbol{\tau} \boldsymbol{\tau} + (T_{33})_a \mathbf{k} \mathbf{k}$$

where:

$$\begin{aligned}(T_{11})_a &= \frac{2\mu}{3Re_r}(2e_{11} - e_{22} - e_{33}) \\(T_{12})_a &= \frac{2\mu}{3Re_r}e_{12} \\(T_{22})_a &= \frac{2\mu}{3Re_r}(2e_{22} - e_{11} - e_{33}) \\(T_{33})_a &= \frac{2\mu}{3Re_r}(2e_{33} - e_{11} - e_{22})\end{aligned}$$

Finally we obtain the expression for  $\Phi$ :

$$(\Phi)_a = (\Phi)_p + \frac{4\mu}{3Re_r} [e_{33}^2 - e_{33}(e_{11} + e_{22})]$$

and for the term  $V_s$  from Eq. (3.2):

$$\begin{aligned}(V_s)_p &= -\frac{1}{T} \sum_{i=1}^{N_c} \tilde{\mu}_i (V_{yi})_p + \frac{R}{p} [(\Phi)_p - (\nabla \cdot \dot{\mathbf{q}})_p] \\(V_s)_a &= -\frac{1}{T} \sum_{i=1}^{N_c} \tilde{\mu}_i (V_{yi})_a + \frac{R}{p} \left[ (\Phi)_a - (\nabla \cdot \dot{\mathbf{q}})_p + \frac{1}{y} (\dot{q}_1 \cos \alpha + \dot{q}_2 \sin \alpha) \right]\end{aligned}$$

and for the term  $V_{yi}$  from (B.1):

$$\begin{aligned}(V_{yi})_p &= \frac{\dot{w}_i}{\rho} - \frac{1}{\rho} (\nabla \cdot \mathbf{j}_i)_p \\(V_{yi})_a &= \frac{\dot{w}_i}{\rho} - \frac{1}{\rho} \left[ (\nabla \cdot \mathbf{j}_i)_p + \frac{1}{y} (j_{i1} \cos \alpha + j_{i2} \sin \alpha) \right]\end{aligned}$$

Note that  $(\dot{\mathbf{q}})_a = (\dot{\mathbf{q}})_p$  and  $(\mathbf{j}_i)_a = (\mathbf{j}_i)_p$ , since  $(\nabla f)_a = (\nabla f)_p$  for a generic scalar  $f$ . Lastly we must derive the expression for  $\mathbf{V}_m$ :

$$(\mathbf{V}_m)_p = \frac{1}{\rho} (\nabla \cdot \mathbb{T})_p \quad (C.2)$$

now letting:

$$\begin{aligned} T_{xy} &= (\mathbf{T} \cdot \mathbf{i}) \cdot \mathbf{j} = T_{11} \sin \alpha \cos \alpha + T_{12}(\cos^2 \alpha - \sin^2 \alpha) - T_{22} \sin \alpha \cos \alpha \\ T_{yy} &= (\mathbf{T} \cdot \mathbf{j}) \cdot \mathbf{j} = T_{11} \sin^2 \alpha + 2T_{12} \sin \alpha \cos \alpha - T_{22} \cos^2 \alpha \end{aligned}$$

the following relation is obtained:

$$\begin{aligned} (\mathbf{V}_m)_a &= (\mathbf{V}_m)_p + \frac{1}{\rho y} [T_{xy} \cos \alpha + (T_{yy} - T_{33}) \sin \alpha] \mathbf{n} + \\ &\quad - \frac{1}{\rho y} [T_{xy} \sin \alpha + (T_{33} - T_{yy}) \cos \alpha] \boldsymbol{\tau} \end{aligned}$$

and expressing the terms explicitly:

$$\begin{aligned} (\mathbf{V}_m)_a &= (\mathbf{V}_m)_p + \frac{2\mu}{\rho Re_r} \left[ \frac{(e_{11} - e_{33}) \sin \alpha + e_{12} \cos \alpha}{y} \right] \mathbf{n} + \\ &\quad + \frac{2\mu}{\rho Re_r} \left[ \frac{(e_{22} - e_{33}) \cos \alpha + e_{12} \sin \alpha}{y} \right] \boldsymbol{\tau} \end{aligned}$$

The axisymmetric expression for the terms  $(V_s)_a$ ,  $(V_{y_i})_a$ , and  $(\mathbf{V}_m)_a$  have been obtained.

---

## Discretization of the in-depth energy balance

A general description of the numerical procedure used to solve the in-depth energy balance in the moving coordinate system has been given in Chapter 9. Here the derivation of the tri-diagonal matrix form obtained by rewriting the in-depth energy balance (Eq. (9.4)) in a finite-difference form is given. As done in Chapter 9 we will refer to the less complex case of planar surface and constant material properties (Eq. (9.5)). The description of the procedure for the general case of non-planar surface and non-constant material properties can be found in [25].

The in depth energy balance (Eq. (9.5)) is rewritten here for the sake of convenience:

$$\frac{\partial T}{\partial t} = \alpha \frac{\partial^2 T}{\partial x^2} + \dot{s} \frac{\partial T}{\partial x} \quad (\text{D.1})$$

the derivatives in Eq. (D.1) rewritten in finite-difference form read:

$$\begin{aligned}\frac{\partial T}{\partial t} &= \frac{T'_n - T_n}{\Delta t} \\ \frac{\partial T}{\partial x} &= \frac{(T'_{n+1} - T'_{n-1}) + (T_{n+1} - T_{n-1})}{4\Delta x} \\ \frac{\partial^2 T}{\partial x^2} &= \frac{(T'_{n+1} - 2T'_n + T'_{n-1}) + (T_{n+1} - 2T_n + T_{n-1})}{2\Delta x^2}\end{aligned}\quad (\text{D.2})$$

## Tri-diagonal matrix form of the in-depth energy balance

In the following the in-depth energy balance is rewritten differentiating the nodes in three “classes” of node: interior, surface (first) and back surface (last). These difference-form of the in-depth energy balance for each material node are then set-up in the matrix form.

### Interior nodes

Substituting the finite-difference derivatives above (Eq. (D.2)) into the Eq. (D.1), results in:

$$\begin{aligned}\frac{T'_n - T_n}{\Delta t} &= \frac{\alpha}{2\Delta x^2} \left( T'_{n+1} - 2T'_n + T'_{n-1} + T_{n+1} - 2T_n + T_{n-1} \right) + \\ &+ \frac{\dot{s}}{4\Delta x} \left( T'_{n+1} - T'_{n-1} + T_{n+1} - T_{n-1} \right)\end{aligned}\quad (\text{D.3})$$

multiplying (D.3) through by  $4\Delta x^2\Delta t$  to eliminate the denominators, and collecting all the terms involving the unknowns  $T_n'$  on the left hand side results in:

$$\begin{aligned} - (2\alpha\Delta t - \dot{s}\Delta x\Delta t)T_{n-1}' + (4\Delta x^2 + 4\alpha\Delta t)T_n' - (2\alpha\Delta t + \dot{s}\Delta x\Delta t)T_{n+1}' &= \\ (2\alpha\Delta t - \dot{s}\Delta x\Delta t)T_{n-1} + (4\Delta x^2 - 4\alpha\Delta t)T_n + (2\alpha\Delta t + \dot{s}\Delta x\Delta t)T_{n+1} & \quad (\text{D.4}) \end{aligned}$$

for each interior node  $n = 2, N$ . It is apparent that the  $T_n'$  cannot individually be written as simple linear combinations of the  $T_n$ , but are simultaneously determined as the solution to this system of linear equations. Since equation (D.4) applies only to the interior grid points, at each time step appropriate boundary conditions (e.g. at  $x_{min}$  and  $x_{max}$ ) have to be used to calculate all the  $T_n'$ .

## The surface node

We almost have a procedure for recursively determining the entire grid of  $T_n'$  starting from the given initial values. Substitution of the difference expressions into the differential equation only gave us a linear equation for each interior point in the grid. That gives  $N - 1$  equation at each time step, which is not sufficient to determine the  $N + 1$  unknowns. The missing two equations must be provided by boundary conditions applied at each time step. It would be desirable for these to be representable in a form that preserves the tri-diagonal form of the system and thus the efficiency of the solution.

The conductive heat flux  $\dot{q}_{cond}$  will play the central role in linking the in-depth solution to the surface energy balance (see Chapter 9). Therefore the energy input to the first node ( $n = 1$ ) will be left simply as  $\dot{q}_{cond}$ , which will replace the

terms of the form:

$$\frac{(T_{n+1} - T_{n-1})}{2\Delta x} = -\frac{\dot{q}_{cond}}{k}$$

$$\frac{(T'_{n+1} - T'_{n-1})}{2\Delta x} = -\frac{\dot{q}'_{cond}}{k}$$

where  $k$  is the material thermal conductivity. Thus we have the energy difference equation for the first node as:

$$\begin{aligned} \frac{T'_1 - T_1}{\Delta t} &= \frac{\alpha}{2\Delta x^2} \left( 2T'_2 - 2T'_1 + \frac{2\Delta x}{k} \dot{q}'_{cond} + 2T_2 - 2T_1 + \frac{2\Delta x}{k} \dot{q}_{cond} \right) + \\ &+ \frac{\dot{s}}{4\Delta x} \left( -\frac{2\Delta x}{k} \dot{q}'_{cond} - \frac{2\Delta x}{k} \dot{q}_{cond} \right) \end{aligned} \quad (\text{D.5})$$

multiplying (Eq.(D.5)) through by  $4\Delta x^2 \Delta t$  to eliminate the denominators, and collecting all the terms involving the unknowns  $T'_n$  and  $\dot{q}'_{cond}$  on the lefthand side results in:

$$\begin{aligned} (4\Delta x^2 + 4\alpha\Delta t)T'_1 - (4\alpha\Delta t)T'_2 - 2\frac{\Delta x\Delta t}{k}(2\alpha - \dot{s}\Delta x)\dot{q}'_{cond} &= \\ (4\Delta x^2 - 4\alpha\Delta t)T_1 + (4\alpha\Delta t)T_2 + 2\frac{\Delta x\Delta t}{k}(2\alpha - \dot{s}\Delta x)\dot{q}_{cond} & \end{aligned} \quad (\text{D.6})$$

## The back-surface node

The energy equation for the last node ( $n = N + 1$ ) must also be considered separately. The last node does not of course conduct energy to an adjacent node. Hence the conduction term is replaced by a temperature-potential convective

transfer communicating with a “reservoir” at temperature  $T_{res}$ :

$$\frac{(T_{n+1} - T_{n-1})}{2\Delta x} = -\frac{h_{res}}{k}(T_n - T_{res})$$

$$\frac{(T'_{n+1} - T'_{n-1})}{2\Delta x} = -\frac{h_{res}}{k}(T'_n - T_{res})$$

where  $h_{res}$  is the heat-transfer coefficient with the external ambient. Thus we have the energy difference equation for the last node as:

$$\begin{aligned} \frac{T'_{N+1} - T_{N+1}}{\Delta t} &= \frac{\alpha}{2\Delta x^2} \left( 2T'_N - 2T'_{N+1} - 2\Delta x \frac{h_{res}}{k} T'_{N+1} + 2T_N - 2T_{N+1} \right. \\ &\quad \left. - 2\Delta x \frac{h_{res}}{k} T_{N+1} + 4\Delta x \frac{h_{res}}{k} T_{res} \right) \frac{\dot{s}}{4\Delta x} \left( -2\Delta x \frac{h_{res}}{k} T'_{N+1} \right. \\ &\quad \left. - 2\Delta x \frac{h_{res}}{k} T_{N+1} + 4\Delta x \frac{h_{res}}{k} T_{res} \right) \end{aligned} \quad (\text{D.7})$$

multiplying (D.7) through by  $4\Delta x^2\Delta t$  to eliminate the denominators, and collecting all the terms involving the unknowns  $T'_n$  and  $\dot{q}'_{cond}$  on the left-hand side results in:

$$\begin{aligned} - (4\alpha\Delta t)T'_N + \left[ 4\Delta x^2 + 4\alpha\Delta t + 2\Delta x\Delta t \frac{h_{res}}{k} (2\alpha + \dot{s}\Delta x) \right] T'_{N+1} = \\ (4\alpha\Delta t)T_N + \left[ 4\Delta x^2 - 4\alpha\Delta t - 2\Delta x\Delta t \frac{h_{res}}{k} (2\alpha + \dot{s}\Delta x) \right] T_{N+1} + \\ 4\Delta x\Delta t \frac{h_{res}}{k} (2\alpha + \dot{s}\Delta x) T_{res} \end{aligned} \quad (\text{D.8})$$

### Tri-diagonal matrix form

The system made up of Eq. (D.4) for the interior nodes and (D.6) and (D.8) for the two boundary nodes has a very convenient structure. Written in the matrix

form already presented in Chapter 9 reads:

$$\begin{bmatrix} B_1 & C_1 & 0 & \dots & \dots & \dots & 0 \\ A_2 & B_2 & C_2 & \ddots & & & \vdots \\ 0 & A_3 & B_3 & C_3 & \ddots & & \vdots \\ \vdots & \ddots & \ddots & \ddots & \ddots & \ddots & \vdots \\ \vdots & & \ddots & A_{N-1} & B_{N-1} & C_{N-1} & 0 \\ \vdots & & & \ddots & A_N & B_N & C_N \\ 0 & \dots & \dots & \dots & 0 & A_{N+1} & B_{N+1} \end{bmatrix} \begin{Bmatrix} T'_1 \\ T'_2 \\ T'_3 \\ \vdots \\ T'_{N-1} \\ T'_N \\ T'_{N+1} \end{Bmatrix} = \begin{Bmatrix} D_1 \\ D_2 \\ D_3 \\ \vdots \\ D_{N-1} \\ D_N \\ D_{N+1} \end{Bmatrix} \quad (\text{D.9})$$

The expressions for the coefficients  $A_n$ ,  $B_n$ ,  $C_n$  and  $D_n$  are readily apparent from the finite difference energy equations (D.4), (D.6) and (D.8). For the interior nodes:

$$\left\{ \begin{array}{l} A_n = -(2\alpha\Delta t - \dot{s}\Delta x\Delta t) \\ B_n = (4\Delta x^2 + 4\alpha\Delta t) \\ C_n = -(2\alpha\Delta t + \dot{s}\Delta x\Delta t) \\ D_n = -A_n T_{n-1} + (4\Delta x^2 - 4\alpha\Delta t) T_n - C_n T_{n+1} \end{array} \right. \quad n = 2, \dots, N \quad (\text{D.10})$$

while for the first node:

$$\left\{ \begin{array}{l} B_1 = (4\Delta x^2 + 4\alpha\Delta t) \\ C_1 = -(4\alpha\Delta t) \\ D_1 = \mathcal{F}(\dot{q}'_{cond}) \end{array} \right. \quad (\text{D.11})$$

with

$$D_1 = (4\Delta x^2 - 4\alpha\Delta t)T_1 - C_1 T_2 + 2\frac{\Delta x\Delta t}{k}(2\alpha - \dot{s}\Delta x)(\dot{q}'_{cond} + \dot{q}_{cond})$$

and for the last node:

$$\begin{cases} A_{N+1} = -(4\alpha\Delta t) \\ B_{N+1} = \left[4\Delta x^2 + 4\alpha\Delta t + 2\Delta x\Delta t\frac{h_{res}}{k}(2\alpha + \dot{s}\Delta x)\right] \\ D_{N+1} = \mathcal{F}(h_{res}, T_{res}) \end{cases} \quad (\text{D.12})$$

with

$$D_{N+1} = -A_{N+1}T_N + \left[4\Delta x^2 - 4\alpha\Delta t - 2\Delta x\Delta t\frac{h_{res}}{k}(2\alpha + \dot{s}\Delta x)\right]T_{N+1} + 4\Delta x\Delta t\frac{h_{res}}{k}(2\alpha + \dot{s}\Delta x)T_{res}$$

For a given node  $n$ , except the first or last, the finite difference energy relation involves three unknown temperatures,  $T'_{n-1}$ ,  $T'_n$ , and  $T'_{n+1}$ . For the last node  $N + 1$ , there are only two unknown temperatures,  $T'_N$  and  $T'_{N+1}$ , while the first node equation involves only  $T'_1$  and  $T'_2$ , in addition to the unknown heat flux  $\dot{q}'_{cond}$ .

## Computational strategy for the coupled solution

It is now possible to see clearly what needs to be done for each time step  $\Delta t$  of the solution in order to prepare for coupling to the CFD code. First, using the current values of  $\dot{s}$  and  $T_n$ , the coefficients of the tri-diagonal energy equation matrix can

be computed. Once this matrix is set up, the required surface energy relation  $\dot{q}_{cond} = \dot{q}_{cond}(T_w)$  may be obtained directly, as described in the following.

## Reduction of the Tri-diagonal matrix

Referring to the array of in-depth energy equations set down symbolically in Eqs. (D.9), it may be seen that, beginning with the last node, the highest-indexed unknown temperature may be eliminated from each equation of Eqs. (D.9) in turn (this is the standard first step in the routine reduction of a tri-diagonal matrix). The resulting simpler set of equations is the following:

$$\begin{bmatrix} B_1^* & 0 & \dots & \dots & \dots & \dots & 0 \\ A_2^* & B_2^* & \ddots & & & & \vdots \\ 0 & A_3^* & B_3^* & \ddots & & & \vdots \\ \vdots & \ddots & \ddots & \ddots & \ddots & & \vdots \\ \vdots & & \ddots & A_{N-1}^* & B_{N-1}^* & \ddots & \vdots \\ \vdots & & & \ddots & A_N^* & B_N^* & 0 \\ 0 & \dots & \dots & \dots & 0 & A_{N+1}^* & B_{N+1}^* \end{bmatrix} \begin{Bmatrix} T'_1 \\ T'_2 \\ T'_3 \\ \vdots \\ T'_{N-1} \\ T'_N \\ T'_{N+1} \end{Bmatrix} = \begin{Bmatrix} D_1^* \\ D_2^* \\ D_3^* \\ \vdots \\ D_{N-1}^* \\ D_N^* \\ D_{N+1}^* \end{Bmatrix} \quad (D.13)$$

It will be noted that this reduction implies that the  $A^*$ ,  $B^*$ ,  $C^*$ , and  $D^*$  terms involve only known quantities evaluated at the beginning of the time step. In particular, the surface recession rate ... is treated in this explicit manner. This cause little error since the energy term involving  $\dot{s}$  are small compared to the other energy terms. The expressions for the coefficients  $A_n^*$ ,  $B_n^*$ ,  $C_n^*$  and  $D_n^*$  are easily expressed. For the last node ( $n = N + 1$ ):

$$\begin{cases} A_{N+1}^* = A_{N+1} \\ B_{N+1}^* = B_{N+1} \\ D_{N+1}^* = D_{N+1} \end{cases} \quad (D.14)$$

for the interior nodes ( $n = 2, \dots, N$ ):

$$\begin{cases} A_n^* = A_n \\ B_n^* = B_n - C_n \frac{A_{n+1}^*}{B_{n+1}^*} \\ D_n^* = D_n - C_n \frac{D_{n+1}^*}{B_{n+1}^*} \end{cases} \quad (\text{D.15})$$

for the first node ( $n = 1$ ):

$$\begin{cases} B_1^* = B_1 - C_1 \frac{A_2^*}{B_2^*} \\ D_1^* = D_1 - C_1 \frac{D_2^*}{B_2^*} \end{cases} \quad (\text{D.16})$$

Of the reduced set of equations (D.13), only the top-most equation is of immediate interest. It may be arranged as:

$$\dot{q}_{cond} = \mathcal{F}_s(T_w) \quad (\text{D.17})$$

where  $\mathcal{F}_s$  is a simple linear relation and  $T_w$  is the unknown surface temperature.

In fact, from Eqs. (D.13)):

$$B_1^* T'_1 = D_1^*$$

now from the expression of  $B_1^*$  and  $D_1^*$  it can be easily found that:

$$\dot{q}'_{cond} = \frac{B_1^*}{C_2} T'_1 - \frac{C_1}{C_2} + \frac{C_1}{C_2} \frac{D_2^*}{B_2^*} - \dot{q}_{cond} \quad (\text{D.18})$$

**Table D.1** – Ablative material properties.

$\rho_s, \text{kg m}^{-3}$	$k_s, \text{W m}^{-1} \text{K}^{-1}$	$c_p, \text{J kg}^{-1} \text{K}^{-1}$
1850	30	2000

with

$$\begin{cases} C_1 &= (4\Delta x^2 - 4\alpha\Delta t)T_1 + (4\alpha\Delta t)T_2 \\ C_2 &= 2\frac{\Delta x\Delta t}{k}(2\alpha - \dot{s}\Delta x) \end{cases}$$

Eq. (D.18) is a simple linear relation of the form:

$$\dot{q}'_{cond} = A_s T'_1 + B_s \quad (\text{D.19})$$

Since  $T'_1 = T_w$ , Eq. (D.19) is the desired relation between  $\dot{q}_{cond}$  and  $T_w$  implied by the in-depth solution.

## Verification of the material response code

To verify the material response models, a constant properties semi-infinite slab was simulated with a thickness large enough to ensure that the final node showed no temperature response during the computation. The selected property values are listed in Table D.1. As explained in [25], the exact solution to the semi-infinite slab problem with uniform initial temperature  $T_0$  and step surface temperature  $T_w$  at time  $t = 0$  is a similarity solution:

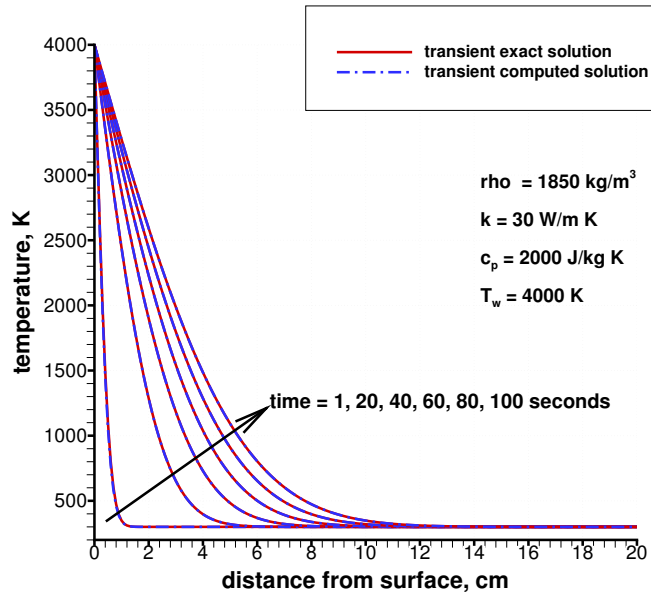
$$\frac{T - T_0}{T_w - T_0} = 1 - \text{erf}(x^*) \quad \text{where } x^* = \frac{x}{2\sqrt{\alpha t}}$$

In this preliminary analysis, the surface and initial temperature,  $T_w$  and  $T_0$ , are taken equal to 4000 K and 300 K, respectively.

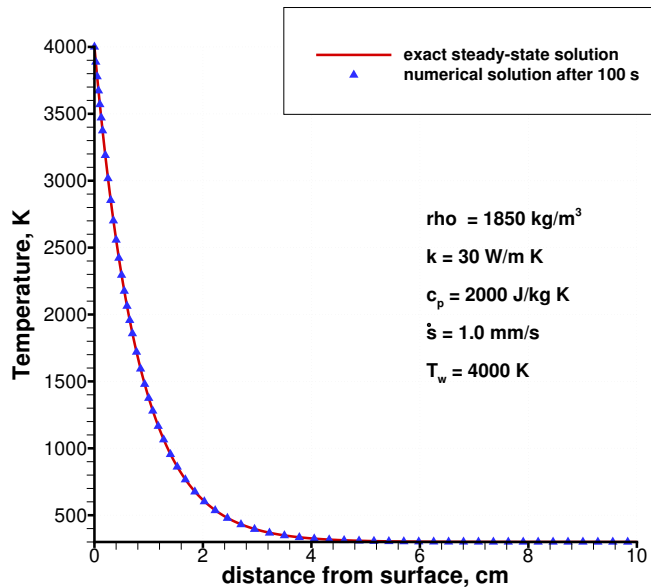
The material thermal response is simulated over a period of 100 s with a material thickness of 20 cm which ensures satisfactorily the condition of no temperature rise of the last node. The time step selected is equal to 0.1 s and the nodal size is equal to 1 mm for each node. Figure D.1(a) shows the exact transient temperature profiles and the computed ones. The agreement between the exact and computed solution is excellent even at the early times which ensures that the transient thermal diffusion process is properly handled. Check-out of the convection aspects of the computation requires a problem with surface recession. An analytical solution is available for the transient response of a semi-infinite slab initially at uniform temperature exposed to a step in surface temperature,  $T_w = 4000$  K, and to a step in surface recession rate,  $\dot{s} = 1$  mm s<sup>-1</sup>. For the constant properties problem, it can be readily shown that the temperature profile approaches a steady form [52]:

$$\frac{T - T_0}{T_w - T_0} = \exp\left(-\frac{\dot{s}x}{\alpha}\right)$$

where the  $x$  coordinate origin is tied to the receding surface. Figure D.1(b) shows the exact steady-state temperature profile compared to the computed profile after 100 seconds. This time is long enough to reach the steady-state for the present conditions and the agreement between computed and exact profile is excellent.



(a) Temperature profiles of a constant properties semi-infinite slab exposed to a step in surface temperature.



(b) Steady-state temperature profile of a semi-infinite slab exposed to a step in surface temperature and recession rate.

**Figure D.1** – Material response code verification tests.